

NGL-21-002-367

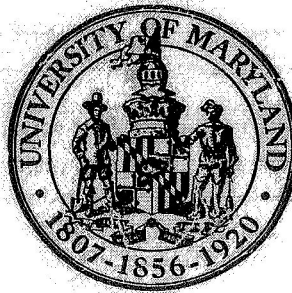
FINAL TECHNICAL REPORT

NASA GRANT - NGL 21-002-367

(NASA-CR-153024) FINAL TECHNICAL REPORT
(Maryland Univ.) 206 p

N77-78264

00/89 Unclass
25133



CLARK LAKE RADIO OBSERVATORY

ASTRONOMY PROGRAM

UNIVERSITY OF MARYLAND

COLLEGE PARK, MARYLAND



**Clark Lake Radio Observatory is owned and operated
by the University of Maryland. Correspondence
relating to the observatory should be addressed to**

**Clark Lake Radio Observatory
Post Office Box
Borrego Springs, Calif. 92004**

**Requests for reprints, preprints, and data should
be sent to**

**Clark Lake Radio Observatory
Astronomy Program
University of Maryland
College Park, Md. 20742**

**The Astronomy Program would appreciate receiving
preprints and reprints related to Astronomy.**

FINAL TECHNICAL REPORT

NASA GRANT - NGL 21-002-367

M. R. Kundu

W. C. Erickson

I. Research in Solar Radio Astronomy

A. Publications

- † 1. "Positions and Motions of Solar Bursts at Decameter Wavelengths", M. R. Kundu, W. C. Erickson, P. D. Jackson and J. Fainberg, 1970, Solar Phys. 14, 394.
2. "Solar Bursts at Decameter and Hectometer Wavelengths", M. R. Kundu, in "Physics of the Solar Corona" (ed. C. J. Macris, D. Reidel Publ. Co.), 1971, p. 287.
- ✓ 3. "Meter and Decameter Wavelength Position of Solar Bursts of July 31-August 7, 1972," M. R. Kundu and W. C. Erickson, IAU Symp. No. 57 "Coronal Disturbances", Sept. 8-11, 1973.
- ✓ 4. "Decameter Type IV Bursts Associated with Coronal Transients," T. E. Gergely and M. R. Kundu, Solar Phys., 34, 433, 1974.
5. "Meter and Decameter Wavelength Positions of Solar Bursts of July 31-August 7, 1972," M. R. Kundu and W. C. Erickson, Solar Phys., 36, 179, 1974.
- # 6. "Type III Burst Positions," T. B. H. Kuiper, Ph.D. Thesis, University of Maryland, 1973.
- # 7. "Decameter Storm and Type IV Radiation," T. E. Gergely, Ph.D. Thesis, University of Maryland, 1974.
- ✓ 8. "Decameter Storm Radiation, I," T. E. Gergely and W. C. Erickson, Solar Phys. 42, 467, 1974.
- ✓ 9. "Decameter Storm Radiation, II," T. E. Gergely and M. R. Kundu, Solar Phys. 41, 163, 1974.
- ✓ 10. "Observations of Coronal Disturbances from 1 to 9 R_⊙ II - Second Event of January 11, 1973," R. T. Stewart, R. Howard, S. F. Hansen, T. E. Gergely and M. R. Kundu, Solar Phys., 36, 219, 1974.
- ✓ 11. "Detailed Correlation of Type III Radio Bursts with H α Activity, I: Active Region of May 22, 1970," T. B. H. Kuiper, and J. M. Pasachoff, Solar Phys., 28, 187, 1973.
- +12. "On the Density of the Corona in Regions of Type III Activity," T. B. H. Kuiper, Proc. of NASA Symp. on "High Energy Phenomena on the Sun," p. 540, 1973.
- ✓ 13. "Detailed Comparison of Type III Radio Bursts with H α Activity, II: The Isolated Type III Activity of March and April, 1971," T. B. H. Kuiper, Solar Phys. 33, 461, 1973.
- ✓ 14. "Coronal Density Structures in Regions of Type III Activity," Y. Leblanc, T. B. H. Kuiper, and S. F. Hansen, Solar Physics, 37, 215, 1974.

15. "On the Probability of Occurrence of the Type IIIb Burst as a Precursor," J. de la Noë, 1974, Solar Phys., 37, 335.
16. "Theory of Type IIIb Radio Bursts", R. A. Smith and J. de la Noë, 1976, Ap. J., 207, 605.
- ✓ 17. "A Decameter Type II Burst, Associated with a Behind-the-Limb Flare," T. E. Gergely and M. R. Kundu, 1976, Solar Phys., (in press).
- † 18. "Observations of the Quiet Sun at Meter and Decameter Wavelengths", M. R. Kundu, T. E. Gergely and W. C. Erickson, Solar Phys. (in press), 1976.
19. "The Decameter Spectrum of the Quiet Sun", W. C. Erickson, T. E. Gergely, M. R. Kundu and M. J. Mahoney, 1977, submitted to Solar Phys.
- † 20. "Relative Positions of the Fine Structure Bursts in Decametric Storms", J. de la Noë and T. E. Gergely, 1976, in preparation (to be submitted to Solar Physics).

II. Research in Cosmic Radio Astronomy

- ✓ # 1. "A 26.3 MHz Radio Source Survey with an Absolute Flux Scale," M. R. Viner, Ph.D. Thesis, University of Maryland, 1973.
- ✓ 2.* "VLBI Observations of the Crab Nebula Pulsar," N. R. Vandenberg, T. A. Clark, W. C. Erickson, G. M. Resch, J. J. Broderick, R. R. Payne, S. H. Knowles and A. B. Youmans, *Astrophys. J.*, 180, L27, 1973.
- + 3.* "Long Wavelength VLBI," T. A. Clark and W. C. Erickson, *Proc. IEEE*, 61, 1230, 1973.
- ✓ 4. "26.3 MHz Radio Source Survey, I - The Absolute Flux Scale," M. R. Viner *Astro. J.*, 80, 83, 1975. (see Appendix V)
- 5. "26.3 MHz Radio Source Survey, II - Source Fluxes and Positions," M. R. Viner and W. C. Erickson, *Astro. J.* 80, 931, 1975.
- + 6.* "Meter Wavelength VLBI: I. Cassiopeia A," L. K. Hutton, T. A. Clark, G. M. Resch, N. R. Vandenberg, W. C. Erickson, and S. H. Knowles, *Astro. J.*, 79, 1248, 1974.
- + 7.* "VLBI Observations of the Crab Nebula Pulsar," N. R. Vandenberg, Ph.D. Thesis, University of Maryland, Aug. 1974.
- + 8.* "Meter Wavelength Observations of Compact Radio Sources," G. M. Resch, Ph.D. Thesis, Florida State University, Nov. 1974.
- ✓ 9. "An Anomaly in the Flux of Cassiopeia A at 38 MHz," W. C. Erickson and R. A. Perley, *Astro. Phys. J. Lett.*, 200, 83, 1975.
- + 10.* "Meter Wavelength VLBI: II. The Observations," T. A. Clark, W. C. Erickson, L. K. Hutton, G. M. Resch, N. R. Vandenberg, J. J. Broderick, S. H. Knowles, and A. B. Youmans, *Astro. J.*, 80, 923, 1975.
- + 11. "26.3 MHz Radio Sources Survey. III - Decametric Wavelength Identification of X-ray Sources," W. C. Erickson, T. A. Matthews, and M. R. Viner (submitted).
- ✓ 12.* "Meter Wavelength VLBI. III. Pulsars", N. R. Vandenberg, T. A. Clark, W. C. Erickson, and G. M. Resch, *Astrophys. J.*, 207, 937, 1976.

* (These VLBI papers are not strictly Clark Lake publications in the sense of using antennas at Clark Lake. However, they were initiated during the construction work in order to maintain a reasonable level of scientific productivity.

The VLBI program did involve some expenditure of Clark Lake funds and made use of Clark Lake equipment and personnel. W.C.E.)

+ Not included

Available upon request

III. Research in Radio Astronomical Instrumentation

- ✓ 1. "The Log Periodic Array at the Clark Lake Radio Observatory," W. C. Erickson and T.B.H. Kuiper, Radio Science, 8, 845, 1973.
- ✓ 2. "The Clark Lake Array," W. C. Erickson, Proc. IEEE, 61, 1276, 1973.
- ✓ 3. "A New Wideband, Fully Steerable, Decametric Array at Clark Lake," W. C. Erickson and J. R. Fisher, Radio Science 9, 387, 1974.

3

METER AND DECAMETER WAVELENGTH POSITIONS OF SOLAR BURSTS OF JULY 31–AUGUST 7, 1972

M. R. KUNDU and W. C. ERICKSON

Astronomy Program, University of Maryland, College Park, Md., U.S.A.

(Received 24 August, 1973; in revised form 30 January, 1974)

Abstract. The positional analysis of solar bursts at meter and decameter wavelengths observed during the period July 31–August 7, 1972 is presented. Most of the activity during this period was associated with the active regions McMath 11976 and 11970. Except near the CMP of region 11976, two regions of continuum emission were observed – one a relatively smooth continuum and the other a continuum superimposed with many type III's and other fine structure. It seems possible to interpret these continua in terms of plasma waves originating from two sources located at different heights or with different electron density gradients. The angular size of type III sources seems to increase with decreasing frequency. This implies that the open field lines along which the type III electrons travel have larger angular extent at greater heights.

1. Introduction

During July 30–August 7, 1972, a series of solar radio storms occurred. These storms produced intense type III bursts and continuum storms in the frequency range 10–120 MHz. Studies of these bursts and other associated electromagnetic radiation, including the H α flares, have appeared in a number of published papers. In the present paper we present the results of positional analysis of burst sources in the range 10–120 MHz during this period of spectacular solar flare activity.

The observations were taken with two arrays – a log periodic array of 16 elements situated on an E–W base line of 3.3 km (Erickson and Kuiper, 1973) and portions of the new Clark Lake array in the form of a Tee (an E–W arm of 32 log spiral antennas and a N–S arm of 16 similar antennas). The new array (Erickson, 1973) operates over the frequency range 10–120 MHz and has angular resolutions of approx. 3'5 at 100 MHz and 8'5 at 40 MHz in the E–W direction. In the N–S direction the instrument has a resolution of 6' at 100 MHz and 15' at 40 MHz.

During this period the activity was often so complex that we represent it only by 'snapshots' taken at representative times. We then note the times when significant changes appear to occur. Positions will be given for the apparent center of activity. No corrections have been made for ionospheric refraction and the positions are most reliable within about 2 hr of solar transit (\sim 1945 UT). In assessing the significance of the positions that we give, the limited angular resolution of the instrument and the large angular size of some of the emissive regions must be borne in mind.

A photograph of some of the original data is presented in Figure 1. In Figures 2 to 5 we diagrammatically represent the data. We generally give three positions, a high frequency position in the 90–110 MHz range, an intermediate frequency in the 60–80 MHz range and a low frequency in the 30–50 MHz range. The lower frequencies

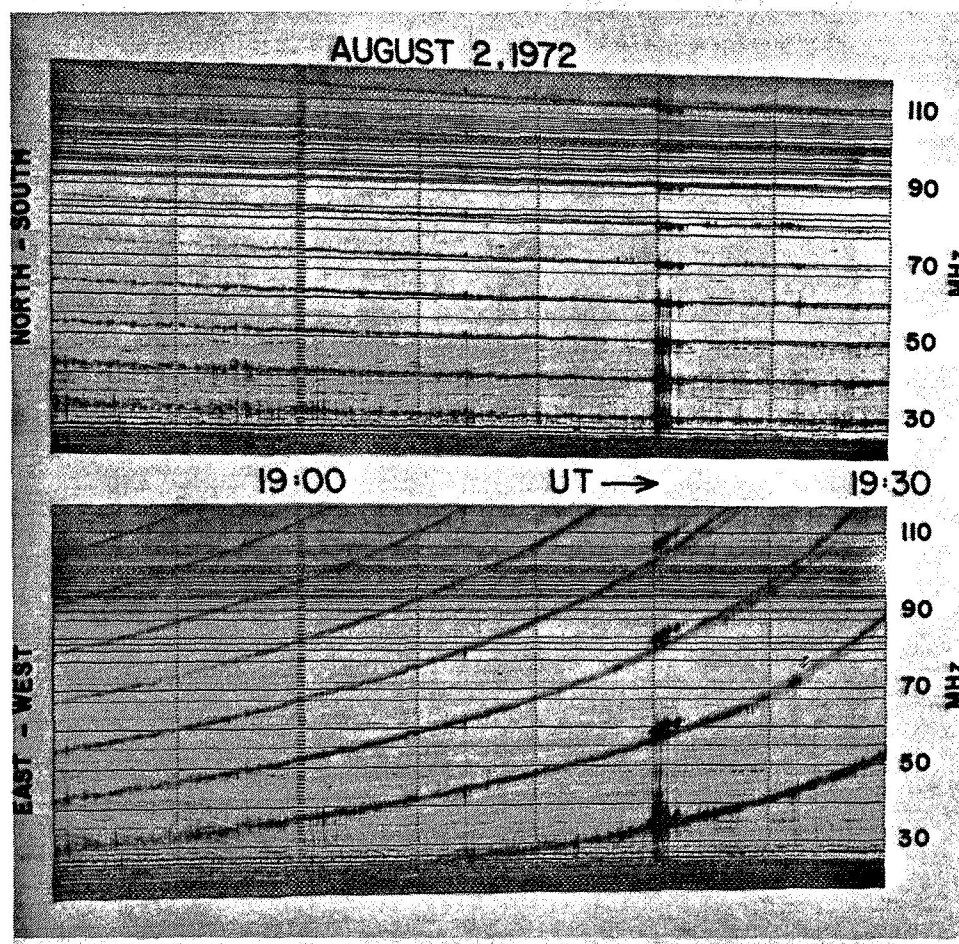


Fig. 1. Radio spectrograms of solar continuum obtained during the period 1848–1930 UT on August 2, 1972. These recordings were taken with swept frequency receivers attached to the output of and E–W grating arrays. The receivers sweep the 20 to 120 MHz spectrum twice per second; as they sweep, lobes of the grating array's response cross the Sun. Determination of time and frequency gives the position of the source. The rather steady sloping bands of continuum originate in regions Ca and Cb as shown in Figure 2. The type III bursts at 1918–1920 UT originate in a region in the S–W (see Figure 2). Interference below 30 MHz and FM transmissions in the 88 to 108 MHz are plainly visible.

are omitted when the Sun is far from transit, since they would be seriously disturbed by ionospheric refraction. The exact choice of frequencies for each measurement depends upon the frequency range of the emission, the positions of the antenna lobes and freedom from terrestrial interference.

If two identical sources are scanned with the perpendicular fan beams of our system, the data are generally ambiguous because the two fan beams intersect at four points where the sources could be located. However when we observe double regions

of solar emission this ambiguity practically never arises because we can easily correlate the intensity variations observed with the E–W and N–S arrays to uniquely determine the position of each source.

2. Observations

The activity in the frequency range 20–120 MHz during the period July 31–August 7, 1972 was mostly in the form of type III and continuum events. The type III's appeared to be associated with two regions McMath 11976 and 11970, and after August 3, possibly also with the region 11977. The source of continuum emission which was sometimes double in structure was associated only with the region 11976. In what follows we give a brief description of important features of the 20–120 MHz activity by means of selected 'snapshots' (Figures 2 to 5).

Several type III bursts observed on July 31 between 1833 and 2014 UT were apparently associated with the region 11976. The burst source (only E–W position available) was situated about $1.3 R_{\odot}$ E from the center of the Sun. On August 1, a strong group of III's observed between 2118.5 and 2120.5 UT was most likely associated with the region 11970. The burst position showed considerable dispersion in frequency (Figure 2). On August 2, a continuum source apparently associated with the region 11976 existed from the start of the observations. Type III bursts were occurring frequently on this day and until 1907 UT were all located near the S–W limb, apparently associated with the region 11970. A type V was observed at 1801.5–1803 UT below 65 MHz and was considerably displaced in position from the accompanying type III. Around 45 MHz the type V was distinguished from type III by its narrow angular size (Figure 2). The large impulsive flare that occurred in region 11976 at ~ 1840 UT produced no radio emission in the 20–120 MHz range. However, at about 1900 UT a second continuum appeared at $\sim 0.2 R_{\odot}$ E of the first continuum in the 70 MHz frequency range, also apparently associated with region 11976. It was smooth and of small angular size. At 1907.5 the first type III occurred in the N–E quadrant (Figure 2) – possibly associated with the activity in McMath 11976. At 1918 UT there was another strong type III group in the S–W quadrant (Figure 2). Dodge (1973) placed this type III group in the N–E quadrant but a glance at Figure 1 shows that the lobes of this group are clearly to the high frequency (western) side of the continuum source. About 1920 UT the second continuum intensified in the 80 to 110 MHz range and by 1924 UT the two continuum sources were clearly resolved at 110 MHz (Figure 2) and the second one became bursty. At 70 MHz the two continuum sources were unresolved in the E–W direction and barely resolved in the N–S direction. At 40 MHz the continuum source was of large angular size and was centered S–E. At 2018 UT a type IIIg occurred at high frequencies (~ 100 MHz) at the N–E limb. This region developed into a continuum which started to increase in intensity after 2018 UT below 50 MHz. By 2033 UT the emission spread over the entire frequency range 20–120 MHz and saturated the receiver. This extremely intense emission was associated with the second large flare in region 11976

at 2000–2030 UT. It is remarkable that this second flare which was very similar in structure to the one that occurred at ~ 1840 UT produced strong radio emission whereas the first one did not produce any obvious effect. At 2100 UT the continuum was in the N–E quadrant; it was strong in intensity and so large in angular size that its possible double structure could not be discerned. The 40 MHz position appears to be displaced to the east (by about $1 R_0$) from the 100 and 70 MHz position. This shift is possibly due to the ionospheric refraction. About 2118 UT there were two reasonably smooth and distinct continua at higher frequencies of 100 MHz (Figure 2). At lower frequencies of 70 and 40 MHz we could recognize only one continuum which appears to have been disturbed by the ionospheric effects (Figure 2). Often the distinction between bursty and smooth continua is quite arbitrary. On many occasions a source will appear relatively smooth in the 100 MHz region while it is bursty at lower frequencies and appears as though it were the result of the superposition of many type III's or type I's. This is illustrated quite clearly in Figure 1 between 1848 and 1906 UT. On the other hand, there do exist definite type III's which are usually displaced from the continuum (e.g. at 1919 UT in Figure 1).

On August 3, smooth continuum existed all day – situated about $0.4 R_0$ E from the center (Figure 3). There was only small dispersion in position with frequency. Around 1742 UT, starting at higher frequencies and spreading gradually to lower frequencies there appeared groups of short duration (~ 1 s) narrowband (2–3 MHz wide) type I-like bursts. But about 1745 UT these bursts occurred at random over the entire frequency range and continued throughout the day.

The smooth continuum continued through the first part of the next day (August 4). During the period 1600–1800 UT the continuum at 110 MHz was located $\sim 0.2 R_0$ S from the center (Figure 3). The angular size of the continuum was large ($\sim 1.2 R_0$) at 60 MHz and smaller at 30 MHz. Below about 50 MHz the emission consisted mostly of type III's superimposed on a weak continuum. The type III's were located in the same position as the continuum (on-band), between the regions McMath 11976 and 11977. At 2030 UT the continuum position at frequencies above 70 MHz remained near the center but it was shifted by $0.8 R_0$ to the SE at lower frequencies where the emission was mostly type III's.

On August 5, both continuum and type III's were still observed. At 1830 UT, the continuum at 110 MHz was barely resolved, indicating possible double structure. The two components (both narrow in size) were located at the center and $0.2 R_0$ W. At 1900 UT the continuum source was definitely double at both 100 and 70 MHz and was located in the N–W quadrant at $0.3 R_0$ and $0.8 R_0$ from the center. At lower frequencies the emission consisted mostly of type III's located at the W-limb. At 1924 UT the continuum located near the center became bursty at 100 and 70 MHz; at 40 MHz only one bursty continuum appeared at $0.7 R_0$ W from the center. Later the continuum at 40 MHz showed double structure and the easterly one was bursty as shown in Figure 4 for 2018 UT. By 2100 UT the previously observed smooth continuum source at 100 MHz had almost died and the bursty continuum became

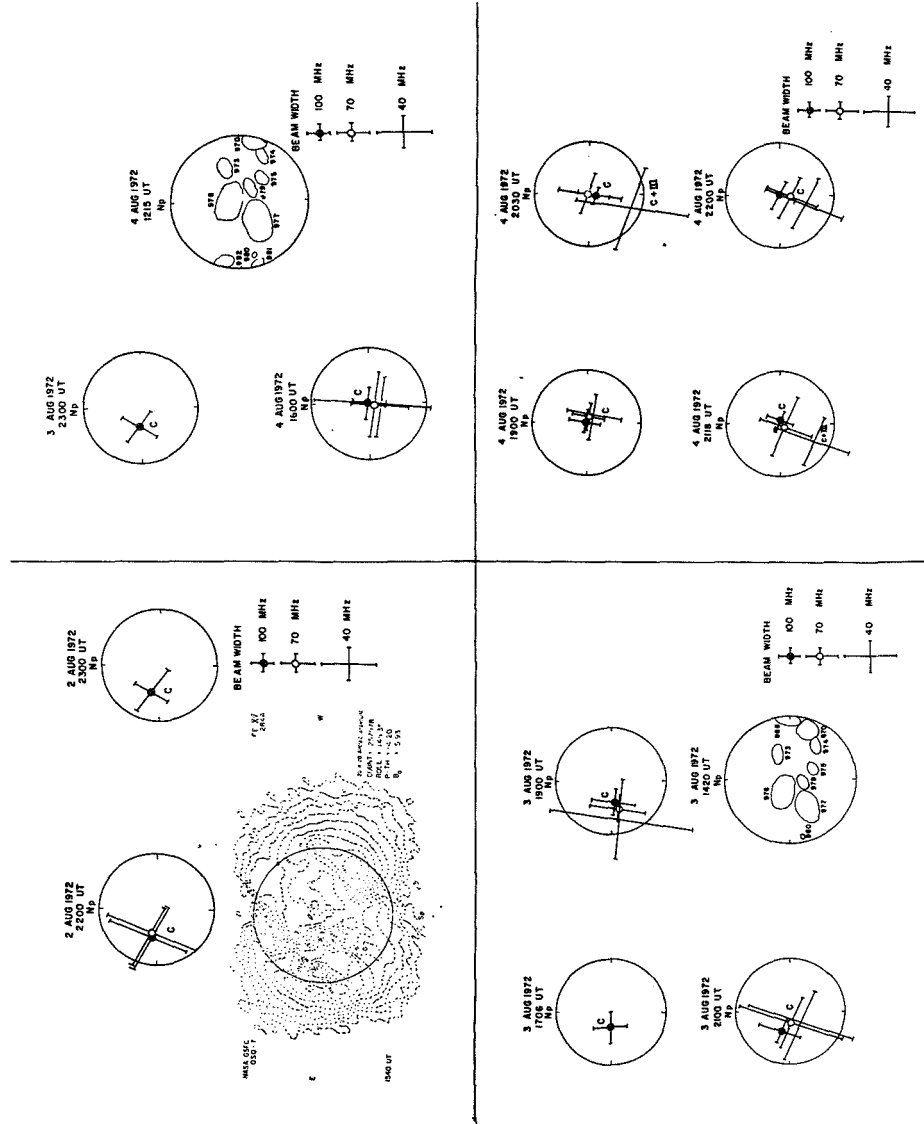


Fig. 3. Positions of bursts observed on August 2 (2200-2300 UT), August 3 and August 4, along with the Fe xv line (284 Å) map for August 2 obtained by NASA-GSFC OSO-7. The radio positions are indicated in the same way as in Figure 2. Also included are the McMath-Hulbert calcium reports for August 3 and 4.

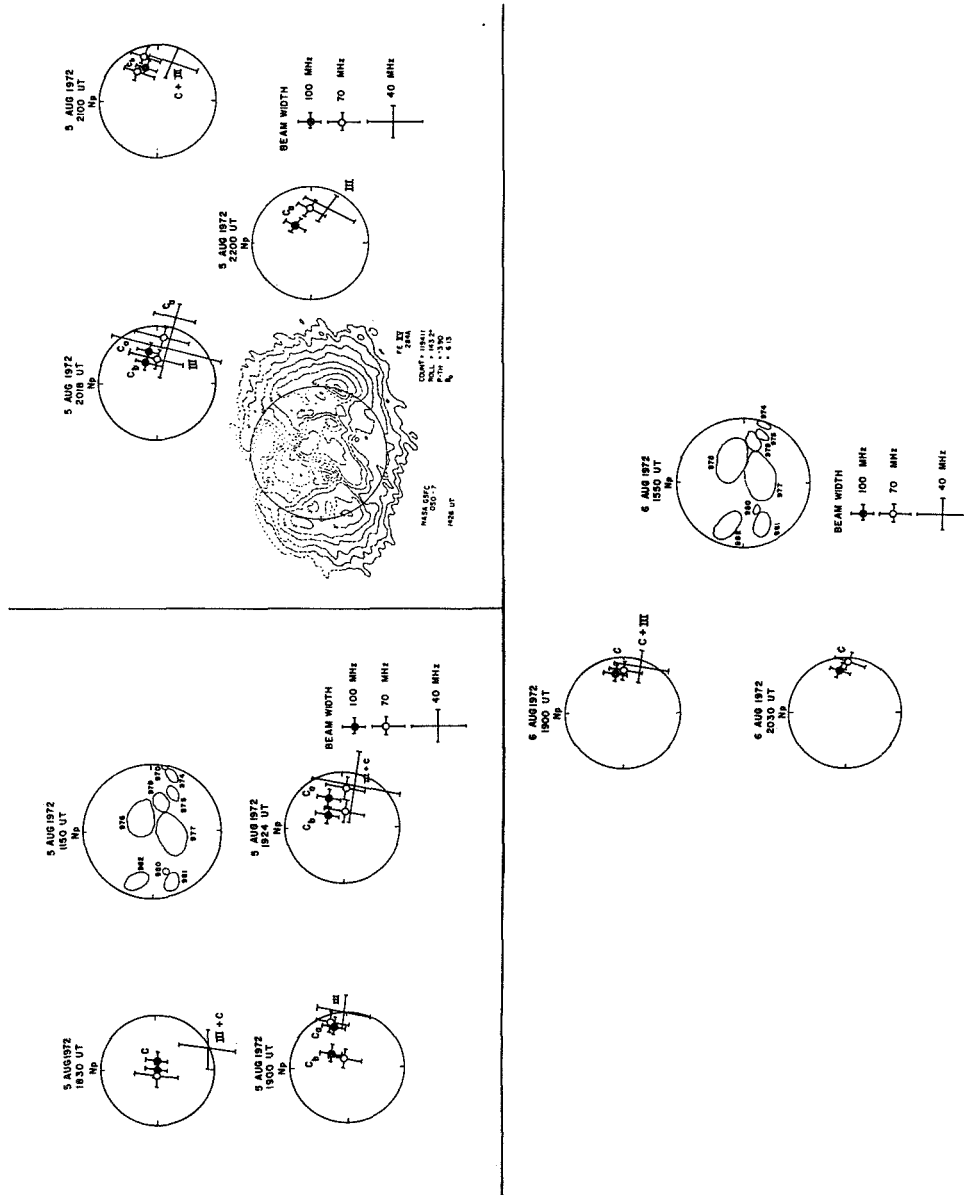


Fig. 4. Positions of bursts for August 5 and 6, together with the McMath-Hulbert calcium reports. Also included is the Fe xv line (284 Å) map for August 5, obtained by NASA-GSFC OSO-7. The radio positions are indicated in the same way as in Figure 2.

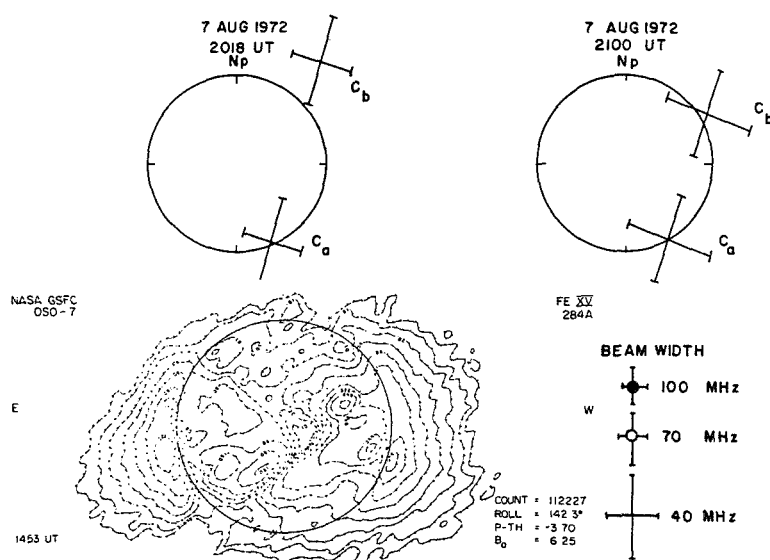
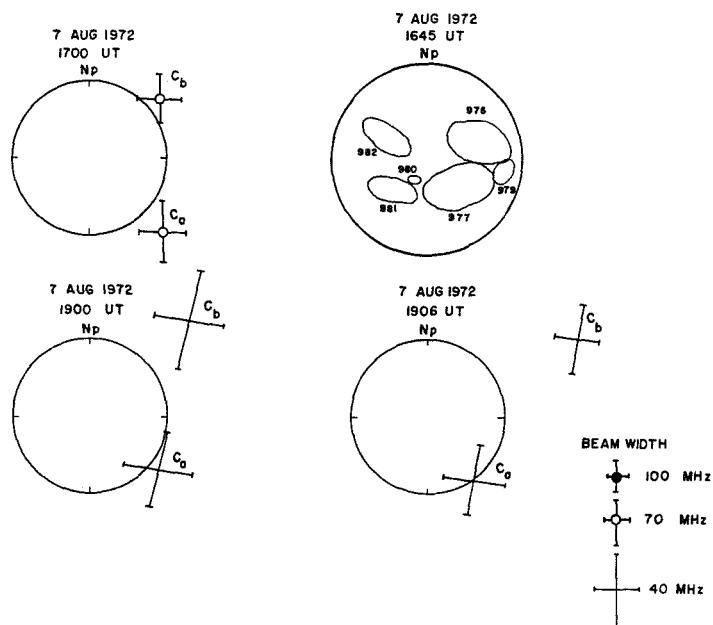


Fig. 5. Positions of bursts for August 7, together with the McMath-Hulbert calcium report and the Fe xv line (284 Å) map obtained by the NASA-GSFC OSO-7. The positions are indicated in the same way as in Figure 2.

smooth and stronger (Figure 4). At 70 MHz a part of the smooth continuum was still visible, the two positions being in the N–W quadrant at $0.4 R_0$ W and $0.7 R_0$ W. At 40 MHz the continuum source with type III's was of large angular size and was located at a position intermediate between those of the two continua observed earlier.

On August 6, the emission was mostly smooth continuum except that there were some on-band type III's randomly distributed around 1700 UT. The intensity was stronger at higher frequencies. The source was located about $0.8 R_0$ N–W, with some dispersion in position (Figure 4). At 40 MHz the emission consisted mostly of type III's plus a very weak continuum.

On August 7, a great flare occurred around 1510 UT in the region McMath 11976, with its maximum at 1530 UT. Our observations began at 1600 UT in the post-maximum phase of the flare. Initially, the continuum was smooth; very strong at lower frequencies and weak at the high frequency end. At 70 MHz it was located at an apparent position of $2.5 R_0$ S–W. At this time of the day there may have been considerable ionospheric refraction effects at 70 MHz. At 1700 UT the source was double – $1.3 R_0$ S–W and $1.2 R_0$ N–W at 70 MHz (Figure 5). The northern source was bursty. Both continuum sources were weak at higher frequencies. Groups of type III's continued to occur between the two continuum sources as well as on both continuum sources. By 1900 UT the continuum was very weak at higher frequencies. At 35 MHz the source was double – located at $1.1 R_0$ S–W and $1.8 R_0$ N–W (Figure 5). At 1905–08 UT the northern bursty continuum source became smooth and moved to the west (Figure 5) from $1.8 R_0$ at 1900 UT to $2.2 R_0$ at 1906 UT. This motion corresponds to a velocity of $1400 \pm 400 \text{ km s}^{-1}$. This moving source appears to be an ejection from the continuum source 'C_b' and by 1909 UT it had disappeared completely. By 2018 UT both continuum sources appeared at lower frequencies; they were fairly smooth and were located at $1.0 R_0$ S–W and $1.4 R_0$ N–W (Figure 5). At 2100 UT the source had the same appearance.

3. Discussion

Most of the activity during the period July 31–August 7, 1972 was associated with the regions McMath 11970 and 11976; another region McMath 11977 possibly became active after August 3. One important characteristic of the region 970 was that no continuum was observed in association with it; only type III's and a type V were observed from this region. The radio emissive activity in region 970 generally intensified during the period of strong activity in region 976. Indeed, the strong type IIIg that occurred at 2100 UT on August 2, followed the maximum of the flare that occurred in region 976.

The continuum emission during this period appears to be associated mostly with the region 976. Frequently, the source was double with one component a relatively smooth continuum and the other a continuum with superimposed type III's and other fine structure. It is interesting to note that the double structure of the source disappeared around the central meridian passage (CMP) of the region (August 3–4) and

appeared again on August 5. On August 6 we also observed only one component but the intensity of the emission had decreased considerably and one of the components may have been too weak to be observed.

The sources at decameter wavelengths (40 MHz), whether they produce continuum or type III's appear to be very well associated with corresponding regions on the OSO-7 maps of Fe xv line at 284 Å (see Figures 3, 4 and 5). This close correspondence between the two possibly indicates that the decametric emissive regions originate in about the same level of the Sun's corona as the Fe xv line.

In general, there appears to be some dispersion of continuum position with frequency. This is true for observations near local transit and when the source is away from the disk-center. For observations at large hour angles, ionospheric effects may be important and the frequency dispersion is not always apparent. We might remark that the continuum sources are narrower in angular size at higher frequencies than at lower frequencies. In general, the sources appear very broad at 40 MHz, especially when the continuum is strong. The size at low frequencies also appears broad when there are type III's superimposed on the continuum. The continuum source at both meter and decameter wavelengths appears to be stationary and it shows some dispersion in position with the frequency. It is generally accepted that such stationary continuum radiation can be produced by Čerenkov plasma waves.

The observed double structure of the continuum source is obviously related to the existence of two separate component sources. If the two component sources were displaced laterally, there would be greater separation between them near the CMP of the region. The fact that the double structure appears only when the region is away from the CMP may imply that the two component sources are situated at different heights. A consequence of this displacement in height is that the higher source should appear farther from the center on either side of CMP. This seems to have been observed, although we cannot unambiguously distinguish between two components, since both contain bursty structure.

As we know, the continuum emission results from plasma radiation propagating in the ordinary mode in a strong magnetic field (Takakura, 1963). Therefore, it is conceivable that the two component sources are situated either along two streamers with different densities or more likely, one along a streamer with open field lines and the other in the strong magnetic field lines above an active region, somewhat similar to the model proposed by Stewart and Labrum (1972). Open field lines provide a path for the type III electrons; the electrons seem to be ejected continuously from the continuum which therefore appears bursty. The relatively smooth continuum source is situated in the closed field lines. In our frequency range, we see very few type I's on the continuum; sometimes at the lower frequencies we see type I – like bursts constituting and superimposed on the continuum. In this context, we might consider the mechanism proposed by Gordon (1971), in which the low phase-velocity plasma waves (responsible for type I bursts) are scattered to high phase velocities (0.1–0.6 c). These waves are ultimately responsible for the acceleration of type III electrons. One consequence of such a mechanism is that it may produce

type I and type III bursts from the same source; this seems to have been observed to some extent. This simple interpretation seems to be borne out by the result that the continuum systematically appears at a lower height than the type III's. The only exception to this appears in the case of the flare-associated continuum observed on August 7, 1900 UT. We believe that in this case we were dealing with a continuum at decametric wavelengths, that had been ejected from the parent smooth continuum. In the Stewart and Labrum model one distinguishes between the type I and type III sources. However, at decameter wavelengths (~ 40 MHz) we often see continuum with superimposed fine structure which resemble type III's rather than type I's. Indeed, it is often extremely difficult to distinguish continuum from almost continuously occurring sources of type III's at decameter wavelengths. In their model, Stewart and Labrum postulated that the type III electrons are accelerated near the observed 80 MHz source position and that the required energy is released by the triggering of a magnetic instability at this point by a magnetohydrodynamic disturbance propagating from the type I source region. We often observe a relatively smooth continuum in the 90–120 MHz region; this continuum source, situated in the strong field lines above an active region, is a likely source of mhd waves. When sufficiently energetic mhd waves reach the top of closed field lines and trigger an instability at the cusp of a helmet magnetic structure, type III bursts begin to be observed. Our observations indicate that this height, where type III bursts start, is situated around 50–60 MHz plasma level.

We would like to draw attention to another property of type III bursts. The angular size of strong type III increases with decreasing frequency and sometimes reaches up to $4\text{--}5 R_0$ at 40 MHz. However, we should point out that these intense low frequency bursts saturated the records and accurate angular size measurements were difficult. We do not believe that this large size can be fully accounted for by coronal scattering. Consequently, this result would imply that the open field lines along which type III electrons travel has a rather large lateral extent.

Acknowledgements

This work was supported by NSF grant GP-19401 and NASA grant NGR 21-002-367. The computer time for this project was supported by National Aeronautics and Space Administration Grant NSG-398 to the Computer Science Center of the University of Maryland.

References

- Dodge, J. C.: 1973, preprint, Solar System Radio Observations, SN-1, of the University of Colorado.
- Erickson, W. C.: 1973, *Proc. IEEE* **61**, 1276.
- Erickson, W. C. and Kuiper, T. B. H.: 1973, *Radio Sci.* **8**, 845.
- Gordon, I. M.: 1971, *Astrophys. Letters* **5**, 251.
- Stewart, R. T. and Labrum, N. R.: 1972, *Solar Phys.* **27**, 192.
- Takakura, T.: 1963, *Publ. Astron. Soc. Japan* **15**, 462.

DECAMETER TYPE IV BURSTS ASSOCIATED WITH CORONAL TRANSIENTS

T. E. GERGELY and M. R. KUNDU

Astronomy Program, University of Maryland, College Park, Md., U.S.A.

(Received 24 August; in revised form 6 December, 1973)

Abstract. The characteristics of four moving type IV bursts, observed with the 65–20 MHz swept-frequency interferometer of the Clark Lake Radio Observatory are discussed. All four bursts were associated with depletions in the electron content of the white light corona. Characteristics of the bursts are not unique, i.e. they differ in source size, structure, duration and their association with other radio bursts. Following Smerd and Dulk (1971) we believe that a shock wave, moving out from the flare site is responsible for the expansion of a magnetic arch or the ejection of a plasmoid which is observed as the usual type IV burst. Behind the shock wave, the compressed coronal gas moves outward, and as it expands it causes a depletion of electrons in the inner corona. After the passage of the shock wave, sometimes the coronal magnetic field structure is restored to its initial situation, as evidenced by the observation of homologous transients.

1. Introduction

Coronal transient-events during which an entire coronal feature is depleted have been observed on a number of occasions in recent years. These events are well observed in the K-corona (Hansen *et al.*, 1971); in the inner corona they are sometimes seen as realignments or accelerated expansion of an arch system in the green coronal line ($\lambda 5303 \text{ \AA}$) (De Mastus and Wagner, 1973). They are usually, but not always, associated with strong moving type IV bursts in the meter and decameter wavelength range. In this paper we present the characteristics of some of these bursts as observed with the swept frequency interferometer of the Clark Lake Radio Observatory operated by the University of Maryland. This array (hereinafter referred to as the L.P.A.) consists of sixteen log-periodic antennas, equally spaced on a two mile east-west baseline. The array is swept in frequency over the range 20–65 MHz once per second. This system gives the one dimensional position and angular size of emissive regions on the Sun nearly simultaneously at all frequencies. The array beam spacing and width are such that only one beam is on the Sun at one time. The angular resolution is about $5'$ at 60 MHz decreasing to $15'$ at 20 MHz. A more detailed description of this instrument was given by Erickson and Kuiper (1973).

2. Observations

A. THE EVENT OF MAY 13, 1971

A coronal depletion associated with a flare spray was observed on May 13, 1971. The flare (of importance 2B) which took place in the region McMath 11294 started at 1751 UT, and reached its maximum at 1756 UT. Bursts at 10 cm wavelength were

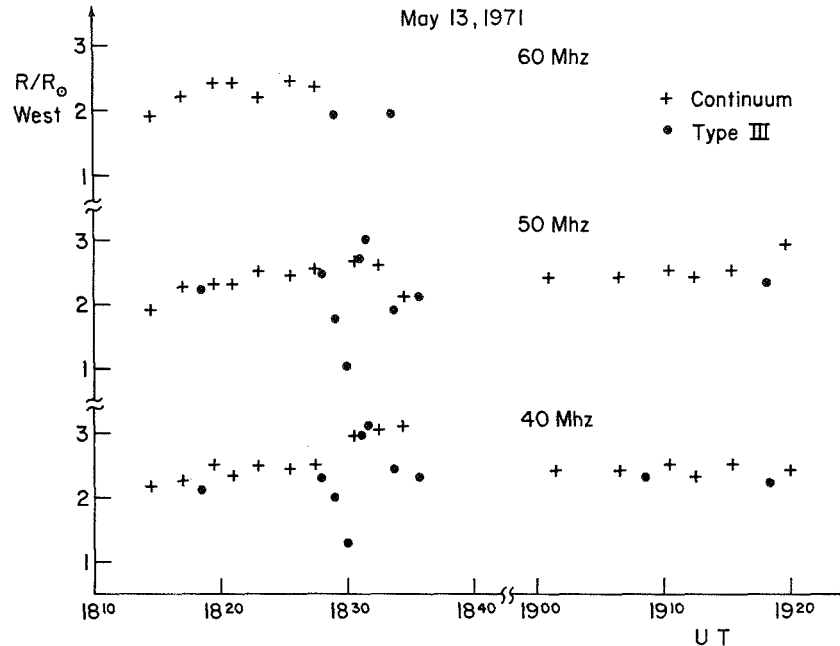


Fig. 1. Positions of the type IV and associated type III bursts observed on May 13, 1971, at 60, 50 and 40 MHz. The crosses refer to the continuum emission, filled circles indicate the type III bursts.

reported by the Sagamore Hill Observatory at 1751, 1826, and 1906 UT. These bursts reached maxima at 1801, 1835, and 1923 UT respectively. A moving type IV burst was observed at decameter wavelengths starting at 1812 UT. The motion of the source at 60, 50, and 40 MHz is illustrated in Figure 1. Assuming the movement to be radial, the burst source at 60 MHz moved from $1.9 R_{\odot}$ to $2.5 R_{\odot}$ in about 6 min. It was observed at this height until 1830 UT and then it faded. At 40 MHz the burst was observed for a longer period; it continued to move until about 1835 UT, ascending to $3.2 R_{\odot}$. Several type III bursts were observed during the occurrence of this type IV burst, some of them coincident in position with the type IV source at 40 and 50 MHz, even at altitudes as high as $1-2 R_{\odot}$ above the limb. On the other hand, some type III bursts occurred closer to the Sun's center than the moving type IV source. The moving type IV disappeared after 1835 UT. A continuum was observed below 50 MHz once again during the period 1900–1920 UT. Some type III's occurred during this phase, more or less coincident in position with the continuum.

B. THE EVENT OF MAY 14, 1971

The same active region gave rise to another coronal transient on May 14; it was also associated with a type IV burst. At the time of occurrence of this event, the active region (McMath 11294) was approximately 15° behind the west limb. No flare or other optical activity was observed. A 10 cm burst started around 1756 UT reaching its peak at 1759 UT.

In our frequency range, 20 to 65 MHz, continuum radiation started at 1800 UT at 65 MHz and extended gradually to lower frequencies. In Figure 2 is plotted as a function of time the lowest frequency at which the burst was observed. The drift of the burst from high to low frequencies as indicated in the figure is interpreted to be due to the gradual emergence of the source as it ascends through the corona. It is believed that a plasma cloud containing energetic electrons is responsible for the synchrotron radiation of the moving type IV burst. As the plasma cloud moves upward through the corona progressively lower frequencies become visible. The heights corresponding to the plasma frequencies in a two times Newkirk streamer model are

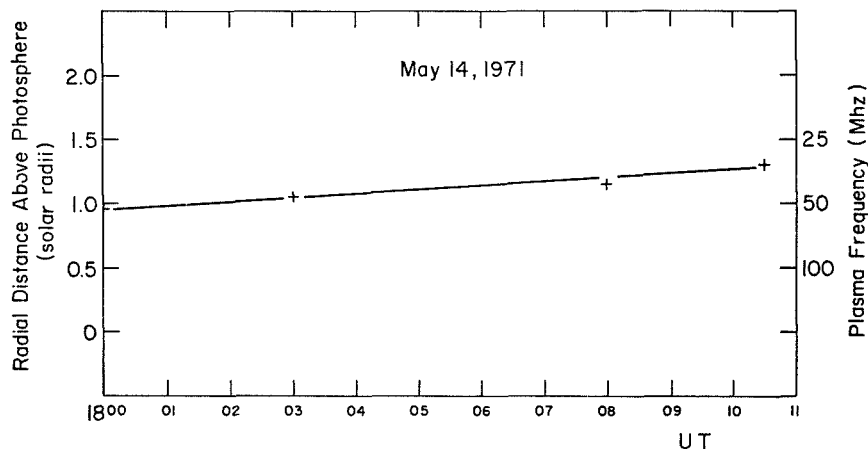


Fig. 2. Gradual emergence of the type IV source of May 14, 1971. Radial distances correspond to a two times Newkirk streamer model.

also indicated in Figure 2. Assuming that the burst moves out radially and that the densities are given by the above mentioned streamer model, we derive from the drift a velocity of 800 km s^{-1} . This velocity agrees closely with the observed velocity of the source, which was 830 km s^{-1} at 60 MHz and 600 km s^{-1} at 40 MHz. (Table I). The burst reached maximum intensity at 1815 UT at all frequencies. The initial width of the source was $0.7 R_{\odot}$ at 60 MHz and $1.2 R_{\odot}$ at 30 MHz but it broadened to $1.2 R_{\odot}$ and $1.8 R_{\odot}$ respectively in about 4 min. The reason for this apparent broadening is possibly due to the fact that the source became split into two components, one of which moved out to a distance of $3.8 R_{\odot}$, and disappeared at 1825 UT. The other source remained stationary at a height of $2.5 R_{\odot}$ and was visible until 1832 UT. It brightened again at 1855 UT, remaining at the same position for another 10 min and then it gradually faded. This source possibly corresponds to the late, stationary phase of the type IV event, as described by Pick (1961). A group of type III bursts was observed at the position of the stationary source at 1953 UT. The detailed motion of both components as seen at 50, 40, and 30 MHz is represented in Figure 3.

TABLE I
Characteristics of moving type IV bursts at 60 and 40 MHz

| Date | Time (UT) | | Duration (min) | Distance from center (R_{\odot}) | | Velocity (km sec) | Source size (R_{\odot}) | | Associated activity | Radio |
|-----------------|-----------|------|-------------------|---|-------|----------------------|--------------------------------|----------|--|---------------------------|
| | Start | End | | First | Last | | Initial | Final | | |
| May 13, 1971 | 1812 | 1830 | 18 (7) | 1.9 | 2.5 | 1000 | 0.5 | 0.7 | 2B, 17 ^h 51 ^m W90; N10 Flare spray, LPS ^b | cm- λ I, III's |
| | 1814 | 1920 | 66 (19) | 2.2 | 3.2 | 610 | 0.8 | 1.8 | | |
| May 14, 1971 | 1800 | 1900 | 60 (14) | 1.9 | 2.9 | 830 | 0.7 | 1.2 | | cm- λ I, III's |
| | 1805 | 1902 | 57 (23) | 2.5 | 3.5 | 610 | 1.4 | 1.4, 1.9 | | |
| Feb. 17, 1972 | 2048 | 2136 | 48 (16) | 1.5 | 2.5 | 730 | 1.3 | 1.2 | EPL ^a LPS ^b | cm- λ IIIG, II |
| | 2048 | 2148 | 60 (25) | 1.9 | 3.3 | 650 | 1.4 | 1.6 | | |
| August 12, 1972 | 2056 | 2200 | > 64 (> 64) | 3.2 | > 5.0 | 420 | 0.9 | 1.0 | EPL ^a | cm- λ , III |

^a EPL = Eruptive prominence on limb.

^b LPS = Loop prominence system.

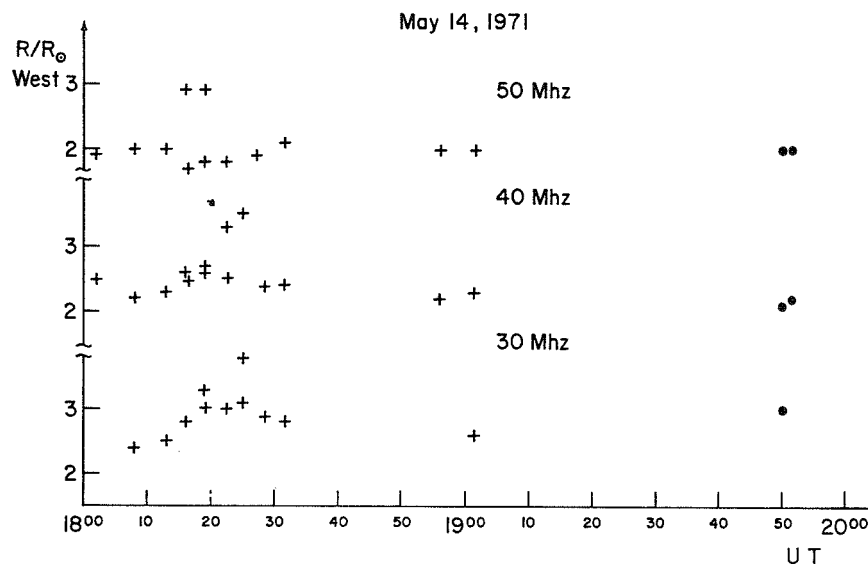


Fig. 3. Positions of the type IV bursts observed on May 14, 1971 at 50, 40 and 30 MHz.

C. THE EVENT OF FEBRUARY 17, 1972

A major coronal event took place on this day. A surge in $H\alpha$ was observed at the east limb from 1830 to 1920 UT, moving radially outwards. Another $H\alpha$ surge occurred south of the first one during the period 1943–2002 UT. At radio wavelengths, we observed groups of type III bursts during the periods 1824–1831 UT, 1915–1918 UT and 1929–1938 UT. The first two groups were moderately intense whereas the last one was very intense and was followed by weak type V emission. From positional analysis it appears that these type III groups were not related to the coronal event that took place afterwards. The first group is situated $0.2 R_{\odot}$ west of the center of the disk over the entire frequency range. The position of the second and third group is $0.6 R_{\odot}$ above the west limb. Two isolated type III bursts occurred later, from 2000 to 2033 UT, over a more limited frequency range extending from 65 MHz to about 50 MHz. The position line corresponding to these bursts lies $1.2 R_{\odot}$ east of the center of the disk.

A coronal depletion took place at a height of $1.31 R_{\odot}$, (Figure 6b) between successive scans of the coronal activity monitor (Mauna Loa, Hawaii) beginning at 1826 and 2110 UT. The change, which was also observed at $1.82 R_{\odot}$, took place above the south-eastern part of the limb, (Wagner *et al.*, 1973). A type IV burst was seen moving off the east limb (Figure 6c) from approximately 2050 to 2110 UT showing good coincidence in position, as well as in time with the activity observed in the K-corona.

In the green coronal line ($\lambda 5303$) the transient was observed as an expansion of the pre-existent arch system (2033–2038 UT) followed by ejection of material (2035–2040 UT) and finally a realignment of the arch system (2038–2041 UT) (De Mastus

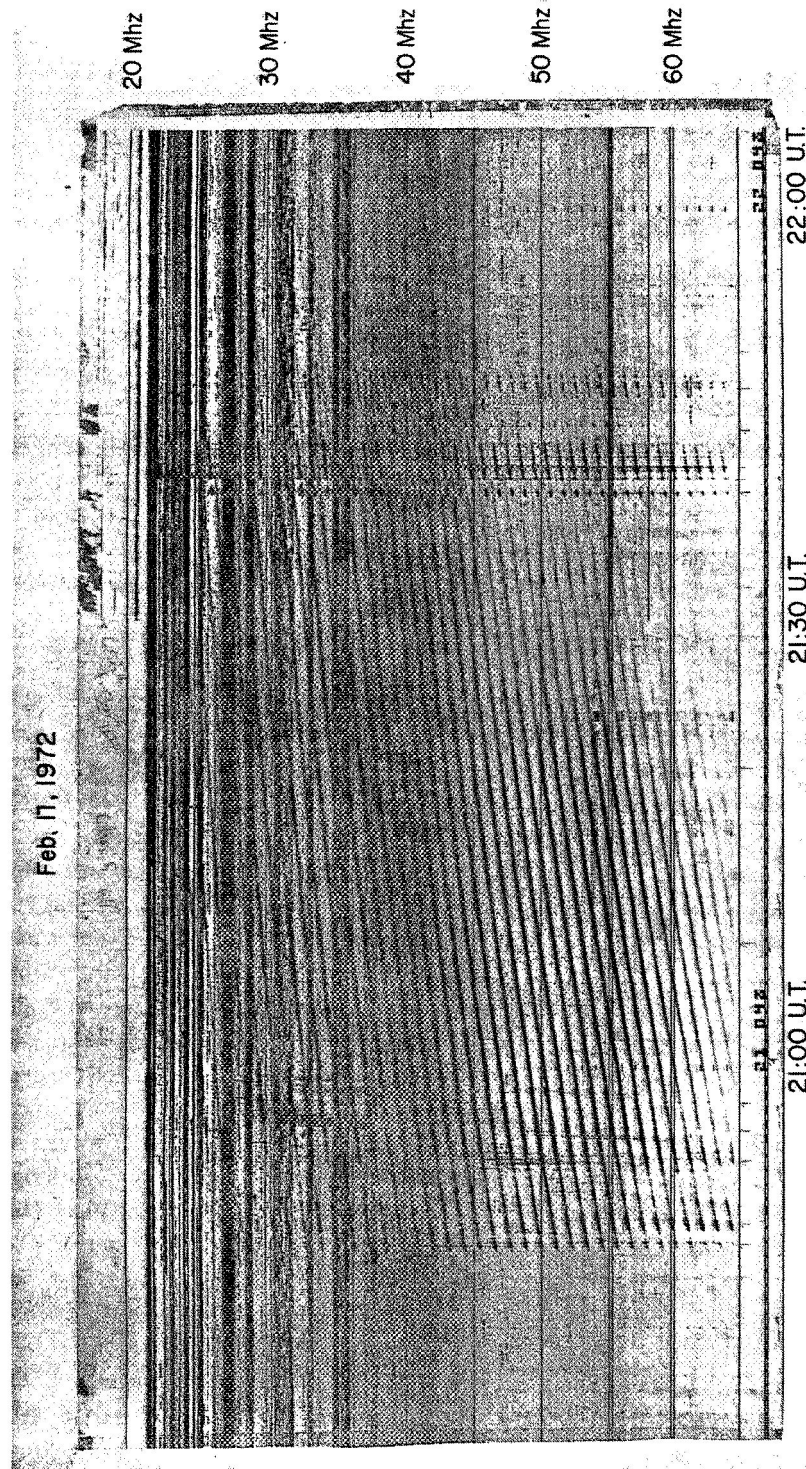


Fig. 4. Swept frequency interferometer record of the event of February 17, 1972.

and Wagner, 1973). An intense centimeter burst started at 2035 UT simultaneously with the coronal phenomenon and reached maximum at 2134 UT. At meter and decameter wavelengths the event started with a group of type III bursts. This was followed by a type IV burst and two harmonically unrelated type II bursts. The swept frequency interferometer record is shown in Figure 4. The type II bursts can be recognized because of the drifting structure and their high intensity relative to the underlying continuum. Further, the fringe systems originating from the type II bursts merged with that due to the type IV burst. As a consequence we can only measure the position of the centroid of the combined type II-type IV sources for the duration of the

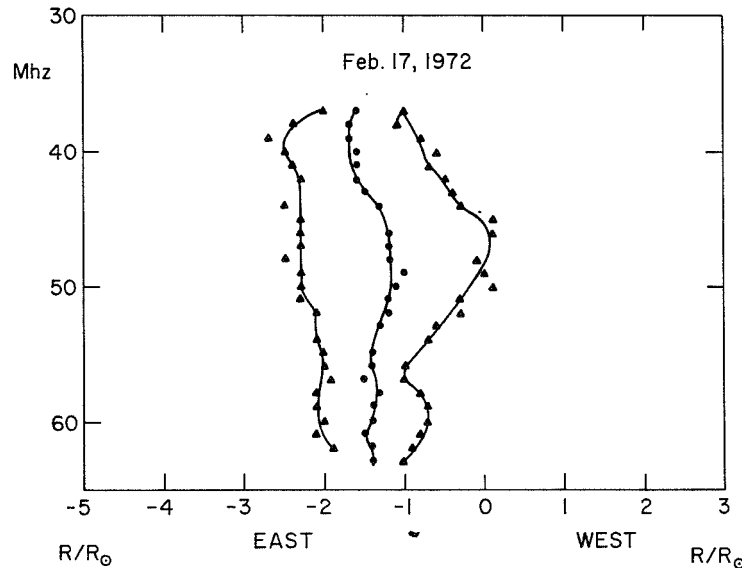


Fig. 5. Source position vs frequency of the combined type IV-type II sources observed on February 17, 1972 at 2053 UT. Triangles refer to the positions of the edges of the fringe, full circles to the center. Note that the two maxima at 46 and 59 MHz correspond to the two type II bursts (see text).

type II bursts. The ascending motion of the type IV source continued after the type II sources disappeared. Because of the merging of the two fringe systems, the source appears broader at the frequencies where the type II is observed than at other frequencies. This is seen clearly in Figure 5, where we have plotted at time 2053 UT the positions corresponding to the mid-points as well as the edges of the fringes as a function of frequency. One can clearly see two maxima in the angular size of the source at 46 and 59 MHz indicating the presence of two type II bursts. From the frequencies of such maxima at different times the drift rate of the bursts can be calculated. The drift rate turns out to be 0.04 MHz s^{-1} and 0.06 MHz s^{-1} for the first and second burst respectively (Figure 6a). Figure 6b shows two scans at $1.31 R_{\odot}$ of the K-corona, one before and one after the transient. The coronal feature which was depleted is cross hatched. Referring to Figure 6c, we see that the type IV source moved outward

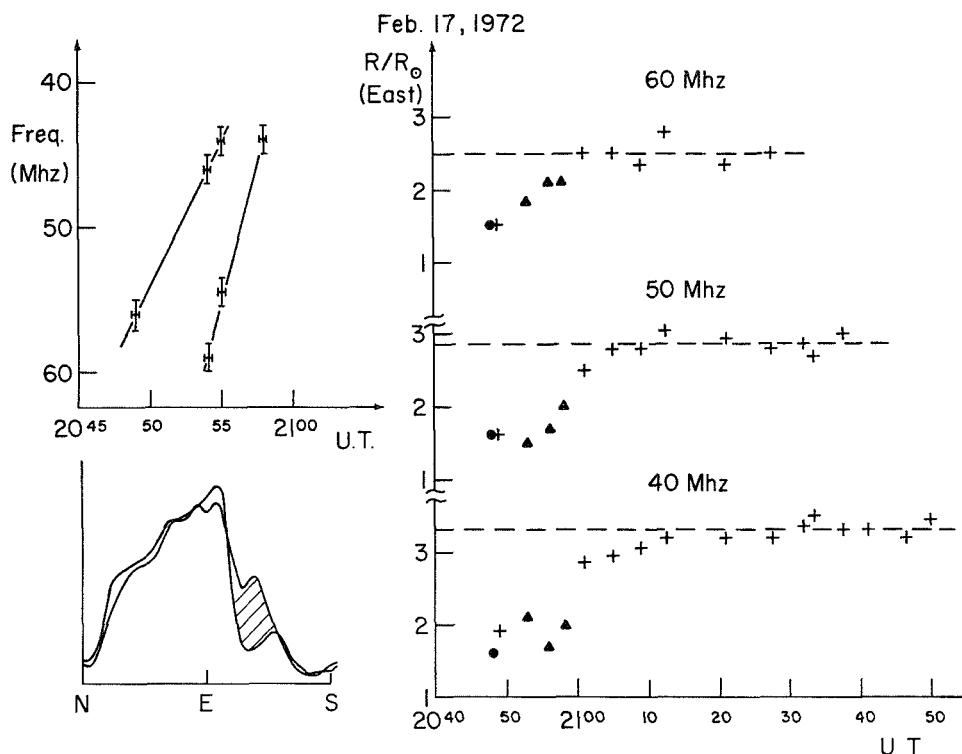


Fig. 6. (a) Frequency drift of the two type II bursts observed on February 17, 1972. (b) Scans of the K-corona at $1.31 R_{\odot}$ before and after the transient event (courtesy of R. T. Hansen). (c) Source positions at 60, 50, and 40 MHz of the same event. Crosses indicate the continuum, triangles the centroid of type IV and type II emission, circles the type III burst.

from the center. Assuming this motion to be radial and over the observed K-coronal feature that disappeared, we can compute the positions of the type IV source at different times. The moving burst started at a height of $1.5 R_{\odot}$, ascending to maximum height of $2.5 R_{\odot}$ at 60 MHz in approximately 16 min thus moving at a velocity of 730 km s^{-1} . The source became stationary at this height radiating for another 20 min approximately. The difference in the position at different frequencies during the first part of the movement is probably due to the fact that during this period we measure the position of the centroid of the type II and type IV bursts. The late, stationary source showed significant dispersion, the higher frequencies lying closer to the sun's center than the lower frequencies.

D. THE EVENT OF AUGUST 12, 1973

No flare was observed in association with this event, but a surge was reported on the west limb (latitude $N25^{\circ}$) starting at 2022 UT (Lincoln and Leighton, 1972). Coronal observations from Hawaii showed an $H\alpha$ spray extending to $1 R_{\odot}$ above the limb at a latitude of $N29^{\circ}$. The optical and the radio burst activity appear to be associated

with the region McMath 11976 which was responsible for the series of spectacular flares and radio storms observed in August 1972. At the time of the present observations the region was 17° behind the west limb.

A centimeter burst started around 2035 UT, reaching maxima at 2040, 2044 and 2122 UT. A weak type III burst was reported at 2038 UT (Riddle, 1973) in the frequency range 8–80 MHz, but is not present on the Clark Lake records. The major radio event in the 65–20 MHz range started at 2056 UT and it was of continuum type. The emission was weak, but constant in intensity throughout the whole event and was seen mostly in the frequency range 50–30 MHz. This is possibly due to an instrumental effect, since the sensitivity of the receiver is somewhat higher in this range.

Figure 7 shows the Fraunhofer map for this day. The ascending prominence is superimposed on the map at the position where it was seen at 2059 UT. We indicated on this map the average position line for the frequencies 50–40 MHz at a number of times. The broken line indicates the fringe line, corrected for ionospheric refraction at 2059 UT, assuming that all frequencies originate from the same source. In this case the positions corresponding to different frequencies were fitted to a function

$$\frac{R}{R_\odot} = A + Bf^{-2}$$

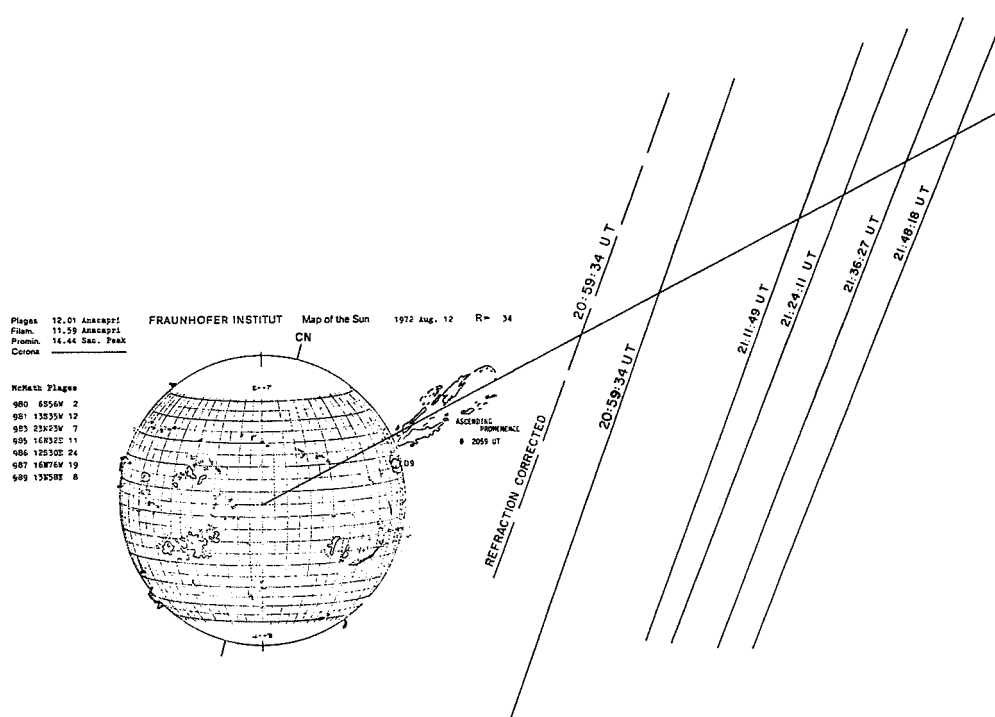


Fig. 7. Position lines of 40–50 MHz emission at different times during the August 12, 1972 event are shown, superimposed on a composite picture of the Fraunhofer Institute map and the ejected prominence at 2059 UT.

where A represents the true positions of the source at a given instant of time and the term Bf^{-2} accounts for ionospheric refraction effects (Kuiper, 1973). We note that either the apparent or the true position (derived by this method) appears much higher at this time than the visible prominence. Assuming the direction of movement for the radio source to be radial, we determine its velocity to be 420 km s^{-1} . The velocity of the moving source was also determined by Riddle (1973), who used data obtained with the Colorado University (CU) swept-frequency interferometer. By averaging the positions in the frequency range 18–40 MHz, and using the radial hypothesis he derived a velocity of 340 km s^{-1} for the type IV burst. We note that the inclination of the fringe lines with respect to the axis of rotation of the Sun was very different for the CU and Clark Lake interferometers. Under these conditions the velocity, as derived from the two sets of data should coincide only if the motion of the source was strictly radial. The reasonably good agreement of Riddle's value with the velocity derived by us indicates that the motion was indeed nearly radial in this case. Combining the positions obtained with the CU and Clark Lake instruments, Riddle *et al.* (1973) determined the two dimensional position of the type IV source several times during the event. The direction of the movement agrees perfectly with that of the identifiable features in the H α spray (Riddle *et al.*, 1973). The radio burst is found to move out well ahead of the material observed in H α . Finally, we note that the size of the source was small, and remained approximately constant during the entire event; its value is $0.8 R_{\odot}$, about twice the size of the beam at 50 MHz.

3. Discussion

In the preceding section we have described four moving type IV bursts, all of which were associated with the depletion of some coronal features, observed with the coronal activity monitor at Mauna Loa, Hawaii (R. Hansen, private communication). Some characteristics of these bursts are listed in Table I.

At 60 MHz, the initial distance of the sources from the disk center, derived on the basis of the radial hypothesis was, on the average $1.8 R_{\odot}$, approximately $0.1 R_{\odot}$ above the corresponding plasma level in a two times Newkirk streamer model. At 40 MHz, the mean initial distance was $2.2 R_{\odot}$ except for the event of August 12, when the distance was $3.2 R_{\odot}$. The mean distance was also somewhat higher than the corresponding plasma level in the same density model. On the average the sources were last seen at a distance of $2.7 R_{\odot}$ and $4.1 R_{\odot}$ at 60 and 40 MHz respectively, the distances being always greater at the lower frequencies. The average speed derived for the bursts was 850 km s^{-1} at 60 MHz and 560 km s^{-1} at 40 MHz. Although all four events occurred close to the limb, within $\pm 17^{\circ}$, the derived values are somewhat dependent on the radial hypothesis, since tangential displacements are often observed in the course of motion of the type IV sources. The duration of the events varied from 18 to 70 min. In Table I, under the column 'duration' we have indicated in parenthesis the duration of motion in each case.

Only one of the four events reported here (February 17, 1972) was preceded by

type III bursts; this event was also accompanied by multiple type II bursts. The absence of type II bursts in the events of May 14, 1971 and August 12, 1972 is possibly due to the fact that they occurred one day after the limb passage of the corresponding active region, thus rendering difficult the observation of plasma frequency radiation at the Earth. The fact that coronal transients are not necessarily associated with type II bursts, however, is documented by the May 13, 1971 event, which occurred just at the limb and for which no type II burst was observed or reported by other observatories. It is interesting to note that several type III bursts were observed during the moving phase of both May 13 and May 14, 1971 events. Some of these type III bursts coincided in position with the moving type IV source. During the May 13, 1971 event, for example, a type III burst was seen at a distance as great as $2.1 R_{\odot}$ above the limb at 40 MHz (Figure 1). Other type III bursts were observed during the same period, but they occurred much closer to the disk center, approximately at the 40 MHz plasma level.

At meter wavelengths, the appearance of a stationary component after the disappearance or weakening of the moving burst is quite common. This seems to be true at decameter wavelengths also. Stationary continuum following the moving type IV bursts was observed in all cases, except in the case of the August 12, 1972 event, when observations ended before the movement had ceased. In one case (February 17, 1972) the stationary source exhibited significant dispersion in height with frequency. In two other cases, the dispersion in position, if present, was less clear, because the emission was much weaker at the high frequency end.

Essentially two radiation mechanisms have been invoked to explain the observed emission from moving type IV bursts. Synchrotron radiation at the higher harmonics of the relativistic and Doppler-shifted gyro-frequency has been invoked to explain the type IV radiation (Boischot and Denisse, 1957; Takakura, 1960a, b). The high energy cut-off of the radiating electrons is often considered to be 1 MeV, from bandwidth and polarization considerations. Further, the synchrotron radiation in the medium will be suppressed by 'Razin-Tsytoich effect' unless the energy $E > \frac{1}{2}(f/f_p)$, where f_p is the ambient plasma frequency (Ginzburg and Syrovatskii, 1965). The effect of the medium on the radiation emitted by the outward moving source leads to a gradual onset of the burst from high to low frequencies. This slow drift of the moving burst seems to have been observed in the event of May 14, 1971. Zheleznyakov and Trakhtengerts (1966) sought to explain the type IV radiation in terms of synchrotron radiation from electrons trapped in a moving and expanding plasma cloud. In this expanding source model, the linear size L of the moving plasma is related to f_p^2/f_H^2 by $f_p^2/f_H^2 \sim N_e/H^2 \sim L$, where N_e is the electron density, H is the magnetic field and f_H is the gyro-frequency.

On the other hand, gyromagnetic radiation in the extraordinary mode and at the fundamental gyro-frequency f_H has been proposed by Fung (1969) to explain the moving type IV. Some features of the events of May 13 and May 14, 1971 may indeed be attributed to gyromagnetic radiation from an expanding cloud, as proposed by Fung (1969). This model accounts for: (1) the presence of narrow-band features at the beginning of both events superimposed on the background continuum, (2) the fairly

narrow frequency range of the continuum, and (3) a rapid increase in the size of the source, its breakup and its subsequent fast fade-out. However, Fung's model requires large magnetic fields to be frozen in the expanding plasma cloud. At 40 MHz, for example, a field of ≈ 15 G is required to produce gyro-radiation at the fundamental frequency. Moreover such a large field, when combined with the observed size of the source ($1.5 R_{\odot}$ at 40 MHz, for the May 14, 1971 event) would require the storage of $\approx 10^{35}$ erg in magnetic energy in the source. Such a large amount of energy is not available even during the largest flares. The size obviously plays an important role in the evolution of radiation from a moving type IV source, particularly in the mechanism involving gyromagnetic radiation (Fung, 1969).

In this context it is useful to consider the linear size of the type IV sources observed by us. At 60 MHz, the initial size of the source was of the order of $0.8 R_{\odot}$ in all cases. An increase in the size of the source was observed at the low frequencies during the May 13 and May 14, 1971 events. During the May 14, 1971 event, for example, the source size increased from $1.4 R_{\odot}$ to $2.0 R_{\odot}$ at 40 MHz until the time when the source was split into two components, each about $1.1 R_{\odot}$ in diam. During the May 13, 1971 event we observed an increase in size from $0.8 R_{\odot}$ to $1.8 R_{\odot}$ at 40 MHz. It is likely that this increase was also due to the presence of an unresolved double or multiple sources. In both cases the late, stationary source appeared smaller in size, about $1.0 R_{\odot}$. On the other hand, no increase in size was observed in the other two events at any frequency. This observation seems to indicate, in agreement with the classification scheme suggested by Smerd and Dulk (1971) that an expanding plasma cloud model cannot always be invoked to explain the evolution of moving type IV sources.

Dulk (1973) computed models for an expanding source, taking into account synchrotron self-absorption and Razin-Tsytovich effect. For a homogeneous source: $f_{sa} \sim \sigma^{-3.5}$, where f_{sa} is the turnover frequency due to self-absorption and σ is the source size relative to the initial size. During the May 14, 1971 event the lowest observed frequency drifted from 50 MHz to 30 MHz, while the source expanded from $0.8 R_{\odot}$ to $1.8 R_{\odot}$ at 40 MHz. The expansion ratio $L_1/L_2 \approx 2.2$. This ratio would require a frequency drift f_{sa1}/f_{sa2} of the order of 20, which was not observed. On the other hand, for a Razin-Tsytovich cut-off mechanism, the cut-off frequency is proportional to σ^{-1} . Indeed, during the May 14 event the frequency drifts only by a factor of $50/30 \approx 1.7$, which is closer to the requirement of this mechanism. It should be noted however that no single model explains the observations completely. An inspection of the coronal magnetic field maps produced by the regression analysis method described by Altschuler and Newkirk (1969) reveals a low magnetic arcade (LMA) and some open field lines around the flare site. It would appear that the type IV sources traveled outwards along the open field lines. The smooth, broadband character of the February 17, 1972 event points to the synchrotron origin of the radiation. The arch-system observed in the green line indicates that this event took place in a region of closed magnetic field lines, where the radiating electrons must be trapped.

The moving type IV bursts at decameter wavelengths that we have discussed here were all associated with coronal transients. The radio bursts occurred in the general vicinity of the corona where the depletion took place (K-coronameter data supplied by R. T. Hansen).

Shock waves, both parallel and perpendicular to the magnetic field have been involved in the interpretation of moving type IV bursts (Lacombe and Mangeney, 1969; Mangeney, 1973; Warwick, 1965). Referring to the classification scheme proposed by Smerd and Dulk (1971), it is difficult to see how an 'advancing front' model could account for the type IV bursts which are associated with coronal transients. This mechanism would seem to require a close association of type II with moving type IV bursts. Such association was not observed by us; only one of the 4 events reported here was accompanied by multiple type II bursts. It is conceivable that the absence of type II bursts in some cases could be attributed to insufficient strength of the shock that must be associated with moving type IV. Uchida *et al.* (1973) have given a detailed discussion of how strong shocks can be inhibited by high Alfvén-wave velocity regions.

On the other hand, both the expanding arch or the isolated source mechanism could account for the coronal transient in the way proposed by Smerd and Dulk (1971). An impinging shock front, initiated by the H α flare could be responsible for the expansion of a magnetic arch, or trigger the outward movement of a plasmoid, which would be observed as a moving type IV sources. In some cases, magnetic reconnection may occur, resulting in a self-contained plasmoid which appears as an isolated source; in other cases, the field structure may remain tied to the photosphere, resulting in an expanding arch. Behind the shock wave, densities are compressed resulting in a temporary increase in brightness of the K-corona, which was observed by Hansen *et al.* (1971) simultaneously with the peak of radio emission during the August 11, 1970 event. In all cases some of the electrons must be accelerated to relativistic energies to account for the observed radio emission. The mechanism by which this acceleration takes place is not well understood at present. As the gas cloud moves outward it causes a depletion of electrons at heights of about 1.2–1.8 R_{\odot} , as observed by the K-coronameter. After the passage of the shock wave, the magnetic arch may contract to its original lower position or similar arches may be generated by photospheric currents (Smerd and Dulk, 1971). The regeneration of the magnetic arches probably takes place over a time scale of several hours since the occurrence of homologous transients is not unusual. Indeed, the May 13 and 14, 1971 transients originated in flares occurring in the same active region with a time interval of 24 h. Another homologous pair of events was observed on January 11, 1973 (Stewart *et al.*, 1973). In this case the two events were separated by only about 18 h. It should be noted that two of the events discussed here (May 13, 1971 and February 17, 1972) were associated with the formation of a loop prominence system (Machado *et al.*, 1972; Wagner *et al.*, 1973). Alternately the expanding magnetic loop might be carried out by the solar wind, which seems to have been the case for the August 12, 1972 transient. The fading of the type IV source is frequently accompanied by the appearance of a stationary

type IV continuum source at decametric wavelengths. This source is always situated close to the flare site. It is generally believed that this emission is due to plasma radiation. The dispersion in position of this continuum with frequency observed by us supports this interpretation.

Acknowledgement

Support for this work was provided under NASA grants NGL 21-002-033, NGR 21-002-367 and NSF grant GP-19401. We thank R. T. Hansen for providing us with K-coronameter data in advance of publication, as well as Figure 6b and the prominence montage, Figure 7. Thanks are also due to M. D. Altschuler and D. Trotter who provided us with coronal magnetic field maps. The computer time for this project was supported by National Aeronautics and Space Administration grant NsG-398 to the Computer Science Center of the University of Maryland. We thank the referee for some very useful comments on the paper.

Portions of this paper are based on the thesis research of one of the authors (T.E.G.) in partial fulfilment of the requirements for the Degree of Doctor of Philosophy at the University of Maryland.

References

- Altschuler, M. D. and Newkirk, G., Jr.: 1969, *Solar Phys.* **9**, 131.
 Boischot, A. and Denisse, J. F.: 1957, *Compt. Rend. Acad. Sci. Paris* **245**, 2194.
 DeMastus, H. L. and Wagner, W. J.: 1973, AAS Solar Physics Division Meeting, Las Cruces, New Mexico.
 Dulk, G.: 1973, in G. Newkirk (ed.), 'Coronal Disturbances', *IAU Symp.* **57**, in press.
 Erickson, W. C. and Kuiper, T. B. H.: 1973, *Radioscience*, in press.
 Fung, P. C. W.: 1969, *Can. J. Phys.* **47**, 179.
 Ginsburg, V. L. and Syrovatskii, S. I.: 1965, *Ann. Rev. Astron. Astrophys.* **3**, 297.
 Hansen, R. T., Garcia, C. J., Groganard, R. J. M., and Sheridan, K. V.: 1971, *Proc. Austr. Soc. Astron.* **2**, 57.
 Hansen, R. T.: 1973, private communication.
 Kuiper, T. B. H.: 1973, Ph.D. thesis, University of Maryland.
 Lacombe, C. and Mangeney, A.: 1969, *Astron. Astrophys.* **1**, 325.
 Lincoln, J. V. and Leighton, H. I.: 1972, World Data Center A, Upper Atmosphere Geophysics Report, UAG-1221, 61.
 Machado, M. E., Grossi-Gallegos, H., and Silva, A. F.: 1972, *Solar Phys.* **25**, 402.
 Mangeney, A.: 1973, in G. Newkirk (ed.), 'Coronal Disturbances', *IAU Symp.* **57**, in press.
 Pick, M.: 1961, *Ann. Astrophys.* **24**, 183.
 Riddle, A. C.: 1973, University of Colorado, Radio Astronomy Observatory Report, SN-2.
 Riddle, A. C., Tandberg-Hanssen, E., and Hansen, R. T.: 1973, in G. Newkirk (ed.), 'Coronal Disturbances', *IAU Symp.* **57**, in press.
 Smerd, S. F. and Dulk, G. A.: 1971, in R. Howard (ed.), 'Solar Magnetic Fields', *IAU Symp.* **43**, 616.
 Stewart, R. T., McCabe, M., Hansen, R. T., Koomen, M. J., and Dulk, G. A.: 1973, in G. Newkirk (ed.), 'Coronal Disturbances', *IAU Symp.* **57**, in press.
 Takakura, T.: 1960a, *Publ. Astron. Soc. Japan* **12**, 325.
 Takakura, T.: 1960b, *Publ. Astron. Soc. Japan* **12**, 352.
 Uchida, Y., Altschuler, M. D., and Newkirk, G. Jr.: 1973, *Solar Phys.* **26**, 495.
 Wagner, W. J., Hansen, R. T., and Hansen, S. F.: 1973, in G. Newkirk (ed.), 'Coronal Disturbances', *IAU Symp.* **57**, in press.
 Warwick, J. W.: 1965, in J. Aarons (ed.), *Solar System Radio Astronomy*, Plenum Press, New York, p. 166.
 Zheleznyakov, V. V. and Trakhtengerts, V. Yu.: 1965, *Soviet Astron. AJ* **9**, 775.

8

DECAMETER STORM RADIATION, I

TOMAS E. GERGELY and WILLIAM C. ERICKSON

Astronomy Program, University of Maryland, College Park, 20742, U.S.A.

(Received 18 April; in revised form 24 October, 1974)

Abstract. A log-periodic array, 3 km long in the E-W direction is in operation at the Clark Lake Radio Observatory. The solar brightness distribution is swept once per second in the 65–20 MHz frequency range. The analysis of the interferometer records allows the determination of one dimensional solar burst positions, to an accuracy of $0.1 R_{\odot}$ at 60 MHz and $0.3 R_{\odot}$ at 30 MHz, approximately.

Six long duration noise storms have been observed over an eight month period, extending from January to September, 1971. The storms are described and their relation to chromospheric active regions and flares is discussed. Decametric storms are found to be related to complexes of interacting active regions. The interaction is studied in terms of the number of 'simultaneous' flares observed to occur in the various active regions. On the average, twice as many 'simultaneous' flares are observed than would be expected if flares occurred at random. An analysis of coronal magnetic field maps computed from longitudinal photospheric fields shows magnetic arcades and some divergent field lines at the site of storm regions. Decimeter and meter wavelength sources are found to be associated with all decameter storms. At decimeter wavelengths double or multiple sources are often seen above individual active regions forming part of the chromospheric complex.

1. Introduction

Noise storms, type II and type III bursts have been observed from heights of about $0.2 R_{\odot}$ above the photosphere all the way to 1 AU. These bursts present radio evidence of disturbed conditions in the solar corona. Noise storms are particularly interesting, since they are long lasting (of the order of days), and thus enable us to study relatively persistent features which might be present in the corona.

Meter wavelength noise storms consist of a more or less steady continuum and of superimposed type I bursts. Comprehensive reviews of noise storms at meter wavelengths have been given by Wild *et al.* (1973), Kundu (1965) and by the Solar Radio Group at Utrecht (1974). Fine structure in metric storms has been discussed recently by Rosenberg (1971, 1972) and Rosenberg and Tarnstrom (1972). At the kilometer and hectometer wavelengths the storms have been studied with the aid of satellite-borne equipment (Fainberg and Stone, 1974). Storms at decameter wavelengths have been first described by Warwick (1965). At these wavelengths the storms are seen to consist of type III bursts and other fine structure (de la Noë *et al.*, 1973) superimposed on a more or less steady continuum. The radiation originates at heights from approximately $0.5 R_{\odot}$ to $2.5 R_{\odot}$ above the photosphere. Thus the study of decametric storms is of interest not only because it provides a link between metric and kilometric observations of the storms, but also because it provides some insights into the properties of coronal regions where the solar wind originates.

In this paper we describe the evolution of six decametric storms which took place during the period January to August, 1971. We discuss the relationships of decametric

storms with chromospheric active regions, coronal magnetic fields, and meter and decimeter wave activity.

The storms described here were observed with the swept frequency interferometer of the Clark Lake Radio Observatory operated by the University of Maryland. This array (hereinafter referred to as the LPA) consists of sixteen log-periodic antennas, equally spaced on a two mile east-west baseline. The array is swept in frequency over the range 20–65 MHz once per second. This system gives the one dimensional position and angular size of emissive regions on the Sun nearly simultaneously at all frequencies. The array beam spacing and width are such that only one beam is on the Sun at one time. The angular resolution is about 5' at 60 MHz decreasing to 15' at 20 MHz. A more detailed description of this instrument was given by Erickson and Kuiper (1973).

2. Observations

When observed with a time and frequency resolution of about 1 s and 10 kHz respectively, decametric storms are seen to consist of a background continuum of varying intensity, often with considerable structure in frequency. Superimposed on this background we often observe a large number of type III bursts. These bursts can be distinguished from the underlying continuum because of their much higher intensity and characteristic frequency drift. Type I bursts are seen much less frequently at decameter wavelengths than on meter wavelengths. Although type I bursts are known to occur less frequently at longer wavelengths, the low number seen on the Clark Lake records may be partly attributed to instrumental effects. Since the duration of these bursts is usually less than a second, at a one per second sweep rate the bursts are often integrated into the background continuum. There are extended periods during some of the storms when no type III or I bursts can be seen.

At the maximum of solar activity noise storms can be observed about 80% of the time on meter wavelength dynamic spectra. Good correspondence has been shown to exist in time between the meter and decameter storms by Boischot *et al.* (1971). Thus, it can be expected that decametric and metric storms will occur with approximately the same frequency. In their studies of metric and decimetric storms, Malinge (1963) and Clavelier (1967) defined storms on a day-to-day basis. In view of the evident continuity of the phenomenon when following a storm day by day, we prefer to define a storm as the whole of the activity related to a center during its disk passage. We shall show that a decametric storm can be related to several active regions on the disk. Therefore, the above statement should not be interpreted as implying a one-to-one correspondence between storms and active regions. The storms at long wavelengths often show much detail and occasionally consist of double sources. For this study we selected a relatively quiet period during which there was only one storm region on the Sun at a time. According to our definition a total of six storms were observed during the period considered, which extends from January to August, 1971. Typical examples of storms, corresponding to the dates of 1971, January 9 (decametric region 1) and of 1971, April 14 (decametric region 3) are shown in Figures 1a and 1b. A list of the

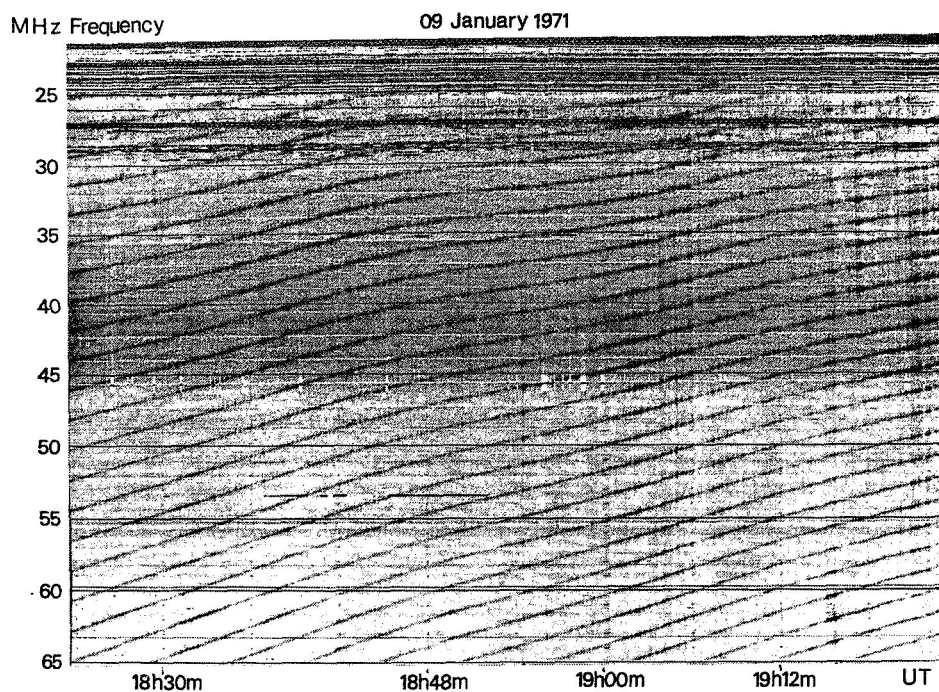


Fig. 1a. Typical examples of a decametric storm recorded at Clark Lake, in 1971, January 9 (storm region 1).

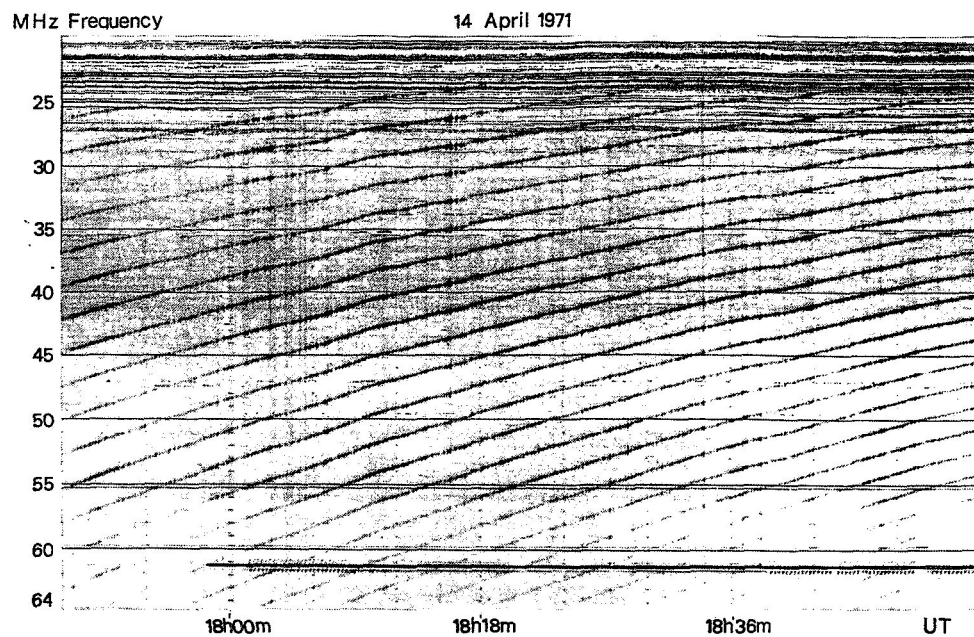


Fig. 1b. Same as Figure 1a for 1971, April 14 (storm region 3).

TABLE I
Periods of type III and continuum activity related to decametric storms

| Decametric region | Type III activity | | Continuum activity | | Peak of activity |
|-------------------|-------------------|---------|--------------------|---------|------------------|
| | Start | End | Start | End | |
| 1 | Jan. 4 | Jan. 17 | Jan. 5 | Jan. 12 | Jan. 7-9 |
| 2 | Jan. 19? | Jan. 24 | Jan. 19? | Jan. 24 | Jan. 19-21 |
| 3 | Apr. 6 | Apr. 19 | Apr. 11 | Apr. 17 | Apr. 14-16 |
| 4 | May 4 | May 12 | May 7 | May 12 | May 7-9 |
| 5 | July 13 | July 22 | July 14 | July 19 | July 15-17 |
| 6 | Aug. 15 | Aug. 29 | Aug. 19 | Aug. 25 | Aug. 20-24 |

storms observed, the first and last day of continuum and of type III activity, as well as the days when the storms peaked are given in Table I. There was no overlap between the several storms observed. Occasionally the type III or the continuum emission, or both, stopped for a couple of hours or even for an entire observing period. Periods with no emission at all occurred in course of decametric storm 2, in 1971, January 22 and decametric storm 3 in 1971, April 10. Periods lacking type III emission occurred on January 9, from about 19:40 to 21:00 UT and on January 11, from 18:00 to 18:30 UT during decametric storm 1; and for the entire observing period in 1971, August 24, in course of decametric storm 6. It is worth mentioning that on these occasions the continuum emission was extremely intense and was always modulated by strong ionospheric refraction. Moving type IV or type II-type IV events, related to the storm centers described here have been observed on April 20 (Region 3); May 13 and 14 (Region 4), and September 1 (Region 6). These bursts have been discussed elsewhere in detail (Gergely and Kundu, 1974; Gergely, 1974). The intensity of both the type III and the continuum emission fluctuated widely during all storms. The rate of occurrence and the starting frequency of type III bursts was also highly variable. These topics will be discussed in a forthcoming paper. Some shortlived storms, exhibiting sporadic activity, also occurred during the period discussed here. Such sporadic storms last for a couple of hours and occasionally reappear the next day. These storms are not discussed here. In February and March, 1971, the Sun was exceptionally quiet in the decametric range. Isolated type III bursts were the only form of activity observed during these months and were studied in detail by Kuiper (1973).

3. Association with Optical Activity and Photospheric Fields

The association of storms with active regions can be studied in two ways. First, the storms have long duration and we can associate their central meridian passage (CMP) with that of active regions. Second, we may look for a correlation between the onset or the intensification of a given storm and related chromospheric activity. Both methods have drawbacks. The CMP of storm regions normally differs by as much as 0.5 days when observed at different frequencies in the 20-65 MHz range. Parts of

several active regions are sometimes observed at the central meridian during this period. More importantly, the decametric storms may originate in non-radially oriented coronal structures (Malinge, 1963; Stewart and Labrum, 1972). The second method can also give rise to erroneous identifications because several flares may occur in a given period of time preceding or following the onset of a storm. To minimize errors due to these possibilities we studied the association using both methods.

Table II presents the CMP date for each storm observed at different frequencies. The CMP times are accurate to approximately 0.4 days. The table also shows the CMP date for the active regions that might be associated with the storm regions (for the cases where CMP active region = CMP storm \pm 3 days).

The CMP of region 1 occurred on January 10; the active regions with the nearest

TABLE II
CMP date of decametric and metric storms and of associated active regions

| Decametric region | Freq. (MHz) | CMP date | McMath number | CMP date | Age and magnetic field of region |
|-------------------|-------------|-----------|---------------|-----------|----------------------------------|
| 1 | 60 | Jan. 10.0 | 11114 | Jan. 11.5 | young region; strong fields |
| | 50 | Jan. 9.9 | 11111 | Jan. 10.6 | old region; weak fields |
| | 40 | Jan. 9.7 | 11112 | Jan. 10.2 | |
| | 30 | Jan. 9.6 | 11120 | Jan. 9.6 | |
| | | | 11110 | Jan. 9.1 | |
| | 169 | Jan. 10.1 | 11124 | Jan. 9.0 | |
| | | | 11108 | Jan. 8.3 | decaying region; weak field |
| 2 | 50 | Jan. 20.8 | 11128 | Jan. 20.5 | strong fields, young regions, |
| | | | 11129 | Jan. 23.5 | satellite spots in McMath |
| | | | 11130 | Jan. 23.0 | 11128 |
| | 169 | Jan. 21.2 | 11133 | Jan. 25.0 | |
| 3 | 50 | Apr. 15.1 | 11253 | Apr. 14.1 | emerging region; strong fields |
| | 40 | Apr. 15.0 | 11249 | Apr. 16.2 | young region; intense fields |
| | | | 11250 | Apr. 16.8 | weak fields |
| | 169 | Apr. 15.7 | 11256 | Apr. 17.7 | young region; intense fields |
| | | | 11257 | Apr. 17.7 | young region; intense fields |
| 4 | 60 | May 7.7 | 11294 | May 6.9 | developed region; strong field |
| | 50 | May 7.6 | 11296 | May 8.4 | emerging region; weaker field |
| | 40 | May 7.7 | | | |
| | 30 | May 7.9 | | | |
| | 169 | May 6.9 | | | |
| 5 | 50 | July 19.0 | 11423 | July 16.2 | |
| | 30 | July 18.8 | 11424 | July 18 | old region; weak field |
| | | | 11425 | July 18.8 | young region; strong field |
| | | | 11429 | July 20.0 | young region; strong field |
| | | | | | |
| 6 | 50 | Aug. 20.6 | 11480 | Aug. 22.4 | strong field |
| | 40 | Aug. 20.8 | 11482 | Aug. 23.4 | complex region; extremely |
| | 169 | Aug. 22 | | | strong field |
| | 169 | Aug. 23.9 | | | |

CMP date being McMath 11 120, 11 111, 11 112. However the region McMath 11 120 developed on January 11, at a time when the noise storm has already reached its maximum. At decameter wavelengths the region 2 crossed the central meridian between January 20 and 21, shortly after the large active region McMath 11 128.

At 50 MHz the CMP of region 3 occurred on April 15.1. The three regions with closest CMP date were McMath 11 253, 11 249 and 11 250. The CMP of the next two regions (Nos. 4 and 5) falls between that of two active regions. For region 4 the CMP at 60 MHz occurred on May 7.7 between the plages McMath 11 294 and 11 296. The CMP of region 5 occurred on July 19.0, between plages McMath 11 425 and 11 429. Finally, the CMP of region 6 occurred on August 20.6. No active region passed the central meridian on this day. It can be seen that no clearcut association of storms with chromospheric active regions can be established purely on the basis of the CMP date.

A total of 48 storm intensifications and onsets occurred during our observing period at Clark Lake. To establish the beginning of a storm from the interferometer records presents no difficulty. Since no quantitative flux measurements were available, personal judgment had to be exercised to establish the times of intensifications. It must be emphasized that since the sensitivity of the system varies with direction, galactic background temperature, and receiver settings, all intensifications noted are relative to the emission level that existed in the preceding few minutes. The build-up of a storm was very gradual in all but a few cases and intensification or onset should be taken as approximate to ± 10 min.

A complete list of the flares and subflares which occurred during the three hour period preceding each decametric storm onset or intensification has been given elsewhere (Gergely, 1974). The occurrence of some flares prior to a storm onset must be considered accidental on the basis of the relative position of the flaring region and the decametric source. Eliminating these flares from the sample two interesting facts emerge. First, the flares which preceded the onsets or intensification which occurred in course of a given storm did not always originate in the same chromospheric active region. For example, from the flares preceding the eight observed intensifications or onsets related to decametric storm region 5, four occurred in McMath region 11 425, three in McMath region 11 429, and one in McMath region 11 423. We recall that the decametric source appeared to cross the central meridian between the McMath regions 11 425 and 11 429.

Six onsets or intensifications were observed at Clark Lake, related to storm region 3. Four of them occurred following subflares in McMath region 11 253. Out of the other two, one occurred in between two subflares which were reported to occur in McMath region 11 250, the other one followed a subflare in McMath region 11 257. The decametric source crossed the central meridian shortly before the complex of active regions McMath 11 249-50-56-57; and approximately a day after the McMath region 11 253.

Secondly, flares and subflares occurred very closely in time in several neighboring active regions before and after some of the storm intensifications. For example prior

to a storm onset on July 15 at 17:45 UT subflares occurred in McMath regions 11423 and 11425 at 17:20 and 17:18 UT respectively. Another storm intensification on April 11 at 19:35 UT was preceded by subflares which started at 18:04 and 18:02 in McMath regions 11257 and 11249 respectively. A storm intensification on April 13 at 22:36 UT was preceded by a subflare at 22:33 UT in McMath region 11253 and was in turn followed by a subflare at 22:40 UT in McMath region 11250. In the above we have only given some examples of quasi-simultaneous flare activity in several active regions during decametric storms. Other examples have been given by Gergely (1974). Quasi-simultaneous flare activity in several active regions is often observed not only at the onset time but also while the decametric storm is in progress. Figure 2 illustrates this kind of behavior. The flare activity in neighboring active

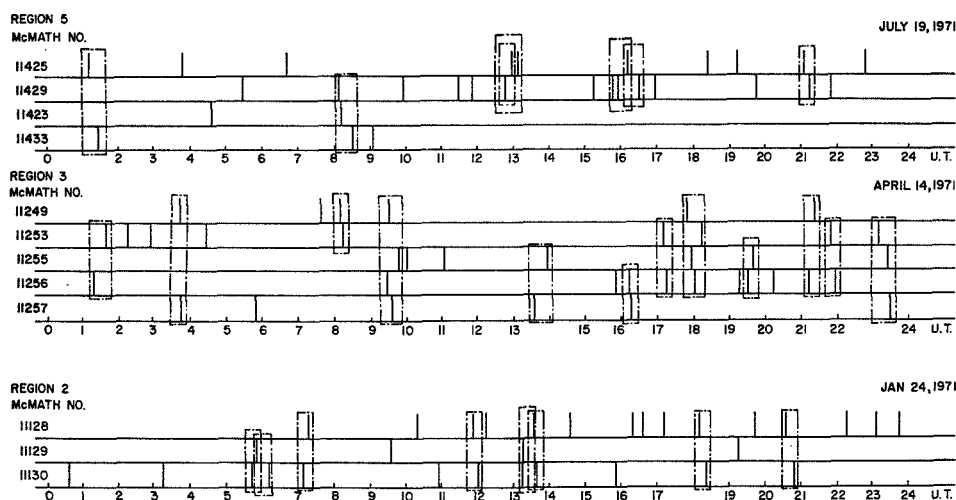


Fig. 2. Quasi-simultaneous flare activity in active regions related to decametric storms 5, 2 and 3. The subflares which are enclosed in boxes occurred with a separation in time of less than 20 min.

regions, which underlie the decametric storms 2, 3, and 5 is shown for one day in each case. The starting times of flares and subflares is indicated by the vertical lines. The flares which occurred in different active regions and were separated in time by 20 min or less are shown in enclosed in boxes. The clustering of flares at certain times is obvious. These observations suggest that a given decametric storm may be related to several, interacting active regions, rather than to a single active region. 'Sympathetic' flares have been discussed previously by Waldmeier (1938), Becker (1958), Fritzová (1959), and Smith (1962) among others. These authors studied either some well documented, albeit isolated cases of simultaneous flare activity in distant active regions, or the global flare statistics over extended periods of time. In the latter case no physical relation was known to exist between the regions considered and the results have not been conclusive. In what follows we analyze statistically the flare occurrences in the

active regions which, due to their position, appeared to be related to each decametric storm. This approach provides us with a reasonable time interval over which to consider possibly correlated activity, as well as with a criterion which permits us to consider only those regions which might indeed be physically related.

Let us assume that a given active region produced N_1 flares and subflares in a given period of time T . Subdividing this period of time into I intervals of duration Δt each, the probability for a flare to occur in any interval Δt is given by

$$P_1 = \frac{N_1}{I}. \quad (1)$$

If a second region is flare-active over the same period T , we can predict the number of 'simultaneous' flares where 'simultaneous' is defined as flares occurring in both active regions within the same interval Δt . We chose the time interval Δt to be 20 min in order to consider two flares as 'simultaneous', and in the rest of this paper the word 'simultaneous' will be used in this context.

Assuming that the activity in the two regions is uncorrelated, the number of intervals, N_{12} , containing simultaneous flares is given by

$$\frac{N_{12}}{I} = p_1 p_2 = \frac{N_1 N_2}{I^2}, \quad (2)$$

where N_2 and p_2 are the total number of flares and the flare probability in region 2. If the actual number of simultaneous flares, N'_{12} , exceeds the estimate N_{12} to a statistically significant degree, then the flare activity in the two regions must be correlated. The standard deviation of the estimate, N_{12} will be

$$\Delta N_{12} = \frac{1}{I} (N_1 \sqrt{N_2} + N_2 \sqrt{N_1}) \quad (3)$$

assuming that the flare occurrences in both active regions follow a Poisson distribution. It will be shown below that in several cases, N'_{12} is approximately two times N_{12} and this excess is statistically significant. Therefore, we conclude that when active regions show evidence of physical interaction through their association with a single decametric source, then the flare activity in the regions is often significantly correlated. The interacting regions will now be discussed in more detail.

Figures 3a to f show the Fraunhofer Institute maps close to the CMP of each storm region. The active regions underlying each decametric source are indicated by their McMath numbers. The mean position of the radio source is indicated by the heavy line and its size by the two broken lines at the highest frequency of measurement. Since the times of observation of the plages and the radio sources do not coincide exactly, we interpolated the radio positions between two consecutive days. We analyze below the flare activity related to each radio region along with its magnetic field and filament configuration.

The projected position of the centroid of radio source 1 appears at the location of McMath regions 11111 and 11112 (Figure 3a). Other active regions also apparently

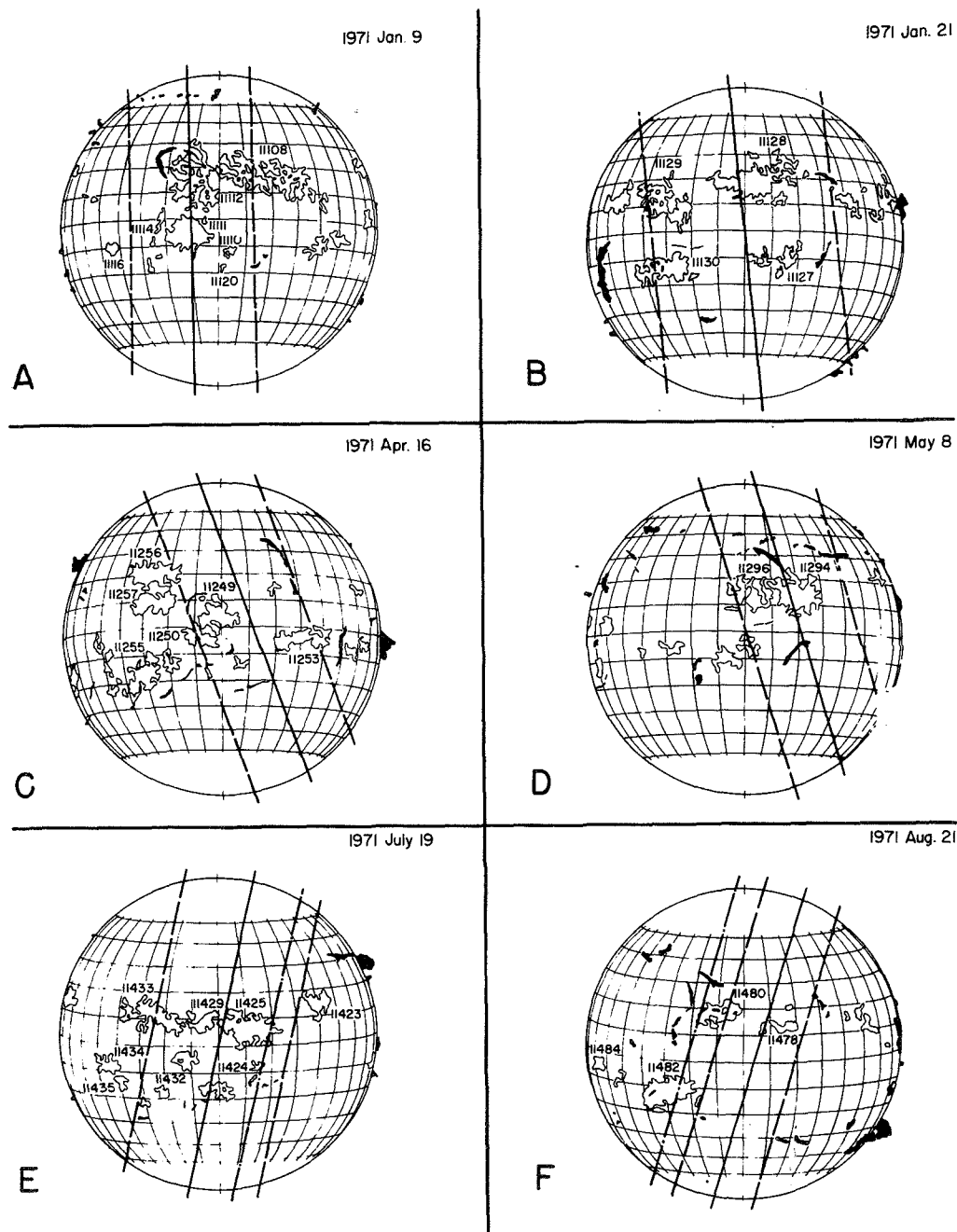


Fig. 3. (a) Projected position of the decametric storm 1, 1971, January 9, is indicated on the Fraunhofer Institut Map. Associated active regions are identified by their McMath numbers. The solid line indicates the centroid of the source at 60 MHz, and the two dashed lines indicate its size. (b) Same for decametric storm 2, 1971, January 21. (c) Same for decametric storm 3, 1971, April 16. (d) Same for decametric storm 4, 1971, May 8. (e) Same for decametric storm 5, 1971, July 19. The line indicates the centroid of the type III group mentioned in the text. (f) Same for decametric storm 6, 1971, August 21. The line indicates the centroid of the type III's, displaced eastward from the continuum source which occurred this day.

associated with the decametric source are McMath 11 108-10-14-20. A large stable filament separated McMath regions 11 112 and 11 108; smaller filaments were observed delineating the neutral line in McMath regions 11 111 and in some of the other regions. Most of the flare activity was produced by McMath region 11 111. It produced 63 flares and subflares between January 6 and 12. Only four simultaneous flare pairs were observed to occur during the period January 6 to 12; all four involved the region McMath 11 111 and one or the other of the regions mentioned. This small number of simultaneous flare pairs was judged to be insufficient to perform a meaningful statistical analysis. However, it should be pointed out that Caroubalos *et al.* (1973) analyzed a pulsating radio event that occurred in 1971, January 14 at meter wavelengths and was related to the continuum source we have studied. They reported that during most of the disk passage of the meter wavelength storm two stable sources were observed at 80 MHz; one was located above the complex of regions McMath 111-10-20, the other one above McMath 11 108. The occasional interaction of these two sources at 80 MHz was reported (Caroubalos *et al.*, 1973).

The decametric region 2 was located above the large active region McMath 11 128 (Figure 3b) which gave origin to the proton flare of 1971, January 24. Active regions McMath 11 127, 11 129 and 11 130 were also located under the decametric source. The McMath region 11 127 contained weak magnetic fields and produced only two subflares during disk passage. The other three active regions contained intense magnetic fields. The magnetic configuration of McMath 11 128 was especially complex. This was the most active of the three regions associated with the decametric storm. It produced 132 flares and subflares between January 17 and 26. A large number of simultaneous flares occurred between January 17 and 26. The number of expected and observed simultaneous flares which occurred in these regions, as well as the standard deviation of the expected number of simultaneous flares is shown in Table IIIa. In those cases where the formal standard deviation is less than 0.5 it is shown as zero in the table.

The number of observed simultaneous flares indicates strong interaction between McMath regions 11 128-11 129 and 11 128-11 130, and a smaller degree of interaction between the regions McMath 11 129-11 130. This result is not unexpected in view of the magnetic configuration and the dominant flare activity in McMath region 11 128. Further evidence for interaction between McMath region 11 128 and the other two regions comes from 80 MHz observations of the radio event, related to the proton flare of 1971, January 24 (Riddle and Sheridan, 1973). Numerous sources were observed during the early phase of this event, most of them close to, or above, the west limb of the Sun. However two of the sources (designated *E* and *F* by the authors) appeared approximately above the active regions McMath 11 129 and 11 130.

Several active regions were found to be associated with decametric storm region 3 (Figure 3c). Slightly to the east of the projected position of the centroid of the decametric source we find the complex of regions McMath 11 249-50-55-56-57. To the west is located McMath region 11 253. We noted already that some of the intensifications of the decametric source took place following subflares that occurred in McMath

TABLE III
Simultaneous flare activity in active regions related to decametric storms

(a) Active regions related to storm 2

| McMath region | 11 128 | 11 129 | 11 130 |
|---------------|--------|-------------------|--------------------|
| 11 128 | — | (13) 5 ± 2 | (24) 10 ± 2 |
| 11 129 | — | — | (4) 2 ± 1 |
| 11 130 | — | — | — |

(b) Active regions related to storm 3

| McMath region | 11 249 | 11 250 | 11 253 | 11 255 | 11 256 | 11 257 |
|---------------|--------|------------------|------------------|------------------|------------------|-------------------|
| 11 249 | — | (0) 1 ± 1 | (4) 1 ± 1 | (2) 0 ± 0 | (3) 2 ± 1 | (2) 1 ± 0 |
| 11 250 | | — | (2) 2 ± 1 | (1) 1 ± 0 | (7) 3 ± 1 | (2) 1 ± 1 |
| 11 253 | | | — | (3) 1 ± 0 | (4) 6 ± 1 | (4) 2 ± 1 |
| 11 255 | | | | — | (5) 2 ± 1 | (2) 1 ± 0 |
| 11 256 | | | | | — | (10) 3 ± 1 |
| 11 257 | | | | | | — |

(c) Active regions related to storm 5

| McMath region | 11 423 | 11 425 | 11 429 | 11 430 | 11 433 |
|---------------|--------|------------------|------------------|------------------|-------------------|
| 11 423 | — | (7) 3 ± 1 | (1) 1 ± 0 | (2) 0 ± 0 | (1) 2 ± 1 |
| 11 425 | | — | (8) 3 ± 1 | (7) 1 ± 0 | (12) 6 ± 1 |
| 11 429 | | | — | (3) 0 ± 0 | (3) 2 ± 0 |
| 11 430 | | | | — | (0) 1 ± 0 |
| 11 433 | | | | | — |

The upper figure at the intersection of a given column and row indicates the number of observed flare coincidences for the pair of regions involved. The lower figure indicates the number of expected flare coincidences and the error; assuming random flare occurrence in both regions.

region 11253, while others occurred after subflares in McMath regions 11250 and 11256. Several long filaments appear near the active regions McMath 11256-57-50-49-55. These filaments separate regions of predominantly positive fields from predominantly negative fields, as observed on the corresponding Mt. Wilson magnetograms. The simultaneous flares for the active regions involved is shown in Table IIIb. The regions which appear to interact most strongly are McMath 11249-57; 11249-53; 11250-56; 11253-55; and 11256-57. These regions are the same as the ones that produced flares before the intensifications of storms.

Two active regions were associated with decametric storm region 4. One of them, McMath 11294 was very flare active, producing 52 flares and subflares between May 6 and May 13. It was the site of several major flares during this time; moving type IV bursts related to two of these were observed at Clark Lake. The other region, McMath 11296 produced only two subflares, both simultaneous with flares in McMath 11294. A stable filament existed between the two active regions (Figure 3d).

Numerous active regions were associated with decametric source 5 (Figure 3e). The disk passage of these regions was characterized by a high level of flare activity; 190 flares and subflares were observed from the complex between 1971, July 12 and 24. We already noted that storm intensifications followed subflares that occurred in McMath regions 11425 and 11429. The numbers of simultaneous flares for these regions are given in Table IIIc. A high degree of correlation between some of the active regions involved is obvious.

The active regions McMath 11478 and 11480 were associated with decametric

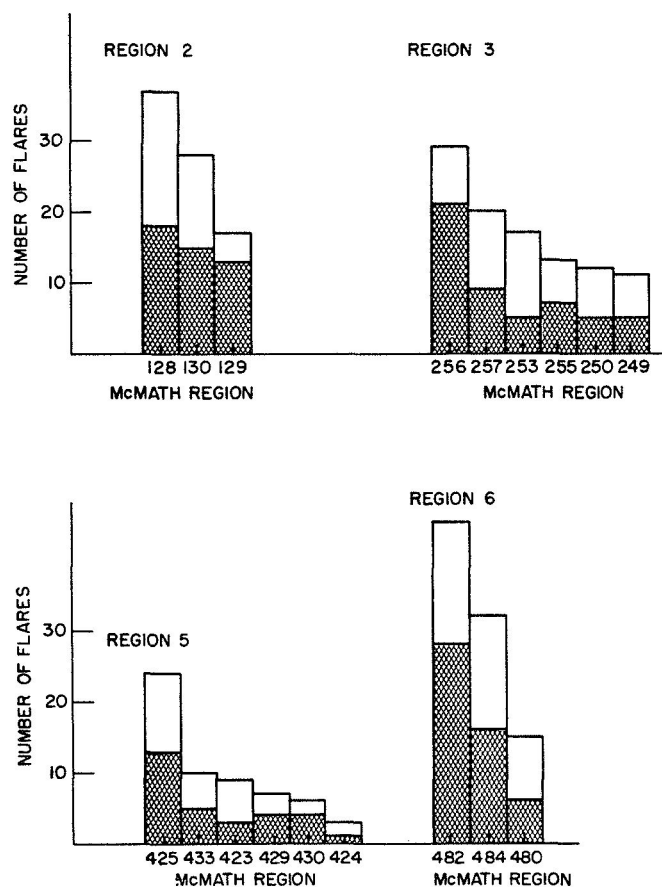


Fig. 4. Histograms of simultaneous flares in storm related active regions. 'Cross-hatching' indicates the flare pairs which started in the region.

source 6 (Figure 3f). The McMath region 11478 was marginally active during the storm and will not be considered here. To the east of the decametric source we observe the McMath region 11482. There is no doubt that this region was related to the decametric storm. It was extremely flare active, some of the flares giving rise to very intense type III groups. These type III groups occurred slightly to the east of the continuum source. Both active regions McMath 11480 and 11482 contained intense magnetic fields. A long filament, stretching in the north-south direction again separated magnetic regions of opposite polarity. During the period August 16 to 26, 28 flares occurred in McMath region 11480, 12 of these simultaneous with flares that occurred in McMath region 11482. The McMath region 11484 also interacted strongly with the McMath region 11482 and produced 32 simultaneous flares from a total of 54.

Figure 4 shows a histogram of the simultaneous flares involving the active regions associated with each storm. The coincidences corresponding to the occurrence of the first flare of the pair occurring the region are shown in dark. Even for the most flare-active regions, such as McMath 11482 or 11128 about 50% of the initial flares of a pair occurred in some other, less active region. In every case that we studied, a decametric storm appeared to be associated with multiple active regions and there is at least some evidence of interaction between these regions.

In order to determine whether or not a direct association between flares and decametric storms could be established, we considered the distribution of the time differences between the start of a flare and the associated radio storm. The distribution peaked at a time interval of about 20 min between the start of a flare or subflare and the associated radio storm. However, the average time between flares and subflares was also about 20 min during these periods so it was impossible to make an unambiguous relationship between the radio events and the chromospheric flares and to determine an average time difference between the chromospheric flares and to determine an average time difference between the chromospheric flare and the radio storm onset or intensification. With the exception of one Imp 1 flare, all the storm onsets or intensifications were preceded by subflares.

4. Relation of Decametric Storms to Coronal Magnetic Fields

Altschuler and Newkirk (1969) computed coronal magnetic fields from observations of the longitudinal component of photospheric fields. They used a current-free approximation and assumed that the field lines reaching up as high as $2.5 R_{\odot}$ were drawn out by the solar wind into interplanetary space. Since only the longitudinal component of the photospheric field is available for the computations, data collected over half a solar rotation must be used to construct the map for any given day. Rapid changes in the magnetic fields are not reflected in the maps for this reason. Newkirk and Altschuler (1970) compared the coronal structures observed in white light with the calculated magnetic fields and found good agreement between the density structure of the corona and the calculated field configurations. Several characteristic shapes of these configurations were described by them. Diverging fields (DF) reach out from a

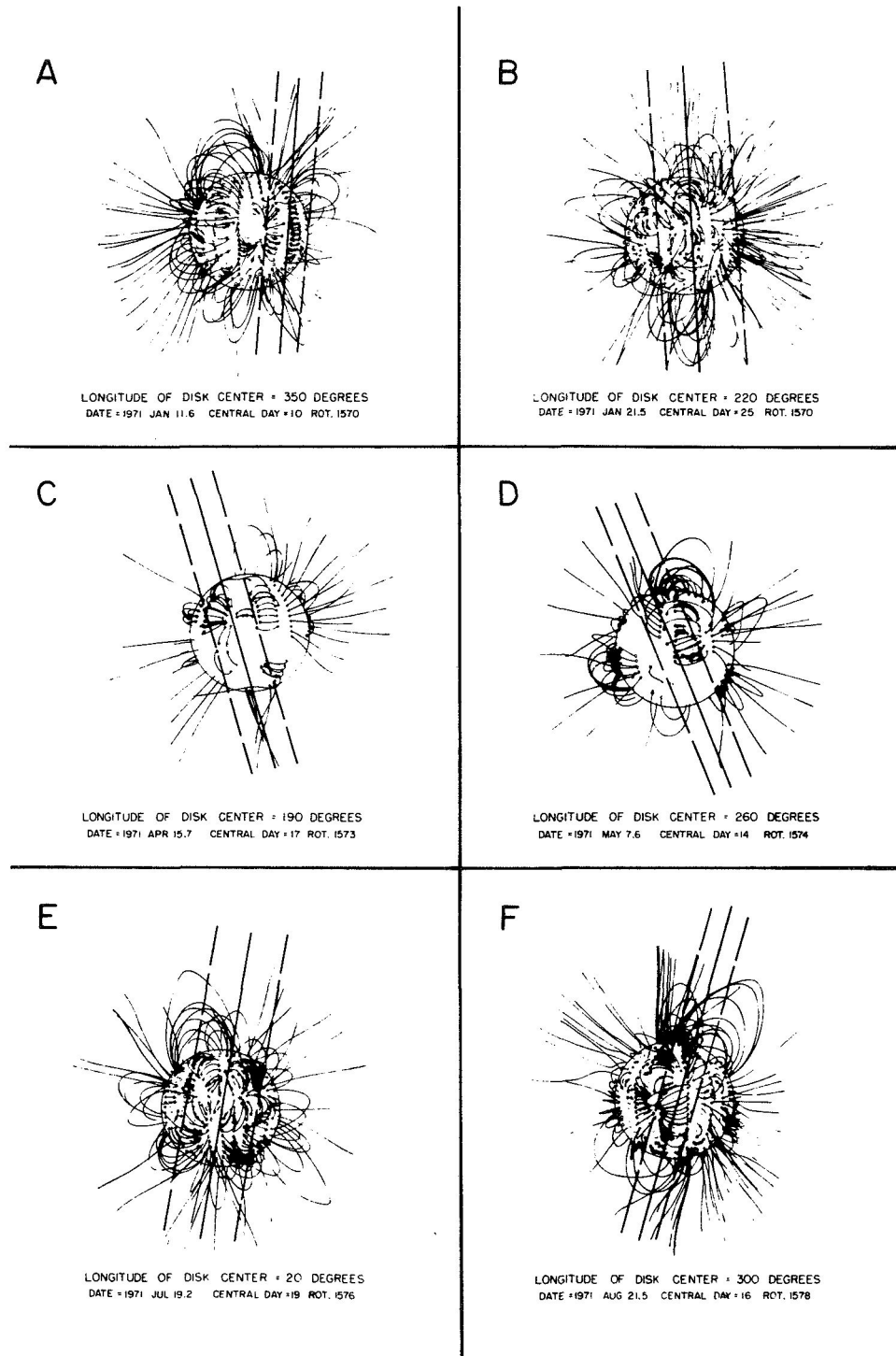


Fig. 5. (a) Magnetic fields related to decametric source 1. The centroid of the source is indicated by the solid line, its size by the two dashed lines. (Magnetic maps courtesy of Ms. D. Trotter, High Altitude Observatory.) (b) Same as Figure 4a for decametric storm region 2. (c) Same as Figure 4a for decametric storm region 3. (d) Same as Figure 4a for decametric storm region 4. (e) Same as Figure 4a for decametric storm region 5. (f) Same as Figure 4a for decametric storm region 6.

central focal point to neighboring, low field regions. Low magnetic arcades (LMA) consist of loops, forming long corridors; the top of these loops do not exceed $0.5 R_{\odot}$ above the photosphere. High magnetic arcades (HMA) are similar, except that they do extend to greater heights and may appear distorted because they were computed using an artificial boundary condition simulating the solar wind surface. Finally, magnetic rays (MR) show the presence of open field lines which extend so high above the surface that their point of reconnection is outside the domain of calculations.

We examined the calculated potential fields (provided kindly by Miss D. Trotter, High Altitude Observatory, Boulder, Colorado) for each storm around the CMP date. Figure 5 shows the magnetic fields, as well as the continuum source for the day shown. All the regions appear to be characterized by magnetic arcades, low in some cases and high in others.

Region No. 1 was characterized by an arcade, running in the north-south direction (Figure 5a). A tightly wound LMA stretches over McMath regions 11 108, 11 110 and 11 120. The field lines are closed in the corona above McMath region 11 111. A more open structure (DF) is found to the north, above McMath 11 112, which is an old, decaying region. That DF's and LMA's are not mutually exclusive structures have been noted by Newkirk and Altschuler (1970), since LMA's sometimes form an annulus, partially surrounding a DF. An LMA extends under an HMA at the location of active regions 11 128 and 11 129, associated with decametric source No. 2 (Figure 5b). Open field lines appear under the south-western end of the arcade. A DF appears at the site of McMath region 11 130; no obvious connection with the northern arcade is seen. Region 3 appears to have the most open configuration of all regions considered here. An LMA is seen running in the north-south direction over McMath regions 11 256-57-55. The field lines appear to diverge around McMath regions 11 249-50; another arcade is seen to the west, above McMath regions 11 252-53. All the regions appear to be magnetically connected (Figure 5c).

An LMA stretching under an HMA towards the north pole appears at the site of region 4. Note that the LMA once again embraces the eastern portion of a DF. A substantial number of type III bursts displaced towards the west from the continuum source and generally starting at the high frequencies were observed during this storm (Figure 5d).

Region 5 coincided with an HMA running in the east-west direction, approximately over the solar equator. We note that only a small number of type III bursts were recorded during this storm and that the continuum source was large (Figure 3e, 5e) as can be expected from the orientation of the magnetic arcade.

Finally, the magnetic structure related to region 6 is a complex one, just as the storm itself was complex (Figure 5f). Two LMA's, slightly twisted, embrace a region, from which field lines are diverging. The decametric source was situated above the western arcade. Two sources were observed at 169 MHz for the entire duration of the storm, one above each of the magnetic arcades. These magnetic arcades were situated on each side of McMath 11 482, an extremely flare-active region. A series of very intense type III bursts, all of them flare associated were observed from this region.

These type III bursts were clearly of a different nature than those occurring during the storm. They were much more intense, to the point of saturating the records, almost always occurred in groups and their starting frequency was always higher than 65 MHz.

The magnetic configurations were examined one solar rotation after the dates considered here. Most of the structures described were still recognizable, but all of them appeared to be more open than at the time of the storm. Such open field lines often extend to interplanetary space.

The general appearance of the magnetic fields supports the evidence presented in the previous section for interaction between several active regions. As Newkirk and Altschuler pointed out, although the coincidence of a given field line with a particular region is meaningless, a comparison between the shapes of the field configurations and the coronal structures is still valid. In the case of the decametric storms, the magnetic structures appear to connect the underlying chromospheric regions and possibly provide a channel along which energetic particles can travel.

5. Association with Decimeter and Meter Wavelength Activity

No burst activity at centimeter wavelengths is known to be associated with noise storms. It has been observed (Malinge, 1963) that the occurrence of a large centimeter wave burst during a metric noise storm seems to inhibit the production of type I bursts. We examined the rate of occurrence of centimeter bursts during the three hours preceding and following storm onsets and intensifications, and found no correlation between these two phenomena. The rate of occurrence of centimeter wavelength bursts was found to be the same during these periods as when storms were in progress, or even at times when no storm was present at all.

If decametric storms are associated with interacting active regions as discussed earlier, we may expect to find multiple sources at the lower heights in the corona during storms. Indeed, the Nançay interferometric observations at 408 MHz (published in *Solar Geophysical Data*) confirm this (Figure 6). In this figure the crosses indicate the position of the sources at 408 MHz, the heavy lines indicate the trajectory which would be followed by a source located above the active regions whose McMath numbers are indicated.

Two sources were observed on January 19, the day decametric source 2 appeared. One of them was located above McMath region 11128, the other above McMath regions 11129-11130. Three sources were present on January 20 and 21, when the decametric emission was strongest. Decametric emission was much weaker or was entirely absent during the next three days, when only one source appeared at 408 MHz. Multiple sources were seen from April 12 to April 17 at 408 MHz, simultaneously with decametric source 3. The east-west position of these sources corresponds rather well with the position located radially above McMath regions 11253 and 11257 at a height of $1.3 R_{\odot}$, and above McMath region 11250 at a height of $1.05 R_{\odot}$. We note that no multiple source at 408 MHz was observed after April 17, and that after this day the

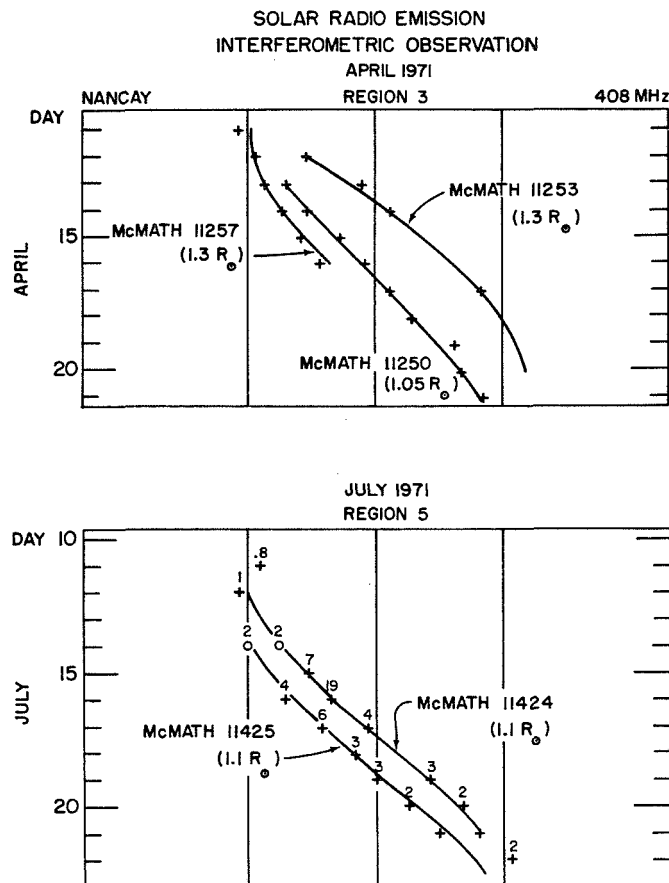


Fig. 6. Positions of 408 MHz regions associated with decametric storm regions 3 and 5. The crosses indicate the positions of 408 MHz sources; the heavy lines indicate the trajectory that would be followed by a source located at the indicated heights above the active regions.

decametric emission also ceased completely. Multiple sources were observed for the whole duration of decametric source No. 5. The east-west position of the 408 MHz sources corresponds to that of sources located at $1.1 R_{\odot}$ above McMath regions 11424 and 11425. Once again the decametric source lasted only as long as multiple sources were observed at the lower heights.

Similar situations are found for decametric sources No. 4 and 6. Double sources were observed for the whole duration of decametric storm 6 and for most of the duration of decametric source 4. A double source was observed one day only while storm 1 was in progress. It is likely, however, that a double source was present, since such a source-oriented in the north-south direction was indeed observed at 80 MHz (Caroubalos *et al.*, 1973).

Boischot *et al.* (1970) suggested that metric storms, consisting generally of type I

bursts, and decametric storms, consisting mainly of type III bursts, constitute different manifestations of the storm phenomenon. Using the data obtained in 1967 they found that in 86% of the cases when a metric storm was present a decametric storm was also observed. Conversely, 87% of the decametric storms could be associated with a metric storm. No positional observations were involved, the association was made only on the basis of coincidence in time. We investigated this association, examining the Nançay 169 MHz interferometric observations (*Solar Geophysical Data*) along with our positional data. Thus we were able to compare not only the coincidence in time but also the position of metric and decametric storms. We found that a metric storm was indeed associated with each of the decametric sources. Good agreement was found between the metric and decametric storms; the CMP of the decametric storm coincided usually within 1.5 days with that of the metric storm. The CMP dates for the metric storms are given in Table II. A systematic correction was included, to account for the fact that the 169 MHz positional observations were made at the local meridian (approximately 12:00 UT). During the period considered by us, a decametric storm was present on the disk on 75% of the days when a metric storm was reported. On the other hand, a metric storm was reported to occur on 92% of the days when a decametric storm occurred. From a total of 37 days of decametric storm emission a metric storm was not reported for only three days. Three storms not examined

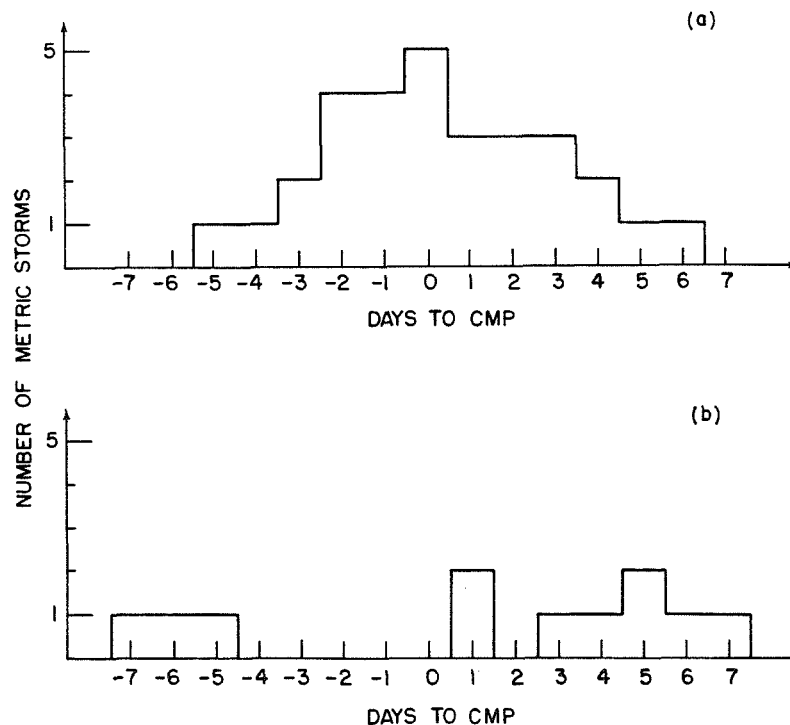


Fig. 7. (a) Longitude distribution of metric storms associated with decametric storms. (b) Same for metric storms without associated decametric storm.

here can be observed on the Nançay charts during the period 1971, January-August. Decametric storms of shorter duration were observed on the date of the metric storm or on the following day in each case. The coincidence of meter and decameter storms can be considered even more significant, since there is no overlap between the observing periods at Nançay and Clark Lake. Figure 7 shows the longitude distribution of metric storms (a) with no decametric counterpart and (b) with decameter storm. The figure suggests that the absence of decametric storms for some of the days when metric storms have been observed can be explained by a higher directivity of the decametric storms.

6. Conclusion

Until recently, solar activity was discussed in terms of independent active regions. Wild (1968) pointed out the existence of several interacting centers in the case of a noise storm observed with the Culgoora radioheliograph. In the case he reported, activity correlated in time and arising from several sources was observed for half an hour before the start of a major flare (imp. 2). This flare was followed by a noise storm. Some of the participating regions were separated by large distances and the triggering of activity in one center by another would have required faster-than-light particles. For this reason, Wild assumed an initiating disturbance located at a central point high in the corona. Kai (1969) also presented several events, showing the interaction of various centers, sometimes separated by as much as $1.0 R_{\odot}$. Both Kai and Wild observed that the sources involved had opposite senses of polarization in most cases, suggesting that they were connected by magnetic fields looping through the corona. In agreement with Kai, we find that a given source may sometimes be the initiating and at other times the triggered disturbance.

Further, Wild (1969) suggested that interaction between active regions may occur in two ways; through MHD shock waves, travelling at speeds of 10^3 km s^{-1} triggering eruptions at distant centers, and by fast particles travelling along magnetic field lines. These two classes of interactions have rather different manifestations in the radio regime. The former is seen in the form of type II or type II-IV bursts, while the latter may be represented by type III bursts, 'U'-bursts and reverse drift bursts, all commonly observed during metric noise storms.

In this paper we have studied the relationship of decametric storm sources with other aspects of solar activity. Specifically, we related the storm sources to interacting active region complexes in the chromosphere. In every case that we studied, a decametric storm implied evidence of interaction between pairs of active regions. In most cases the flare occurrence in neighboring regions turned out to be non-random with the number of simultaneous flares approximately twice as large as that expected on the basis of random occurrences. We have not addressed the opposite question of whether or not interacting regions always produce decametric storms. Intensifications or onsets of decametric storms do not seem to relate *directly* to flares.

We showed that decametric storms are always associated with storms at the meter and decimeter wavelengths, and that multiple sources are often observed at these

wavelengths. The magnetic structures associated with the storm sources were found to be high or low magnetic arcades, the latter sometimes partially surrounding regions of open or diverging field lines. The centroid of the continuum source frequently coincides with filaments or chains of filaments, known to indicate the presence of neutral sheets higher in the corona.

Acknowledgements

Support for this work was provided under NASA grants NGL 21-002-033, NGR 21-002-367 and NSF grant GP-19401. We thank M. R. Kundu, J. de la Noë, H. Rosenberg and D. G. Wentzel for many helpful discussions and suggestions. Thanks are also due to D. Trotter of the High Altitude Observatory who provided us with coronal field maps. For the operation and maintenance of the LPA, the work of K. Barbier, P. Dooley and J. Hubbard is gratefully acknowledged. The computer time for this project was supported by NASA grant NsG-398 to the Computer Science Center of the University of Maryland.

Portions of this paper are based on the thesis of one of the authors (T.E.G.) in partial fulfillment of the requirements for the Degree of Doctor of Philosophy at the University of Maryland.

References

- Altschuler, M. D. and Newkirk, G., Jr.: 1969, *Solar Phys.* **9**, 131.
 Becker, V.: 1958, *Z. Astrophys.* **44**, 243.
 Boischot, A., de la Noë, J., and Møller-Pedersen, B.: 1970, *Astron. Astrophys.* **4**, 159.
 Boischot, A., de la Noë, J., du Chaffaut, M., and Rosolen, C.: 1971, *Compt. Rend. Acad. Sci.* **272**, 166.
 Caroubalos, C., Pick, M., Rosenberg, H., and Slottje, C.: 1973, *Solar Phys.* **31**, 473.
 Clavelier, B.: 1967, *Ann. Astrophys.* **30**, 895.
 de la Noë, J., Boischot, A., and Aubier, M.: 1973, in R. Ramaty and R. G. Stone (eds.), *High Energy Phenomena on the Sun*, NASA-GSFC Preprint, p. 602.
 Erickson, W. C. and Kuiper, T. B. H.: 1973, *Radio Sci.* **8**, 845.
 Fainberg, J. and Stone, R. G.: 1974, *Space Sci. Rev.* **16**, 145.
 Fritzová, L.: 1959, *Bull. Astron. Inst. Czech.* **10**, 145.
 Gergely, T. E.: 1974, Ph.D. Thesis, University of Maryland.
 Gergely, T. E. and Kundu, M. R.: 1974, *Solar Phys.* **34**, 433.
 Kai, K.: 1969, *Proc. ASA* **1**, 186.
 Kuiper, T. B. H.: 1973, Ph.D. Thesis, University of Maryland.
 Kundu, M. R.: 1965, *Solar Radio Astronomy*, Wiley-Interscience, New York.
 Malinge, A. M.: 1963, *Ann. Astrophys.* **26**, 97.
 Newkirk, G., Jr. and Altschuler, M. D.: 1970, *Solar Phys.* **13**, 131.
 Riddle, A. C. and Sheridan, K. V.: 1971, *Proc. ASA* **2**, 62.
 Rosenberg, H.: 1971, in R. Howard (ed.), 'Solar Magnetic Fields', *IAU Symp.* **43**, 652.
 Rosenberg, H.: 1972, *Solar Phys.* **25**, 188.
 Rosenberg, H. and Tarnstrom, G. L.: 1972, *Solar Phys.* **24**, 210.
 Smith, H. J.: 1962, GRD Res. Notes, No. 58.
 Solar Radio Group Utrecht: 1974, *Space Sci. Rev.* **16**, 45.
 Stewart, R. T. and Labrum, N.: 1972, *Solar Phys.* **27**, 192.
 Waldmeier, M.: 1938, *Z. Astrophys.* **16**, 276.
 Warwick, J. W.: 1965, in J. Aarons (ed.), *Solar System Radio Astronomy*, Plenum Press, New York.
 Wild, J. P.: 1968, *Proc. ASA* **1**, 137.
 Wild, J. P.: 1969, *Proc. ASA* **1**, 181.
 Wild, J. P., Smerd, J. F., and Weiss, A. A.: 1963, *Ann. Rev. Astron. Astrophys.* **1**, 291.

DECAMETER STORM RADIATION, II

T. E. GERGELY and M. R. KUNDU

Astronomy Program, University of Maryland, College Park, Md. 20742, U.S.A.

(Received 18 April; in revised form 24 October, 1974)

Abstract. The physical properties of six decametric storms, observed at Clark Lake Radio Observatory are studied. The height of the storm continuum sources was determined from the rotation rate. Assuming that the radiation originates at the plasma frequency we computed the gradient of electron density for the regions where the storms originate. The mean angular size of the decametric continuum sources is large; it increases with decreasing frequency. The storm continuum is found to be strongly directive toward the disk center. The east-west asymmetry, well observed at meter wavelengths is also observed at decameter wavelengths.

The occurrence of two distinct classes of type III bursts in storms is discussed: 'off-fringe' and 'on-fringe' type III's. The 'off-fringe' III's are found to be displaced in position from the continuum source; on the other hand, the 'on-fringe' ones coincide in position with the continuum. These two kinds of bursts differ in other properties as well.

A model of the storm region is proposed. The continuum radiation and the 'on-fringe' type III's are believed to originate above closed magnetic loops, in regions of diverging field lines; the 'off-fringe' type III's are thought to be excited by energetic electron streams, having access to open magnetic field lines at the base of the loops.

1. Introduction

Gergely and Erickson (1974, hereinafter referred to as Paper I) studied the relationship of decametric storms with other aspects of solar activity. In this paper we study the height, size, directivity and lifetime of the decametric sources. The time period considered is the same as in Paper I, and the storm regions are designated by the same number as before. We also discuss the type III bursts observed during storms. These bursts frequently appear displaced in position from the continuum. On the swept frequency interferometer records this displacement appears as an independent system of fringes, quite distinct from that due to continuum radiation. Bursts coinciding with, and displaced from the continuum shall be designated as 'on' and 'off'-fringe type III's. It is likely, that the 'on' and 'off-fringe' type III's correspond to the same as type IIIS and type III bursts respectively, used occasionally in the literature to designate the bursts at meter wavelengths. Figure 1 shows a record of a storm, illustrating two types of bursts. An empirical model of the storm region is presented in the final section.

2. Height of Decametric Storm Sources

The height of the source of continuum storm radiation was determined by Clavelier (1967) at 408 MHz and at 169 MHz by Malinge (1963). Clavelier (1967) used two different methods to determine the height of the sources. In the first method he associated a radio storm region with an optical center of activity. By assuming that the radio source was located radially above the associated active region, its height with

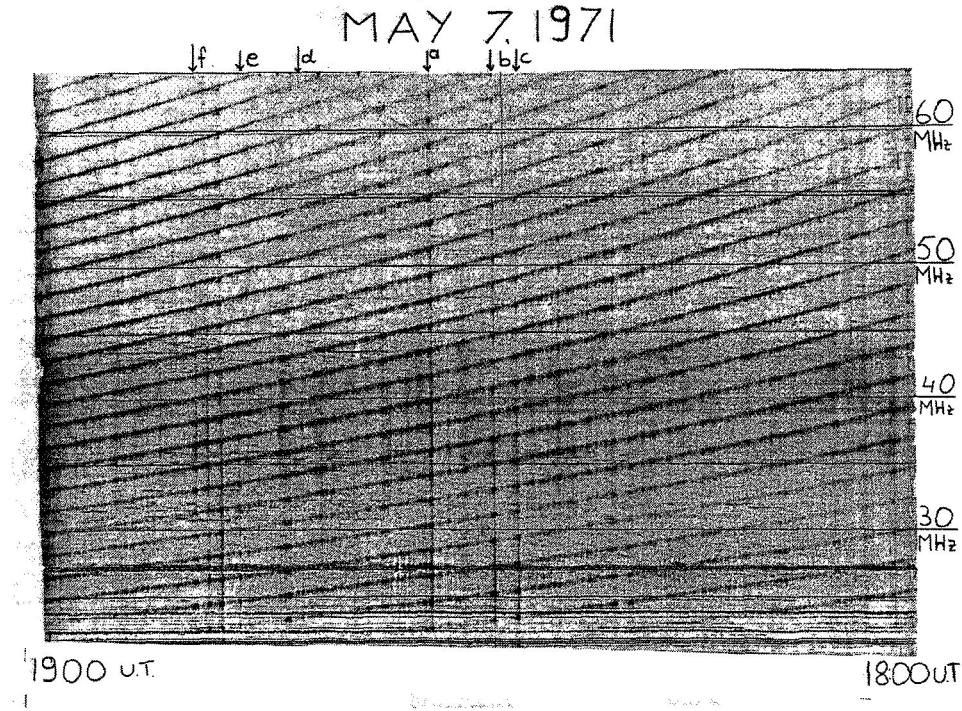


Fig. 1. 'On' and 'off-fringe' type III bursts, observed during the 1971 May 7 storm. a, b and c are 'off-'; d, e and f are 'on-fringe' bursts.

respect to the photosphere could then be determined. The second method made use of the apparent velocity of the radio source close to the CMP date. These two methods are complementary, insofar as the accuracy is concerned. The first method gives good results for sources located close to the limb, while the second one is more accurate for sources close to the central meridian.

The mean height of the sources at 408 MHz, determined by using the first method was $1.1 R_{\odot}$. The second method gave $1.08 \pm 0.03 R_{\odot}$ (Clavelier, 1967). A total of 77 sources was studied by the first method; 10 sources were studied by the second method. Malinge (1963) used the second method at 169 MHz, and found a rather large scatter in her determinations, the sources being distributed between 1.2 and $2.7 R_{\odot}$. The mean height was found to be $1.5 R_{\odot}$. To our knowledge no determinations exist of the height of long lasting sources at decameter wavelengths. In Paper I, we have shown that decametric storm sources cannot generally be associated with a single active region, rather the sources appear to be associated with a complex of active regions. Further the sources are directive towards the center of the disk. Consequently little use can be made of the first method discussed earlier, which requires a definite association at the limb, of a storm center with an active region. In our work, we have performed a least squares analysis based on the second method in order to determine the height of the noise storm sources at 60, 50, 40 and 30 MHz.

The east-west position of the sources was determined several times daily. Details of the reduction procedure have been given elsewhere (Kuiper, 1973; Gergely, 1974). The position of the source was determined at a given time and frequency by averaging the positions of the fringes in a 4 MHz band, centered on the desired frequency. For example, to obtain the position of a source at 40 MHz we averaged the positions given by the fringe lines in the band 38–42 MHz. Such a 4-MHz band contains from 1 to 4 fringes depending on the time of the day. All positions obtained this way at a given frequency and on a given day were averaged to obtain the mean daily position of the source. By averaging a large number of measurements we hope to minimize the effects of ionospheric refraction. For the same reason only measurements up to two hours before and after the local meridian transit were used.

Let us assume that a source situated at R solar radii from the center of the Sun and latitude λ corotates with the photosphere. Its east-west position (measured with the L.P.A.) is then given by

$$\varrho = R [\cos \lambda \cos \omega t \sin (P + \phi) \sin B + \cos \lambda \sin \omega t \cos (P + \phi) - \sin \lambda \sin (P + \phi) \cos B], \quad (1)$$

where P is the position angle of the solar axis of rotation, measured to the east from the celestial north, B is the heliographic latitude of the center of the disk, ϕ is the position angle of the interferometer fringes measured to the west from the celestial north, and ω is the angular velocity and t is the time; $t=0$ corresponds to central meridian passage. We define

$$\chi^2 = \sum_i [\varrho(t_i) - \varrho_i]^2, \quad (2)$$

where $\varrho(t_i)$ is the position of the source corotating with the Sun and situated at height R and latitude λ , as given by Equation (1), and the ϱ_i are the observed daily positions. It appears that minimizing χ^2 simultaneously with respect to R and λ allows the determination of both these parameters of the source. Further, by varying the CMP date (maintained constant up to this point) it, too, can be determined. However the determination of the latitude of the source is not possible to a good degree of accuracy. It has been shown (Paper I) that although it is not possible to associate a decametric storm with an individual active region, it is still possible to associate each storm with a complex of active regions. Consequently, in determining the height of the storm regions, the search for minimum in χ^2 has been restricted to those latitudes occupied by these complexes of activity.

For each of the six decametric storms considered, χ^2 was computed from Equation (2). For a fixed CMP date, the value of R was varied in steps of $0.05 R_\odot$ between 1.05 and $3.0 R_\odot$. The latitude was varied in steps of 5° , between 45° north and 45° south. The procedure was then repeated by varying the initial value of the CMP date in steps of 0.1 days. Rather severe restrictions were imposed on the data:

- Days for which less than four position determinations were available at a given frequency were not included in the analysis at that frequency.

– When data were available for less than five days around the CMP date for a given frequency no height was determined at that frequency.

– Only data taken up to four days before or after the CMP were included in the height determinations.

The last restriction of the data was imposed because the sources usually appear higher at the limb (Malinge, 1963); either because the effect of scattering is larger (Riddle, 1972a) or because the emission of second harmonic is prevalent close to the limb.

It is important to note that the method employed does not imply that the radio source is located radially above an optical center, an assumption used by most workers. The method does, however, imply a constant rotation rate for the sources. An angular velocity of $14.4 \text{ deg day}^{-1}$ was used in the computations. Variation of the rotation rate with latitude was neglected.

TABLE I
Latitude of decametric sources and associated active regions

| Decametric region | McMath region | Latitude | Latitude range of χ^2 search | Latitude χ^2_{\min} | | |
|-------------------|---------------|----------|-----------------------------------|--------------------------|---------|---------|
| | | | | 408 MHz | 169 MHz | 50 MHz |
| 1 | 11108 | N19 | N20–S15 | S10–S15 | S15 | S5–N20 |
| | 11112 | N10 | | | | |
| | 11111 | S3 | | | | |
| | 11110 | S13 | | | | |
| | 11114 | S14 | | | | |
| 2 | 11128 | N20 | N20–S15 | S15 | N20 | N20 |
| | 11129 | N12 | | | | |
| | 11130 | S13 | | | | |
| 3 | 11256 | N20 | N20–S20 | S5–0 | S20 | S10 |
| | 11257 | N9 | | | | |
| | 11249 | N4 | | | | |
| | 11250 | S5 | | | | |
| | 11253 | S5 | | | | |
| | 11255 | S18 | | | | |
| 4 | 11294 | N14 | N10–N15 | N5–N10 | N10–N15 | N10–N15 |
| | 11296 | N15 | | | | |
| 5 | 11423 | N15 | N15–S10 | S15–S10 | – | N15 |
| | 11433 | N12 | | | | |
| | 11429 | N10 | | | | |
| | 11425 | N6 | | | | |
| | 11430 | S5 | | | | |
| | 11424 | S7 | | | | |
| 6 | 11480 | N18 | N20–S15 | N20 | N20–S15 | N5–N20 |
| | 11478 | N14 | | | | |
| | 11482 | S12 | | | | |

Table I shows the McMath number of the active regions associated with each storm, the latitudes at which they were located, the latitude range searched for minima for each storm region and the latitude of minimum χ^2 at 408, 169 and 50 MHz. We have determined the height of two decametric sources at 60 MHz, all six sources at 50 MHz, four at 40 MHz and two at 30 MHz. These results are shown in Table II. Also included in this table are the heights of the noise storm sources at 408 and 169 MHz. The heights at these frequencies were computed by using data published in the *Solar-Geophysical Data*. The same method of computation was used as for the decametric

TABLE II
Distance of storm regions from the center of the Sun^a

| Region | 408 MHz | 169 MHz | 60 MHz | 50 MHz | 40 MHz | 30 MHz |
|--------|-----------------------|----------------------|-----------------------|------------------------|-----------------------|-----------------------|
| 1 | 1.05±0.0 | 1.25±0.15 | 1.7 ±0.2 1.7 ±0.2 | 2.0 ±0.2 2.0 ±0.2 | 2.5 ±0.2 2.25±0.2 | — |
| 2 | 1.05±0.05 | 1.35±0.20 | — | 1.6 ±0.15 1.55±0.15 | — | — |
| 3 | 1.05±0.1 | 1.35±0.1 | — | 2.0 ±0.3 2.0 ±0.3 | 2.35±0.55 2.3 ±0.5 | — |
| 4 | 1.25±0.15 | 1.5 ±0.05 | 1.75±0.2 1.75±0.15 | 1.8 ±0.15 1.8 ±0.1 | 2.0 ±0.1 1.9 ±0.15 | 2.35±0.3 2.3 ±0.25 |
| 5 | 1.10±0.1 1.10±0.1 | — | — | 1.40±0.1 1.4 ±0.1 | — | 1.60±0.25 1.55±0.2 |
| 6 | 1.15±0.1 1.05±0.05 | 1.25±0.1 1.20±0.1 | — | 1.5 ±0.2 1.5 ±0.2 | 1.85±0.2 1.75 ±0.2 | — |

^a The top line for each region shows the heights uncorrected for refraction and scattering, the bottom line shows the corrected heights. All distances are in solar radii. The errors given correspond to $\chi^2 = 1.5 \chi^2_{\min}$ levels.

sources. The errors given in the table refer to the heights where χ^2 reaches a value $\chi^2 = 1.5 \chi^2_{\min}$. Figure 2 shows two of the χ^2 contour plots. As can be seen from the errors given in Table II, and also from Figure 2, the minima in χ^2 are well defined along the R -axis. On the other hand, the minima appear rather elongated in the direction of the λ -axis.

Figure 3 presents the 60 MHz observations for decametric region 1 and the 50 MHz observations for decametric region 6. The crosses indicate the observed mean position of the source for each day. The continuous line indicates the locus of the points traced by a source located at a height of $1.7 R_{\odot}$ and latitude 0° for region 1 and a height of $1.5 R_{\odot}$ and latitude $N10^\circ$ for region 6. The position corresponding to August 25 (region 6) was not used in the least squares analysis, as the source was then five days away from the CMP.

At 408 MHz the height of the sources varies between $1.05 R_{\odot}$ and $1.25 R_{\odot}$, the average height of the eight sources being $1.1 R_{\odot}$, in excellent agreement with the results of Clavelier (1967). At 169 MHz the average value of the height of the sources turns

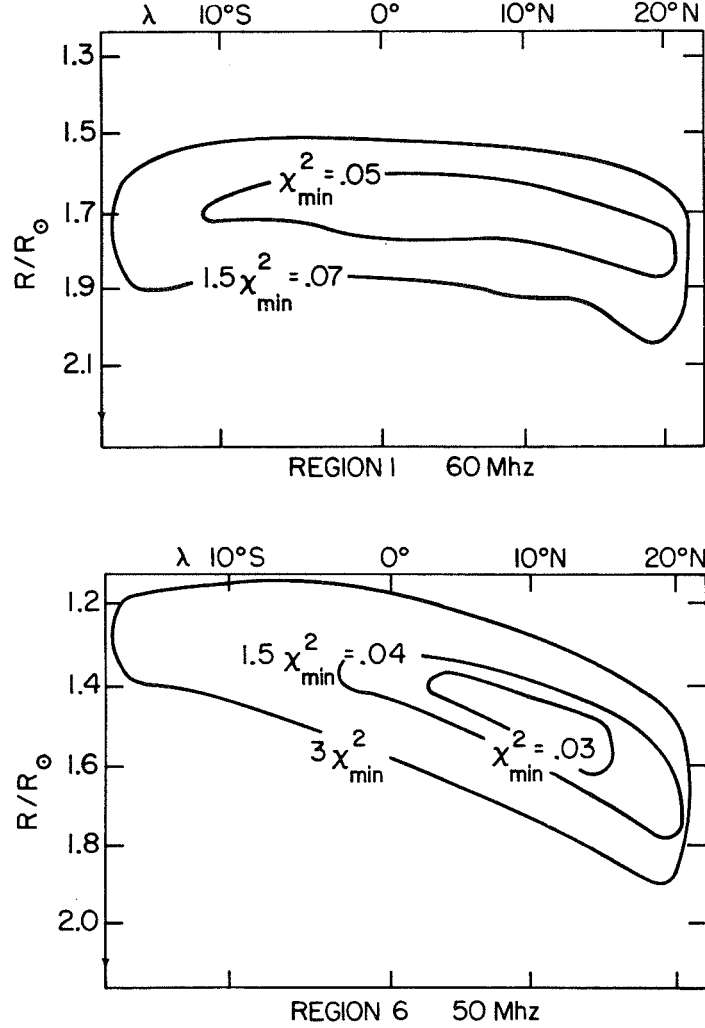


Fig. 2. χ^2 contours for decametric region 1 at 60 MHz, and for decametric region 6 at 50 MHz (see text).

out to be $1.3 R_{\odot}$, slightly lower than the value obtained by Malinge (1963). The small discrepancy can most certainly be attributed to the fact that we have excluded the limb sources from our analysis. As pointed out by Malinge (1963) limb sources tend to appear higher than sources close to the center of the disk, thereby increasing the average height of the sources.

At 50 MHz the six sources studied appear to be distributed between 1.4 and $2.0 R_{\odot}$. The average height of the sources at this frequency is $1.7 R_{\odot}$. At 40 MHz the mean height of the sources is higher, approximately $2.1 R_{\odot}$. The scatter in the height of the sources at 50 MHz is smaller than for the 169 MHz sources observed by Malinge (1963). Again, this is likely to be the result of the elimination of the limb sources from

the sample. The observed scatter of the height of the sources at a given frequency is still large. However, the dispersion with frequency of the height of emission appears to be characteristic for each source.

The propagation of radio waves between a coronal source and the Earth is influenced by three effects. These effects are: (1) refraction in the Earth's ionosphere; (2) refraction in the Sun's corona; and (3) coronal scattering. We shall make no attempt to correct our results for ionospheric refraction, except that we use only observations up to two hours before and after the transit of the Sun. Ionospheric refraction is minimum at this time.

Refraction in the corona arises because the corona is an inhomogeneous medium. Due to the effect of coronal refraction the position of limb sources will appear to be shifted towards the center of the disk. For sources close to the center of the disk the shift will be small, if any (Kundu, 1965).

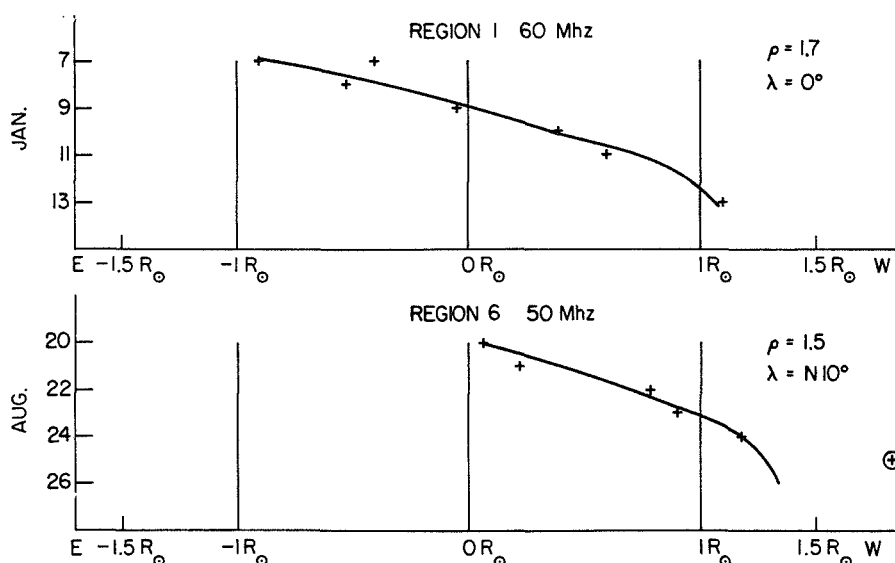


Fig. 3. East-west positions of decametric region 1 at 60 MHz and of decametric region 6 at 50 MHz. The crosses indicate the measured source positions; the heavy line is the result of the least-squares fit at the latitude and height indicated.

In addition to the smooth variation of the electron density, the corona shows small scale electron density fluctuations. Radio emission scattered off these density fluctuations will be deviated towards the limb and will tend to cancel the shift due to refraction (Fokker, 1965). The effect of both refraction and scattering were taken into account recently by Leblanc (1973). According to her brightness distribution diagrams (Leblanc, 1973) the shift of the centroid of the source of 30 MHz fundamental radiation increases almost linearly with heliographic longitude, until the source reaches about 75 deg. We corrected the height of the decametric sources for refraction and

scattering based on this calculation. At 30 MHz we assumed a shift in the position of the source towards the limb of

$$(\Delta\varrho)_{30 \text{ MHz}} = 1.25 \times 10^{-3} L \quad (3)$$

which fits closely the published brightness distribution diagrams (Leblanc, 1973). In Equation (3), $\Delta\varrho$ is expressed in solar radii and L is the longitude of the source, expressed in degrees. From the above relation one gets a shift of $1.8'$ for a 30 MHz source, radiating at the fundamental plasma frequency and located at $\pm 85^\circ$ longitude. As we know, the angular deviation of a ray varies as f^{-2} for both refraction and scattering and both effects vanish at high frequencies. Consequently, in order to compute the shift of the sources at frequencies other than 30 MHz we used the expression

$$(\Delta\varrho)_f \text{ MHz} = \frac{900}{f^2 (\text{MHz})} \times (\Delta\varrho)_{30 \text{ MHz}}. \quad (4)$$

This correction was incorporated in the χ^2 relation in the form

$$\varrho_{Ti} = \varrho_i - \Delta\varrho_i, \quad (5)$$

where the ϱ_{Ti} are the true east-west positions of the source, the ϱ_i have been defined earlier and the $\Delta\varrho$ are the corrections given by Equations (4) and (5).

Redefining χ^2 as

$$\chi^2 = \sum_i [\varrho(t_i) - \varrho_{Ti}]^2 \quad (6)$$

we recomputed the height for the decametric sources. The results so obtained are shown in Table II. It is clear that the scattering correction influences only slightly the heights obtained before. This is due to the fact that only the positions obtained up to four days before or after the CMP were used in the original calculations. At these longitudes ($L \leq \pm 56^\circ$) the combined effect of scattering and refraction on the source position is small. We have adopted the corrected heights as the true heights for the sources. Subsequent discussions will be based on these heights.

3. Electron Densities in Storm Regions

Both synchrotron and plasma radiation has been invoked to account for continuum storms (Denisse, 1960; Takakura, 1960). In the case of synchrotron radiation we expect a broad spectrum of frequencies to be radiated at the same height in the corona. For plasma radiation on the other hand, the radiated frequency is close to the plasma frequency $f \simeq f_p$. Thus a narrow range of frequencies is emitted at each height, in the vicinity of the local plasma frequency. This should be manifest as a dispersion in position with frequency of the storm radiation, as is indeed found to be true in every storm we have studied (Table II). Since the electron density decreases with increasing height, the lower frequencies originate in each case at higher levels in the corona, in

agreement with the plasma hypothesis. Objections to the plasma hypothesis have been made (Wild *et al.*, 1963), since storm sources are found to be located above the average plasma level for a given frequency. This behaviour is commonly found only close to the limbs, probably due to scattering of the radiation in the corona (Riddle, 1972b). Further, each storm appears to have its own characteristic dispersion of height with frequency. Thus comparison of the height of individual sources with an average plasma level may not be meaningful.

It appears that the synchrotron hypothesis could explain the observed frequency dispersion with position if we include the 'Razin-Tsyrovitch' effect. Current density

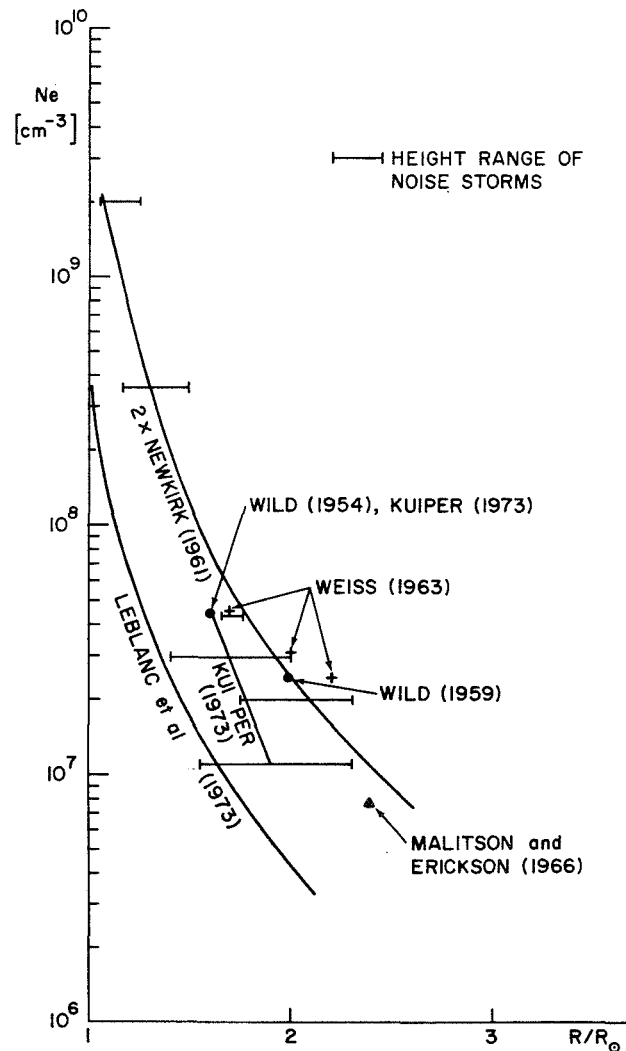


Fig. 4. Electron density of the corona according to various models. The range of heights where the decametric storms were observed is indicated by bars.

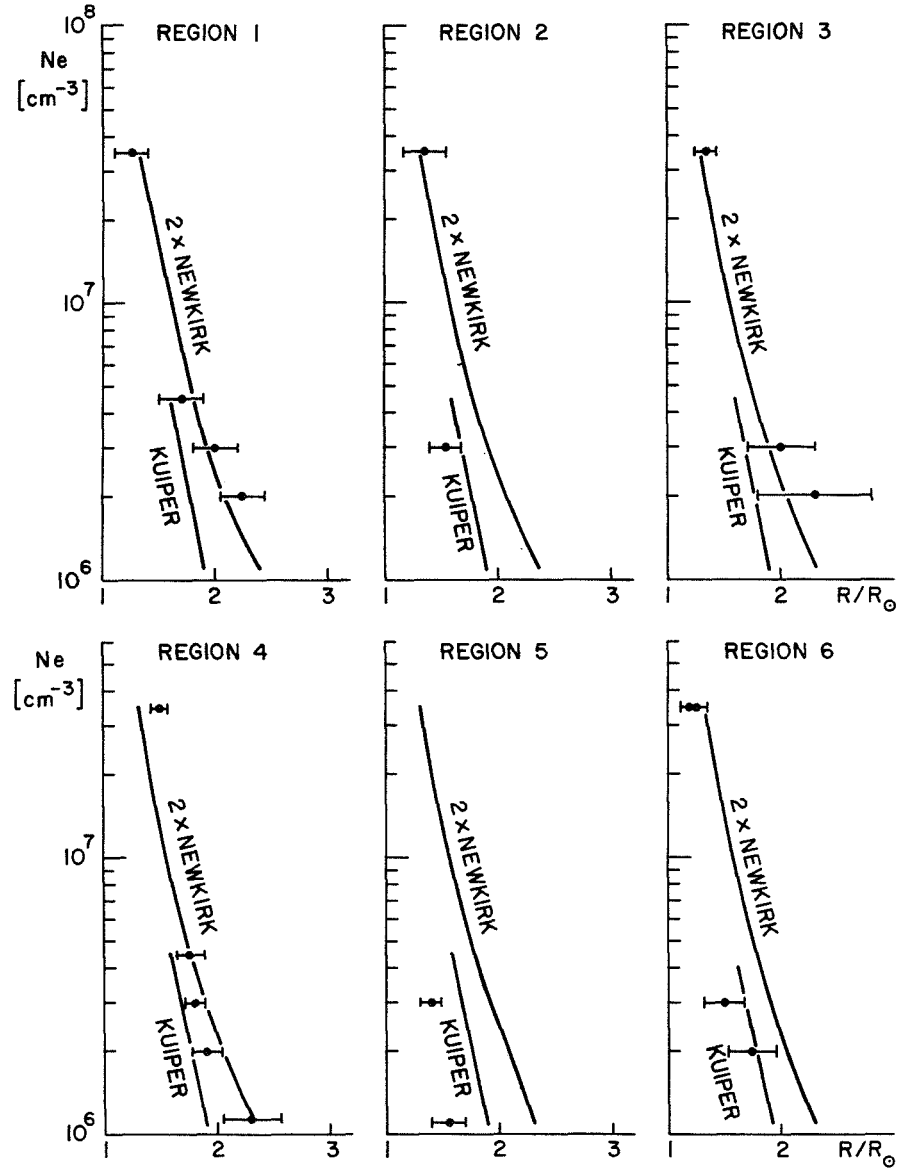


Fig. 5. Electron density distributions in individual storm regions. The distribution obtained by Kuiper (1973) in the 65–20 MHz range, and the $2 \times$ Newkirk streamer model are also indicated.

models for the corona (Figure 4) would, however, require magnetic fields of the order of 2–15 gauss to exist at a height of $2.0 R_{\odot}$, to explain the emission of 40 MHz radiation at the same height (Table II). As this field strength seems rather high, we prefer to explain the origin of the storms by the plasma radiation hypothesis. Other observational evidence exists in favor of the plasma hypothesis. We mentioned earlier that a large number of type III bursts appear ‘on-fringe’ during noise storms, indicating

that the III's coincide in position with the continuum over the observed frequency range of 65–20 MHz. Since the plasma hypothesis has been advanced to explain the observed frequency dispersion of position for the type III's, the same explanation should be valid for the continuum. As it appears that the storms are due to plasma radiation, it follows that the frequency of emission of storm continuum radiation is related to the electron density in the corona.

We now discuss the density structure of coronal regions where the decametric storm radiation originates. Densities in the various coronal structures above active regions have been determined by optical and radio measurements. A summary of the methods used, and the results obtained has been given by Newkirk (1967). In streamers above active regions, density enhancements up to two times over the background corona have been found by optical methods (Newkirk, 1967). On the other hand, the radio observations (Wild *et al.*, 1959; Weiss, 1963; Malitson and Erickson, 1966) suggest densities which are two to three times enhanced above the values obtained by optical methods. Kuiper (1973) analyzed the position of 190 isolated type III bursts and found their mean height to be $1.6 \pm 0.13 R_{\odot}$ at 60 MHz. His analysis showed a faster decrease of electron density with height, compared to that observed by others.

Figure 4 shows the density variation of the corona according to several models that have been proposed. Also included in the figure are the measurements of Wild *et al.* (1959), Weiss (1963), Malitson and Erickson (1966), and Kuiper (1973). The dashed line shows the density variation found by Kuiper in the range 65–20 MHz. Bars in the diagram identify the region which corresponds to our decametric observations, and to the Nançay observations at 169 MHz, assuming that the radiation occurs at the fundamental plasma frequency. The wide spread of the observations is apparent and indicates that noise storms can be generated under fairly wide variety of conditions.

The variation of density with height for each of the individual storm regions is shown in Figure 5. Again, we assume that radiation at the fundamental frequency was observed. The error bars in the figure correspond to the $\chi^2 = 1.5\chi_{\min}^2$ level in the computation of the height of the sources. For comparison, we also show the densities corresponding to a two times Newkirk streamer model and the slope derived by Kuiper (1973). It is obvious that both moderately low and high density regions are involved. Regions 2, 5 and 6 belong to the first category and regions 1, 3 and 4 to the second. We have shown in Paper I that the storms are associated with magnetic arcades and loops. It seems likely that the difference in the density gradients between the regions studied arise due to the different heights at which the magnetic loops close in the corona. Below the closed magnetic field lines, the plasma is contained, and the densities are high (Pneumann, 1968). Above the loops, where open configurations exist, the plasma expands, constrained only by gravitational forces and the electron density drops to lower values. This suggests that magnetic field lines which were closed at low altitudes in the corona were associated with regions 2, 5 and 6. On the other hand the closed field lines extended to greater heights above the other three regions studied. The age of the active regions associated with the storms appear to substantiate this suggestion. The most active chromospheric regions associated with

the storms 2, 5 and 6 were McMath 11128, 11425, and 11482, respectively. Of these three regions McMath 11128 and 11425 were very young active regions, undergoing their first rotation. We expect therefore that the associated magnetic field lines closed low in the corona (Newkirk, 1967). The region McMath 11128 was undergoing its second rotation. The most flare active regions associated with the other three storms were McMath 11256 and 11294, in course of their second rotation, and McMath 11111 in course of its first rotation at the time of the storm, but situated in the midst of two very old plages (McMath 11108 and 11112). The flare activity was generally higher in those complexes of active regions which were associated with low density coronal regions. The most active regions associated with the storms 2, 5 and 6 produced 132, 87 and 292 flares respectively over the duration of the storm. On the other hand 63, 34 and 92 subflares occurred in the most active regions associated with the decametric storms 1, 3 and 4 respectively.

4. Size of Decametric Sources

One dimensional size of the sources of storm radiation was determined by Clavelier (1967) at 408 MHz and by Malinge (1963) at 169 MHz. At 408 MHz, the diameter of the sources was found to vary between 1' and 2', approximately $0.1 R_{\odot}$. The size of the sources at 169 MHz was found to be greater, the mean diameter being about $0.25 R_{\odot}$, but sources as large as $0.6 R_{\odot}$ have been observed occasionally. No variation in size of the sources with heliographic longitude was found at 169 MHz (Malinge, 1963), implying that the height and width of the sources was approximately equal. No relation was found between the size of the source and the intensity of emission.

In the following discussion we shall assume that the brightness distribution of the decametric sources, as well as the interferometer lobe patterns are approximately gaussian. The angular size of a source is then given by the expression

$$\theta^2 = \theta_0^2 - \theta_A^2 \quad (7)$$

for sources that are larger than the beamwidth. In the above equation θ_0 is the observed width of the source and θ_A is the beamwidth. For the L.P.A., the beamwidth near the meridian is about $0.3 R_{\odot}$ at 60 MHz and $0.6 R_{\odot}$ at 30 MHz. When the intensity of the emission is high, the record becomes saturated and Equation (7) is no longer valid. While such cases are relatively common for type III bursts and type II-IV events, they are rare for continuum storms. We exclude from our analysis of source sizes the observations of one day (1971 August 24) when this happened. At 60 MHz the source size ranges from $0.3 R_{\odot}$ to $0.8 R_{\odot}$. One very large source of $1.2 R_{\odot}$ was observed. The mean diameter of 26 sources turns out to be $0.51 R_{\odot}$. At 50 MHz the source size ranges from $0.4 R_{\odot}$ to $0.9 R_{\odot}$. Again we found the source of very large diameter; at this frequency it was about $1.3 R_{\odot}$. The mean diameter of 36 sources turns out to be $0.75 R_{\odot}$. The size of the sources is even larger at lower frequencies. At 40 and 30 MHz the mean diameter of the sources was found to be 1.0 and $1.3 R_{\odot}$ respectively. The large diameter source that we observed at 60 and 50 MHz was found

to be even larger at these frequencies; its size was $2.0 R_{\odot}$ at 40 MHz and $3.0 R_{\odot}$ at 30 MHz. The variation of the mean source size and the beamwidth with frequency is represented in Figure 6. In the decameter range the dependence of mean source size on frequency can be described by the equation

$$\bar{D}_{(R_{\odot})} = 5.2 - 2.6 \log f_{(\text{MHz})}. \quad (8)$$

Figure 6 also shows the mean diameter of the sources at 408 and 169 MHz, as given by Clavelier (1967) and Malinge (1963). It is seen that the source size increases much more rapidly in the decameter than in the meter range.

We will show that the steeper increase of source size with frequency in the decameter range corresponds to a steeper increase of the source size with height above the chromosphere as well. Let us call the variation in source size ΔR and the variation in height above the chromosphere Δh , both considered over the same frequency range. Then, for the two times Newkirk streamer model (Newkirk, 1961) $\Delta R/\Delta h \simeq 0.66$ in the 408–169 MHz range, while $\Delta R/\Delta h \simeq 1.46$ in the 60–30 MHz range. If instead of a density model we make use of the direct height determinations of Malinge (1963), Clavelier (1967) and this paper, the ratio $\Delta R/\Delta h$ turns out to be 0.36 in the 408–169 MHz range. In the 50–40 MHz range (the only one for which more than two height determinations are available at each frequency), the ratio turns out to be 0.63.

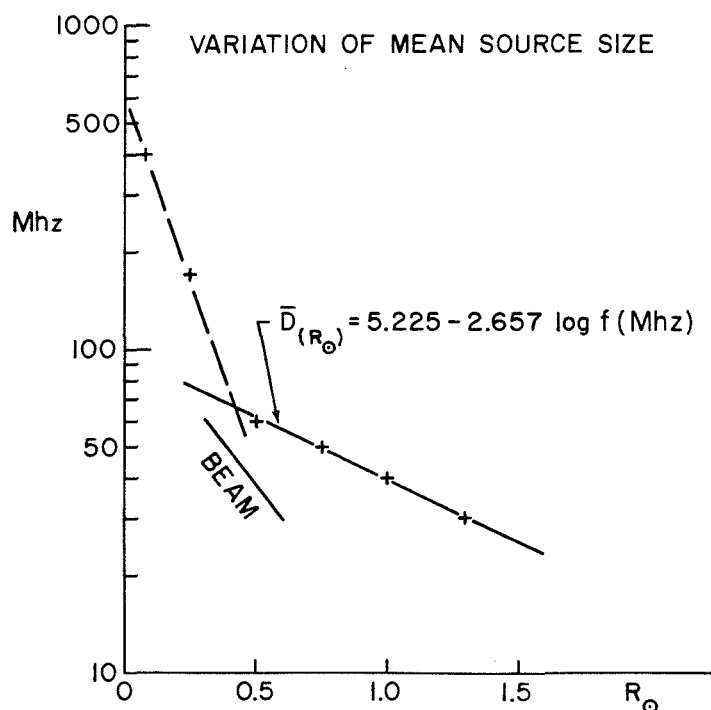


Fig. 6. Variation of mean source size as a function of frequency in the decimeter-meter and decameter ranges. The size of the beam in the 65–20 MHz range is also indicated.

In either case the rate of increase of source size approximately doubles in the decameter range, compared with the meter-decimeter ranges.

To investigate the variation of source size with disk longitude, we divided the sources in three groups. The first group included all sources within ± 1 day of CMP. The second group included the sources located between 1 and 4 days away from the central meridian, and the third one the sources situated more than 4 days away from the central meridian. The result of this investigation is shown in Table III. For the group closest to the central meridian we have also indicated in parenthesis, the average obtained when the large source previously mentioned (1971 July 19) is omitted. In agreement with the results of Malinge (1963), no systematic center-to-limb effect was observed, although a slight increase from center to limb was noticed at 50 and 40 MHz. No correlation between source size and height above the photosphere was observed at 50 MHz. A visual inspection of the records reveals no correlation between source size and intensity. Steinberg *et al.* (1971) computed the size of the scattered image due to a point source radiating at 169 MHz and located at $1.2 R_{\odot}$. They used Hansen's electron density distribution for the background corona (Hansen *et al.*, 1969) and isotropic inhomogeneities. For large electron density fluctuations $\delta \approx 4\%$, they obtained a considerable increase in source size with heliographic longitude. For a smaller fluctuation in electron density, a smaller increase in source size was found. Kerdraon (1973) observed only a small increase in the size of type I sources with longitude at 169 MHz. Our observations tend to confirm his results. Two possible interpretations are consistent with the observations:

- The extension in height of the decametric sources is smaller than their width. In this case, scattering by large electron density fluctuations compensates for the decrease in source size at the limbs.
- The width and the extension in height of the decametric sources are approximately

TABLE III
The average size of decametric sources at various longitudes
(sizes in R_{\odot})

| $f(\text{MHz}) \backslash$ Time: Longitudes: | $T = T_{\text{CMP}} \pm 1\text{d}$ $0 \leq L \leq 20^\circ$ | $T_{\text{CMP}} \pm 1 < T < T_{\text{CMP}} \pm 4\text{d}$ $20^\circ < L \leq 55^\circ$ | $T > T_{\text{CMP}} \pm 4\text{d}$ $L > 55^\circ$ |
|--|--|---|--|
| 60 | 0.57 (0.5) | 0.5 | 0.5 |
| 50 | 0.66 (0.54) | 0.65 | 0.8 |
| 40 | 1.19 (1.12) | 0.92 | 1.3 |
| 30 | 1.56 (1.2) | 1.22 | 1.2 |

equal. Then the electron density fluctuation in coronal inhomogeneities is small, possibly of the order of 1% or less.

Finally, we should mention here that the size of the decametric sources is by no means constant, but it changes considerably even over short periods of time. These variations in source size are uncorrelated over frequencies separated by as little as 10 MHz, and are likely to be due to the fine structure observed at these wavelengths.

5. Lifetime and Directivity of Decameter Storms

The number of storm regions studied by us was relatively small; further, no flux measurements were available. Therefore we shall discuss here only briefly the directivity and lifetime of storms. Figure 7 shows an histogram of the number of sources observed as a function of their longitude from the central meridian. Since the first interval on this histogram covers a period of three days ($\text{CMP date} \pm 1 \text{ day}$) and all other intervals cover only two days, we have indicated in the first interval the number of sources corresponding to two days by the dashed line. The histogram indicates a smooth variation

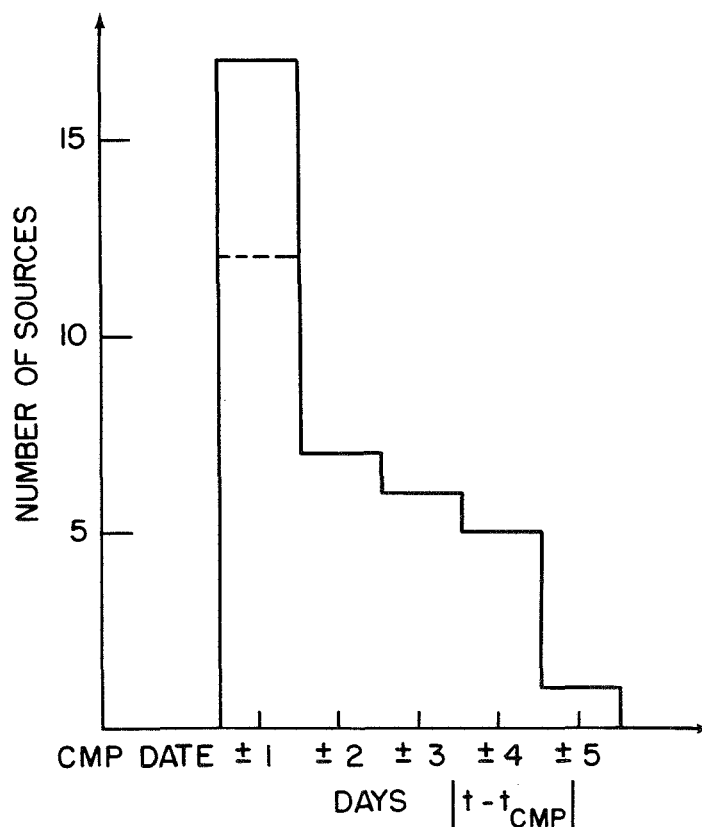


Fig. 7. Number of decametric sources observed as a function of days from the central meridian passage.

of the number of sources observed with heliographic longitude. It also indicates an observed cut-off of the sources at approximately ± 5 days from the central meridian, corresponding to about 70° in longitude. Intense moving type IV events were observed several times at higher longitudes during the period considered here. Some of these type IV sources were associated with the storm regions considered here; however no storm radiation was recorded immediately before the type IV burst. A stationary continuum after the moving burst was observed for a short time in some cases. When storm continuum was observed close to the limbs it was generally weaker than when it was observed near the disk center.

No variation with frequency of the directivity of continuum storms was observed within the available frequency range. Four of the six storms studied were seen for seven days. One of the other two regions was observed for six days and the remaining one for five days. At least in one case (region 2) the storm ceased altogether for one day but did reappear before the observing was resumed the next day.

Finally we might remark that the east-west asymmetry found by Malinge (1963) at 169 MHz seems to persist at decameter wavelengths also. Out of a total of 37 sources observed at 60 MHz, 20 were situated on the western hemisphere and only 11 on the eastern hemisphere, the other six being observed at the CMP. Further, no source was observed for more than three days before CMP, whereas several sources were observed for four and even five days after they passed the central meridian.

6. Type III Bursts Related to Decametric Storms

We have discussed so far the properties of storm continuum sources observed at decameter wavelengths. It is well known that many type III bursts are observed at these wavelengths during the storms. The type III's occur both 'on-' and 'off-fringe'; in other words they are coincident with or displaced in position from the continuum sources. Displacements of type I burst positions from the continuum source at 408 and 169 MHz have been observed by Daigne *et al.* (1971). Further, Kai (1970) observed differences in the positions of type I and type III sources at 80 MHz which occurred in the course of storms. From the difference in the position and polarization of the two classes of bursts he concluded that the type III bursts originated in regions of weak or zero magnetic fields, while the type I bursts originated close to regions of strong magnetic fields. We describe now some properties of the type III bursts in storms as they appear on the Clark Lake records. In particular we shall discuss their association with flares and the distribution of their starting frequencies.

Because of the large number of type III bursts occurring in noise storms it is difficult to decide when a given burst is or is not flare associated. The criterion used in this work was the following: (1) If a type III burst or group of bursts starts during the flash-phase of a flare, and (2) if the intensity of the burst is noticeably higher than the intensity of the preceding bursts, we considered the burst to be flare associated. In practice flare-associated bursts are easy to recognize because their intensity is always much higher than that of the run-of-the-mill type III bursts in storms. The reverse is not true however;

occasionally an exceptionally intense type III burst could not be associated with any flare reported in the *Solar-Geophysical Data*. Figure 8 presents an example of a flare associated type III group, which occurred on 1971 August 21. The contrast in intensity between the flare associated group and other type III bursts is obvious. Without exception the flare associated type III bursts started above 65 MHz, our highest observing frequency. Most of the bursts was observed over the entire range of 65–20 MHz. Some bursts, however, disappeared before reaching the low frequency limit of 20 MHz. The first burst of the 1971 August 21 group is an example of a burst with such a low-frequency cut-off.

Flare associated type III bursts have only been observed by us during the 1971 July and August storms (regions 5 and 6). The burst associated with region 5 was observed on 1971 July 19. A minor flare (imp. – F) occurred in McMath region 11425 at 21:05 UT. Very weak continuum emission was recorded preceding the flare. Simultaneously with the flare, an intense type III group started and was followed by a type V. The duration

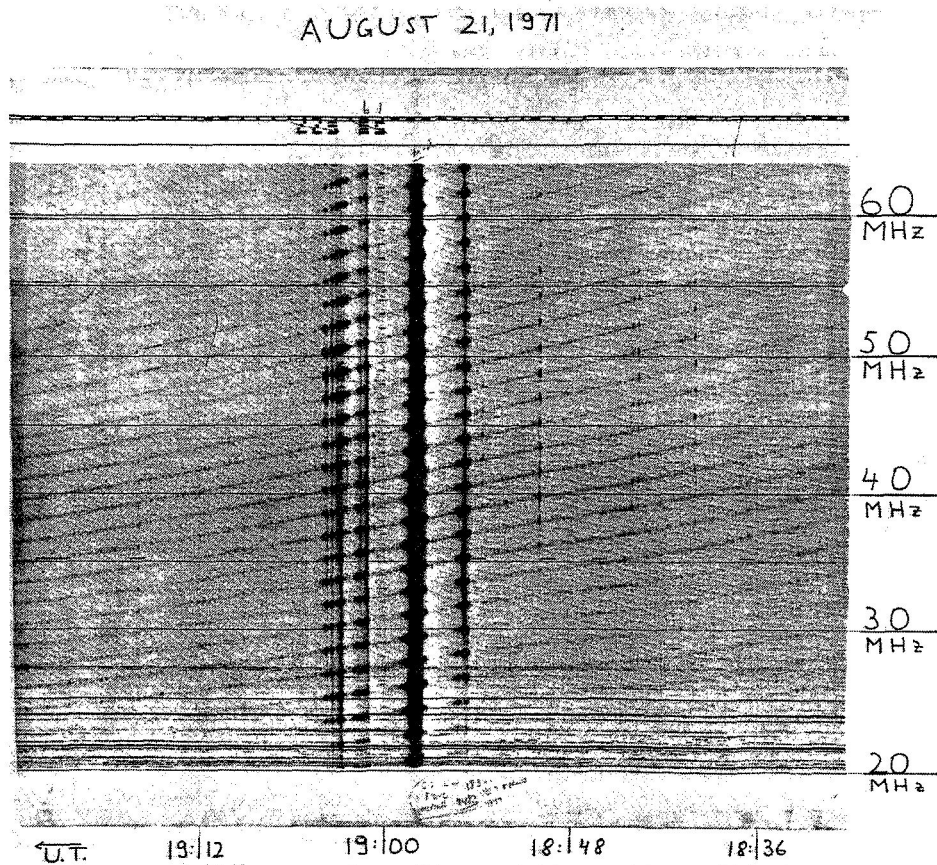


Fig. 8. A flare associated 'off-fringe' type III group observed on 1971 August 21. Note the low-frequency cut-off in the first burst of the group.

of the type III group was approximately 7 minutes. Enhanced continuum emission was observed thereafter, until the end of the observing period. Occasional type III bursts were seen later that day but no other flare was reported. The type III group was 'off-fringe', it was located about $0.3 R_{\odot}$ west of the subsequent continuum source at all frequencies.

Numerous flare associated type III groups were observed during decametric storm region 6. All of these bursts were associated with flare activity in McMath region 11482 (Lazareff and Zirin, 1973). Most of the bursts were very intense and saturated the records (Figure 8), rendering precise positional measurement difficult. On August 20, the first intense type III groups occurred $0.4 R_{\odot}$ to the east of the continuum source, at 60 as well as at 40 MHz. This separation of the continuum and type III sources remained constant through August 21 and 22; no flare associated III was observed after this date.

Many other 'off-fringe' type III's were observed during these two storms as well as during other storms. No flare association could be found for these bursts on the basis of the flare list published in *Solar-Geophysical Data*. On the other hand, no flare associated 'on-fringe' type III burst was ever observed. In order to investigate further this point we studied the rate of occurrence of 'on-' and 'off-fringe' type III bursts relative to the occurrence of flares. We counted the number of type III's which occurred in 12 minute intervals during the storm of 1971 May 8. Three subflares occurred during the observing period on this day. No significant increase in the number of either 'on-' or 'off-fringe' type III's was observed during the flash phase of these subflares. A small increase in the number of bursts is suggested by the data, with a 12–24 minute delay after the flash-phase of the flares. Some other features of the statistics deserve further comment:

- The rate of occurrence of 'off-fringe' type III's is much lower than the rate of occurrence of 'on-fringe' type III's.
- A much higher number of bursts is found at lower frequencies (25–35 MHz) than at higher frequencies (55–65 MHz). These are characteristic features of all the storms observed. Finally, the rate of occurrence of bursts, about one burst per six minutes at 60 MHz and one burst per minute at 30 MHz may be considered typical during decametric storms.

Malville (1962) found that during noise storms the starting frequency of most type III bursts coincided with the upper frequency of the storm activity. The distribution of the starting frequencies of type III bursts associated with storms of specified upper frequency range was found to be bimodal. We investigated the distribution of starting frequencies of both 'on-' and 'off-fringe' type III bursts separately. The results for two storms considered here are shown in Figure 9. Relatively few type III's have been observed during decametric storm region 5. The starting frequencies of all bursts occurring when continuum radiation was present is shown in Figure 9a. The average starting frequency of the 'off-fringe' type III bursts was above 55 MHz. On the other hand, the average starting frequency of the 'on-fringe' type III's was only about 43 MHz. A similar result was found for the other storm. In Figure 9b, is shown the

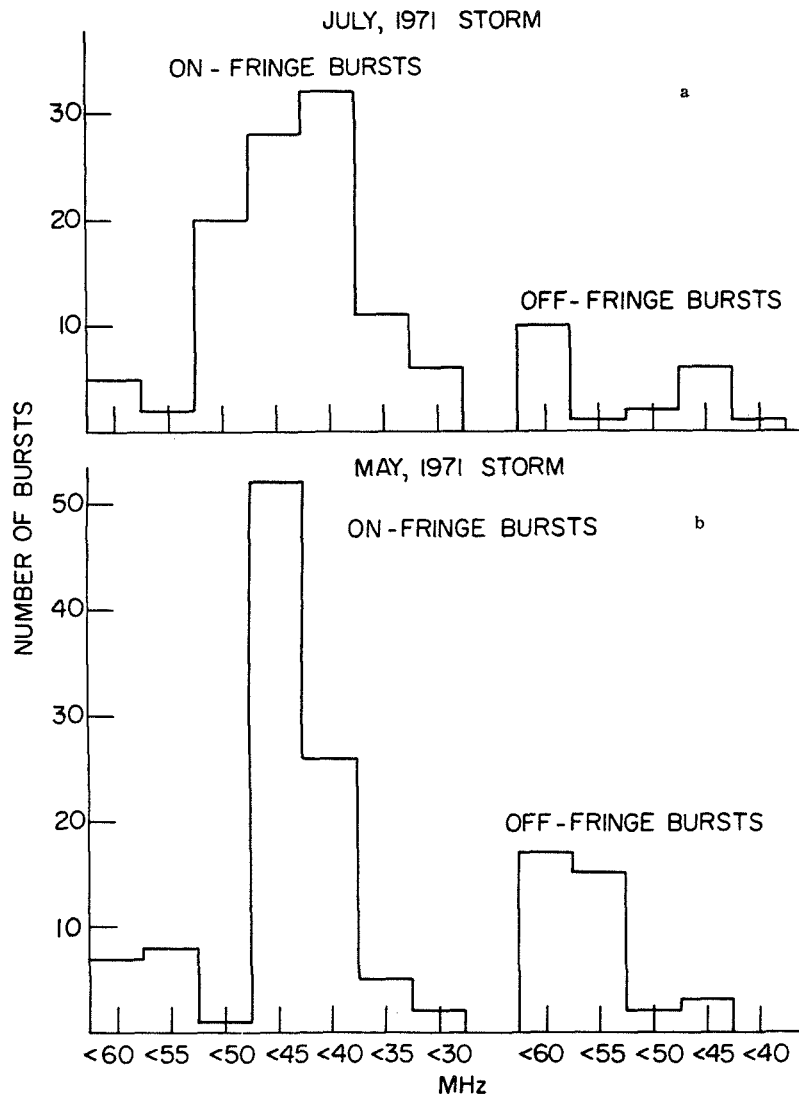


Fig. 9. Distribution of starting frequencies of 'on' and 'off-fringe' type III bursts, (a) in course of the July 1971 storm and (b) on one day (May 7), during the 1971 May storm. Type III bursts were much more frequent during the May storm than during the July one.

histogram of the starting frequencies of all 'off-fringe' type III's observed on 1971 May 7, and of the 'on-fringe' type III's observed on this day during a three hour period. The average starting frequency of the 'off-fringe' bursts is clearly higher than that of the 'on-fringe' bursts. As in the case of Malville's (1962) results, the histograms given in this section should be viewed with caution. The sensitivity of the instrument is certainly not uniform over the whole frequency range. The L.P.A. is most sensitive in

the mid-frequencies, approximately 45–35 MHz. It seems to us, however, that the variation in the sensitivity of the instrument alone could not account for the systematic differences found between the starting frequencies of the ‘on-’ and ‘off-fringe’ bursts.

The data presented here suggests that the type III bursts observed in the course of decametric storms originate in two different sources. The ‘off-fringe’ type III bursts which are displaced in position from the continuum source often appear associated with flare activity. The higher starting frequencies of these bursts seem to indicate that they originate lower in the corona than the ‘on-fringe’ type III’s which start, on the average, at lower frequencies. Further, the flare-associated ‘off-fringe’ bursts are more intense and of broader bandwidth than the ‘on-fringe’ ones. It is conceivable that the bimodal distributions of type III starting frequencies found by Malville (1962) were due to the two groups of type III’s occurring in different positions. Clearly, further studies of simultaneous position and flux density measurements are desirable to eliminate the possibility of these effects being due to sensitivity variations of the instrument in different spectral regions. Until such data become available the results presented here must be considered as tentative.

In most cases the ‘off-fringe’ type III bursts appeared to be displaced toward regions of open or diverging field lines on the magnetic maps (see Paper I). For example, in the case of storm region 4 all ‘off-fringe’ type III’s occurred west of the continuum source where the field lines appeared divergent (Figure 3d of Paper I). The very intense ‘off-fringe’ III’s observed during the decametric storm 6 were displaced to the east of the continuum source. Diverging field configuration can be seen to the east of the magnetic arcade above which the continuum source was situated (Figure 3f of Paper I). Thus it seems likely that the ‘off-fringe’ type III bursts are excited by electron streams travelling along open field lines. They appear to be similar in this respect to the isolated type III bursts studied by Kuiper (1973).

A number of other parameters related to type III bursts occurring in storms are of interest. The accurate measurement of the size and duration of type III’s in storms requires the measurement of relative intensities, since both ‘on-’ and ‘off-fringe’ bursts overlap to a certain extent with the background continuum. Such measurements of intensity, simultaneously with position determinations over a wide range of frequencies (e.g. 20–120 MHz) will certainly provide a better understanding of storm-related type III’s.

7. Model of the Storm Region

We have discussed various aspects of noise storm phenomena as observed at decameter wavelengths. We described the properties of the continuum source and the associated ‘on-’ and ‘off-fringe’ type III burst sources. We now present a consistent physical picture of the decametric storm phenomenon in all its different aspects and its relation to radio emission at other wavelengths.

During the storms, which are stationary and long lasting (up to several days) there are usually present on the solar disk several active regions. Some of these active regions, which appear to form complexes at the chromospheric level, present a high level of

flare activity. In Paper I we have shown that the active regions which constitute a given complex interact with each other. We studied this interaction by the number of subflares that occurred in a given region and that followed a subflare in another region of the complex in less than 20 minutes. Typically twice as many subflares occurred in this interval of time than expected on the basis of random occurrences. Similar results could be obtained by varying the interval of time within reasonable limits (i.e. by choosing it anywhere between 2–3 minutes and half an hour). Interconnections between widely separated active regions were suggested previously from observations of a different nature (Wild, 1969; Kai, 1969). Kai and Sheridan (1973), derived coronal magnetic field configurations from the simultaneous 80 and 160 MHz observations of two noise storms. From the position and polarization of type I and type III sources they concluded that magnetic flux tubes, looping in the corona, constituted the link between several active regions that were visible on the disk. Even more spectacular evidence for magnetic interconnections between active regions has been revealed by soft X-ray pictures obtained on rocket flights (Krieger *et al.*, 1970). When compared with longitudinal photospheric fields these interconnections are manifest by the linkings of opposite magnetic polarities in widely separated active regions. The beautiful X-ray pictures obtained in the course of the Skylab experiment also show complex interconnections between several active regions (Vaiana *et al.*, 1973). Vaiana *et al.* (1973) concluded that the majority of the coronal features observed presented closed loop configurations. The association of decameter storms with both high and low magnetic arcades also points to a magnetic origin of the interconnections between active regions.

No bursts in the cm or dcm wavelength range appear to be associated with noise storms. However, the CMP of decameter storm regions coincided, within a day or two, with the CMP of intense cm wavelength sources. Consequently, the decameter sources observed must overlie the slowly varying regions. When a noise storm is in progress there are usually two or more decimetric sources present, each associated with a distinct chromospheric active region. At lower frequencies (below 400 MHz) type I bursts begin to appear superimposed on the continuum.

At even lower frequencies (below 100 MHz) the rate of occurrence of type I bursts diminishes. Instead a large number of type III bursts appear. Previous studies of noise storms show that this spectral pattern is frequently observed (Malville, 1962; Hanasz, 1966; Stewart and Labrum, 1972). Further, in some cases observed by Hanasz (1966) the type III bursts appeared to 'grow' out of chains of type I bursts. At decameter wavelengths the continuum itself appears to be very bursty due to the fine structure (de la Noë *et al.*, 1973) and it is often difficult to separate the continuum from the bursts.

All decameter bursts studied by us showed dispersion in the height of emission with frequency, the higher frequencies originating at lower heights. This observation is consistent with the suggestion made by Denisse (1960), that the storms are due to Cerenkov-plasma radiation. Accordingly, from a knowledge of the height and frequency of emission, and assuming either the fundamental plasma frequency or its

harmonic, the variation of the electron density with height can be determined in the storm region. In this paper we have assumed that radiation occurs at the fundamental plasma frequency. It must be emphasized that we made use only of data related to decametric sources which were close to the center of the disk (heliographic longitude $|L| \leq 56^\circ$). Since meter and decameter sources frequently appear higher near the limb, than at the disk center, by limiting ourselves to disk sources we have computed a lower limit to the height of the sources.

The mean linear size of the decameter source is found to be large; it increases with decreasing frequency, and consequently with height above the photosphere. This increase in the size of the source appears to be much more pronounced in the decameter range than in the meter and decimeter ranges. No increase in the source size was found with heliographic longitude of the source. This result is similar to that observed at meter wavelengths; it seems to indicate that the width and the extension in altitude of the emissive regions are approximately equal at decameter wavelengths too. The storm continuum was found to be strongly directive towards the disk center. No storm was observed more than five days away from the disk center, and the source appears to be weaker toward the limbs. No variation of the directivity with frequency was found over the frequency range 65–20 MHz. The east-west asymmetry, found by Malinge

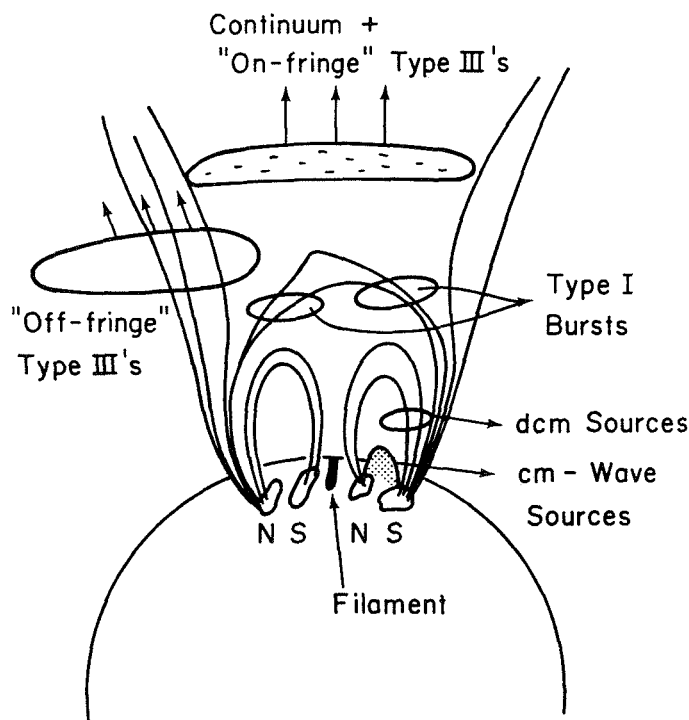


Fig. 10. A proposed model of the storm region, indicating the positions of 'on-' and 'off-fringe' type III bursts.

(1963) at meter wavelengths have been observed at decameter wavelengths also. The lifetime of a source was usually less than a solar rotation.

Two different classes of type III bursts occur during decametric storms: (a) the 'on-fringe' type III bursts which coincide in position with the continuum; (b) the 'off-fringe' type III bursts, which are displaced from the continuum by $0.1\text{--}0.5 R_{\odot}$. These bursts can also be termed 'in-continuum' and 'off-continuum' type III's. The starting frequency of the 'on-fringe' type III bursts was generally below 50 MHz. On the other hand, the 'off-fringe' type III bursts usually start above 65 MHz, our highest frequency. The 'off-fringe' type III's are generally more intense than the 'on-fringe' ones, and at least in some cases the 'off-fringe' type III's were clearly flare-associated. No flare-associated 'on-fringe' bursts were ever found. Most 'off-fringe' type III bursts covered the whole frequency range 65–20 MHz. On the other hand, the 'on-fringe' type III bursts frequently have a narrow frequency range of 20–30 MHz and merge into the background.

We now present an empirical model of a typical storm region. The proposed model is shown in schematic form in Figure 10. As discussed in Paper I, the storms are located above active regions, which usually contain some spots; some of these spots have strong magnetic fields. Magnetic loops join regions of opposite polarity within a spot group; distant spot groups are also magnetically connected by loops or arcades. Numerous minor flares are produced during the lifetime of a storm. In the course of a typical storm subflares occur on the average at the rate of one every one or two hours in one of the associated active regions. The energetic electrons that are released or accelerated during a flare are injected at the base of the loops. A fraction of these electrons become trapped, and mirror between the footpoints in the closed magnetic configurations. The mirroring time of subrelativistic electrons in a dipole configuration is given by

$$T = 2 \sqrt{\frac{2m}{K}} r_0 F(\lambda_m), \quad (9)$$

where m is the electron mass, K is the kinetic energy, r_0 is the distance from the base to the top of the loops, and $F(\lambda_m)$ is a function of the order of unity (Rossi, 1970). For a loop extending $1.0 R_{\odot}$ above the photosphere the mirroring time for 50 keV electrons is about 20 seconds. Thus, it is possible for electrons and other particles following magnetic field lines to impinge upon far-away regions into the chromosphere and trigger 'simultaneous' flares and associated bursts. The trapped particles diffuse somehow slowly through the magnetic field lines and excite plasma waves in the manner proposed by Denisse (1960), giving rise to the storm continuum radiation. Indeed, the source of continuum radiation is usually situated above filaments lying in regions of weak or zero magnetic fields; the filaments indicate the presence of neutral sheets higher in the corona along which electrons can travel. In order to explain the brightness temperatures of 10^{11} K observed at meter wavelengths, by means of fundamental plasma waves which are converted into electromagnetic waves by Rayleigh scattering one requires $N_s/N \simeq 10^{-2}$, where N_s is the density of electrons in

the stream and N is the ambient electron density (Wild *et al.*, 1963). Now, if we assume a linear size of $0.75 R_{\odot}$ for the source at 50 MHz, electrons of 50 keV and a ratio $N_s/N \simeq 10^{-2}$ we find that an electron flux of about 9×10^{26} electrons per second is involved. Approximately 2×10^{33} subrelativistic particles are involved in a medium sized flare; the number involved in small flares may be one or two orders of magnitude less (de Jager, 1970). Thus the electrons injected during a flare can easily account for the electron fluxes required over a period of several hours.

We now consider the possible locations where the 'off-' and 'on-fringe' type III's can be generated. We believe that the 'off-fringe' type III's are excited by electrons having direct access to open field lines (Figure 10). Several observations support this assumption. First, the bursts are displaced in position from the continuum. Secondly, the higher starting frequency and larger bandwidth of the bursts indicate that the generating electron streams start deep in the corona and travel unimpeded along their path. Thirdly, when one compares the position of 'off-fringe' III's with that of the coronal magnetic structures (Newkirk and Altschuler, 1970), the bursts are usually found to be situated near open or diverging field lines. Finally, these bursts are more closely associated with flares than the non-flare associated 'on-fringe' III's. The latter have lower starting frequencies; so they must be produced higher up in the corona. In this context it is useful to consider the generating mechanism of type III bursts proposed by Gordon (1971). This mechanism is based on the observation that type III bursts frequently appear to grow out of chains of type I bursts, and that most type III's start close to the low frequency limit of type I activity. The suprathermal electrons responsible for type I bursts excite turbulent plasma waves. By a non-linear mechanism the plasma waves then scatter the electrons to accelerate them to velocities of the order of $0.1-0.6c$, which become the exciters of type III bursts. An objection to this mechanism has been raised by Stewart and Labrum (1972), in that the transformation time needed to excite the III's is too low ($10^{-2}-10^{-3}$ s in the 10-100 MHz range) to explain the difference in position of the type I and type III sources observed at 80 MHz. At decameter wavelengths, however, most type III's are of the 'on-fringe' variety and an inspection of the interferometer records shows that most of the type I bursts also coincide in position with the continuum. As stated in Paper I, the type I bursts are not easy to identify on the basis of interferometer records alone. A detailed comparison of the positions of type I and type III bursts in course of some decametric storms, making use of both interferometric and spectral information is now under way (de la Noë and Gergely, in preparation).

The displaced type III bursts observed at 80 MHz are probably the 'off-fringe' type III's referred to in this paper. According to Boischoy *et al.* (1971) the type I-type III transition region corresponds to the transition from closed to open field lines in the corona. This suggestion appears to be supported by the large angular size of the sources, which increases rapidly with decreasing frequency and, therefore, with increasing heights.

Clearly, our tentative model leaves at least one feature of decameter storms unexplained, namely, the repeated injection of electrons by subflares does not reflect in the

impulsive nature of radio emission. Since the relaxation time for the nonthermal electron beams is short, one needs an additional mechanism to *smooth* the supply of nonthermal electrons. At the present time it is not understood which 'smoothing' mechanism is responsible for this effect.

Acknowledgements

Support for this work was provided under NASA grants NGL 21-002-033, NGR 21-002-367 and NSF grant GP-19401. We thank W. C. Erickson, E. v. P. Smith, R. G. Stone, and J. de la Noë, and T. B. H. Kuiper for some useful discussions. We also thank Dr Kuiper for the use of his excellent computer reduction programs. The work of M. Reardon, J. Pressman and N. Roth who reduced the facsimile records is gratefully acknowledged. The computer time for this project was supported by NASA grant NsG-398 to the Computer Science Center of the University of Maryland. We are grateful to the referee for some very useful comments which resulted in an improvement of the paper.

Portions of this paper are based on the thesis research of one of the authors (T.E.G.) in partial fulfillment of the requirements for the Degree of Doctor of Philosophy at the University of Maryland.

References

- Boischot, A., de la Noë, J., du Chaffaut, M., and Rosolen, C.: 1971, *Compt. Rend. Acad. Sci. Paris* **272**, 166.
- Clavelier, B.: 1967, *Ann. Astrophys.* **30**, 895.
- Daigne, G., Lantos-Jarry, M. F., and Pick, M.: 1970, in R. Howard (ed.), 'Solar Magnetic Fields', *IAU Symp.* **43**, 609.
- De Jager, C.: 1970, in E. R. Dyer (ed.), *Solar Terrestrial Physics/1970*, D. Reidel Publishing Co., Dordrecht, Part I, p. 1.
- de la Noë, J., Boischot, A., and Aubier, M.: 1973, in R. Ramaty and R. G. Stone (eds.), *High Energy Phenomena on the Sun*, NASA-GSFC, Greenbelt, Maryland, p. 602.
- Denisse, J. F.: 1960, *Inf. Bull. Europ. Solar Radio Obs.*, No. 4.
- Fokker, A. D.: 1965, *Bull. Astron. Inst. Neth.* **11**, 118.
- Gergely, T. E.: 1974, Ph. D. Thesis, University of Maryland.
- Gergely, T. E. and Erickson, W. C.: 1974, submitted to *Solar Phys.*
- Gordon, I. M.: 1971, *Astrophys. Letters* **5**, 251.
- Hanasz, J.: 1966, *Australian J. Phys.* **19**, 635.
- Hansen, R. T., Garcia, C. J., Hansen, S. F., and Loomis, H. G.: 1969, *Solar Phys.* **7**, 417.
- Kai, K.: 1969, *Proc. Astron. Soc. Australia* **1**, 186.
- Kai, K.: 1970, *Solar Phys.* **11**, 456.
- Kai, K. and Sheridan, K. V.: 1973, in G. Newkirk (ed.), 'Coronal Disturbances', *IAU Symp.* **57**, 97.
- Kerdraon, A.: 1973, *Astron. Astrophys.* **27**, 361.
- Krieger, A. S., Vaiana, G. S., and van Speybroeck, L. P.: 1970, in R. Howard (ed.), 'Solar Magnetic Fields', *IAU Symp.* **43**, 397.
- Kuiper, T. B. H.: 1973, Ph. D. Thesis, University of Maryland.
- Kundu, M. R.: 1965, *Solar Radio Astronomy*, Wiley-Interscience, New York.
- Lazareff, B. and Zirin, H.: 1973, BBSO preprint, No. 130.
- Leblanc, Y.: 1973, *Astrophys. Letters* **14**, 41.
- Malinge, A. M.: 1963, *Ann. Astrophys.* **26**, 97.
- Malitson, M. H. and Erickson, W. C.: 1966, *Astrophys. J.* **144**, 337.
- Malville, J. M.: 1962, *Astrophys. J.* **136**, 266.

- Newkirk, G., Jr.: 1961, *Astrophys. J.* **133**, 983.
Newkirk, G., Jr.: 1967, *Ann. Rev. Astron. Astrophys.* **5**, 213.
Newkirk, G., Jr. and Altschuler, M. D.: 1970, *Solar Phys.* **13**, 131.
Pneumann, G. W.: 1968, *Solar Phys.* **3**, 578.
Riddle, A. C.: 1972a, *Proc. Astron. Soc. Australia* **2**, 98.
Riddle, A. C.: 1972b, *Proc. Astron. Soc. Australia* **2**, 148.
Rossi, B. and Olbert, S.: 1970, *Introduction to the Physics of Space*, McGraw-Hill, New York.
Stewart, R. T. and Labrum, N.: 1972, *Solar Phys.* **27**, 192.
Steinberg, J. L., Aubier-Giraud, M., Leblanc, Y., and Boischot, A.: 1971, *Astron. Astrophys.* **10**, 362.
Takakura, T.: 1960, *Publ. Astron. Soc. Japan* **12**, 352.
Vaiana, G. S., Davis, J. M., Giacconi, R., Krieger, A. S., Silk, J. K., Timothy, A. F., and Zombeck, M.: 1973, *Astrophys. J.* **185**, L47.
Weiss, A. A.: 1963, *Australian J. Phys.* **16**, 240.
Wild, J. P.: 1969, *Proc. Astron. Soc. Australia* **1**, 181.
Wild, J. P., Sheridan, K. V., and Neylan, A. A.: 1959, *Australian J. Phys.* **12**, 369.
Wild, J. P., Smerd, S. F., and Weiss, A. A.: 1963, *Ann. Rev. Astron. Astrophys.* **1**, 291.

OBSERVATIONS OF CORONAL DISTURBANCES FROM 1 TO 9 R_{\odot}

II: Second Event of 1973 January 11

R. T. STEWART*

Institute for Astronomy, University of Hawaii, Honolulu, HI., U.S.A.

R. A. HOWARD

Naval Research Laboratory, Washington, D.C., U.S.A.

F. HANSEN

High Altitude Observatory, NCAR, Boulder, Colo., U.S.A.

T. GERGELY and M. KUNDU

Astronomy Program, University of Maryland, College Park, Md., U.S.A.

(Received 18 January, 1974)

Abstract. Observations of a coronal disturbance on 1973 January 11 commencing at 18^h01^m UT are described. The event is homologous with an earlier disturbance from the same region of the corona. The observations suggest that a cloud of coronal gas containing $\sim 4 \times 10^{39}$ electrons propagated outwards to $\geq 5 R_{\odot}$ behind a piston-driven shock wave travelling at a velocity of 800 to 1200 km s⁻¹.

1. Introduction

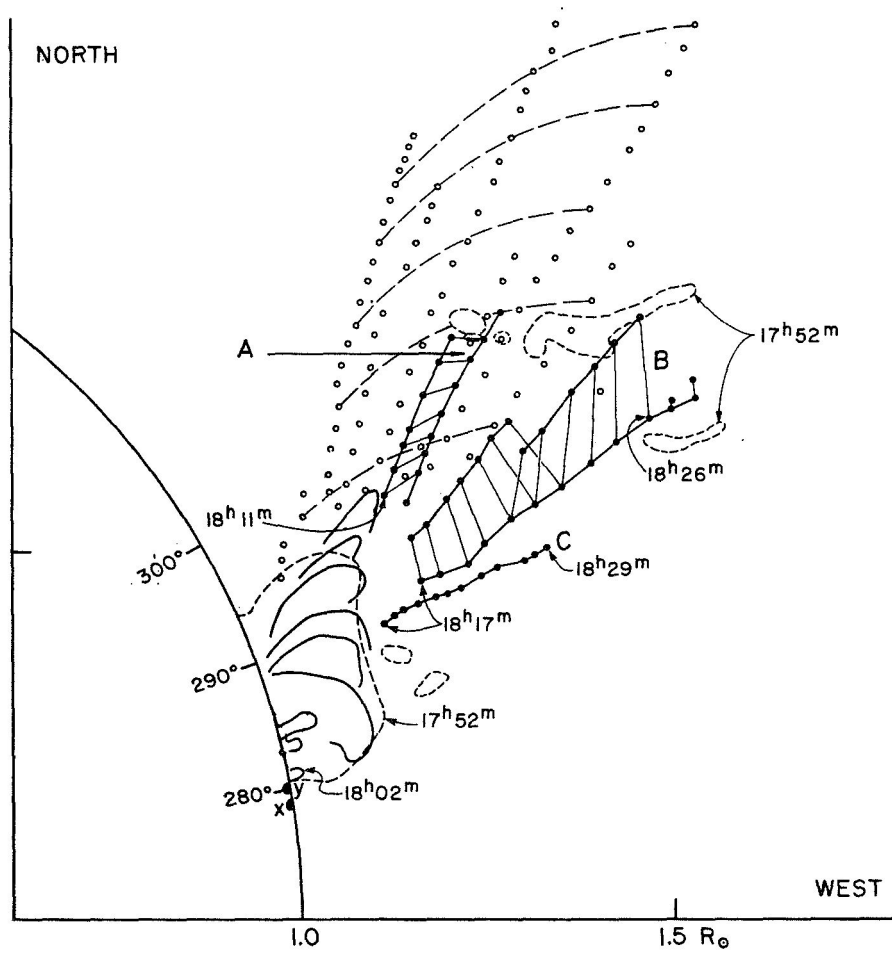
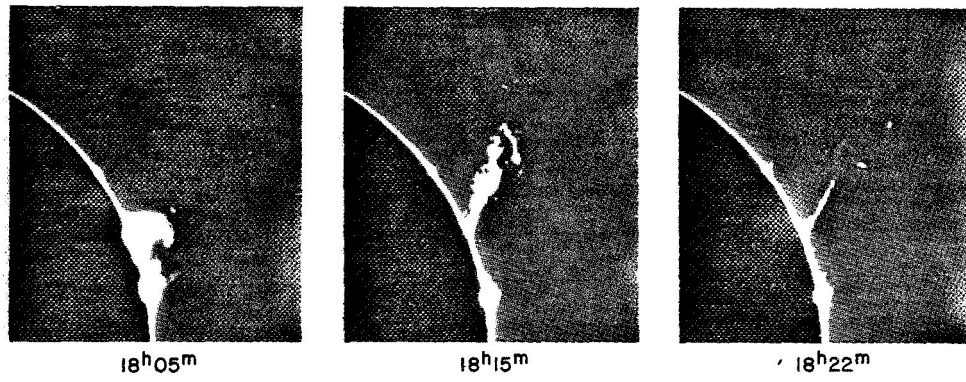
On 1973 January 11 two coronal disturbances were observed at H α , white-light and radio wavelengths. The first disturbance commencing at 00^h36^m UT has been described in Paper I (Stewart *et al.*, 1974). In this paper we describe observations of the second disturbance commencing at 18^h01^m. The radio data were recorded at Clark Lake Observatory, University of Maryland. H α observations of the spray were obtained at Mauna Loa, High Altitude Observatory. The brightness of the white-light corona during the event was measured by the coronal activity monitor at Mauna Loa and the whitelight coronagraph on OSO-7, US Naval Research Laboratory experiment.

The combined observations show that the second event was remarkably similar in detail to that of the first one 17 h earlier. This result extends the concept of homology, originally applied to H α chromospheric flares (Ellison *et al.*, 1960); to the complete coronal disturbance at 1 to 9 R_{\odot} .

2. H α Observations

The H α spray recorded by the Mauna Loa coronagraph (10 Å band-pass) began at 18^h01^m as a bright mound at position angle 285°. The associated chromospheric H α

* On leave from Division of Radiophysics, CSIRO, Sydney, Australia.



flare occurred in the plage region of McMath No. 12160. Flare brightenings were observed near the edge of the solar disk (positions x and y of Figure 1) with the Haleakala (University of Hawaii) flare patrol telescope from 18^h09^m. The bright mound on the coronagraph pictures rapidly expanded outwards in the form of an expanding hook (see coronagraph pictures at top of Figure 1). From 18^h11^m to 18^h29^m several bright blobs of spray material were traced outwards to $\leq 1.7 R_{\odot}$ along linear trajectories (A, B and C of Figure 1) and found to have very nearly constant projected velocities of 450, 480 and 230 km s⁻¹ (respectively).

The spray cone outlined by ejecta A, B and C of Figure 1 was similar to that of the event described in Paper I (open circles and dashed arcs of Figure 1) but tilted 10° closer to the radial direction. Another eruptive H α event occurred in the same region from $\sim 17^{\text{h}}20^{\text{m}}$ to 18^h00^m associated with a chromospheric flare (N10°, W90°) beginning at 17^h15^m. When coronagraph recording began at 17^h50^m material from this earlier event was at heights $\leq 1.7 R_{\odot}$ (see dashed outlines of Figure 1). To avoid confusion with the first (Paper I) and second (18^h01^m) coronal disturbances we will refer to the 17^h15^m to 18^h00^m event as the ‘earlier eruptive H α event’.

3. Radio Observations

The radio observations were obtained with the Clark Lake sweep-frequency interferometer operating in the 20 to 65 MHz range on an east-west baseline. This instrument provides both spectra and one-dimensional positions. We have also used the 10 to 2000 MHz spectra from Harvard Radio Observatory (A. Maxwell, private communication) to help identify spectral types. The Clark Lake spectral record from 17^h00^m to 19^h00^m is reproduced in Figure 2. Position measurements from 18^h06^m to 19^h00^m are plotted in Figure 3.

An intense type III-V burst group and a short-wave fadeout was recorded at 17^h15^m (Figure 2) at the starting time of a small flare at 10°N 90°W. The main radio event began at 18^h00^m (at the same starting time as the main H α spray) with an importance 2+ short-wave fade-out and an intense group of type III-V bursts from 18^h00^m to 18^h05^m. During this period the Clark Lake interferometer was being calibrated. Recording recommenced at 18^h06^m and continued until the end of the event at 19^h00^m (Figure 2). We distinguish four phases of activity on the interferometer record:

Fig. 1. *Top*: Selected broad band-pass (10 Å) H α coronagraph pictures of the second flare spray of 1973 January 11. *Bottom*: Sketch of the moving spray material from 18^h02^m to 18^h26^m at 1-min intervals. Filled circles joined by heavy lines show the trajectory of several bright blobs in the spray. A, B and C refer to separate ejections of spray material travelling at velocities of 450, 480 and 230 km s⁻¹ respectively. Within A and B, points corresponding to the same time are joined. Only the outline of the spray is shown from 18^h02^m to 18^h10^m. The dashed contours indicate the position of material at 17^h52^m associated with the earlier eruptive H α event (see text). The open circles give the positions of bright blobs (equal times joined by dashed arcs) in the first spray event commencing at 00^h36^m (Paper I). The dark areas on the disk labelled x and y indicate the chromospheric flare regions.

(1) A source of continuum of unknown classification from $18^{\text{h}}06^{\text{m}}$ to $>18^{\text{h}}09^{\text{m}}$ at an east-west position of $2.0 R_{\odot}$ (50 MHz) to $2.4 R_{\odot}$ (30 MHz) (crosses of Figure 3). This continuum source is seen on Figure 2 again at $\sim 18^{\text{h}}12^{\text{m}}$ and may be present as a background source until at least $18^{\text{h}}17^{\text{m}}$.

(2) Intense broad-band bursts from $18^{\text{h}}09^{\text{m}}$ to $18^{\text{h}}12^{\text{m}}$, which may be a mixture of type II and type III bursts, with source positions of $1.5 R_{\odot}$ (50 MHz) to $2.2 R_{\odot}$ (30 MHz) (open circle of Figure 3). From $18^{\text{h}}07^{\text{m}}$ to $18^{\text{h}}11^{\text{m}}$ a great microwave burst was recorded at Sagamore Hill (World Data Centre A for Solar Terrestrial Physics).

(3) An intense complex type II burst from $18^{\text{h}}12^{\text{m}}$ to $18^{\text{h}}21^{\text{m}}$. The leading edge of this burst was clearly defined on both the Clark Lake and Harvard spectral records from $18^{\text{h}}13^{\text{m}}$ to $18^{\text{h}}17^{\text{m}}$. During this period the leading edge drifted from 45 to 30 MHz

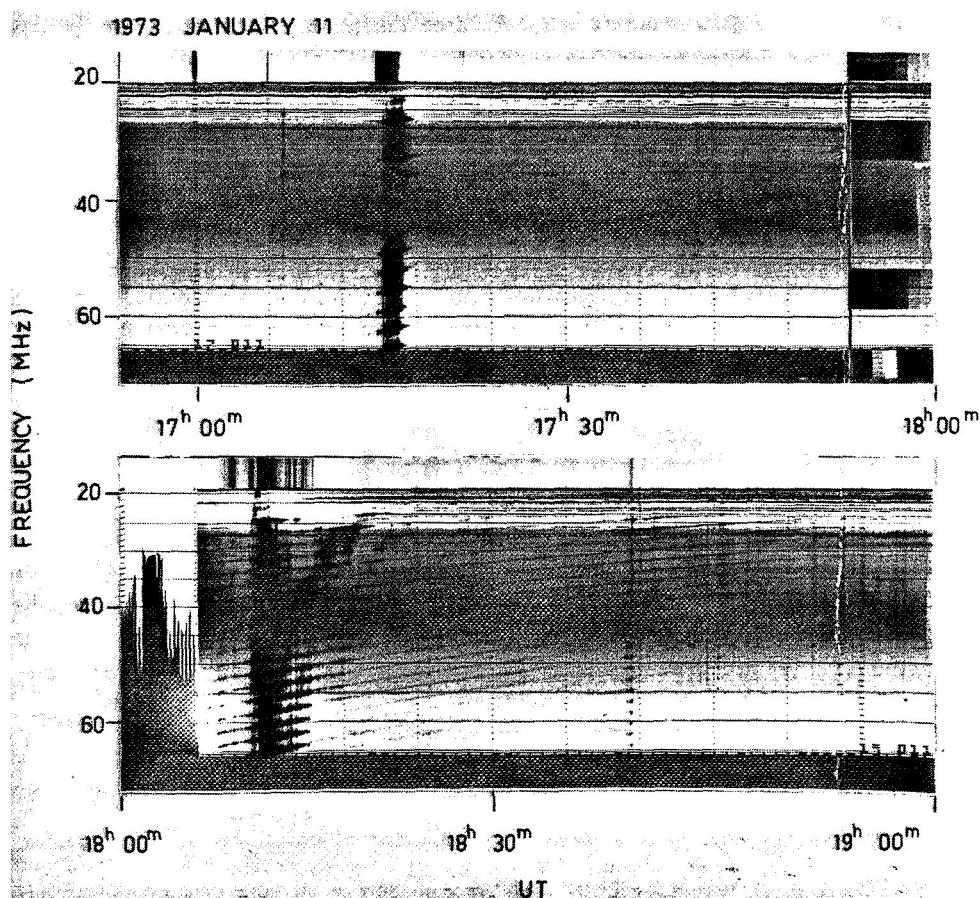


Fig. 2. Dynamic spectrum from $17^{\text{h}}00^{\text{m}}$ to $18^{\text{h}}00^{\text{m}}$ 1973 January 11 recorded in the 20 to 65 MHz range by the Clark Lake sweep-frequency interferometer. Dark fringes indicate bursts; the continuous fringes after $18^{\text{h}}00^{\text{m}}$ are caused by a long-lived continuum burst. The patterns from $17^{\text{h}}54^{\text{m}}$ to $18^{\text{h}}06^{\text{m}}$ are caused by an aerial calibration. Vertical dots are 6-min time markers.

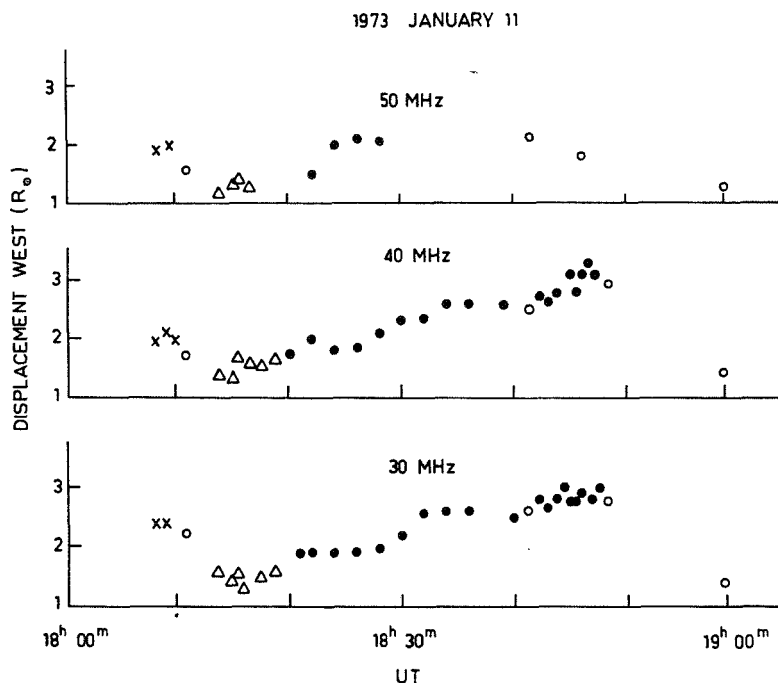


Fig. 3. Measured one-dimensional displacement (west from the centre of the Sun) of the centroids of burst sources during the second coronal disturbance of 1973 January 11. Crosses refer to an unidentified continuum burst, open circles to type III bursts, triangles to type II bursts and closed circles to a moving type IV burst.

with a constant drift rate of -0.06 MHz s^{-1} . The observed drift rate corresponds to a radial velocity of 800 km s^{-1} if $1 \times$ Newkirk (1961) coronal streamer densities are used, and 1050 km s^{-1} if $2 \times$ Newkirk values are used (Figure 4). Position measurements of the leading edge of the burst (from the interferometer fringes) give a projected (east-west) velocity of 1170 km s^{-1} (Figure 4). Since we do not know either the correct densities or the effects of ray refraction and scattering on the position measurements we cannot say which estimate is correct. We also note that for the type II burst of the first event (Paper I) a similar range of velocities 800 to 1200 km s^{-1} was derived.

The type II burst positions (triangles of Figure 3) differ significantly from those of the continuum and type III sources. The latter are probably located radially above the flare region while the type II source may be radially above the spray cone (see filled circles of Figure 5).

(4) A moving type IV burst from $18^{\text{h}}17^{\text{m}}$ to $18^{\text{h}}50^{\text{m}}$ with similar source positions at 30 and 40 MHz. The source moved outwards systematically with a projected (east-west) velocity of 580 km s^{-1} . If the moving type IV source travelled outwards along a similar path to that of the first event (which was measured by the heliograph, and is shown by the dashed arrow of Figure 5) the projected velocity would

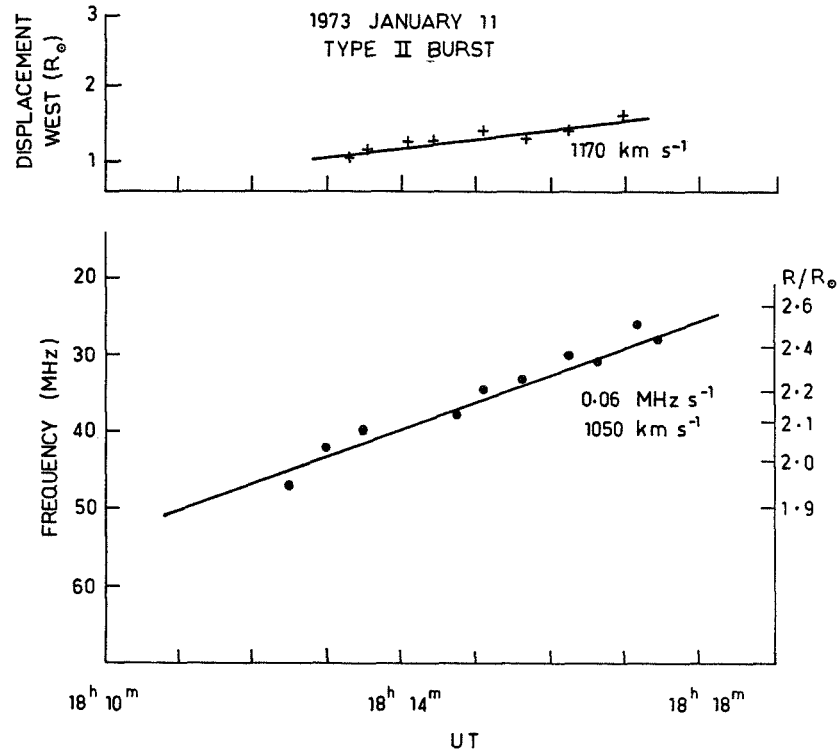


Fig. 4. *Top plot:* Measured displacement (west) of the leading edge of the type II burst. *Bottom plot:* Frequency versus time plot of the leading edge of the type II burst. If the frequencies are converted to heights (right-hand axis) using $2 \times$ Newkirk (1961) coronal streamer densities the observed drift rate of 0.06 MHz s^{-1} corresponds with a radial velocity of 1050 km s^{-1} (see text).

be $\sim 700 \text{ km s}^{-1}$; in addition, the height of the final position of the moving type IV burst would be in good agreement with the height of the leading edge of the white-light cloud observed at $18^{\text{h}}52^{\text{m}}$ (see light contour of Figure 5, and Section 5).

When the moving type IV burst faded at $\sim 18^{\text{h}}50^{\text{m}}$ there was no sign of the earlier continuum source. The only other sources during the late stage of the radio event were isolated type III bursts at $18^{\text{h}}41^{\text{m}}$, $18^{\text{h}}48^{\text{m}}$ and $18^{\text{h}}58^{\text{m}}$ (open circles of Figure 3). The projected position of the $18^{\text{h}}58^{\text{m}}$ type III burst nearer the centre of the Sun could be due to its association with a flare on the solar disk at $\text{N } 12^{\circ} \text{ W } 03^{\circ}$ and an X-ray burst at $18^{\text{h}}57^{\text{m}}$ (World Data Center A for Solar Terrestrial Physics).

4. White-Light Observations below $2 R_{\odot}$

The brightness of the K-corona below $2 R_{\odot}$ was measured from $18^{\text{h}}25^{\text{m}}$ by the coronal activity monitor at Mauna Loa. The first recording began about 25 min after the start of the main $\text{H}\alpha$ spray and about 1 h after the earlier eruptive $\text{H}\alpha$ event. Only a small

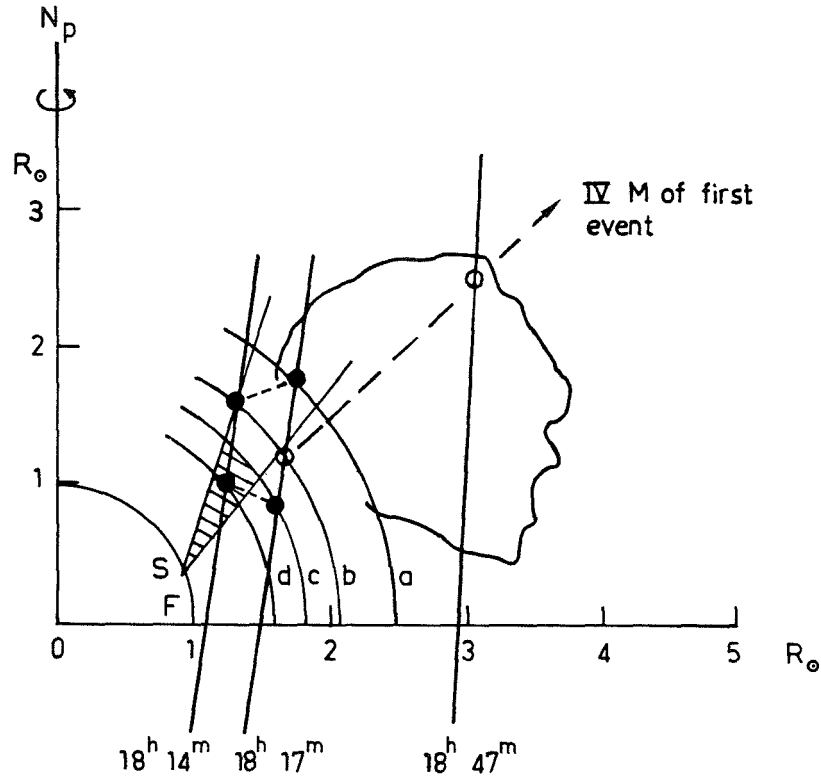


Fig. 5. Possible two-dimensional positions at three times of the type II burst and moving type IV burst of the second event of 1973 January 11 (filled and open circles respectively). Filled circles indicate the intersection of the interferometer fringes (heavy lines) with the 40 and 30 MHz plasma levels in a $2 \times$ Newkirk (1961) coronal streamer model (b and a arcs) and in a Newkirk quiet corona model (d and c arcs). The dotted lines joining these points indicate the corresponding two possible trajectories of the type II burst. Open circles indicate the intersection of the interferometer fringes with the path of the moving type IV source of Paper I, given by the dashed arrow (see text). S and F indicate the $H\alpha$ spray and flare centres. The hatched area indicates the spray cone. The light contour outlines the bright cloud observed by the OSO-7 white-light coronagraph at $18^h 52^m$.

change in brightness level was noted at this height ($1.5 R_{\odot}$). (Compare full and dashed lines in top plot of Figure 6.) Later scans at other heights showed steady brightness levels very similar to the decreased brightness levels observed during the first event. (Compare full and dashed lines in bottom plot of Figure 6, and see also Figure 4 of Paper I.) Since for this second event the pre-event levels were not measured it is not possible to determine if the brightness decreased during the second disturbance. All we can say is that if the corona below $2 R_{\odot}$ did recover in the intervening 17 h between the first and second events then the electrons were depleted in much the same way during the second disturbance as they were during the first disturbance.

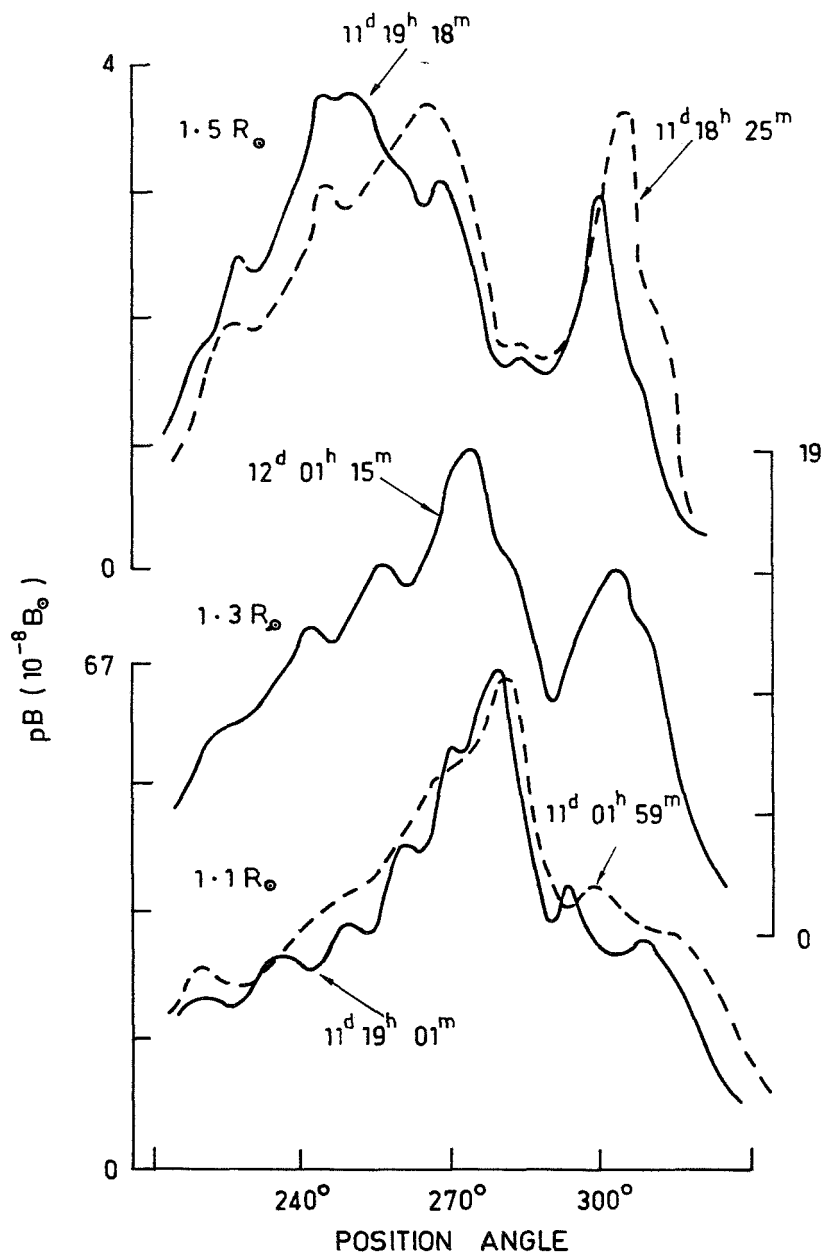


Fig. 6. Coronal activity monitor scans of the polarized *K*-corona brightness pB (where p is the polarization tangential to the limb and B is the radiance of the corona in units of 10^{-8} of the radiance B_{\odot} of the centre of the solar disk) at three heights – 1.1, 1.3 and $1.5 R_{\odot}$. The times of the scans are indicated. The dashed line (top plot) shows a small change in brightness possibly associated with the end of a transient event. The dashed line (bottom plot) shows the (decreased) brightness after the first transient event 17 h earlier (see text).

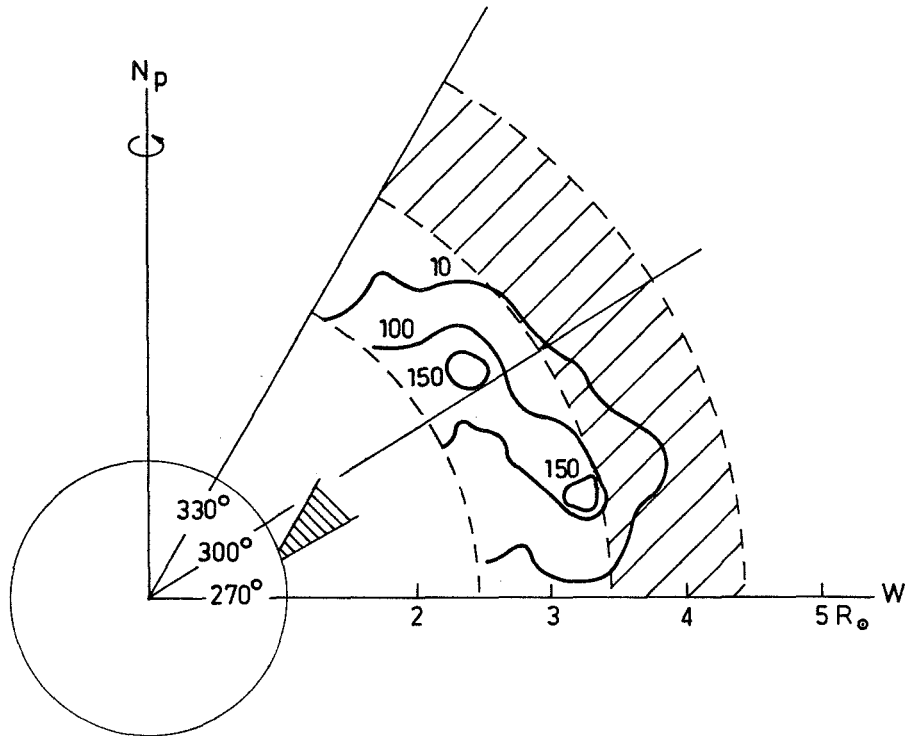


Fig. 7a.

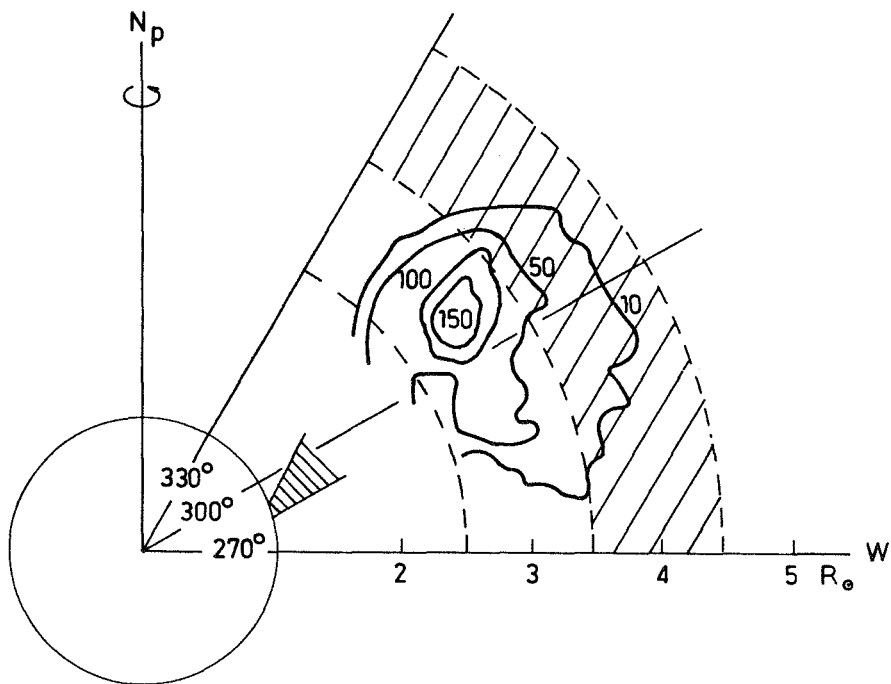


Fig. 7b.

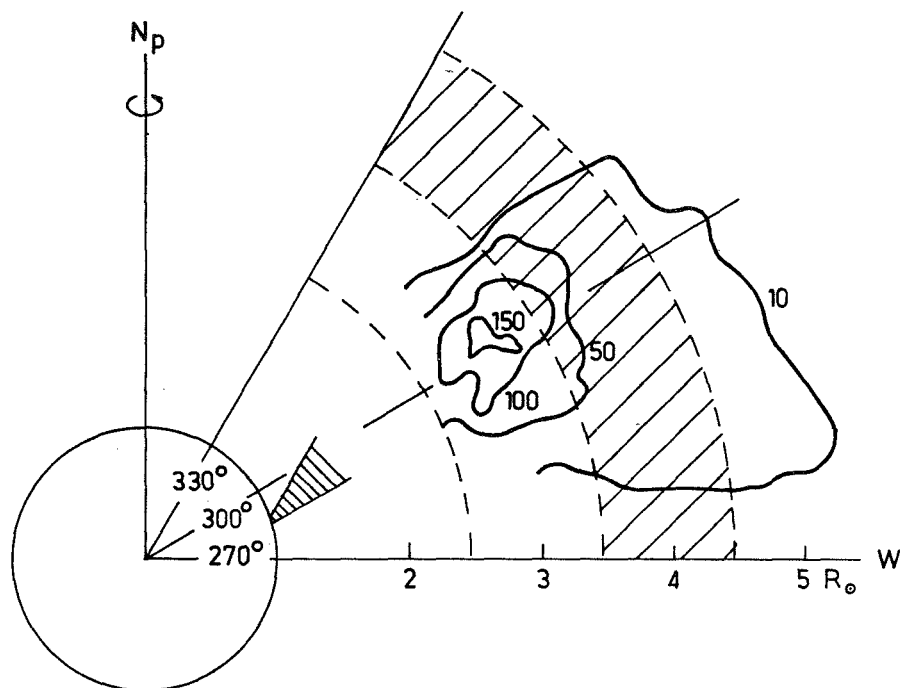


Fig. 7c.

Fig. 7a-c. Contour plots of the excess brightness (above that of the quiet corona at 00^h14^m) observed by the white-light coronagraph on OSO-7 during the second coronal disturbance of 1973 January 11 at (a) 18^h42^m, (b) 18^h52^m and (c) 19^h01^m. Brightness units are $10^{-10} \bar{B}_{\odot}$ (where \bar{B}_{\odot} is the mean radiance of the solar disk). The hatched cone indicates the H α spray direction. The dashed arc at $2.5 R_{\odot}$ indicates the extent of the occulter disk. The polarization of the coronagraph is radial to the Sun in the hatched region between 3.5 and $4.5 R_{\odot}$ but tangential elsewhere.

5. White-Light Observations above $2.5 R_{\odot}$

5.1. MAXIMUM BRIGHTNESS REGION

In the interval 18^h38^m to 18^h39^m an unusually large *K*-corona brightness (polarized component) of $0.3 \times 10^{-8} B_{\odot}$ was recorded at a height of $2.67 R_{\odot}$ and a position angle of 310° by the Mauna Loa coronal activity monitor. Several minutes later the white-light coronagraph on OSO-7 recorded a maximum *K*-corona brightness (tangential component) of $1.5 \times 10^{-8} \bar{B}_{\odot}$ at a similar height and position angle. The north-west quadrant of the corona was observed at 18^h42^m, 18^h52^m and 19^h01^m and the full corona was observed at 21^h47^m. To enhance the contrast of the coronagraph pictures we have subtracted an earlier quiet corona picture recorded at 00^h14^m. The first picture at 18^h42^m (Figure 7a) showed two brightness maxima, one at a height of $2.8 R_{\odot}$ and position angle of 307° , the other at a height of $3.3 R_{\odot}$ and position angle of 284° . The former could be associated with the large brightness recorded by the Mauna Loa coronal activity monitor at 18^h38^m–39^m. At 18^h52^m and 19^h01^m this

peak brightness region had moved out to heights of 3.0 and 3.15 R_{\odot} respectively (Figures 7b and 7c). This bright region appeared to move outwards radially above the spray cone (hatched area of Figure 7) with a velocity $\sim 230 \text{ km s}^{-1}$ (short dashed line of Figure 8). If it continued to move at this velocity it should have been observed at a height $\sim 6 R_{\odot}$ (i.e. within the field of view of the coronagraph) at 21^h47^m; but it was not detected. Either this bright region expanded and faded or else it travelled outwards at a faster velocity ($v \geq 400 \text{ km s}^{-1}$) than estimated. A velocity of 230 km s^{-1} is consistent with this bright region's being associated with ejecta from the early eruptive H α event (starting at $\sim 17^{\text{h}}15^{\text{m}}$); a velocity $\geq 400 \text{ km s}^{-1}$ is consistent with its being associated with the second spray event (starting at $\sim 18^{\text{h}}00^{\text{m}}$). The second bright region at position angle of 284° (Figure 7a) was not observed at 18^h52^m or 19^h01^m (Figures 7b and c).

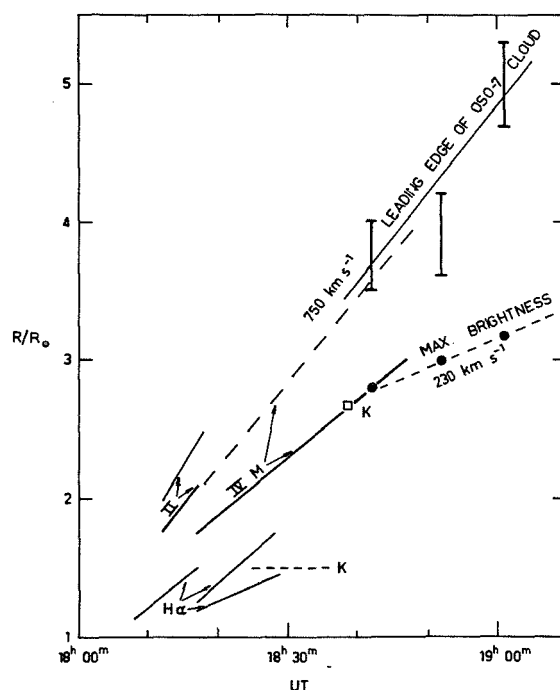


Fig. 8. Combined projected height-time plots of the observed moving sources in the second coronal disturbance of 1973 January 11. The light lines (labelled H α) refer to the spray trajectories of Figure 1. The dashed line (labelled K) refers to a brightness change recorded by the coronal activity monitor (see Figure 6 top plot). The heavy and light lines (labelled II) refer to the leading edge of the type II burst (plotted using $1 \times$ Newkirk (1961) and $2 \times$ Newkirk coronal streamer densities respectively). The heavy full line and dashed line (labelled IV M) give the minimum and maximum heights of the moving type IV burst (see text and Figure 5). The open square (labelled K) shows the height of the maximum brightness recorded by the coronal activity monitor at 18^h38^m–39^m. The dashed line and filled circles (labelled max. brightness) give the height of the maximum brightness recorded by the white-light coronagraph on OSO-7 at the times indicated. The error bars show the variation in height of the leading edge of the OSO-7 cloud (at position angles between 280° to 310°) at the times indicated.

5.2. LEADING EDGE OF THE OSO-7 CLOUD

The leading edge of the OSO-7 cloud (associated with the faster spray event) was difficult to define because its brightness level was only 10% higher than the background corona (see Paper I). From Figure 7 it can be seen that in the second event the lowest brightness contour observed had a ragged edge but seemed to be more or less tangential to the Sun and confined within position angles of 275° to 320° . However, the field of view of the OSO-7 coronagraph was restricted to only the north-west quadrant for these pictures. A later picture recorded at $21^{\text{h}}47^{\text{m}}$, nearly 4 h after the start of the event, shows bright corona extending over heights from 2.5 to $9 R_\odot$ and position angles from 250° to 300° (over about the same range of position angles as in the first disturbance; see Figure 5 of Paper I). The height of the leading edge of the OSO-7 cloud (at position angles between 280° to 310°) is plotted in Figure 8 at $18^{\text{h}}42^{\text{m}}$, $18^{\text{h}}52^{\text{m}}$ and $19^{\text{h}}00^{\text{m}}$. The height-time plot of the leading edge extrapolated back to the photosphere intersects it at the starting time of the $\text{H}\alpha$ spray at $18^{\text{h}}01^{\text{m}}$ and gives a projected radial velocity of 750 km s^{-1} for the disturbance. We note, however, that only a small percentage of the electrons in the white-light cloud originated in the $\text{H}\alpha$ spray (see Figure 5); in Paper I it was shown that most of the electrons came from a coronal enhancement below $2 R_\odot$.

6. Discussion

6.1. MODEL OF THE CORONAL DISTURBANCE

The close agreement between the height-time plots of the type II burst and the leading edge of the OSO-7 cloud shown in Figure 8 can be explained by postulating that a piston-driven shock-wave disturbance propagated outwards through the corona. We identify the OSO-7 cloud, the moving type IV burst and the spray material with the ejecta forming the piston; we identify the type II burst with the shock wave (see Paper I, Figure 7). The front edge of the piston, as defined by the leading edge of the OSO-7 cloud, is seen to be only a small distance behind the shock front if the lower ($\sim 800 \text{ km s}^{-1}$) rather than the higher ($\sim 1200 \text{ km s}^{-1}$) velocity derived for the type II burst is the correct one (heavy line labelled II in Figure 8).

6.2. HOMOLOGOUS EVENTS

The present observations tend to confirm earlier evidence that flares from the same active region on the Sun occurring within a period of several days can have very similar characteristics at both optical (Ellison *et al.*, 1960) and radio (Fokker and Roosen, 1961) wavelengths. Stewart and Hardwick (1969) extended the concept of homology to include explosive flare events in which the passage of fast electrons and shock waves through the corona produce radio spectra with almost a one-to-one correspondence in detail – e.g. a similar type III burst group followed by a similar type II burst with almost identical fine structure and frequency drift rate. They concluded that the spectral data were strong evidence that the coronal magnetic field and

electron density structures above complex active regions show remarkable resilience over periods of several days despite the occurrence in the meantime of several large explosive flares. (See also Hansen and Gordon, 1960.)

The two coronal disturbances on 1973 January 11 allow us to extend the concept of homology to explosive flare events in which there are also ejecta. Both disturbances produced $H\alpha$ sprays, moving type IV bursts and white-light clouds which not only occurred in similar regions of the corona but also travelled outwards at almost identical velocities (compare Figure 6 of Paper I with Figure 8 of this paper). The present evidence suggests that a shock wave propagates outwards from the lower corona at a velocity of 800 to 1200 km s^{-1} and is probably driven by the flare ejecta travelling at 400 to 700 km s^{-1} . We estimate $\sim 10^{40}$ electrons are expelled in the first event (see Paper I) and $\sim 4 \times 10^{39}$ electrons in the second event. Comparable or slightly higher masses are measured in interplanetary shock waves (Hundhausen, 1972; Hirshberg *et al.*, 1972); hence it would appear that a lot of this material is supplied from the lower corona (i.e. $< 2 R_{\odot}$ in the first event and $\lesssim 3 R_{\odot}$ in the second event), as Hirshberg *et al.* (1972) predicted.

If the two events are indeed homologous, as we have inferred, the unhinging of large-scale magnetic loops which produced a decrease in the electron content of a $\sim 60^\circ$ sector of the inner corona during the first event must have been followed by a re-forming of the coronal loops and a corresponding increase in electron content during the 17 h before the second event.

Acknowledgement

The work of RTS was supported by NSF grant GA-25903, and of T.G. and M.K. by NSF grant GP-19401 and NASA grant NGR 21-002-367. The NRL OSO-7 white-light coronagraph experiment and data reduction was fully supported by NASA.

References

- Ellison, M. A., McKenna, S. M. P., and Reid, J. H.: 1960, *Dunsink Obs. Publ.* **1**, No. 1.
- Fokker, A. D. and Roosen, J.: 1961, *Bull. Astron. Inst. Neth.* **16**, 83.
- Hansen, R. T. and Gordon, Diane: 1960, *Publ. Astron. Soc. Pacific* **72**, 194.
- Hirshberg, J., Bame, S. J., and Robbins, D. E.: 1972, *Solar Phys.* **23**, 467.
- Hundhausen, A. J.: 1972, *Coronal Expansion and Solar Wind*, Springer-Verlag, N.Y.
- Newkirk, G.: 1961, *Astrophys. J.* **133**, 983.
- Stewart, R. T. and Hardwick, B.: 1969, *Proc. Astron. Soc. Australia* **1**, 185.
- Stewart, R. T., McCabe, Marie K., Koomen, M. J., Hansen, R. T., and Dulk, G. A.: 1974, this issue, p. 203 (Paper I).

11

DETAILED CORRELATION OF TYPE III RADIO BURSTS WITH $H\alpha$ ACTIVITY

I: *Active Region of 22 May 1970*

T. B. H. KUIPER

*Clark Lake Radio Observatory, Astronomy Program, University of Maryland,
College Park, Md. 20742, U.S.A.*

and

JAY M. PASACHOFF*

*Big Bear Solar Observatory, Hale Observatories, Carnegie Institution of Washington
California Institute of Technology, Pasadena, Calif. 91109, U.S.A.*

(Received 14 August, 1972)

Abstract. We compare observations of type III impulsive radio bursts made at the Clark Lake Radio Observatory with high-spatial-resolution cinematographic observations taken at the Big Bear Solar Observatory. Use of the log-periodic radio interferometer allows us to localize the radio emission uniquely. This study concentrates on the particularly active region close to the limb on 22 May 1970. Sixteen of the 17 groups were associated with some $H\alpha$ activity, 11 of them with the start of such activity.

1. Introduction

Statistical studies of the correlation of type III bursts with flares showed that, at the maximum of solar cycle 19, 60% of these bursts occurred during the life of a flare (Swarup *et al.*, 1960). Only half of this number were truly associated with the flare, however, the remainder representing chance occurrences. It had also been noted that flares occurring in certain active regions showed a high degree of correlation with bursts, while those in other regions showed little or no correlation (Loughhead *et al.*, 1957). Zirin and Werner (1967) reported that $H\alpha$ brightenings could usually be found at the times of strong type III bursts. Our more complete time coverage of both $H\alpha$ structure and radio events justifies a re-examination of this correlation. Further, use of an interferometer allows us to localize the radio emission correlation. As a first step, we wish to report the detailed analysis of the activity in McMath 10743, a region showing inverted polarity, between 1700 and 2230 UT on 22 May 1970. This region was particularly well-suited for study as it was near the limb and especially active.

On that day, a series of spectacular surges occurred, including the one shown in Figure 1a (Zirin, 1971; Pasachoff, 1972). We have identified the various active parts of this activity center in Figure 1b. The most impressive surges appeared to be emitted out of region 5, streaming along 1. Streaming also followed 2 and 3, the latter being the more important. Surges along 3 generally appeared in 'mid-air' and then moved outwards. Surges along 2 appeared to come from the southern part of loop 4. Loop 4

* as of September 1972: Williams College-Hopkins Observatory, Williamstown, Massachusetts 01267.

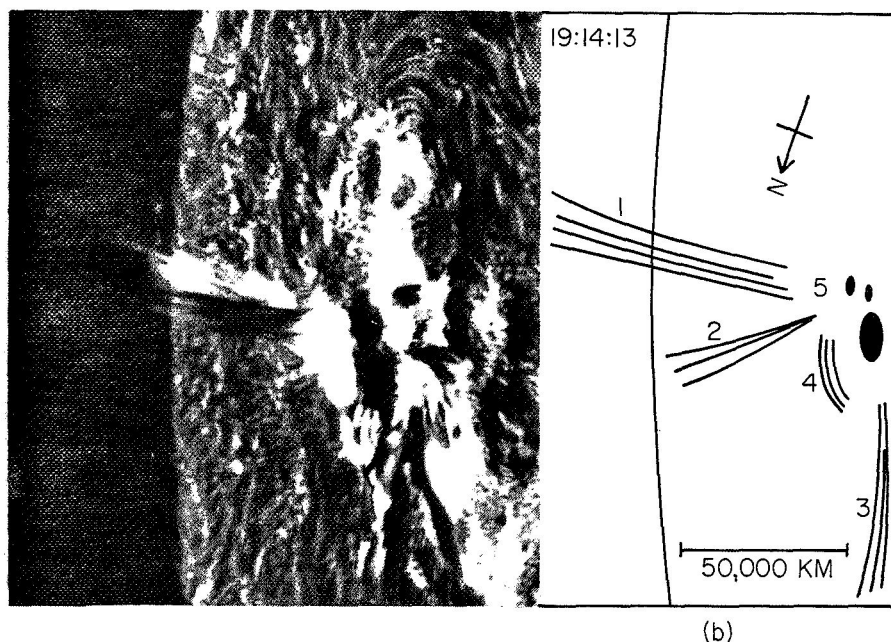


Fig. 1. (a) The spectacular surge of 19:05 UT on 22 May 1970 achieved its maximum extent at 19:14:13. This and all subsequent photographs have north to the bottom. (b) The active elements of the region. 1, 2 and 3 are trajectories along which material appeared to be ejected. 4 appears occasionally to be a closed set of field lines, though this feature is not apparent here due to the brightness of the flare. 5 is a plage region of complex structure in which the major flares occurred. (Big Bear Solar Observatory photograph.)

is not apparent in Figure 1 because of the bright flare. Figure 7 shows the best example of the loop structure in 4. The loop itself also showed activity, generally bulging outwards and then subsiding again. Within each group the flares seemed homologous. These events were photographed with a ten-inch refractor at the Big Bear Solar Observatory through a $\frac{1}{2}$ Å filter centered in the $H\alpha$ line center. Exposures were made every fifteen seconds.

At the same time, a series of type III (impulsive) bursts were observed at the Clark Lake Radio Observatory on the log-periodic array. This instrument is a sixteen-element swept-frequency interferometer, having an east-west extent of 3.3 km. It scans from 65 to 20 MHz once per second. The principle of operation has been described by Sheridan (1963). Some early results were reported by Kundu *et al.* (1970).

2. Positions of the Radio Bursts

Since the Big Bear $H\alpha$ cinematograph covers only one activity center at a time, any type III bursts without corresponding $H\alpha$ activity could be attributed to centers not in the field. For this reason, it is important to observe the positions of the radio bursts.

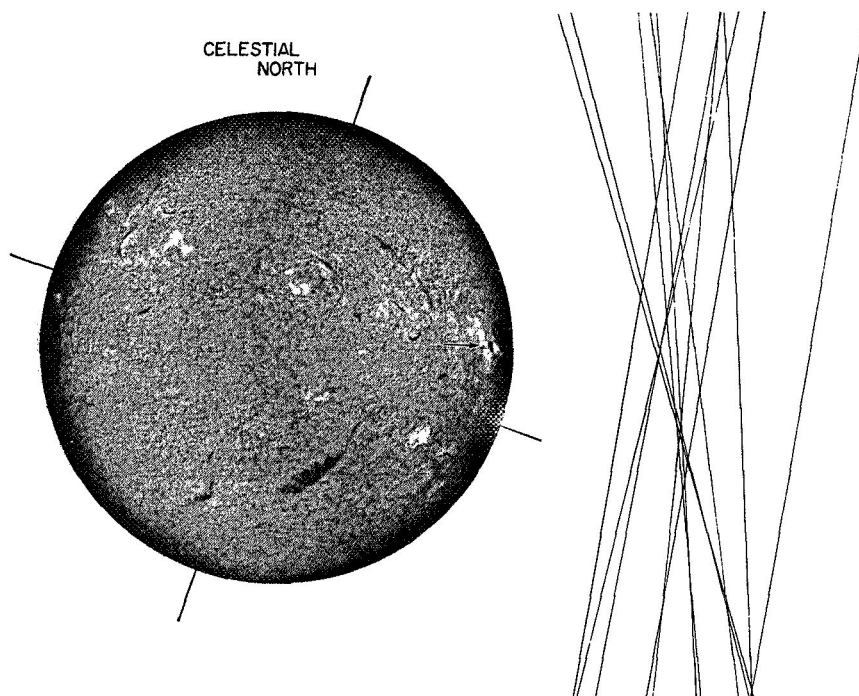


Fig. 2. The positions of the type III burst groups relative to the active region. The interferometer has only east-west resolution, so that the bursts may have occurred anywhere along the position lines plotted. The position lines have various tilts because the orientation of the interferometer baseline varies as the Earth rotates. (Lockheed Solar Observatory photograph.)

Figure 2 shows the 60 MHz position lines for the groups of bursts observed between 1700 and 2230. In this context, 'group' may mean either a single, isolated burst, or any collection of bursts separated by less than a minute. Since the array does not resolve in the north-south direction, we can only give a position line for each group; the bursts could have occurred anywhere along this line. As the Earth rotates, however, the orientation of the telescope changes relative to the Sun, just as the solar image reflected from a heliostat rotates. The intersection of the position lines observed at different times gives some measure of the north-south position, assuming that all bursts have about the same position. The source of radio bursts at 60 MHz appears to have been located above McMath 10743 on an extension of the lines of force implied by the structure seen in $H\alpha$ in region 1. We note that the bursts lie considerably above the expected 60 MHz plasma level. If we assume that the bursts occur more or less radially above the active region, then they are at an apparent height of 1 solar radius. Ionospheric refraction effects are calculated not to exceed 0.2 radius. Because of the difficulties of propagation in a non-uniform corona and our lack of knowledge about whether the bursts represent fundamentals or harmonics, we cannot more properly assess the height of the bursts and hence infer coronal densities.

3. Detailed Description of the Correlation

In the description which follows, times are given to the nearest second, the resolution used at Clark Lake. It should be borne in mind, however, that the Big Bear frames were taken every quarter minute. In addition, there was a one-minute ambiguity in reading the minute hand of the Big Bear clock. It is thus possible that the times for the H α events are one minute later, although we believe the stated times to be correct. The times of the type III events refer to a frequency of 60 MHz. At lower frequencies, times were a few seconds later because of the frequency drift of the bursts. The reader must also allow for a possible systematic error of a few seconds in the Clark Lake times.

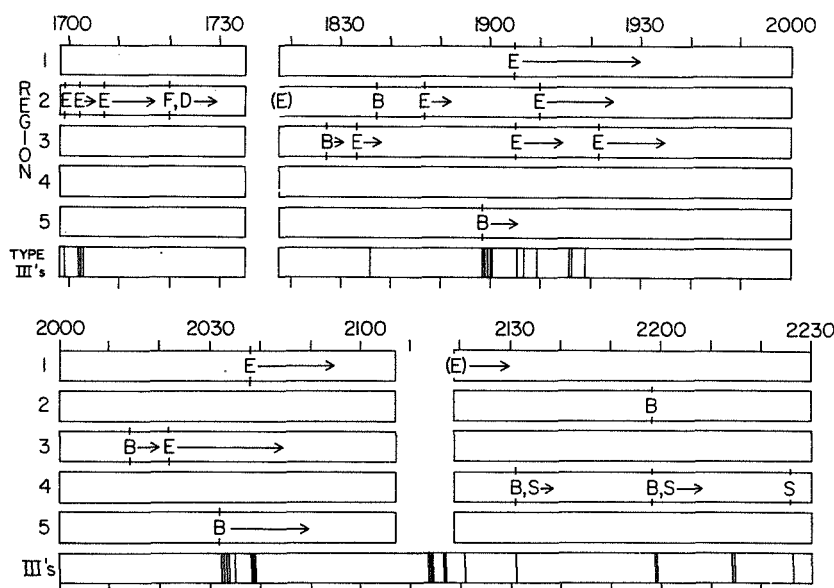


Fig. 3. A schematic representation of the activity in McMath 10743. The regions labeled 1 through 5 are identified in Figure 1. We use the following codes: B – brightening, D – diminishing, E – ejection, F – fan-like structure, S – stretching or bulging, () – in progress, → – continuing.

Figure 3 is a schematic representation of the activity, and is useful for seeing the general correlation between type III bursts and H α events. A detailed description of the correlation is given in semi-tabular form below. It is based on a study of the film sequence, part of which has been included in the 'show film' available from the Big Bear Solar Observatory (1971). For purposes of demonstration, certain details are represented in Figures 4 through 7.

The first event described was reported in *Solar Geophysical Data* as an unconfirmed subflare with several brilliant points, which lasted from 16:58 to 17:15.

16:59:04–16:59:13 type II burst.

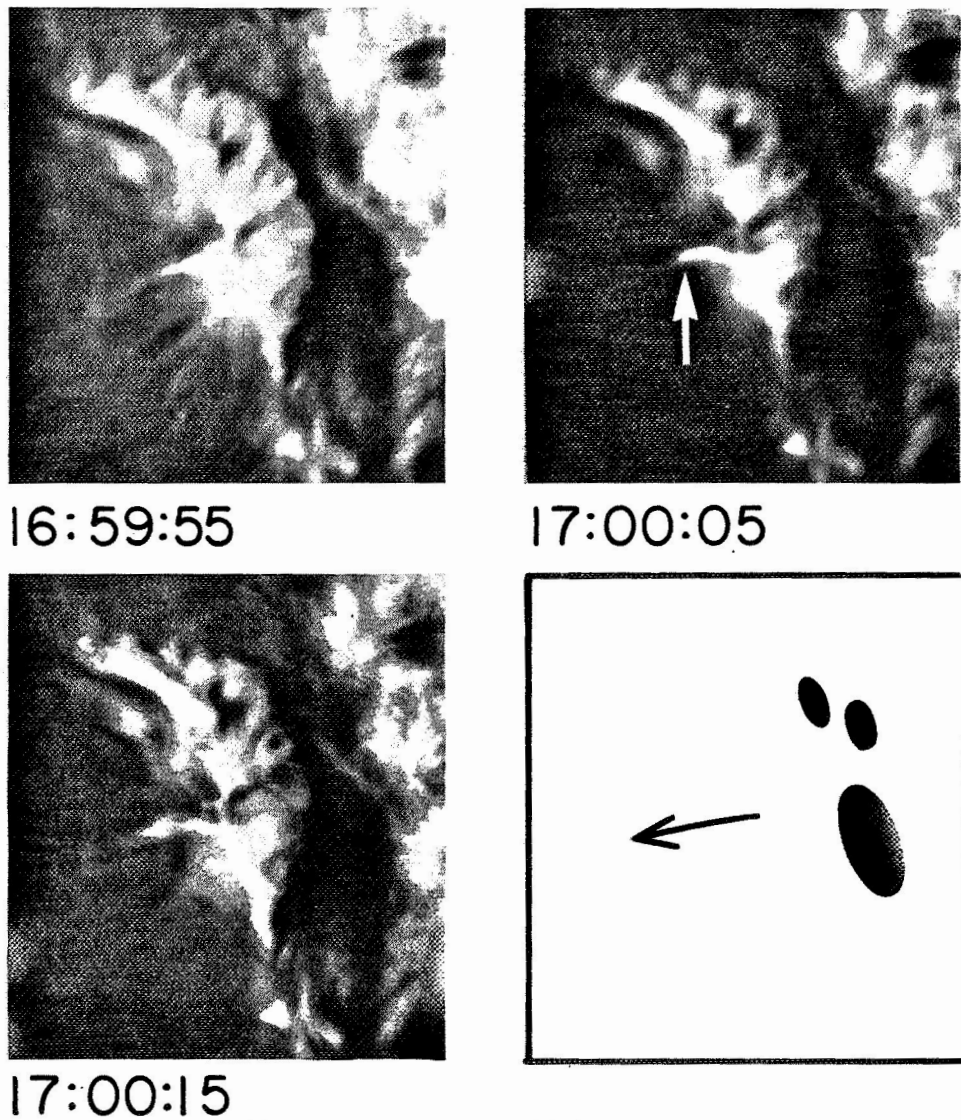


Fig. 4. An ejection of material along 2 at 17:00.

- 16:59:55 bright spot appeared at the base of 2 and was ejected (Figure 2).
 17:02:02–17:02:10 type III burst.
 17:02:05 some more bright material began to move along 2.
 17:02:23–17:02:35 a pair of type III bursts.
- 17:06:55–17:20 a whole sequence of ejections along 2.
 17:20 a dark fan-like structure became apparent at 2, and then gradually faded away.
- The next series of events described were not reported in *Solar Geophysical Data*.
 18:17:50 a small ejection of material along 2. No type III burst was recorded at Clark



Fig. 5. The flare in region 5 at 18:59.

- 18:27:25 Lake, although Uccle Observatory in Belgium reported a small burst at 18:17, lasting half a minute, at 600 MHz.
a bright region at the base of 3 began to develop a small tail outwards along 3.
- 18:33:25–18:38:25 a faint ejection of material along 3.
- 18:36:01–18:36:11 faint type III burst.
- 18:37:40 the region at the base of 2 showed a brief brightening.
- 18:40:20 very faint type III burst.
- 18:46:50–18:53 a small spray in 2. No bursts were seen at Clark Lake but Uccle reported bursts at 18:43 and 18:51.

The main event of our mutual observing period was reported in *Solar Geophysical Data* as a confirmed bright subflare (Grp 30106) with several bright points and a high velocity dark surge, and lasted from 18:58 to 19:17, with a maximum at 19:01.

- 18:58:46 a sudden flare in 5 (Figure 5).
- 18:58:45–19:00:35 a strong, complex group of type III bursts.
- 19:04:45 material began to stream out of 1.
- 19:05:15 streaming along 3 became apparent (Figure 6).
- 19:05:19–19:05:29 type III burst of moderate intensity.
- 19:06:31 a weak type III burst.
- 19:09:19–19:09:50 a faint group of type III bursts.
- 19:10:00 streaming started along 2, while streaming along 3 had stopped.
- 19:15:20 a very faint type III burst.
- 19:15:51–19:16:01 a type III burst of moderate intensity.
- 19:16:17 a weak type III burst.
- 19:19:00 a very faint type III burst.
- 19:21:40 streaming appeared again in 3. Since this material appeared to condense out along the stream at this time, it seems likely that the ejection started at an

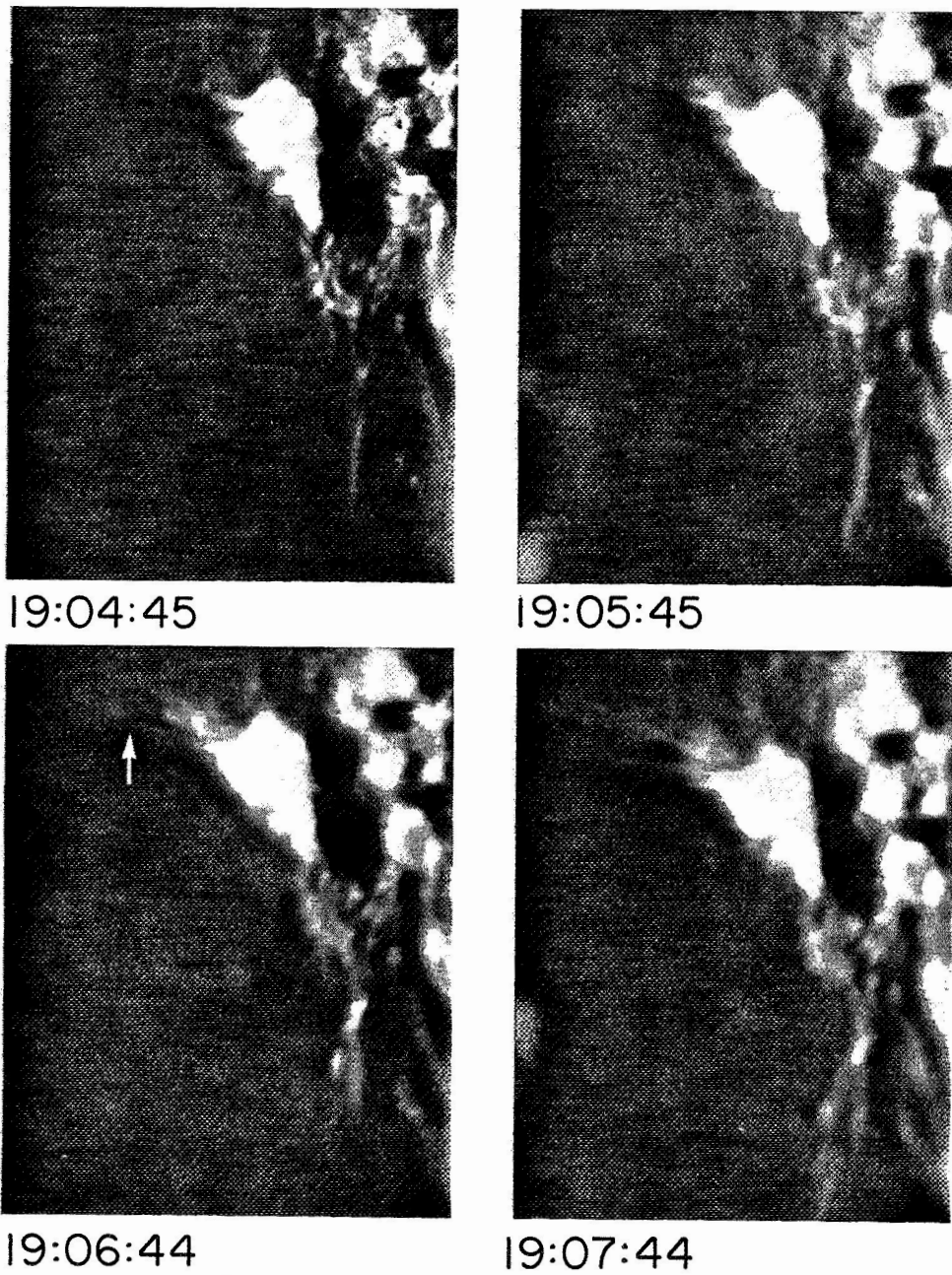


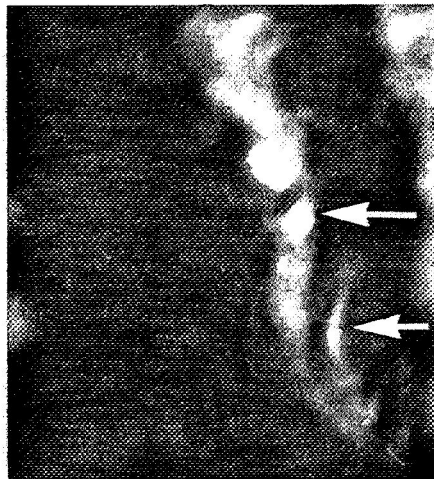
Fig. 6. Expulsion of material along 1 and 3 following the 18:59 flare.

19:35 earlier time nearer the active center, and may have been associated with the type III burst 3 min earlier.
activity ceased.

The next event was also reported as a confirmed subflare (Grp 30107) with several bright points, a



22:24:38



22:25:32



22:26:17



22:27:02

Fig. 7. Region 4 brightens and then develops a small hook attached to the southern foot. This may be similar to an outward 'bulge' of 4, but with bright material along only part of the bulging region.

high velocity dark surge, an extensive active region, and marked intensity variations in the active plage. It reportedly began at 20:27, reached a maximum at 20:38, and ended at 20:51.

20:14:10 brightening occurred at the base of 3.

20:21:50 streaming along 3 became noticeable.

20:32:05 region 5 began to brighten as streaming along 3 reached a maximum intensity.

20:32:34–20:34:08 an intense group of type III bursts.

20:34:45 brightening in 5 achieved its maximum.

20:35:14–20:35:19 type III burst.

20:38:00 faint streaming along 1 began.
 20:38:38–20:39:02 faint group of type III's.

20:45 streaming along 3 stopped.
 20:55 streaming along 1 stopped.
 An unconfirmed subflare with an extensive active region was reported from 21:06 to 21:20, with a maximum at 21:10. There was no Big Bear coverage until 21:19:05.
 21:13:55–21:14:42 a group of type III bursts of moderate intensity.
 21:16:56–21:17:21 a pair of type III bursts.
 21:19:05 Big Bear coverage resumed. Streaming along 1 was in progress.
 21:21:01–21:21:07 type III burst.

21:31:00 the streaming along 1 had subsided when loop 4 suddenly brightened and bulged outward.
 21:31:15 loop 4 achieved its maximum extension.
 21:31:16 type III burst of moderate intensity.

21:35:30 outward motion along 1 became briefly apparent.
 21:37 loop 4 returned to its normal configuration.
 There was an unconfirmed subflare in progress at 21:57 which lasted until 22:12, according to *Solar Geophysical Data*.
 21:58:25 a small bright spot appeared at the base of 2 and 4.
 21:59:10–21:59:35 a group of type III bursts.
 21:59:55 loop 4 began to bulge.
 22:01:40 loop 4 achieved its maximum extension.

22:14:33–22:14:50 a pair of type III bursts.
 22:15 a possible brightening in loop 4, weak enough to be attributed to seeing effects.
 The last event described was not reported in *Solar Geophysical Data*.
 22:25:30 loop 4 showed a faint brightening.
 22:26:00 a small hook appeared to come out of the southern end of loop 4 (Figure 7).
 22:26:13–22:26:23 type III burst.

4. Conclusions

We have found a very high degree of correlation of type III bursts with H α activity. Of a total of 17 groups (as previously defined), 11 were clearly associated with the start of some activity in H α . Five others occurred while H α activity was in progress, but could not be associated with any specific phenomenon. Only one rather weak pair of bursts (2214) may have occurred during the absence of H α activity, although even in that case there was a hint of some activity. Such a high degree of correlation could not have been detected without the resolution of the Big Bear observations. This may explain the lower correlation reported by previous workers. Further, the radio positions were isolated by use of an interferometer.

The occurrence of type III bursts was a necessary but not a sufficient condition for flaring in this active region. It is difficult to analyze this quantitatively because the H α phenomenology is so complicated. Yet we have clear instance of H α events for which no type III bursts were seen. We do not know of difference between type III-associated H α events and those events which do not have type III's but shall investigate this point in subsequent studies. It is possible that, in the latter cases, no energetic

particles were produced, or alternately that they were produced but trapped. Analysis of X-ray and centimeter-wavelength data may clarify this point.

It is not possible to generalize from a single day's observations. Yet it is interesting that there are apparently some conditions under which the correlation of type III bursts with $H\alpha$ events is high. In the majority of these cases, the events have a clearly impulsive character. The analysis of other periods of activity will determine whether this is a general property of type III bursts.

Acknowledgements

Our appreciation is due to Drs William C. Erickson and Harold Zirin, who initiated the collaboration between the Clark Lake Radio Observatory and the Big Bear Solar Observatory, and whose assistance and criticisms were invaluable to this work. We thank Drs E. v. P. Smith, R. G. Stone and D. Wentzel for their comments. Nancy Roth and Geoffrey Pressman assisted with the reduction of the radio activity records. Susan Mellerup, Robert V. Webber, and Robert Hippard aided with the Big Bear films in Pasadena.

The log-periodic array at Clark Lake is operated as a joint project between the Laboratory for Extraterrestrial Physics of Goddard Space Flight Center and the Astronomy Program of the University of Maryland under National Aeronautics and Space Administration Grant NGR 21-002-029. The Clark Lake Radio Observatory is supported by the National Science Foundation under Grant GP 19401. The Big Bear Solar Observatory is operated on NASA Grant NGR 05-002-034 and NSF Grant Ga. 24015. The computer time for the radio burst analysis was supported by NASA Grant NsG 398 to the Computer Science Center of the University of Maryland. One of us (T.B.H.K.) thanks the Graduate School of the University of Maryland for permission to publish this part of his thesis.

References

- Big Bear Solar Observatory: 1971, *Solar Phys.* **18**, 340.
Kundu, M. R., Erikson, W. C., Jackson, P. D., and Fainberg, J.: 1970, *Solar Phys.* **14**, 394.
Loughhead, R. E., Roberts, J. A., and McCabe, M. K.: 1957, *Australian J. Phys.* **10**, 483.
Pasachoff, Jay M.: 1972, *Proc. IAU Colloq. on Stellar Chromospheres* **19**, in press.
Sheridan, K. V.: 1963, *Proc. I.R.E. Australia* **24**, 174.
Swarup, G., Stone, P. H., and Maxwell, A.: 1960, *Astrophys. J.* **131**, 725.
Zirin, H.: 1971, *Solar Phys.* **18**, 194.
Zirin, H. and Werner, S.: 1967, *Solar Phys.* **1**, 66.

13

DETAILED COMPARISON OF TYPE III RADIO BURSTS WITH H α ACTIVITY

II. *The Isolated Type III Activity of March and April, 1971*

T. B. H. KUIPER *

*Clark Lake Radio Observatory, Astronomy Program, University of Maryland,
College Park, Md. 20742, U.S.A.*

(Received 16 April, 1973; Revised 29 June, 1973)

Abstract. Isolated type III radio burst activity was observed at Clark Lake Radio Observatory in March and the first part of April, 1971, to occur in discrete regions of the corona above certain active regions. When these regions were examined under high resolution in H α all the type III events appeared to have associated activity in H α . The potential coronal magnetic field in these regions appeared to be either open or diverging, whereas the field over a rather active region which did not have radio burst activity was closed in a magnetic arcade. The latter feature has been associated with streamers. Streamers have also been associated with dark filaments. The occurrence of a stable dark filament in an active region appeared to have an inhibiting effect on type III activity. It is suggested that a streamer field configuration is not favorable to the escape of isolated type III exciters.

1. Introduction

It has long been recognized that there is a relationship between type III bursts and flares (Loughhead *et al.*, 1957; Swarup *et al.*, 1960; Malville, 1961). Malville included the greatest number of subflares in his sample and found that 76% of the type III bursts occurred while a flare was in progress. In an analysis which used only isolated flares, he estimated that 44% of the bursts which occurred during the flare period are truly associated with the flare. Of the type III bursts which occurred between the start and the maximum of the flare 61% were truly associated. A similar conclusion had been drawn by Swarup *et al.* Thus, only some 35% of all type III bursts could be considered to be truly associated with flares or subflares, although there was a suggestion that this increased with the completeness of the flare sample. Malville suggested that, while many of the metric fast-drift bursts might result directly from flares, a sizeable fraction could be independent of flares or originate in some other form of solar activity not visible in H α or with dimensions below the limits of resolution. In the preceding paper of this series (Kuiper and Pasachoff, 1973, hereafter referred to as Paper I) we gave an example of one active region in which nearly all the type III bursts had associated H α activity.[†] In this paper several other regions are examined for type III-associated H α activity, using the high-resolution H α observations made at Big Bear Solar Observatory.

Loughhead *et al.* (1957) first suggested that type III bursts might be associated

* Current address: Jet Propulsion Laboratory, 183B-365, California Institute of Technology, Pasadena, Calif. 91103, U.S.A.

[†] In that paper we used the word 'correlation'. Since much H α activity is not associated with type III bursts (with fluxes in excess of about $5 \times 10^{-22} \text{ W m}^{-2} \text{ Hz}^{-1}$) the word 'association' seems more suitable.

with particular active regions. They noted that the association between type III bursts and flares was higher than average in some regions, whereas other regions showed no association with type III bursts. Erickson (1963), by measuring the positions of type III bursts on a day-to-day basis, was able to show that the rotation of regions of type III activity was consistent with the rotation of active regions. His positional accuracy, however, did not allow him to conclude that all the bursts were associated with active regions. A method for removing most of the effect of ionospheric refraction (Kuiper, 1973a, b) permits, below, a re-examination of this question.

Flares and type III bursts are generally considered as two aspects of the same phenomenon, owing to the correlation, albeit partial, between them. If the suggestion of Loughhead *et al.* (1957) that some active regions have no type III activity is correct, then one would inquire what property of these regions inhibits type III activity. Since type III bursts result from particle streams ejected to great heights in the corona, open lines of magnetic field, or at least loop structures of very large dimensions, would seem to be a prerequisite.

The schematic configuration generally associated with type III bursts involves a magnetic field drawn out into a streamer configuration by the interplanetary wind (e.g. Wild and Smerd, 1972). The density determinations of Wild *et al.* (1959) and Weiss (1963), which suggested a value twice that of the Newkirk (1959) streamer model, appeared to necessitate such an explanation. The observations of McLean (1970) of type III bursts distributed along a line on the solar disk are also taken as suggestive of a neutral-sheet configuration. (See below for a discussion of the relationship between streamers and magnetic neutral sheets). The apparent heights of the radio bursts may, however, exceed the true heights. Scattering of radio waves in the corona would cause such an effect (Riddle, 1972). Also, it is often not clear whether the bursts are observed at the fundamental frequency or the harmonic. For limb bursts the latter is probably the case, so that the bursts would appear above their appropriate plasma levels (Kuiper, 1973a, b). In an attempt to clarify whether bursts occur in streamers or not, we will consider the magnetic field configuration in regions of type III activity.

Newkirk (1967) has suggested that a white-light coronal feature forms over a young active region initially as an *enhancement* of the lower corona, evolving to an *active streamer* as the region grows in importance. With further development, the photospheric magnetic field organizes itself into two extended areas of opposite sense and the streamer takes on a characteristic *helmet* configuration. It has been suggested that the streamer is a neutral sheet in the coronal field, formed over the boundary between two magnetic regions of opposite polarity (e.g. Sturrock and Smith, 1968). The magnetic configuration is like that proposed by Carmichael (1964) as a possible site for flares with a filament supported by the closed field lines near the base. Axisa *et al.* (1971) have suggested that, as in the case of helmet streamers, the presence of a filament is a necessary condition for the existence of active streamers, and that both have the same basic magnetic structure.

Newkirk and Altschuler (1970) have compared coronal structures observed during

an eclipse to the potential magnetic field of the corona. This field is calculated from line-of-sight observations of the photospheric field, made during one solar rotation, on the assumption that the corona is current-free (Altschuler and Newkirk, 1969). A number of magnetic structures were recognized. *Magnetic rays* (MR's) are open field lines by which particles can escape from the Sun. *Diverging fields* (DF's) occur over active regions, either because of a real excess of photospheric field of one polarity or because the photospheric field observations are not sufficiently accurate. Changes in the region during the two week period when it is observed could also contribute to an erroneous excess of photospheric field. *Magnetic arcades* are series of loops which form a corridor. MA's, which indicate a boundary between two rather extended regions of opposite polarity, correlate with streamers. (Altschuler and Newkirk did not distinguish between AR streamers and helmets in their paper.) In this paper we will consider the magnetic configurations in which type III bursts occur. Similar studies have already been reported for type II bursts (Dulk *et al.*, 1971) and for type IV bursts (Dulk and Altschuler, 1971).

2. Observations

Observations of the east-west positions of type III radio bursts were made between 20 and 65 MHz with the log-periodic array at Clark Lake Radio Observatory (Erickson and Kuiper, 1973). These positions were corrected for ionospheric refraction (Kuiper, 1973a, b). In many instances the radio data alone are sufficient to locate the active region (e.g. Kuiper, 1973b) even though we lack resolution in the north-south direction. In this paper, however, the occasional coincidences between type III's and flares are used to identify the active regions. It is then shown that the positions of the other bursts are consistent with these regions.

Figure 1 shows the east-west positions at 60 MHz of type III bursts observed in March and April of 1971 plotted as a function of the date. In cases when the data were of sufficient quality to correct for ionospheric refraction, only these corrected positions are shown. One can see discrete regions of type III activity co-rotating with the Sun. Also shown are the loci of points radially above the active regions, which are identified in the figure by the last three digits of their McMath number. These regions, with the exception of McMath 11249 and 11250, were chosen because they showed H α activity coincident with type III bursts. Regions 11249 and 11250 were also plotted since the positions of bursts suggested these regions might be responsible. For the regions represented by solid lines, a height of $0.6 R_{\odot}$ was assumed, corresponding to the apparent height of type III bursts at 60 MHz (Kuiper, 1973a, b). For the regions identified with dashed lines, a height of $1.0 R_{\odot}$ was assumed. It is seen that the positions of the bursts are consistent with locations above the active regions.

3. The Association of Type III Bursts with H α Activity

One five days Big Bear Solar Observatory covered the regions on the Sun above

which type III bursts appeared to occur. Big Bear films were examined for the period 3 March–4 April. In Table I are listed all those bursts or groups of bursts which occurred during times when Big Bear had $H\alpha$ data. Below are given a description of $H\alpha$ and radio burst activity which showed association with each other. Such a description cannot however substitute for an actual viewing of the films.

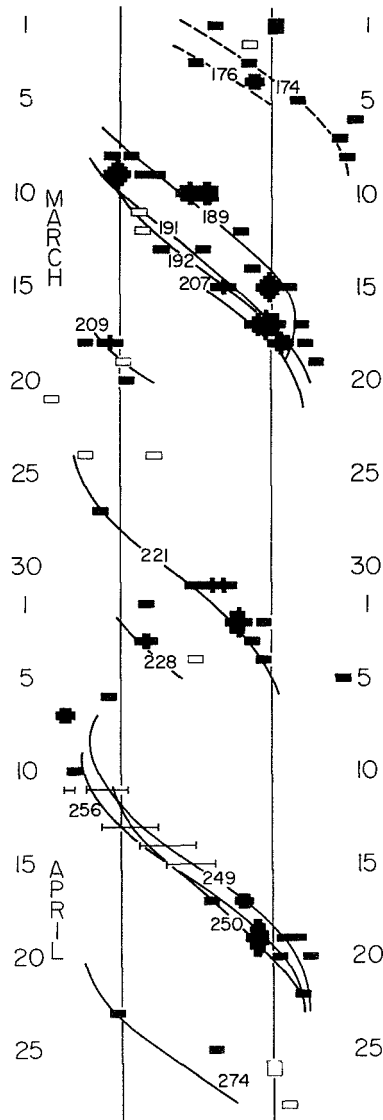


Fig. 1. Positions of type III radio bursts as a function of solar rotation. Positions corrected for ionospheric refraction are shown as solid blocks, those not corrected as open. The size of the block represents the number of groups measured. The approximate positions of continuum storms are shown by error bars. The loci of points 0.6 (solid lines) and 1.0 (broken lines) solar radii above certain active regions, identified in Table II, are also shown.

9 March. At 19:48:30 two bright features formed on either side of a dark fibril connecting the major sunspot with a newly emerging spot. The features brightened and moved in opposite directions, one towards the main spot, the other to the new spot. At approximately the time when the brightenings reached the two spots, a series of type III bursts occurred.

18 March. At 18:09 there occurred a type III burst whose position line coincided with the west limb of the Sun. At about this time a very small faint flare occurred near a region of emerging flux which followed the main spot in McMath 11207.

From 19:47:00 to 19:48:30, from 19:50:10 to 19:50:45, and from 19:53:00 to 19:53:20 there occurred groups of type III bursts with position lines on the east limb of the Sun. Very small H α events, possibly surges, were seen at these times in McMath 209. The frames in which they were most apparent were taken at 19:48:15, 19:51:03 and 19:53:48, respectively.

At 20:19 a small bright bridge was seen to connect two plage regions southeast of the spot in 207. A type III burst occurred on the west limb at 20:19:55. Another group of type III's occurred from 20:33:05 to 20:33:20. At 20:36 a small bright bridge in a different position connected the two plages.

At 21:35:25 a sequence of faint type III bursts started near the east limb of the Sun coincident with the start of a small flare near the EFR in McMath 207 (near the Sun's west limb) which reached its maximum at 21:36:25 and had subsided two minutes later. Another type III burst occurred at the east limb at 21:37. This is one of the rare instances of simultaneous activity at two very well separated locations on the Sun. It is not possible to say whether there is a genuine association between these events.

At 23:28 a group of III's occurred a half solar radius beyond the west limb with another burst at 23:29. At this time Big Bear was patrolling McMath 207 but poor seeing and transparency made a close study of the H α phenomena impossible.

20 March. A group of type III's occurred between 20:14:30 and 20:16:40 near the east limb of the Sun. At 20:19:25 a brightening became visible along a long thin plage, reaching a maximum at 20:21:02.

2 April. It is difficult to make a clear case for detailed association of activity between type III bursts and the H α activity for this day. During our period of observation a filament immediately west of the region was continuously active. Tlamicha and Takakura (1963) have suggested a possible association between type III bursts and active dark filaments. In addition, there were two subflares in the region which may have had associated type III bursts.

At 19:09 a subflare began east of the NW spot. The activity continued to be visible until 19:23. A group of strong type III bursts occurred from 19:16:15 to 19:20:45. Another type III burst occurred at 19:23:25.

At 20:05:10 on-band H α coverage was resumed following a wavelength scan. This appeared to coincide with the start of a flare at the end of the filament nearest the sunspots. At this time also a group of type III bursts occurred, lasting from 20:05:07 to 20:07:30. The most active phase of this H α event ended at 20:25.

TABLE I
Association of type III events with activity in BBSO patrol films

| Date/UT | Burst position | Suspected region | SGD flare data | | BBSO patrol | |
|--------------|-------------------|------------------|----------------|-----------|-------------|----------|
| | | | Region | Times | Region | Activity |
| 3 Mar. 1938 | 0 | 176 | | | 173 | |
| 1943 | 0.7 | 174 | 174 | 1943–2004 | 173 | |
| 6 Mar. 2259 | 2.1 | ? | | | 174 | |
| 9 Mar. 1956 | –1.1 | 191 or 192 | | | 191 | yes |
| 2253 | –0.6 | 189 | | | 191 | |
| 10 Mar. 1751 | 0 | 189 | | | 191 | |
| 1955 | 0.2 | 189 | 189 | 1951–2005 | 191 | |
| 2014 | 0.1 | 189 | | | 191 | |
| 12 Mar. 2014 | –0.7 ^a | 191 or 192 | | | 191 | |
| 14 Mar. 2016 | 0.7 | 189 | | | 195 | |
| 15 Mar. 1945 | 0.7 ^a | ? | | | 196 | |
| 2006 | 0.4 ^a | 191/192/207 | | | 196 | |
| 2016 | 0.6 ^a | ? | | | 196 | |
| 2019 | 0.9 | 189 | | | 196 | |
| 2026 | 0.6 ^a | ? | | | 196 | |
| 2038 | 0.5 ^a | ? | | | 196 | |
| 2052 | 1.2 | 189 | | | 196 | |
| 2202 | 1.0 | 189 | | | 196 | |
| 2220 | 1.0 | 189 | 192 | 2117–2222 | 196 | |
| 2230 | 0.4 | 191/192/207 | | | 196 | |
| 17 Mar. 2133 | 1.1 | 191/192/207 | | | 196 | |
| 2142 | 0.7 ^a | ? | | | 196 | |
| 2208 | 0.9 | 191/192/207 | | | 196 | |
| 18 Mar. 1809 | 1.2 | 191/192/207 | | | 207 | yes |
| 1948 | –1.0 | 209 | | | 209 | yes |
| 1950 | –1.2 | 209 | | | 209 | yes |
| 1953 | –1.5 | 209 | | | 209 | yes |
| 2020 | 1.4 | 191/192/207 | | | 207 | yes |
| 2033 | 1.1 | 191/192/207 | | | 207 | yes |
| 2135 | –1.0 ^a | 209 | | | 207 | yes |
| 2137 | –0.9 ^a | 209 | | | 207 | yes |
| 2328 | 1.6 | 191/192/207 | | | 207 | |
| 2334 | –1.1 | 209 | | | 207 | |
| 20 Mar. 2015 | –0.9 | 209 | | | 209 | yes |
| 21 Mar. 1644 | 2.3 ^a | ? | | | 209 | |
| 1 Apr. 1916 | –0.3 ^a | 221 | 221 | 1847–1941 | west limb | |
| 2 Apr. 1734 | 0.5 | 221 | | | 221 | yes |
| 1736 | 0.5 | 221 | | | 221 | yes |
| 1800 | 0.5 | 221 | 221 | 1758–1810 | 221 | yes |
| 1833 | 0.6 | 221 | 221 | 1829–1849 | 221 | yes |
| 1904 | 0.8 | 221 | 221 | 1907–1956 | 221 | yes |
| 1919 | 0.7 | 221 | 221 | 1910–1938 | 221 | yes |
| 1923 | 0.7 | 221 | 221 | 1919–1930 | 221 | yes |
| 1950 | 1.3 ^a | 221 | | | 221 | yes |
| 2002 | 0.7 | 221 | | | 221 | yes |
| 2006 | 0.8 | 221 | 221 | 2015–2022 | 221 | yes |
| 3 Apr. 1925 | 0.8 | 221 | | | 221 | yes |
| 1938 | –0.6 | 228 | 228 | 1937–1946 | 221 | |
| 4 Apr. 1900 | 0 ^a | ? | | | 221 | yes |
| 1908 | 0.9 | 221 | 228 | 1900–1919 | 221 | yes |

^a Not corrected for refraction.

3 April. During the period of Big Bear's patrol McMath 221 was very quiet. A group of type III bursts occurred from 19:24:18 to 19:25:35. At about this time there was a fast faint subflare running in a thin line north of the SE spot. Because of poor seeing, it was not possible to time it precisely, but its most visible phase occurred at 19:27:32.

4 April. During this day McMath 221 was again very active. The filament, which had been almost non-existent the previous day, was even more substantial this day than it had been on April 2. The activity in this filament was very violent on this day. It was not possible to associate the radio bursts with any specific events. The most interesting thing about the radio burst activity on this day was its mildness considering the activity visible in H α .

We see that type III bursts can be attributed to specific active regions, not only in the sense that the bursts originate over these regions as was shown in the previous section, but in that bursts are associated with H α events in these regions. H α activity was seen in all of the 21 bursts or groups of bursts which occurred over active regions patrolled by Big Bear Solar Observatory. In twelve cases specific H α events could be identified as being associated with the bursts on the basis of temporal coincidence. In one additional instance (20:15, 20 March) the timing is less convincing. For eight radio events the H α phenomenology was too complicated to make such an association.

Although further study is in progress on the detailed association of type III bursts with H α phenomena, it appears that the following assertion can be made on the strength of these results and those of Paper I: Nearly all (>95%) type III bursts or groups of bursts with fluxes in excess of about $5 \times 10^{-22} \text{ W m}^{-2} \text{ Hz}^{-1}$ occurring in isolation of other radio activity and not in extended storms of type III bursts are associated with activity in H α .

We find that the distinction suggested by Loughhead *et al.* (1957) between active regions which have type III bursts and those which do not is real. McMath 11196 was a particularly active region which showed no type III activity. McMath 11221 had days when it showed type III activity and days when it showed little or none, in spite of flare activity. In the next section this will be related to the large-scale coronal magnetic field associated with the region.

4. The Coronal Magnetic Field in Regions of Type III Activity

In Figure 2 the plage drawings (*Solar Geophysical Data*, 1971a) and calculated coronal fields (Altschuler, private communication, 1972) are shown for the regions which were associated exclusively with isolated type III activity. In each instance the field is either diverging or, in the cases of the more active of the regions, open. It would appear, therefore, that type III bursts occur in regions of open or at least diverging field, rather than coronal streamers, which are associated with magnetic arcades. In order to confirm the occurrence of open field lines the records of RAE-1, which recorded radio emissions above the ionosphere in the frequency range 0.2–5 MHz, were examined. By the coincidence of type III bursts measured at Clark Lake

with those measured in interplanetary space by the satellite, it was seen that energetic particles escaped each of the active regions, with the exception of McMath 165 for which there was sufficient data.

A particularly active region which did not show any type III activity was McMath 11196. This region is represented in Figure 3. It is seen that the calculated coronal

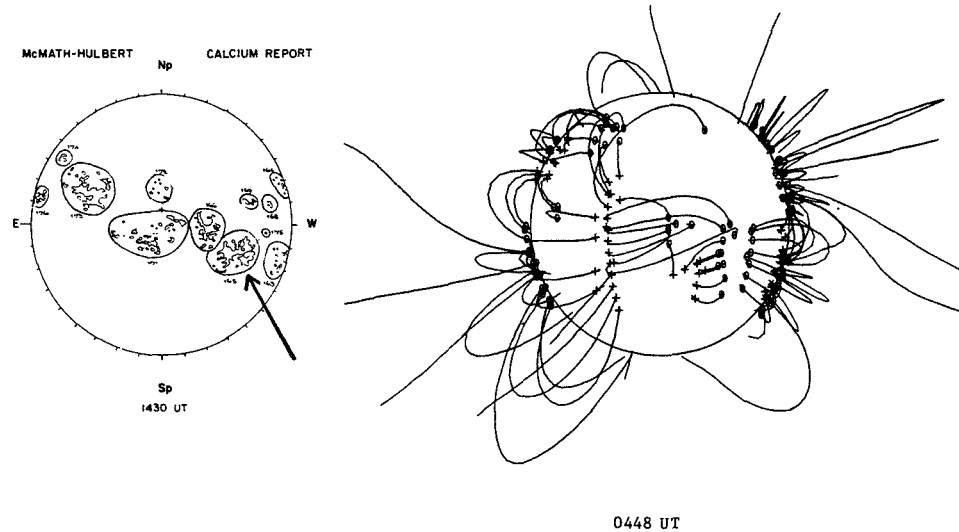


Fig. 2a. Plage drawings and calculated coronal fields for 26 February, 1971; active region McMath 11165.

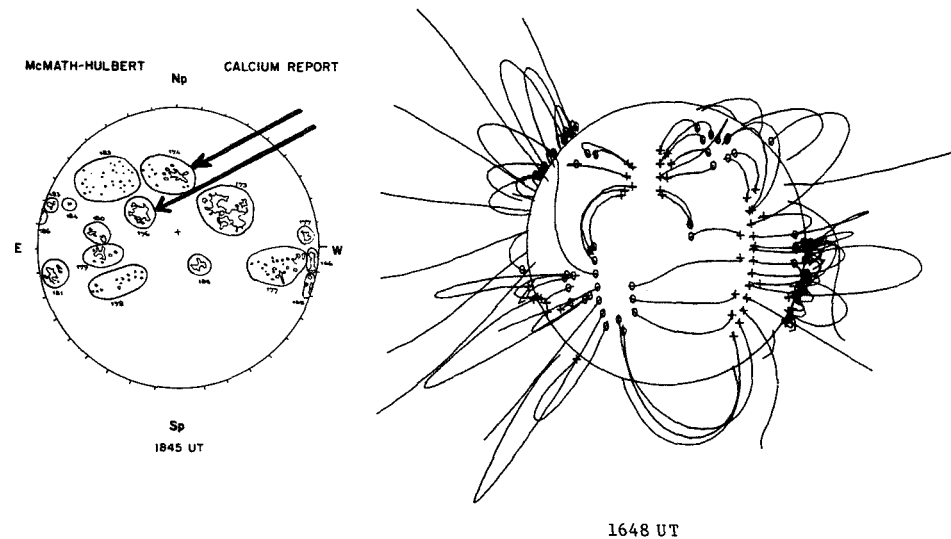


Fig. 2b. Plage drawings and calculated coronal fields for 2 March, 1971; active regions McMath 11174 and 11176.

field is characterized by a tightly closed structure, known as LMA (Low Magnetic Arcade), a feature which is associated with streamers. A filament did occur adjacent to this region, aligned more or less in the direction of the LMA. There were no type III bursts in this region, in spite of all the flare activity so that it would appear that the magnetic configuration was unfavorable.

The behavior of McMath 221 may shed further light on the relationship of the coronal field to type III activity. This region appeared on the east limb on March 25, and was relatively quiet with one reported flare during the Clark Lake observing period on the 26th, and three more flares and two type III groups on the 27th. A large filament was looped around the north of this region. The low level of activity continued on the 28th. On March 29, however, this region was extremely active. Six

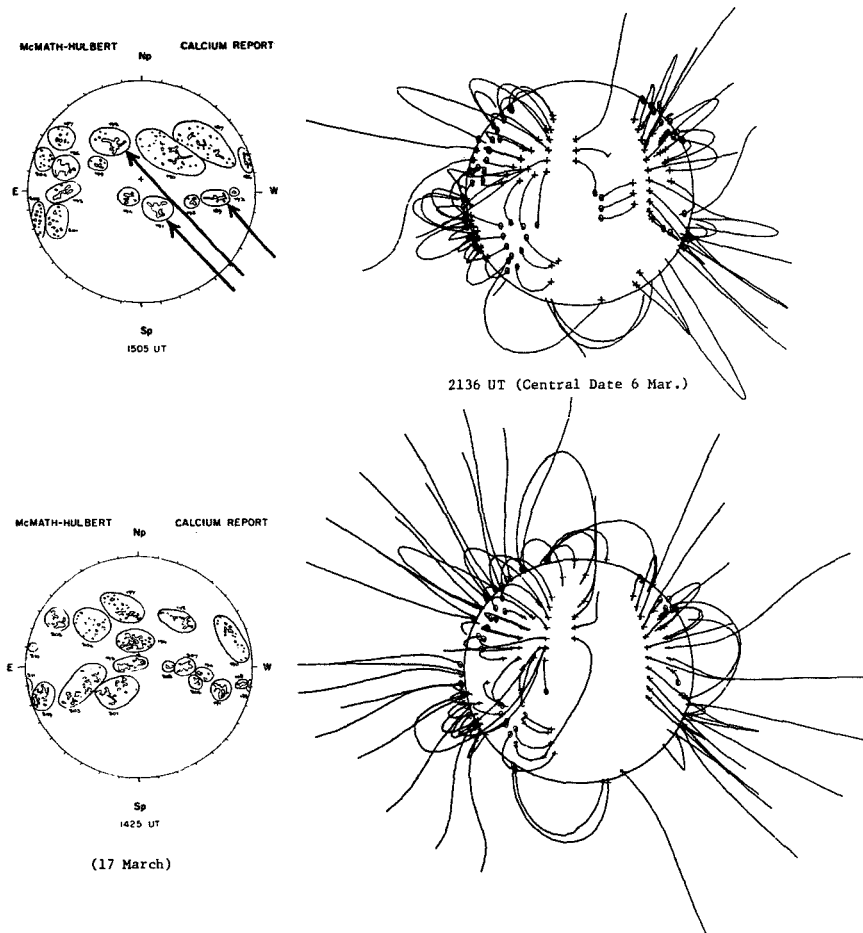


Fig. 2c. Plage drawings for 14 March (upper left) and 17 March (lower left) and calculated coronal fields for 14 March for observations having central dates of 6 March (upper right) and 20 March (lower right); active regions McMath 11189, 191, 192 and 207. Note the emergence of 207 and associated regions between 14 and 17 March.

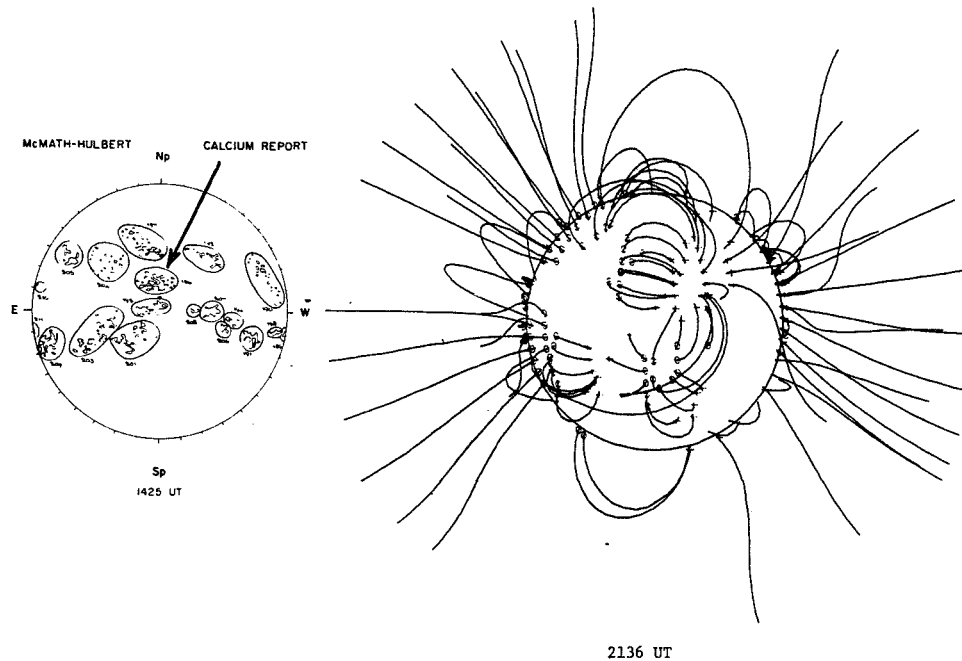


Fig. 3. Plage drawings and calculated coronal fields for 17 March, 1971, showing McMath 11196, an active plage which did not exhibit type III radio bursts.

flares were reported during Clark Lake's normal observing period. The Big Bear $H\alpha$ patrol of this region showed the filament to be highly agitated. Although Clark Lake did not observe this day, other observatories reported no radio activity. On March 30 the filament disappeared. Although three flares were reported, only one extremely faint group was observed at 19:14. The group was too weak to get a reliable position measurement, but it appears to have occurred on the western half of the Sun, away from 221. Lack of any activity in 221 at this time also suggests the burst was not related to this region.

On March 31 six flares were reported. Eleven type III groups occurred, at least eight of which were positionally related to McMath 221. Three of these were coincident with the published flares. On April 1 six flares were reported in this region, but no radio bursts occurred there. By this time a new small filament had formed, running westward from the center of the plage. April 2 was extremely active. The Big Bear patrol shows almost continuous activity, both flares and turbulence in the new filament, accompanied by strong type III activity. On April 3 the region was quiet. The filament which ran west and then north from the plage was barely visible. The only group of type III bursts from this region during Big Bear's patrol period was visible in $H\alpha$. On April 4 the region was extremely active again in $H\alpha$, but relatively quiet in the radio. The filament had grown in importance and was more prominent than it had been on April 2. It was also extremely active. The region

thereafter remained relatively quiet in the radio until its disappearance over the west limits after April 6.

It would appear from the behavior of the filaments, that the field underwent significant changes during the period 27 March–4 April. The calculated coronal field using photospheric data for the rotation having a central date of 20 March is significantly different from the field calculated from data with a central date of 2 April, also indicating that there were changes in the coronal field. This was accompanied by considerable flare activity. Type III bursts, however, were prevented until the field configuration associated with the large filament which existed before April 30 was destroyed. On and after April 4, when a new filament was established in the region, radio burst activity was again inhibited.

5. Conclusion

The positions of type III radio bursts occurring between approx 16:00 and 24:00 UT from 1 March to 5 April, 1971, were determined and corrected for ionospheric refraction wherever possible. It was found that these bursts occurred over active regions whose calculated potential coronal fields were characteristically diverging and generally open. This magnetic field of configuration is not characteristic of streamers. In observations at Culgoora, Dulk (private communication, 1972) has also found that the bursts occur in regions of open field, with or without a streamer nearby. It appears, therefore, that type III bursts need not occur preferentially in streamers, as was first suggested by Wild *et al.* (1959) on the basis of the heights of the bursts.

The type III radio bursts were intimately related to activity in H α . Out of 21 cases for which Big Bear Solar Observatory had coverage of the region responsible for the bursts, H α activity was seen in each instance. In 12 cases the activity was either brief or began at the time of the burst, suggesting that the two phenomena were related. One case was uncertain. In the other eight cases there was continuous and complex activity so that no such identification could be made. A similar result was obtained in the detailed analyses of other periods of activity (Zirin and Werner, 1967; Paper I). It is suggested that almost all, if not all, isolated type III bursts have associated activity in H α .

The H α phenomena associated with type III bursts are not always flares. Martres *et al.* (1972) have shown that in some instances the associated phenomena are seen as small transient absorbing features. In other cases disturbances in filaments seem to be related to type III bursts (Tlamicha and Takakura, 1963; this paper).

The existence of a stable filament in a region represents an unfavorable magnetic field configuration for type III bursts. Active filaments, however, indicate that the field is changing. During this time particles may escape to cause type III bursts. Tlamicha and Takakura (1963) have also noted an association between type III bursts and active filaments. The confinement of fast particles is not in any sense absolute. Some type III activity was seen on March 27 and April 4. Similarly, when a region is open, not all flares yield radio bursts (e.g. Zirin and Werner, 1967; also Paper I).

In all likelihood confinement by small-scale magnetic structures near the chromosphere is also important (e.g. Lazareff and Zirin, 1973).

The type III bursts on which this work is based occurred in isolation of any other radio activity or of flares greater than subflares. For bursts of this kind the following interpretation is believed to be consistent with the observations. Isolated type III bursts or groups of bursts are generally associated with active regions in early stages of development. These regions are characterized by an open field. The acceleration occurs low in the corona or in the chromosphere, since all the bursts have associated H α activity. As the region develops the magnetic field configuration closes, inhibiting the escape of these particles. Only when a major reorganization of the field occurs will paths be temporarily opened for particles to escape.

Acknowledgments

I would like to acknowledge discussions with, suggestions from, and criticisms by M. D. Altschuler, William C. Erickson, T. E. Gergely, R. T. Hansen, M. R. Kundu, J. M. Pasachoff, E. V. P. Smith, R. G. Stone, and H. Zirin. I am particularly grateful to Big Bear Solar Observatory for access to the H α patrol films, to the High Altitude Observatory for coronal potential field maps, and the Radio Astronomy Section at Goddard Space Flight Center for use of the Radio Astronomy Explorer-I data. My thanks go also to J. Pressman and N. Roth who reduced the Clark Lake radio data. Clark Lake Radio Observatory is supported by National Science Foundation grant NSF GP 19411 and National Aeronautics and Space Administration grant NGR 21-002-367. The photospheric magnetic field measurements used to compute the coronal maps were made by R. Howard of the Hale Observatories with the support of the Office of Naval Research.

References

- Altschuler, Martin D. and Gordon Newkirk, Jr.: 1969, *Solar Phys.* **9**, 131.
 Axisa, F., Avignon, Y., Martres, M. J., Pick M., and Simon, P.: 1971, *Solar Phys.* **19**, 110.
 Billings, Donald E.: 1966, *A Guide to the Solar Corona*, Academic Press, New York.
 Carmichael, Hugh: 1964, in W. N. Hess (ed.), *AAS-NASA Symposium on the Physics of Solar Flares*, NASA, Washington, p. 451.
 Dulk, G. A. and Altschuler, M. D.: 1971, *Solar Phys.* **20**, 438.
 Dulk, G. A., Altschuler, M. D., and Smerd, S. F.: 1971, *Astrophys. Lett.* **8**, 235.
 Erickson, W. C.: 1963, *J. Geophys. Res.* **68**, 3169.
 Erickson, W. C. and Kuiper, T. B. H.: 1973, *Radio Science* **8**, 845.
 Kuiper, T. B. H.: 1973a, in R. Ramaty and R. G. Stone (eds.), *High Energy Phenomena on the Sun*, Symposium Proceedings, NASA, Washington, p. 540.
 Kuiper, T. B. H.: 1973b, Thesis, University of Maryland.
 Kuiper, T. B. H. and Pasachoff, Jay: 1973, *Solar Phys.* **28**, 187.
 Lazareff, B. and Zirin, H.: 1973, Big Bear Solar Observatory preprint, No. 0130.
 Loughhead, R. E., Roberts, J. A., and McCabe, Marie K.: 1957, *Australian J. Phys.* **10**, 483.
 Malville, J. M.: 1961, Thesis, University of Colorado.
 Martres, M. J., Pick, M., Soru-Escut, I., and Axisa, F.: 1972, *Nature Phys. Sci.* **236**, 25.
 McLean, D. J.: 1970, *Proc. Astron. Soc. Aust.* **1**, 315.
 Newkirk, Gordon J., Jr.: 1959, Paris Symposium on Radio Astronomy, (ed. by R. N. Bracewell), Stanford.

- Newkirk, Gordon J., Jr.: 1967, *ARAA* **5**, 213.
Newkirk, Gordon Jr. and Altschuler, Martin D.: 1970: *Solar Phys.* **13**, 131.
Riddle, A. C.: 1972, *Proc. Astron. Soc. Aust.* **2**, 148.
Solar Geophysical Data: 1971a, No. 321 Part I, 33–63.
Solar Geophysical Data: 1971b, No. 325 Part II, 5–22.
Solar Geophysical Data: 1971c, No. 326 Part II, 4–31.
Sturrock, P. A. and Smith, Sheldon M.: 1968, *Solar Phys.* **5**, 87.
Swarup, G., Stone, P. H., and Maxwell, A.: 1960, *Astrophys J.* **131**, 725.
Tlamicha, A. and Takakura, T.: 1963, *Nature* **200**, 999.
Weiss, A. A.: 1963, *Australian J. Phys.* **16**, 2401.
Wild, J. P. and Smerd, S. F.: 1972, *ARAA* **10**, 159.
Wild, J. P., Sheridan, K. V., and Neylan, A. A.: 1959, *Australian J. Phys.* **12**, 369.
Zirin, Harold and Werner, Susan: 1967, *Solar Phys.* **1**, 66.

CORONAL DENSITY STRUCTURES IN REGIONS OF TYPE III ACTIVITY

Y. LEBLANC

Observatoire de Meudon, Meudon, France

T. B. H. KUIPER*

Clark Lake Radio Observatory, University of Maryland, College Park, Md., U.S.A.

and

S. F. HANSEN

High Altitude Observatory, Boulder, Colo., U.S.A.

(Received 22 February; in revised form 17 April, 1974)

Abstract. The Mauna Loa K-corona data were examined to determine the density in regions of type III activity which were observed during March and April, 1971, at Clark Lake Radio Observatory. It is found that these regions avoided the centres of dense structures in the corona. Both the K-corona data and the radio data indicated densities characteristic of the 'quiet' corona. The density gradients determined from the K-corona and the radio data agreed to within their formal errors.

1. Introduction

It is generally accepted that type III burst excitors travel along neutral sheets in the coronal field, which correspond to the densest parts of streamers (e.g., Wild and Smerd, 1972; McLean, 1970; Sturrock, 1972). Smith and Pneuman (1972), in a theoretical study, point out that the particles responsible for type III bursts cannot travel in the densest part of a coronal streamer due to the transverse magnetic field in the neutral sheet. Some evidence has been presented that not all type III excitors travel at or near the centre of streamers (Kai and Sheridan, 1974; Kuiper, 1973a). In this paper, we present further evidence supporting the latter point of view.

Recently, Kuiper (1973a) analyzed isolated type III bursts observed at Clark Lake Radio Observatory during March and April 1971. By noting the day of transit of the region and comparing the east-west position of the burst at the limb passages, it was possible to deduce the longitude and latitude of the region (see Kuiper, 1973c, Ch. V). It was shown that the bursts occurred in discrete regions corotating with the Sun. By the temporal association of type III bursts with H α activity, the active regions generating the type III excitors were identified and it was shown that the type III burst regions occurred, on the average, radially above these active regions which are identified. On the basis of the computed coronal potential field and the presence or absence of dark filaments in the plages, it was argued that the bursts occurred only when the field was open, or diverging whereas an arcade-like closed structure, which is often associated with the lower part of a streamer, is unfavourable for the escape

* Current address: Jet Propulsion Laboratory, California Institute of Technology, Pasadena, Calif., U.S.A.

of the exciters. In this paper, we examine the density of the corona over these active regions. We have used the same radio data, together with the daily white light coronal observations obtained with the High Altitude Observatory K-coronameter at Mauna Loa, Hawaii. The intensity profiles and the synoptic maps derived from the K-corona data allow us to distinguish between dense structures and low intensity regions. A deconvolution technique developed by Leblanc *et al.* (1970) is applied to calculate the electron density of these structures. For the low intensity regions, van de Hulst's (1950) method has been used to compute the electron density of models.

2. The Density in the Regions of Type III Activity

The K-coronameter measures the scattered light by making concentric small-aperture scans around the Sun at selected heights above the limb. In 1971, the heights of the observations were 3'.6, 5', 9'.1, and 13'.1. As the electron density is closely related to the intensity of the scattered light we were able, by means of isophotal maps at each height and day to day intensity profiles, to distinguish between dense coronal structures and low intensity regions.

In Table I, we give the central meridian passage (CMP) of each active region above which isolated type III bursts occurred, its limb passages (as the K-corona observations are made at the limb), and the K-corona feature at that position. The identification is generally made at the limb passage of the region, as shown in Figure 1. In a

TABLE I
Active regions above which isolated type III bursts occurred (March–April 1971)

| McMath region | CMP | Latitudinal position | East limb passage | K-corona feature | West limb passage | K-corona feature |
|---------------|-----------------------|----------------------|-------------------------|------------------|-------------------------|------------------|
| 11174 | 2 March | 24°–26°N | 22 February | EDS | 9 March | EDS |
| 11176 | 3–4 March | 7°–8°N | 24 February | LDR | 10 March | LDR |
| 11189 | 10–11 March | 8°–10°S | 3–4 March | LDR | 17 March | LDR |
| 11191 | 13 March | 16°–17°S | 6 March | (LDR) | 19 March | LDR |
| 11192 | 15 March | 18°–20°N | 8 March | EDS | 22 March | no obs. (EDS) |
| 11207 | appears on 16th March | 6°S | – | – | 22 March | no obs. |
| 11209 | 22 March | 15°–20°S | 15 March | EDS | 23 March | no obs. (EDS) |
| 11221 | 31 March | 16°–18°S | 24 March | LDR | 6 April (and 10 March) | no obs. (EDS) |
| 11249 | 16 April | 4°–5°S | 9 April (and 13 March) | LDR | 23 April (and 27 March) | no obs. |
| 11250 | 16–17 April | 4°–5°S | 9 April (and 13 March) | LIS | 23 April (and 27 March) | no obs. |
| 11256 | 18 April | 20°–22°N | 11 April (and 15 March) | LIS | 25 April (and 29 March) | no obs. |

EDS: edge of dense structure.

LDR: low density region.

LIS: low intensity structure.

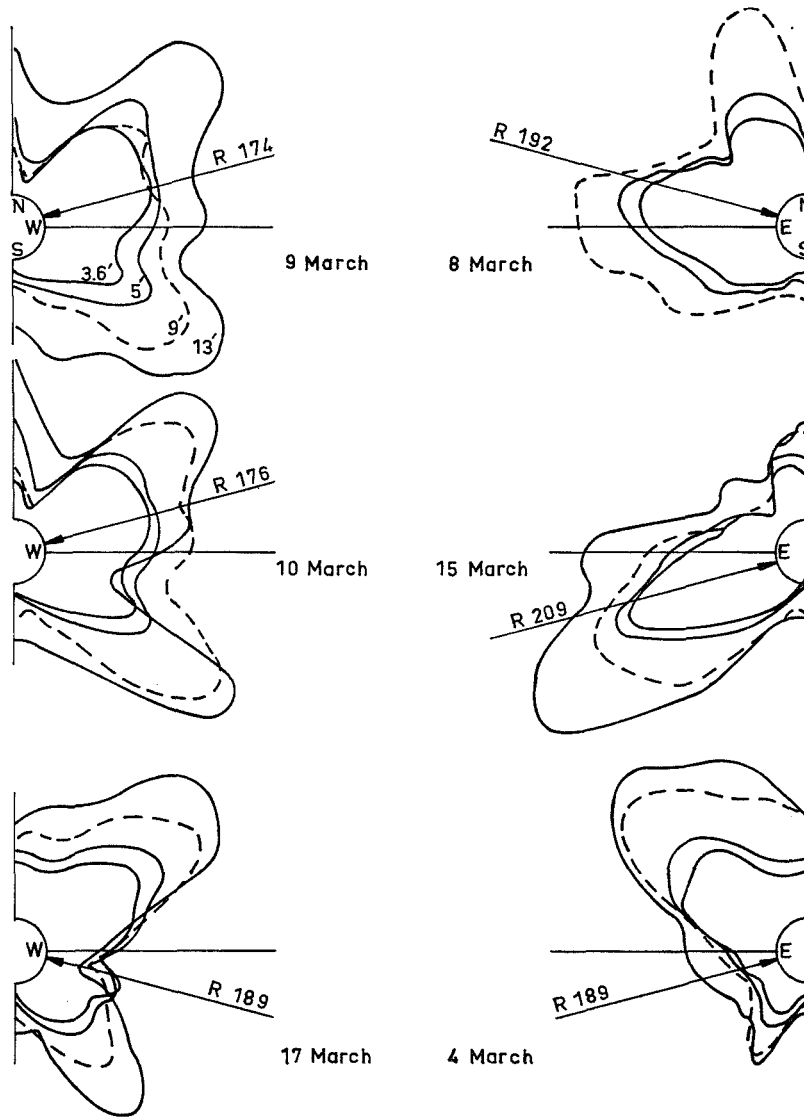


Fig. 1a.

few cases, when no observations were made on the day of limb passage, observations were made for most of these a few days before and after limb passage. In such cases, it was possible to determine the nature of the corona from the synoptic map in Figure 2. It can be seen from Table I and Figures 1 and 2 that most of the active regions (11189, 11176, 11191, 11249, 11221, 11250) associated with emission of isolated type III bursts avoided the coronal high density regions, a few centres (11174, 11192, 11209) appeared adjacent to high density regions, but not any active region associated with type III bursts is on the axis of a large coronal density structure.

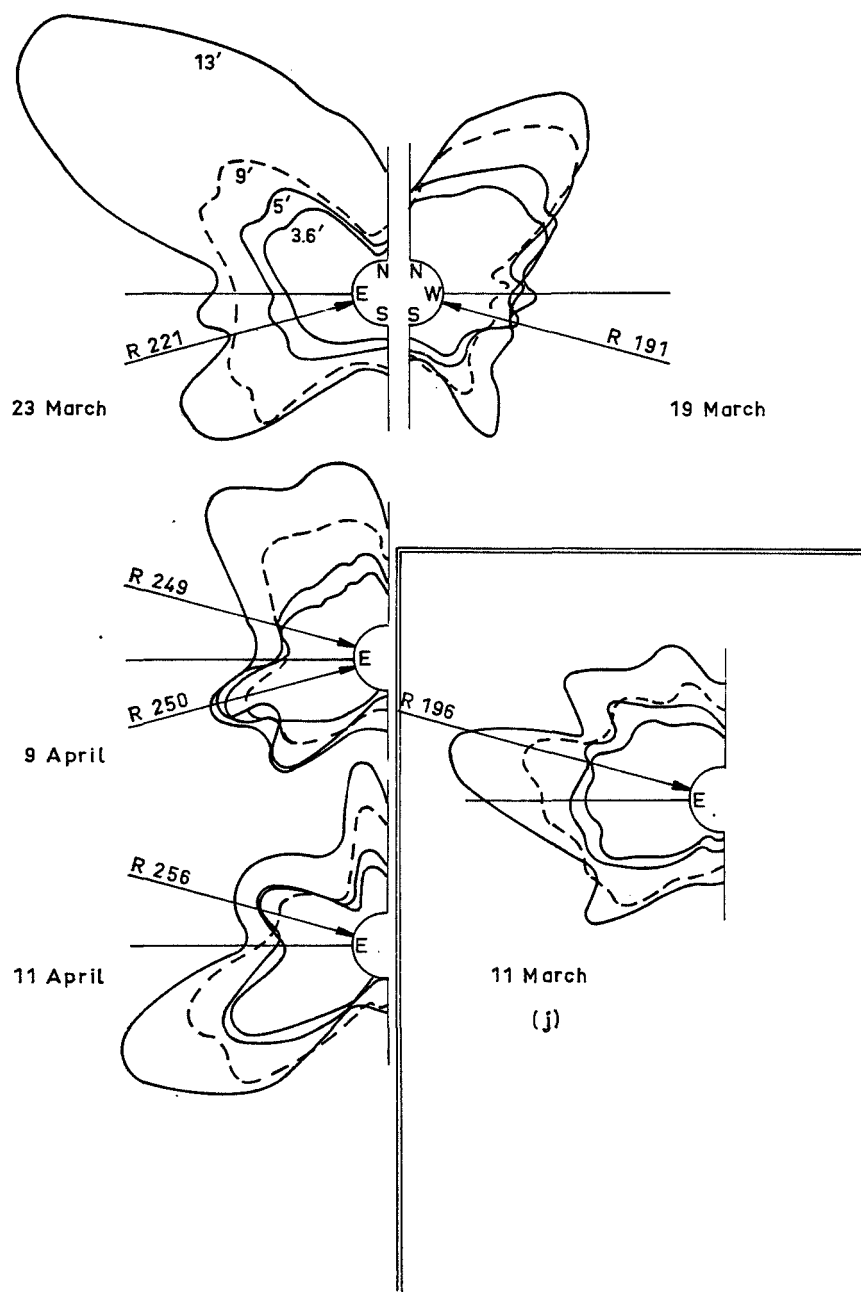


Fig. 1b.

Fig. 1a-b. K-corona observations: Intensity profiles obtained at four heights. The dashed line indicates the intensity at 9' above the limb. The position of the McMath region associated with the solar burst region is shown by an arrow. (j) Region 196 which did not show any type III activity.

It is of interest to consider McMath 196. While it showed considerable H α activity, no type III bursts were associated with this region. On the basis of the closed structure associated with it in the calculated potential field as well as a prominent dark filament, Kuiper (1973a) concluded that this region probably had a closed-over, streamer-like field configuration. We see in Figure 2 that this region is associated with a high density structure.

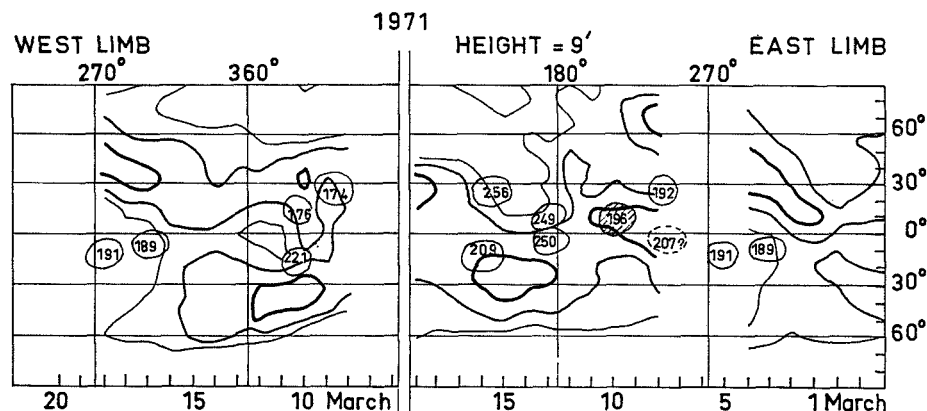


Fig. 2. K-corona observations: synoptic maps. The numbers represent MacMath regions associated with the solar burst regions. The intensity levels are in arbitrary units and represent: — very low; — low; — high intensity.

The average height of the type III bursts gave us a measure of the coronal density. In order to determine the height of the radio bursts, we compared the east-west positions of this activity. All the events occurring in a single region in one day were averaged together. For all the days for which we had such data, it was found that the east-west positions of the bursts at 60 MHz were, on the average, 1.55 ± 0.10 larger than the east-west positions of active regions. As we already pointed out, the regions of type III activity were centered radially above their corresponding active regions. (Note that this statement refers to the centres, and not the individual bursts). Consequently, the apparent height of the type III bursts at 60 MHz was $1.55 R_{\odot}$. When refraction and scattering effects were taken into account (Leblanc, 1973), the true height at 60 MHz was found to be $1.4 R_{\odot}$. By virtue of the observed density gradients (see next section), the height $1.5 R_{\odot}$ corresponds to a type III burst frequency of 50 MHz. Since we do not know in what ratio the observed bursts were fundamental or harmonic emission, we estimate the electron density at $1.5 R_{\odot}$ to be in the range $0.7\text{--}3.0 \times 10^7 \text{ cm}^{-3}$.

These values are less higher than the electron density derived from others radio observations (Wild *et al.*, 1963) which generally favoured a high density model (twice Newkirk's model). The discrepancy between these and our own results may be explained by the fact that scattering effects were not taken into account. It has been demonstrated (Riddle, 1972; Leblanc, 1973) that, due to scattering, the apparent height of type III bursts (fundamental emission) is higher than the real one, and must

TABLE II
Density gradients

| McMath region | $g_R = \beta/\varrho = d(\log N_e)/d\varrho$ ($\varrho = 1.5 R_\odot$) | $g_K = d(\log N_e)/d\varrho$ ($\varrho = 1.5 R_\odot$) | $N_{eK} (\times 10^7 \text{ cm}^{-3})$ |
|------------------|---|--|--|
| 11174 | ? | $\approx 4.5 \pm 1$ | 2.2 and 3.3 |
| 11176 | | | 2.6 |
| 11189 | $\left. \begin{array}{c} 8^{+4}_{-2} \end{array} \right\}$ | $\left. \begin{array}{c} \approx 6.3 \pm 1 \end{array} \right\}$ | 0.8–0.5 |
| 11191 | | | 0.7–1 |
| 11192 | | | 0.8 |
| 11207 | | no obs. | no obs. |
| 11209 | ? | $\approx 4.5 \pm 1$ | 4 |
| 11221 | $3.1^{+0.7}_{-0.5}$ | $\approx 4.1 \pm 1$ | 1.7 |
| 11249 | $\left. \begin{array}{c} 3.6^{+0.5}_{-1} \end{array} \right\}$ | $\left. \begin{array}{c} \approx 5.3 \pm 1 \end{array} \right\}$ | 1.4 |
| 11250 | | | 1.7 |
| 11256 | | | 1.5 |

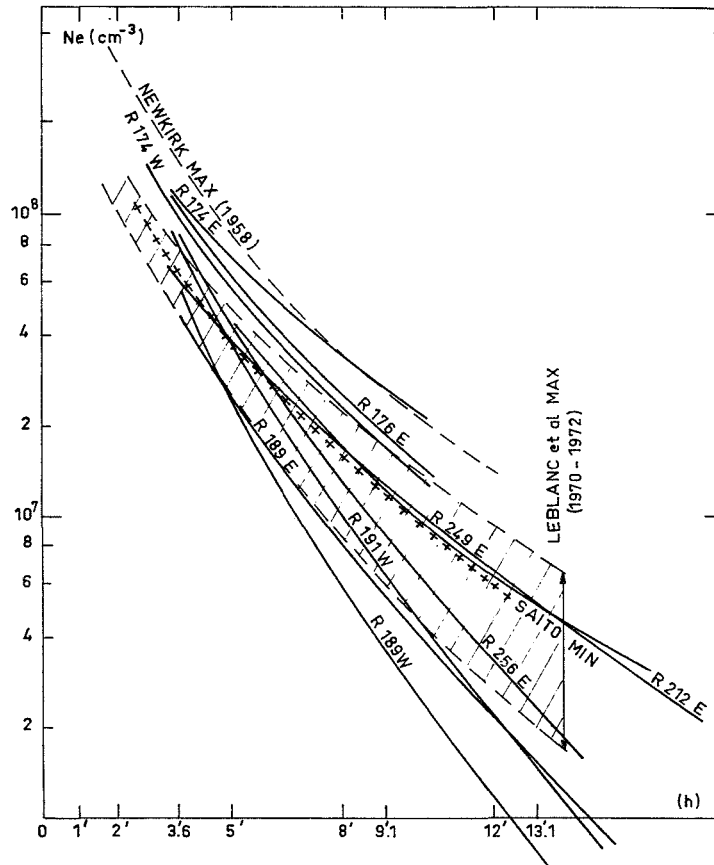


Fig. 3. Calculated electron density models. For comparison, we also give Newkirk's (1967) model for the 1956–1958 solar maximum, Saito's (1970) average model for solar minimum, and the range of values for the quiet corona determined by Leblanc *et al.* (1973) for the 1970–1972 maximum (hatched region).

coincide with that of the harmonic emission; this means that the electron densities derived by assuming an emission at the fundamental frequency will be about four times too large at each level.

In Table II, the densities at $1.5 R_{\odot}$, as determined from the K-corona observations, are given for the corona above the type III-associated active regions. The densities range from 0.7 to $4 \times 10^7 \text{ cm}^{-3}$. Thus, there is quite good agreement between the radio and optical determinations of the density. The results are also consistent with the values determined for the quiet corona at solar maximum obtained by Newkirk (1967) and Leblanc *et al.* (1973):

| | | |
|----------------|----------------|---|
| Newkirk | (1958 maximum) | $3 \times 10^7 \text{ cm}^{-3}$ |
| Leblanc et al. | (1971 maximum) | $0.9\text{--}2.5 \times 10^7 \text{ cm}^{-3}$. |

The coronal density at different heights, as determined from the K-corona scans, is given for the various type III-active regions in Figure 3.

3. The Density Gradients in the Regions of Type III Activity

The density gradient of some regions of type III activity was determined from the radio data by a method described by Kuiper (1973b). The density of the corona was assumed to be of the form $N \sim \varrho^{-\beta}$, where ϱ is the height measured from the centre of the Sun. Not all regions had enough bursts to give a statistically meaningful result. Consequently, it was necessary to group together a number of nearby regions, and even then, only three sets of data gave meaningful results. The results of the analysis are listed in Table II.

In the K-corona analysis, a density model of the form $N \sim \exp(-K/\varrho)$ was assumed. The gradient was determined for five regions, including the three used in the radio analysis. The results are given in Table II.

Because of the different models assumed in the two analyses, a parameter

$$\begin{aligned} g_K &= -d(\log N)/d\varrho = K/\varrho_K^2 \\ g_R &= \beta/\varrho_R \end{aligned}$$

was defined, where ϱ_K and ϱ_R are the mean heights at which the K-corona and radio burst density gradients were determined. The values of g for both analyses can be compared directly in Table II. It is seen that the agreement is reasonably good.

4. Discussion

We have examined the coronal density above active regions which showed type III activity during March and April of 1971. We recapitulate our findings:

(1) The centres of type III activity avoided the regions of high density in the corona, the centres occurring either in regions of low density or, in a few cases, to the side of dense structures. On the other hand, a particularly flare-active region which occurred under a dense structure had no associated type III activity.

(2) The average height of the type III bursts during this period, when corrected for the effects of refraction and scattering, was consistent with the densities derived from the K-corona data, and both were characteristic of the 'quiet' corona at solar maximum.

(3) The density gradients derived from the radio data and the K-corona data agreed to within their observational uncertainties.

We conclude that the observed isolated type burst exciters did not travel in coronal streamers. It is interesting to note that Caroubalos *et al.* (1974) reach the same conclusion to explain the directivity of fundamental and harmonic sources observed during the Stereo experiment (Steinberg and Caroubalos, 1970).

Particularly in view of the theoretical study of Smith and Pneuman (1972), we caution against attaching undue significance to those centres of activity which occurred to the side of dense structure. We have dealt here with the average properties of regions of type III activity, and not individual bursts. The characteristics of individual bursts (position, height, frequency drift) vary significantly among the bursts in a given center (e.g. McLean, 1969, 1970; Palmer and Lin, 1972; Kai and Sheridan, 1974). Also, the bursts at these frequencies are large, possibly due to the effects of scattering. In these instances where the regions of activity occurred to the side of dense structures, we point out merely that they did not occur near the centres of these structures.

Acknowledgements

The authors are indebted to A. Boischot, W. C. Erickson, R. T. Hansen, M. R. Kundu, and J. de la Noë for reading the manuscript and making many helpful suggestions.

Clark Lake Radio Observatory is supported by National Science Foundation grant NSF GP 19411 and National Aeronautics and Space Administration grant NGR 21 002 367. The analysis of the radio burst positions was supported by NASA grant NSG 398 to the Computer Sciences Center of the University of Maryland.

References

- Caroubalos, C., Poquérusse, M., Steinberg, J. L.: 1974, *Astron. Astrophys.*, in press.
- van de Hulst, H. C.: 1950, *Bull. Astron. Inst. Neth.* **11**, 135.
- Kai, K. and Sheridan, K. V.: 1974, in G. Newkirk, Jr. (ed.), 'Coronal Disturbances', *IAU Symp.* **57**, in press.
- Kuiper, T. B. H.: 1973a, *Solar Phys.* **33**, 461.
- Kuiper, T. B. H.: 1973b, in R. Ramaty and R. G. Stone (eds.), *High Energy Phenomena on the Sun, Symposium Proceedings*, NASA (X-694-73-193) Washington, D.C., p. 540.
- Kuiper, T. B. H.: 1973c, Ph. D. dissertation, University of Maryland.
- Leblanc, Y.: 1973, *Astrophys. Letters* **14**, 41.
- Leblanc, Y., Leroy, J. L., and Poulain, J.: 1970, *Astron. Astrophys.* **5**, 391.
- Leblanc, Y., Leroy, J. L., and Pecantet, P.: 1973, *Solar Phys.* **31**, 343.
- McLean, D. J.: 1969, *Proc. Astron. Soc. Aust.* **1**, 188.
- McLean, D. J.: 1970, *Proc. Astron. Soc. Aust.* **1**, 315.
- Newkirk, G.: 1967, *Ann. Rev. Astron. Astrophys.* **5**, 213.
- Palmer, J. D. and Lin, R. P.: 1972, *Proc. Astron. Soc. Aust.* **2**, 213.
- Riddle, A. C.: 1972, *Proc. Astron. Soc. Aust.* **2**, 98.

- Saito, K.: 1970, *Ann. Tokyo Astron. Obs.* **12**, 461.
Smith, D. G. and Pneuman, G. W.: 1972, *Solar Phys.* **25**, 461.
Steinberg, J. L. and Caroubalos, C.: 1970, *Astron. Astrophys.* **9**, 329.
Sturrock, P. A.: 1972, *Solar Phys.* **23**, 438.
Wild, J. P. and Smerd, S. F.: 1972, *Ann. Rev. Astron. Astrophys.* **10**, 159.
Wild, J. P., Smerd, S. F., and Weiss, A. A.: 1963, *Ann. Rev. Astron. Astrophys.* **1**, 291.

19

A DECAMETER TYPE II BURST ASSOCIATED WITH A BEHIND-THE-LIMB FLARE

(Research Note)

TOMAS E. GERGELY* and MUKUL R. KUNDU

Astronomy Program, University of Maryland, College Park, Maryland 20742, U.S.A.

(Received 13 February, 1976)

Abstract. The characteristics of a decameter type II burst associated with a possible behind-the-limb flare are discussed. The burst source had an unusually high velocity. Assuming that the disturbance propagated as an MHD wave, the magnetic field strength at the 40 MHz plasma level is estimated to be 5.6 gauss.

At meter and decameter wavelengths the velocities of type II burst sources usually lie within the range $1000\text{--}2000\text{ km s}^{-1}$ (Kundu, 1965). A small number of type II sources attaining higher velocities have been reported in the literature (Kundu, 1971; Smerd, 1970). We describe here a complex radio event involving a type II source that moved with a higher-than-usual velocity and was associated with a solar proton event. The observations were made with the swept frequency interferometer of the Clark Lake Radio Observatory operated by the University of Maryland. This array consists of sixteen log-periodic antennas, equally spaced on a two mile east-west baseline. The array is swept in frequency over the range 20–65 MHz once per second. This system gives the one-dimensional position and angular size of emissive regions on the Sun nearly simultaneously at all frequencies. The array beam spacing and width are such that only one beam is on the Sun at one time. The angular resolution is about $5'$ at 60 MHz decreasing to $15'$ at 20 MHz. A more detailed description of this instrument was given by Erickson and Kuiper (1973).

The event described here occurred on September 1, 1971. The swept frequency interferometer record has been published elsewhere (Sakurai, 1972). The radio burst was accompanied by copious particle emissions and a host of geomagnetic phenomena. Since no flare was observed during the 15 hours preceding the event, the radio burst was most likely related to a behind-the-limb flare. The region concerned must have been McMath region 11482, which crossed the west limb two days earlier and produced several imp. 2 and 3 flares during its disk passage. It was situated at S12 and about 30° behind the limb at the time of the flare.

An intense microwave burst started at 19:26 U.T. at 10 cm-wavelength. A type II burst was reported by the Fort Davis Radio Observatory starting at

* Present address: Instituto Argentino de Radioastronomia, C.C.5, Villa Elisa, Prov. de Buenos Aires, Argentina.

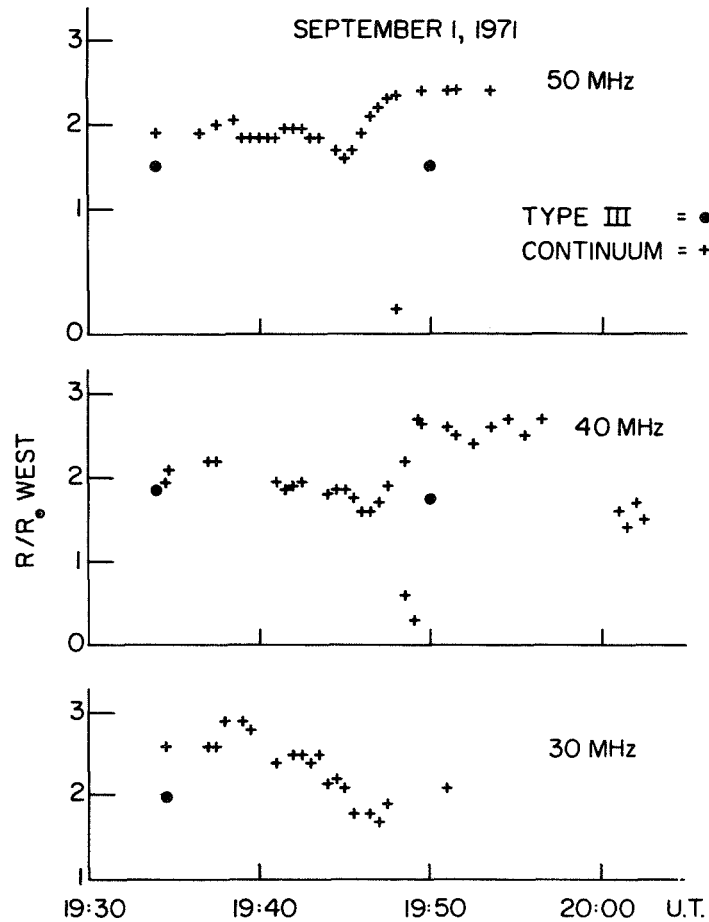


Fig. 1. Positions of the type II-IV continuum and associated type III bursts observed on September 1, 1971, at 50, 40 and 30 MHz. The crosses refer to the continuum emission, filled circles indicate the type III bursts.

19:34 U.T.; it lasted until 19:48 U.T. and was observed to drift from decimeter to decameter wavelengths. The type II was followed by an intense type IV burst.

At the Clark Lake Radio Observatory a moderately intense type III group was observed at 19:34 U.T., followed by an intense continuum emission. The continuum was short lived; at 60 MHz it faded by 19:48 U.T., at 40 MHz the emission lasted longer, until about 20:06 U.T. For a brief period of time, between 19:43 and 19:48 U.T. a second source became visible in the 25–55 MHz range. By comparing the Clark Lake record with the dynamic spectrum obtained by Maxwell (1972), we were able to identify this short lived source as the type II burst observed at Fort Davis. The east-west motion of the source at 50, 40 and 30 MHz is shown in Figure 1. At 50 MHz the type IV source remained stationary until about 19:43 U.T. At this time the type II source appeared. The type IV

source moved due west with an apparent velocity of 1000 km s^{-1} , while the type II moved eastward with an apparent velocity of 3500 km s^{-1} . The motion of the source at 40 MHz was similar to that at 50 MHz. Only the stationary phase of the type IV and the eastward motion of the type II seem to have been observed at 30 MHz. All positions and velocities given for this event are east-west positions and velocities on the plane of the sky.

Several features of the event just described are worth mentioning. The movement of the type II source, from behind the limb to a position close to the disk center obviously precludes the radial propagation hypothesis. The plane of the sky velocity of the type II (see Figure 1) was 3500 km s^{-1} ; due to the position of the flaring region this must have been close to the tangential velocity. The drift rate at 40 MHz was found to be $df/dt = -0.092 \text{ MHz s}^{-1}$. The radial velocity, calculated from the drift rate and the electron density model derived for this region from one-dimensional positions of noise storm radiation (Gergely and Kundu, 1975), turns out to be 1700 km s^{-1} . On the other hand, assuming for the electron density variation a two times Newkirk streamer model (Newkirk, 1961) yields a radial velocity of 850 km s^{-1} . Thus the true velocity of the burst must have been in the range $3600\text{--}3900 \text{ km s}^{-1}$ and was unusually high. The velocity of the associated type IV, although somewhat higher than average, was well within the observed range for this type of events (Smerd and Dulk, 1971; Gergely and Kundu, 1974). Since the motion of the type IV was westward during the entire course of the event (see Figure 1) the type II and type IV sources must have moved along different paths.

The type II discussed here resembles closely the March 30, 1969 event, analyzed in detail by Smerd (1970). In both cases the geometry of the event required that the disturbance responsible for the type II source propagated along curved paths in the corona with extremely high (and similar) velocities. At such high velocities a disturbance propagates through the corona as an MHD wave. Smerd (1970) suggested that the curved path of the MHD wave may result from propagation along the coronal magnetic field. Further, an MHD wave propagating along the magnetic field does so at the Alfvén velocity. This hypothesis enables us to calculate the magnetic field in the corona at the 40 MHz plasma level; it turns out to be 5.6 G. It is interesting to compare this value with the field strength of 7 G that was required at the height of the 40 MHz plasma level by Tidman *et al.* (1966), in order to explain the band splitting frequently observed in type II bursts.

Acknowledgements

Support for this work was provided under NASA grants NGL 21-002-033, NGR 21-002-367 and NSF grant GP-19401. The computer time for this project was supported by the National Aeronautics and Space Administration grant NSG-398 to the Computer Science Center of the University of Maryland. Portions of this paper are based on the thesis research of one of the authors (T. E. G.) in partial

fulfillment of the requirements for the degree of Doctor of Philosophy at the University of Maryland.

References

- Erickson, W. C. and Kuiper, T. B. H.: 1973, *Radioscience*, **8**, 845.
Gergely, T. E. and Kundu, M. R.: 1974, *Solar Phys.* **34**, 433.
Gergely, T. E. and Kundu, M. R.: 1975, *Solar Phys.* **41**, 163.
Kundu, M. R.: 1965, *Solar Radio Astronomy*, New York, Interscience.
Kundu, M. R.: 1971, in C. J. Macris (ed.) *Physics of the Solar Corona*, D. Reidel Publ. Co., Dordrecht, Netherlands, p. 287.
Maxwell, A.: 1972, in World Data Center A, Report UAG-24, Part II, 347, Boulder, Colorado.
Newkirk, G.: 1961, *Astrophys. J.* **133**, 983.
Sakurai, K.: 1972, in World Data Center A, Report UAG-24, Part II, 354, Boulder, Colorado.
Smerd, S. F.: 1970, *Proc. Austr. Soc. Astron.* **1**, 305.
Smerd, S. F. and Dulk, G. A.: 1971, in R. Howard (ed.), 'Solar Magnetic Fields', *IAU Symp.* **43**, 616.
Tidman, D. A., Birmingham, T. J., and Stainer, H. M.: 1966, *Astrophys. J.* **146**, 207.

26.3-MHz radio source survey. I. The absolute flux scale

M. R. Viner*

University of Maryland, College Park, Maryland 20742

(Received 9 October 1974)

The absolute flux densities of Cyg A, Cas A, Tau A, and Vir A have been measured with an accuracy of about $\pm 5\%$ at 26.3 MHz using a method well suited for use at low radio frequencies where ionospheric scintillation is a limiting factor. No evidence for time variations in any of the four sources has been found.

I. INTRODUCTION

THE spectra of radio sources are poorly defined at radio frequencies below 80 MHz, in part due to the lack of a well-defined flux scale on which relative measurements can be based.

The most successful method of absolute flux-density measurement used until now at low frequencies has involved the use of a pair of standard half-wavelength dipoles as a simple interferometer of known collecting area (Bridle 1967; Parker 1968). Because this collecting area is quite small, and the uncertainty in intensity measurements is inversely proportional to the signal-to-noise ratio, accurate flux densities can be determined only for Cyg A and Cas A using such a configuration.

The present measurements use a variation of the method described by Little (1958) to determine the absolute flux densities of Cyg A, Cas A, Tau A, and Vir A with an accuracy of about $\pm 5\%$ at 26.3 MHz, the lowest frequency at which absolute measurements of such accuracy have been obtained.

Since these measurements are critical to models of the low-frequency turnovers in Cyg A and Cas A (Viner 1973), and form the basis for the flux scale of the Clark Lake 26.3-MHz sky survey (Viner and Erickson 1975), full details of the techniques used are given below.

II. METHOD

The method used here is similar to Little's in that a large array is switched against a standard half-wavelength dipole of known collecting area. However, here we measure the intensity of a discrete source simultaneously with the dipole-array configuration and with the array alone. The observed chart deflections are then combined algebraically to determine the flux density of the source as a function of the collecting area of the standard dipole, the noise power of a calibration signal, and cable attenuations.

As shown in Fig. 1, the signals from a calibration dipole and a grating array are combined in the correlation receiver, while the total-power response of the grating array is measured simultaneously in a second receiver. The coaxial hybrid rings B, C, and D are used as signal splitters.

* Present address: Department of Physics, Stirling Hall, Queen's University, Kingston, Ontario, Canada.

The response of the total-power receiver to a radio source of flux density S relative to a calibration signal of noise power P_c per unit bandwidth is

$$R_t = \frac{\frac{1}{2}\alpha_g A_g S/2}{\frac{1}{4}\alpha_1 P_c} = \frac{\alpha_g A_g S}{\alpha_1 P_c}, \quad (1)$$

where α_1 is the cable loss from hybrid port D3 to the noise source, α_g is the cable loss from port D3 to the grating array, and A_g is the total collecting area of the grating array. The factor $S/2$ arises from the fact that only one polarization is detected. Other factors of 2 correspond to signal splitting in the hybrid rings.

Similarly, the response of the correlation receiver to the radio source relative to the calibration signal is

$$R_p = \sqrt{\frac{\frac{1}{2}\alpha_g A_g S/2}{\frac{1}{4}\alpha_1 P_c}} \cdot \sqrt{\frac{\frac{1}{2}\alpha_c A_c S/2}{\frac{1}{4}\alpha_2 P_c}} = \frac{S}{P_c} \sqrt{\frac{\alpha_g A_g \alpha_c A_c}{\alpha_1 \alpha_2}}, \quad (2)$$

where α_2 is the cable and attenuator loss from port B1 to the noise source, α_c is the cable loss from port B1 to the calibration dipole, and A_c is the collecting area of the calibration dipole.

All cable loss figures should include reflection losses (if any) due to impedance mismatches at the hybrids.

Combining Eqs. 1 and 2, we obtain the flux density of the radio source independent of the collecting area (A_g) and the transmission line attenuation (α_1, α_g) of the grating array:

$$S = \frac{\alpha_2 P_c}{\alpha_c A_c} \frac{R_p^2}{R_t}. \quad (3)$$

One advantage of this method is that the grating array provides a very large collecting area but its properties do not enter into the calculation of the absolute flux densities. Whereas a pair of standard dipoles provide just enough collecting area to measure the two strongest sources, this configuration can easily be used to measure absolute flux densities of sources ten times weaker. In addition, the high resolution of the grating array reduces the effects of confusion due to large-scale galactic background radiation and other discrete sources.

The grating array has been described in detail by Erickson (1965). The power pattern of the array

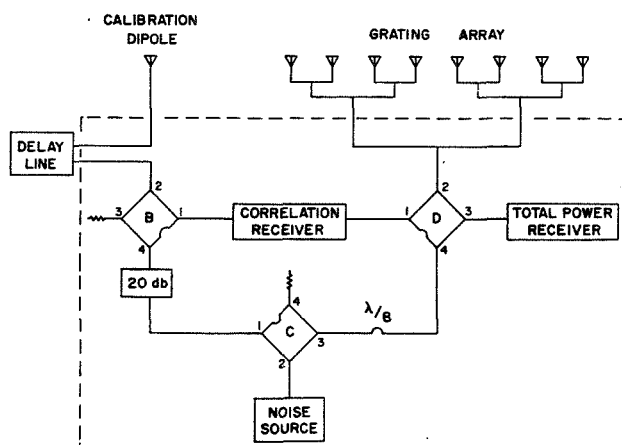


FIG. 1. Block diagram of the equipment configuration used for measuring absolute flux densities. The dashed lines enclose all equipment located within the receiver room.

(10 arcmin \times 3° grating lobes at intervals of 1.5 EW) is illustrated schematically in Fig. 2, which shows the path of a radio source through several grating lobes.

The multiple-response pattern of the grating array constitutes another advantage of this method of measuring absolute flux densities at low radio frequencies with a nonsteerable array. Rather than observing a given radio source only once per night with a precision of ± 15 to 25% (due to ionospheric scintillations), we can make up to 30 independent measurements of the source intensity within an hour or two of transit. This permits us to define the mean intensity of a strong radio source within 5% in a single night. In the measurements reported here, a precision of $\pm 1.5\%$ was obtained for the intensity of each source in 20 to 30 days of observing, at which point about 200 "good" observations had been obtained.

In addition, the capability of observing a radio source many times in the span of a few hours provides a valuable internal check on the degree to which slow ionospheric scintillations have disturbed each day's observations.

A disadvantage of this method is that two dissimilar receivers are used and corrections must be made for any differences in the properties of the receivers and their response to signals from the antennas. The corrections for time constant, bandpass smearing, and partial resolution and their associated uncertainties are discussed further in Sec. VI.

III. EQUIPMENT

A. Antennas

The construction of the calibration dipole is shown in Fig. 3. The dipole and the quarter-wave transformer are made of brass tubing bolted to a phenolic plate for rigid support. The dipole is suspended by fiberglass ropes on a N-S axis above a horizontal ground screen at the electrical center of the grating array. The dipole

was tuned to resonance and matched to the 50- Ω coaxial line with a voltage standing wave ratio (VSWR) better than 1.02 at the center of the receiver bandpass by means of the variable-spacing quarter-wave transformer shown in Fig. 3 and a 4:1 impedance transforming balun. This procedure was repeated each time the height of the dipole above the ground screen was changed. The VSWR at various frequencies in the 150-kHz receiver bandpass was measured several times during the program. The integrated VSWR at the balun was found to be less than 1.10 at all times, corresponding to a maximum reflection loss of 0.007 dB or 0.15%.

During these measurements, impedances were determined by means of a Hewlett-Packard Vector Impedance Meter whose operating frequency was continuously monitored by a frequency counter.

A delay line is required between the calibration dipole and the receiver in order to compensate for the extra transmission line length in the grating array. The required length of delay line was measured electronically with an accuracy of $\pm 0.15 \mu\text{sec}$, corresponding to a maximum signal decorrelation of 0.2% in the bandpass of the correlation receiver.

B. Receivers

The correlation receiver has been fully described by Hubbard and Erickson (1967). It measures the real and imaginary (quadrature) components of the correlated power from two antennas while operating in a closed-loop Ryle-Vonberg mode. The outputs of the receiver are the noise diode currents necessary to generate noise which exactly cancels the correlated signals from the two antennas. The receiver is thus insensitive to amplifier gain changes and phase shifts, and provides a linear power response over a large dynamic range.

The total-power receiver is a standard Aerospace Research Inc. 100 C Mark II riometer. It too is a Ryle-Vonberg receiver and has a linear power response. The linearity of both receivers has been verified within about 1% in the course of this program. The time constants used during most of the absolute flux-density measurements reported here were 2.0 sec for the correlation receiver and 1.3 sec for the total-power receiver. These values were low enough to make corrections to the observed chart deflections small, and to prevent the smearing out of fast ionospheric scintillations, but

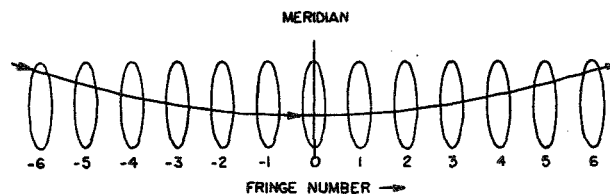
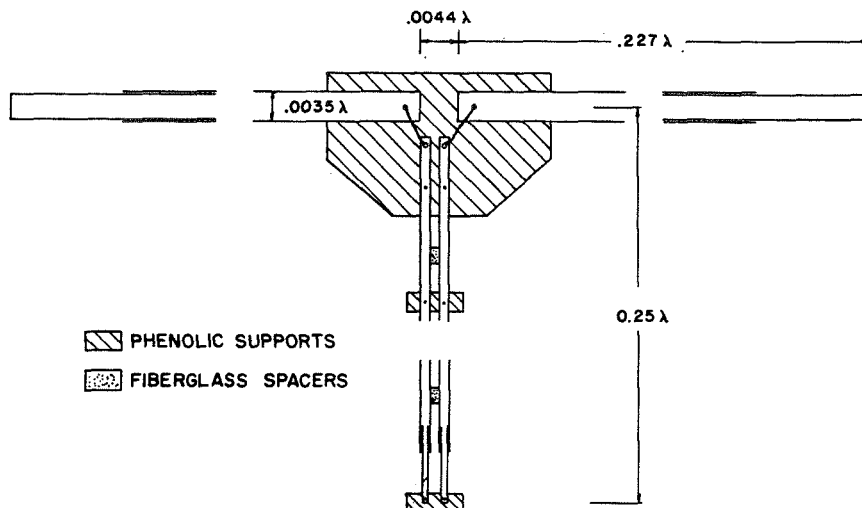


FIG. 2. Schematic illustration of the path of a radio source through part of the grating array response pattern.

FIG. 3. Details of the construction of the calibration dipole.



high enough that the signal-to-noise ratio was not seriously degraded.

Grating lobes off the meridian are affected by decorrelation of signals across the bandpass of a receiver. Since the two receivers used here do not have identical bandpasses, corrections must be applied to the chart deflections R_p and R_T before using them in Eq. 3. In order to keep the corrections small while maintaining a good signal-to-noise ratio, the bandpass of both receivers were kept relatively narrow. Throughout the absolute flux-density measurements the correlation receiver was operated with a 150-kHz bandwidth. The total-power receiver was retuned several times during the measurements, but was generally operated with a bandwidth between 60 and 190 kHz.

The noise source used to calibrate the receivers consists of a temperature-limited noise diode with a

plate current of 10 mA and a load resistance of 1000 Ω . The output impedance is roughly matched to 50 Ω by means of a wide-band 20:1 tapped toroidal transformer. The noise level thus generated is a constant 6×10^4 $^\circ\text{K}$ with a half-power bandwidth of 10 MHz centered on 26.3 MHz.

By appropriate choice of attenuation between the noise source and the receivers, the calibration signal can be set equal to the level produced by any discrete radio source.

IV. OBSERVING PROCEDURE

In order to observe a given source through as many fringes as possible, the grating array was adjusted so that the source would transit slightly south of the center of the meridian fringe, as shown schematically in Fig. 2.

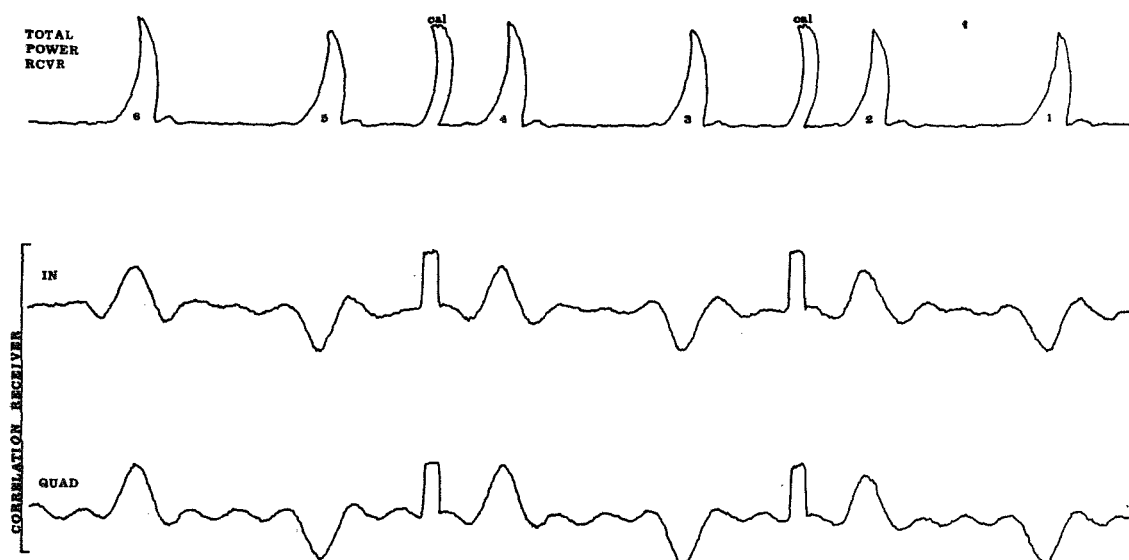


FIG. 4. Sample chart records for absolute measurements on Cyg A, showing passage of the source through fringes +1 to +6 of the grating array on 18 Sept 1969.

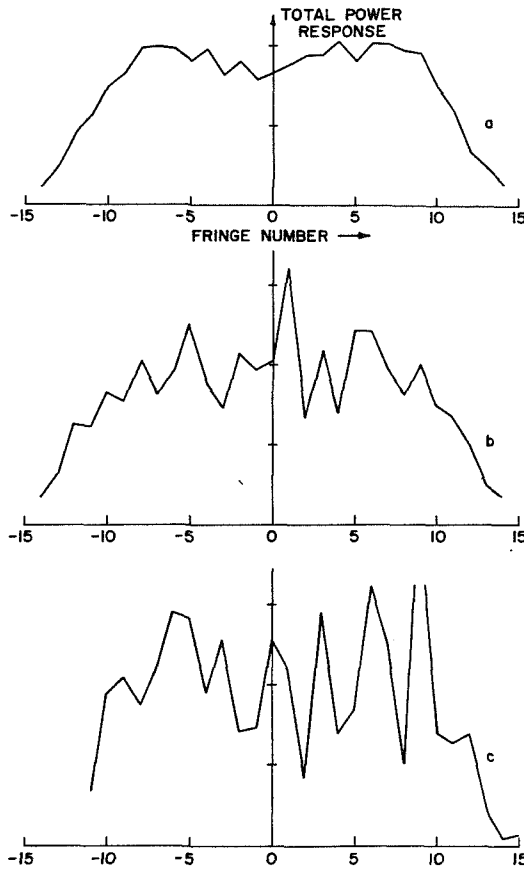


FIG. 5. Peak fringe response as a function of fringe number for Cyg A on (a) 18 Sept 1969, (b) 19 Sept 1969, and (c) 22 Sept 1969, showing the effects of weak, moderate, and strong slow ionospheric scintillation activity, respectively.

The maximum number of usable fringe crossings is a function of the source declination for a given N-S beamwidth. For the four sources studied here, more than 20 independent measurements of absolute flux density could be made in an observing period of three to four hours under ideal interference and scintillation conditions.

The receivers were calibrated at the beginning and end of each of these runs, and occasionally during a run in the time between fringes by injecting a noise reference signal into hybrid port C2 (Fig. 1). This is illustrated in Fig. 4, showing the chart records obtained during part of a run on Cyg A. The parameter R_i used in Eq. 3 to obtain the absolute flux density is simply the ratio of the peak chart deflection for a given fringe divided by the calibration deflection. Because both real (IN-phase) and imaginary (QUADrature-phase) components are extracted in the correlation receiver, the parameter R_p is given by:

$$R_p^2 = \left[\left(\frac{D_N}{D_{CAL}} \right)_{IN}^2 + \left(\frac{D_N}{D_{CAL}} \right)_{QUAD}^2 \right] / 2, \quad (4)$$

where D_N is the peak chart deflection for fringe N and D_{CAL} is the calibration deflection.

The number of fringe crossings obtained on a given run only occasionally approached the maximum possible, due to interference and scintillations. Fast ionospheric scintillations were immediately apparent from the shapes of the drift curves. Slow scintillations with periods longer than a few minutes could only be detected by plotting the peak fringe response of the total-power records against fringe number. The slow scintillations appear as fringe-to-fringe amplitude variations on such plots, as seen in Fig. 5.

The data of 18 September was obtained when the ionosphere was relatively smooth. The dip in the curve near transit occurred because the source was slightly south of the fringe center at that point. The falloff at large fringe numbers corresponds to a N-S beamwidth of 2.7 ± 0.3 for the grating array.

The data of 19 and 22 September were obtained during periods of moderate and strong slow scintillations, respectively. Since the slow scintillations had a period of about 23 min, they did not seriously alter the shapes of the drift curves for each fringe and would have been virtually undetectable with a single-beam antenna.

At 26.3 MHz, all of the runs were affected by scintillations to some extent, the severity generally being least when transit occurred before midnight. When the fast or slow scintillations produced peak-to-peak amplitude variations greater than 30% of the mean amplitude, the data was considered unreliable and was not analyzed. On this basis, about half of the data for each source was rejected. In the acceptable data, the effect of the scintillations was reduced by averaging over many fringes for each run.

V. EQUIPMENT CALIBRATION

A. Noise Source

As described in Sec. III, the noise source used to calibrate the receivers generates a constant signal equivalent to $T_0 = 6 \times 10^4$ °K, which is attenuated to lower levels by a Telonic model TG-950 stepped variable attenuator. The noise power per unit bandwidth matched into hybrid port C2 is given by $kT_0\alpha_{CAL}\alpha_M\alpha_0$, where k is Boltzmann's constant, α_{CAL} is the loss applied by the stepped attenuator, α_M represents mismatch losses at C2, and α_0 is the sum of cable losses and the insertion loss of the stepped attenuator.

In order to determine this noise power, an Aerospace Research Inc. model NS-C variable noise generator was connected to C2 with a short length of coaxial cable and the response of the receivers to a known signal $kT_{ARI}\alpha_M'\alpha_0'$ was measured. The loss in the cable (α_0') was calculated to be $1.0 \pm 0.3\%$. Impedance mismatches at C2 were found to produce less than 1.0% loss for either noise source.

The value of α_{CAL} necessary to make $T_0\alpha_{CAL}\alpha_M\alpha_0 = T_{ARI}\alpha_M'\alpha_0'$ was determined by interpolation for seven values of T_{ARI} between 500 and 12 000°K, giving $T_0\alpha_M\alpha_0 = 47\,000 \pm 400^\circ\text{K}$. This value assumes that the ARI noise generator has no error.

According to the manufacturer, the accuracy of the NS-C noise generator should be better than 2.3% up to 100 MHz. In order to improve (and verify) this accuracy, the output of the NS-C was directly compared with that of a similar model at the Goddard Space Flight Center which had previously been calibrated by the National Bureau of Standards at Boulder, Colorado.

Making a small scale correction on our noise source, we find the absolute value of $T_0\alpha_M\alpha_0$ to be $47\,200 \pm 800^\circ\text{K}$. Therefore, the noise power matched into hybrid port C2 is equivalent to $4.72 \times 10^4 \alpha_{CAL}^\circ\text{K}$ of excess noise temperature. During most of the absolute flux-density measurements, α_{CAL} was set to give a calibration level of $23\,400^\circ\text{K}$ for observations of Cyg A and Cas A, and 2360°K for observations of Tau A and Vir A. In order that these calibration levels produce signals at the receivers comparable with that from the standard dipole as well as the grating array, it was necessary to put a 20-dB attenuator on hybrid B as shown in Fig. 1.

B. Attenuation

The attenuation α_2 between hybrid ports C2 and B1 was measured both piecewise and *in toto* by substitution. In both cases, the value was found to be 21.51 ± 0.03 dB.

The total attenuation between the calibration dipole and hybrid port B1 is given by:

$$\alpha_c = \alpha_{DL} + \alpha_{BAL} + \alpha_{REFL} + \alpha_{IN} + \alpha_{21}, \quad (5)$$

where

α_{DL} = delay line attenuation, measured by substitution with accuracy ± 0.04 dB including interpolation of temperature variations;

α_{BAL} = losses in the balun and in the quarter-wave transformer; measured by an open and short circuit method to be 0.21 ± 0.06 dB;

α_{REFL} = reflection losses at the balun, integrated over the receiver bandpass; calculated to be 0.001 – 0.006 dB with uncertainty ± 0.001 dB;

α_{IN} = cable losses between the balun and the delay line; measured by insertion to be 0.57 ± 0.02 dB;

α_{21} = cable losses in hybrid B between ports 2 and 1; measured by substitution to be 0.76 ± 0.03 dB.

The ultimate standard for attenuation was a Weinschel model 64A stepped attenuator which had been factory calibrated with an accuracy of ± 0.01 dB. The TG-950 stepped attenuator was calibrated against the Weinschel with an accuracy of ± 0.02 dB, and was used to calibrate several other attenuators to ± 0.03 dB. These attenuators and a Shallcross stepped attenuator

with 0.1-dB steps were then used to precisely calibrate a portable square-law detector at 26.3 MHz. The detector provided an accurate interpolation between the 1-dB steps of the comparison attenuators when measuring unknown attenuations by substitution. During all attenuation measurements, any mismatch losses greater than 0.5% were taken into account.

C. Dipole Collecting Area

According to Kraus (1950, Chap. 3), the maximum effective aperture of a lossless resonant antenna is

$$A_{em} = \frac{V^2}{4PR}, \quad (6)$$

where V is the voltage induced across the antenna by the incident wave, $P = E^2/Z$ = power density of the incident wave with field strength E traveling through a medium with impedance Z ($= 120 \pi \Omega$ for free space), and R is the radiation resistance of the antenna.

For a half-wave dipole with a sinusoidal current distribution, $V = E\lambda/\pi$. Substituting for V , P , and Z in Eq. 6, we get

$$A_{em} = \frac{30\lambda^2}{\pi R}. \quad (7)$$

This maximum response will occur when the angle ζ between the dipole axis and the direction of the incident wave is 90° . For other angles, the effective area will be

$$A_e(\zeta, z) = A_{em} \cdot D^2(\zeta) \cdot I^2(z), \quad (8)$$

where $D(\zeta)$ is the voltage response pattern of the dipole in free space, and the image factor,

$$I(z) = 2 \sin\left(\frac{2\pi h}{\lambda} \cos z\right), \quad (9)$$

is produced by the effect of an ideal ground screen a distance h below the horizontal dipole. The angle z is the zenith angle of the incident wave.

The voltage response pattern $D(\zeta) \cdot I(z)$ was calculated for each observed fringe following Schelkunoff and Friis (1952) with allowance for the effects of the center gap s and the capacitive end effect δ . The angles ζ and z were determined from the declination of the source and the hour angle of the fringe.

The loss resistance at 26.3 MHz in the brass cylinders which constitute the dipole can be shown to be $\lesssim 0.07 \Omega$. Hence, the heat losses in the antenna are negligible, and the resistance seen at the antenna terminals is the radiation resistance of the dipole to a high degree of precision.

Rather than calculate the theoretical radiation resistance of the dipole, it was decided to measure the resistance directly by substitution.

TABLE I. Calibration dipole parameters at several heights above the ground screen.

| Height h (m) | Dipole half- length l | Capaci- tive end effect δ | Substitution resistance R_s (ohms) | Correction ΔR (ohms) | Radiation resistance R (ohms) |
|-------------------|-------------------------------|---|---|------------------------------------|--|
| 1.45 | 0.226 λ | 0.0143 λ | 30.6 \pm 0.5 | +1.4 \pm 0.15 | 32.0 \pm 0.6 |
| 1.86 | 0.225 λ | 0.0143 λ | 44.4 \pm 0.5 | +1.1 \pm 0.15 | 45.5 \pm 0.6 |
| 2.42 | 0.228 λ | 0.0143 λ | 68.7 \pm 0.8 | +0.3 \pm 0.5 | 69.0 \pm 0.9 |
| 2.78 | 0.231 λ | 0.0142 λ | 80.5 \pm 1.5 | -0.2 \pm 0.8 | 80.3 \pm 1.6 |

Carbon composition resistors in steps of about 5 Ω were measured on a Boonton R-X Meter in the lab to determine their resistances at 26.3 MHz. These resistors were substituted for the dipole at the end of the quarter-wave transformer, and the impedance at the end of the balun was measured with a Hewlett-Packard Vector Impedance Meter for each resistor and for the dipole itself. The radiation resistance of the dipole was obtained by interpolating between the impedance readings produced by the composition resistors.

This procedure was repeated each time the height of the dipole above the ground screen was changed.

The accuracy of the Boonton bridge was checked at 26.3 MHz for three values of resistance using standard General Radio type 874 50- Ω and 100- Ω terminations, and corrections were applied to the dipole substitution resistance R_s , assuming that the bridge correction varies smoothly with nominal measured resistance. The corrections are listed in Table I along with the values of R_s and the other parameters used to calculate the dipole collecting area for each dipole height.

The ground screen used under the calibration dipole consisted of a double layer of 5.5-cm wire mesh of 22-gauge galvanized steel in contact with the ground. According to Wilson and Cottony (1960), such a wire mesh will have a front/back ratio ≥ 45 dB at 26.3 MHz.

The size of the ground screen is 2.1λ parallel to the dipole and 1.0λ at right angles. For this configuration, the measurements of Wilson and Cottony (1960) indicate that the maximum back radiation diffracted around the edges of the ground screen has a level of -22 dB. However, much of this "spillover" radiation will be reflected back to the dipole by the flat ground beyond the edges of the ground screen.

Hence the effect of the nonideal ground screen is to reduce the effective aperture of the dipole by an amount much less than 1%. This is supported by the measurements of Yates and Wielebinski (1966), who find <2% losses for a one-wavelength square screen with a much coarser grid.

Since the ground under the screen was not perfectly flat, there is an uncertainty of ± 5 cm in the quoted dipole heights. The corresponding uncertainty in the image factor $I(z)$ is 0.2%-2.2%, depending on the dipole height and the zenith angle of the source.

Nonsinusoidal current distributions on the arms of the dipole and uncertainty in the end effect calculations produce an error less than 2% in the dipole factor $D(\zeta)$.

Combining the errors in $I(z)$, $D(\zeta)$, and R , we find the net uncertainty in the dipole collecting area to be 2.6%-3.5%, depending on the height above the ground screen.

However, it should be noted that the absolute measurements were in fact performed with the dipole at four different heights above the ground screen, whereas the customary practice is to select one height depending on impedance matching requirements. The fact that the results show no systematic difference from one height to another is further evidence that there are no serious errors in this method of determining the dipole collecting area.

D. Ionospheric Absorption

Facilities for ionospheric sounding or the measurement of ionospheric absorption were not available at the Clark Lake Radio Observatory. The reason for this is that nighttime absorption at 26.3 MHz is expected to be low (<5%) and daytime observations are generally impossible because of high levels of terrestrial interference. In addition, ionospheric parameters can be determined with reasonable accuracy by interpolating the values found by nearby sounding stations. These stations (White Sands, Point Arguello, and Stanford) have geomagnetic latitudes within 5° of that of Clark Lake (40°5' N) and straddle the observatory in geomagnetic longitude (11°E, 5°W, and 7°W, respectively).

Although ionospheric absorption less than 5% cannot be accurately measured, it can be calculated by combining an ionospheric model (Viner 1973) with estimates of the F2 layer critical frequency (f_oF2) and the exospheric temperature of the ionosphere (T_{exo}). Formulae in the U. S. Standard Atmosphere Supplements (1966) were used to calculate T_{exo} as a function of local time, season, solar activity, and geomagnetic activity. The value of f_oF2 was interpolated with an accuracy better than ± 0.5 MHz from ionosonde data as described above.

The necessary ionospheric sounding data, and the appropriate solar and geomagnetic activity indices were provided by World Data Center A in Boulder, Colorado.

Because the amount of absorption is considerably higher during the day and daytime ionospheric models are more complicated, reduction of data was restricted to observations taken at night. For those observations, the amount of absorption was rarely greater than 2% and could be determined with an uncertainty of less than 1%.

VI. ERROR ANALYSIS AND RESULTS

A. Results

Tables II(a) through (d) summarize the results of data reduction on all acceptable data for the four sources being studied. Column 1 gives the date on which each set of observations was taken. The mean calculated flux density for each run, the standard deviation (rms error) of the mean from internal scatter (σ_{SCATT}), and the number of observed fringes from which data were taken are given in columns 2, 3, and 4, respectively.

Virtually all of the scatter within a given run is caused by slow ionospheric scintillations. Since these scintillations are produced by large irregularities which effectively focus and defocus the radiation from the source being observed, the deviations of apparent intensity from the mean are multiplicative rather than additive in nature. Hence, the mean values and standard deviations quoted were obtained by averaging the logarithms of the flux densities in order to avoid systematic overestimation of the mean. The use of a linear average could give mean values as much as 2% too high for a given run, depending on the magnitude of the internal scatter.

Column 5 gives the square of the relative standard deviation (σ_{REL}^2) for each run, calculated as the difference of the squares of the total rms error and the errors common to all runs. This parameter gives the relative quality of each run, and its inverse was used as a weighting factor when final averages were calculated for each source.

Column 6 gives the absolute flux density corrected for ionospheric absorption, partial resolution, receiver time constant, and time delay decorrelation.

The last column gives the net rms error (σ_T) for each run.

The absorption correction was found to be less than 2% in general. The time constant and partial resolution corrections, which are listed in Table III, were also quite small due to the fact that a *ratio* of receiver responses was used in Eq. 3 to calculate the flux densities.

The Gaussian source widths quoted in Table III were derived from total-power records by measuring the extent to which each source broadened the theoretical antenna pattern (Viner 1973). The partial resolution corrections were calculated using the 26.3-MHz source sizes instead of the generally more precise high-frequency data in order to avoid any systematic errors due to variations of source size with frequency.

The time constant corrections were derived by convolving the true antenna patterns with the step function response of the integrator, using 2.0 ± 0.3 and 1.3 ± 0.3 sec for the time constants of the correlation receiver and the total-power receiver, respectively. The correction factor for the runs of 4 and 5 June was 0.974, corresponding to a total-power receiver time constant of 6 ± 1.5 sec.

TABLE II(a). Summary of data reduction for Cyg A.

| Date | Flux* | σ_{SCATT} | N_{OBS} | σ_{REL}^2 | Corrected flux* | σ_T |
|------------|--------|-------------------------|------------------|-------------------------|-----------------|------------|
| 4 June 69 | 28 700 | 4.6% | 23 | 27 | 28 200 | 6.6% |
| 5 June 69 | 30 400 | 5.6 | 23 | 37 | 29 900 | 7.3 |
| 8 Aug 69 | 24 000 | 3.4 | 11 | 22 | 24 400 | 6.1 |
| 10 Aug 69 | 26 600 | 3.6 | 20 | 22 | 26 900 | 6.1 |
| 27 Aug 69 | 28 400 | 6.3 | 16 | 45 | 28 800 | 7.8 |
| 17 Sept 69 | 31 800 | 2.6 | 7 | 16 | 32 100 | 5.6 |
| 18 Sept 69 | 30 600 | 2.5 | 20 | 15 | 31 000 | 5.6 |
| 20 Sept 69 | 30 100 | 3.9 | 20 | 24 | 30 500 | 6.3 |
| 21 Sept 69 | 28 700 | 4.6 | 9 | 31 | 30 400 | 6.9 |
| 30 Sept 69 | 27 400 | 5.4 | 7 | 58 | 28 000 | 8.6 |
| 2 Oct 69 | 27 500 | 4.4 | 17 | 30 | 27 900 | 6.7 |
| 6 Nov 69 | 27 900 | 2.7 | 7 | 20 | 28 200 | 5.9 |
| 7 Nov 69 | 28 700 | 2.4 | 11 | 12 | 29 500 | 5.1 |
| 8 Nov 69 | 27 900 | 3.2 | 13 | 17 | 28 700 | 5.6 |

TABLE II(b). Summary of data reduction for Cas A.

| Date | Flux* | σ_{SCATT} | N_{OBS} | σ_{REL}^2 | Corrected flux* | σ_T |
|------------|--------|-------------------------|------------------|-------------------------|-----------------|------------|
| 8 Aug 69 | 42 300 | 2.9% | 19 | 19 | 42 800 | 5.8% |
| 17 Aug 69 | 40 800 | 3.8 | 20 | 20 | 41 200 | 5.9 |
| 30 Aug 69 | 42 100 | 5.4 | 6 | 61 | 42 600 | 8.8 |
| 2 Sept 69 | 45 400 | 2.3 | 17 | 11 | 45 800 | 5.0 |
| 23 Sept 69 | 44 300 | 5.8 | 13 | 45 | 44 600 | 7.8 |
| 26 Sept 69 | 45 200 | 2.7 | 20 | 18 | 45 500 | 5.7 |
| 27 Sept 69 | 42 100 | 2.4 | 20 | 17 | 42 400 | 5.6 |
| 28 Sept 69 | 46 200 | 2.1 | 19 | 16 | 46 600 | 5.5 |
| 8 Dec 69 | 41 700 | 4.3 | 17 | 23 | 42 500 | 6.2 |
| 9 Dec 69 | 42 100 | 2.7 | 17 | 12 | 42 900 | 5.2 |
| 10 Dec 69 | 41 100 | 2.5 | 17 | 11 | 41 900 | 5.0 |
| 11 Dec 69 | 43 700 | 2.2 | 17 | 10 | 44 500 | 4.9 |

TABLE II(c). Summary of data reduction for Tau A.

| Date | Flux* | σ_{SCATT} | N_{OBS} | σ_{REL}^2 | Corrected flux* | σ_T |
|-----------|-------|-------------------------|------------------|-------------------------|-----------------|------------|
| 26 Oct 69 | 2930 | 3.3% | 17 | 25 | 2950 | 7.3% |
| 27 Oct 69 | 3060 | 3.5 | 22 | 26 | 3080 | 7.2 |
| 5 Feb 70 | 3610 | 4.7 | 14 | 40 | 3640 | 8.4 |
| 7 Feb 70 | 3040 | 5.1 | 15 | 29 | 3070 | 7.7 |
| 8 Feb 70 | 2830 | 2.3 | 22 | 9 | 2850 | 6.1 |
| 9 Feb 70 | 2890 | 2.8 | 23 | 11 | 2920 | 6.3 |
| 10 Feb 70 | 2830 | 2.2 | 13 | 8 | 2860 | 5.9 |
| 12 Feb 70 | 2910 | 2.3 | 19 | 13 | 2940 | 6.4 |
| 13 Feb 70 | 2870 | 3.3 | 15 | 14 | 2910 | 6.4 |
| 14 Feb 70 | 2980 | 3.6 | 16 | 16 | 3020 | 6.6 |
| 15 Feb 70 | 2930 | 3.5 | 16 | 15 | 2970 | 6.5 |
| 16 Feb 70 | 2870 | 2.4 | 16 | 9 | 2920 | 6.0 |

TABLE II(d). Summary of data reduction for Vir A.

| Date | Flux* | σ_{SCATT} | N_{OBS} | σ_{REL}^2 | Corrected flux* | σ_T |
|-----------|-------|-------------------------|------------------|-------------------------|-----------------|------------|
| 16 Apr 70 | 4150 | 3.8% | 13 | 17 | 4280 | 6.5% |
| 17 Apr 70 | 4550 | 2.7 | 24 | 9 | 4660 | 5.8 |
| 23 Apr 70 | 4580 | 5.0 | 4 | 27 | 4680 | 7.2 |
| 28 Apr 70 | 4830 | 5.8 | 12 | 37 | 4940 | 7.7 |
| 30 Apr 70 | 4290 | 7.6 | 6 | 62 | 4400 | 9.2 |
| 1 May 70 | 4550 | 2.2 | 17 | 8 | 4650 | 5.6 |
| 2 May 70 | 4400 | 4.5 | 12 | 24 | 4520 | 6.9 |
| 11 May 70 | 4600 | 4.0 | 18 | 21 | 4760 | 6.6 |
| 12 May 70 | 4520 | 4.7 | 13 | 26 | 4670 | 7.1 |
| 14 May 70 | 4140 | 3.1 | 26 | 15 | 4290 | 6.4 |
| 15 May 70 | 4280 | 2.9 | 13 | 14 | 4420 | 6.3 |

* In units of 10^{-26} W/m²/Hz.

TABLE III. Corrections to calculated flux densities.

| Source | Source size* | Partial resolution | Time constant |
|--------|---------------|--------------------|---------------|
| Cyg A | $3'2 \pm 1'2$ | 1.002 | 1.003 |
| Cas A | $4'0 \pm 1'8$ | 1.002 | 1.001 |
| Tau A | $< 3'7$ | 1.001 | 1.005 |
| Vir A | $5'9 \pm 0'9$ | 1.013 | 1.004 |

* Assuming Gaussian source distribution.

The overall weighted averages of flux density for each source are presented in Table IV, along with the net (rms) standard deviation and the mean epoch of observation for each source. The values for 8 August (Cyg A) and 5 February (Tau A) deviated from the means by 3.7 and 3.8 times their relative standard deviations, and were not included in the final average. The large deviations may be due to very slow scintillations with periods greater than two hours, or they may be due to a chance synchronization of the scintillation period with the fringe spacing of the grating array (8^m for Cyg A and 6^m5 for Tau A). Inclusion of these values would decrease the average Cyg A flux density by 1.3% and increase the average Tau A flux density by 0.6%.

B. Discussion of Errors

The various contributions to the rms standard deviation are summarized in Table V for each source. Since the magnitudes of some of the errors differ from run to run, the quoted numbers are weighted means of the associated errors for each run.

Some comments on individual sources of error follow:

(1) The correction factor applied to each fringe for bandpass smearing is the ratio of fringe-washing functions (Christiansen and Högbom 1969) for the total-power receiver and the correlation receiver. Since the magnitude of the correction increased with fringe number, the correction was applied during the data reduction for each fringe before calculating the mean flux density for any run.

The uncertainty in the bandpass smearing correction also increased with fringe number. At times, the uncertainty in the width and shape of the total-power receiver bandpass was large enough that the data from some fringes had to be thrown out in order that the systematic error in the mean flux density be less

TABLE IV. Final absolute flux densities of each source.

| Source | Absolute flux density* | Standard error, % | Epoch |
|--------|------------------------|-------------------|--------|
| Cyg A | 29600 | 5.0 | 1969.8 |
| Cas A | 44100 | 4.6 | 1969.8 |
| Tau A | 2990 | 5.7 | 1970.1 |
| Vir A | 4570 | 5.3 | 1970.3 |

* In units of 10^{-26} W/m²/Hz.

TABLE V. Summary of sources of error for each source.

| Sources of error | Cyg A | Cas A | Tau A | Vir A |
|------------------------|-------|-------|-------|-------|
| Noise source | 1.7% | 1.7% | 1.7% | 1.7% |
| Attenuation | 2.1 | 2.0 | 2.0 | 2.0 |
| Standard dipole | 1.9 | 1.9 | 2.1 | 1.6 |
| Resistance | 1.2 | 1.1 | 0.3 | 1.3 |
| Image factor | 2.0 | 2.0 | 2.0 | 2.0 |
| Dipole factor | 0.6 | 0.7 | 0.3 | 0.5 |
| Ionospheric absorption | 1.7 | 1.2 | 0.9 | 0.7 |
| Bandpass smearing | 0.2 | 0.2 | 0.1 | 0.8 |
| Partial resolution | 0.3 | 0.2 | 0.3 | 0.3 |
| Time constant | 1.5 | 1.4 | 3.9 | 3.1 |
| Chart scaling errors | 1.6 | 1.3 | 0.9 | 1.5 |
| Scatter of the mean | | | | |

than 2.0% for that run. Less than 10% of the reduceable data was rejected for this reason.

(2) Three sources of chart scaling errors were considered: (a) confusion due to other sources in the antenna beam, (b) systematic scaling errors in the presence of random noise fluctuations, and (c) the smallest resolvable chart deflection in the absence of noise fluctuations.

Included in (a) were all known sources which pass through some part of the grating array pattern during a run, and which might produce a chart deflection larger than 1% of that of the source being studied. The net contribution of these sources to the mean flux density obtained in a given run was found to be less than 0.5% in all four cases, even though the values for some individual fringes may be high or low by a few percent. The net uncertainty in the mean flux density for each source due to confusion is given in Table VI.

In the presence of "white" noise fluctuations, individual measured chart deflections will have an uncertainty equal to the rms noise level (von Hoerner 1961; Whalen 1971). However, this is a random error, and contributes only to the scatter of the data. We are interested here in the possible systematic measuring errors.

If the fluctuations seen on the chart records are due to fast scintillations, the measured chart deflections will be systematically high. This overestimation is due to the fact that record scaling is a linear procedure, while scintillations are multiplicative. Fast scintillations were common only in the Tau A data reported here, producing a systematic error of about 0.1% in the mean flux density. For the other sources, the possible systematic error due to unrecognized fast scintillations is considerably smaller.

TABLE VI. Sources of scaling errors.

| Source | Confusion | Personal bias | Chart resolution |
|--------|-----------|---------------|------------------|
| Cyg A | 0.2% | 0.6% | 1.4% |
| Cas A | 0.1 | 0.4 | 1.3 |
| Tau A | 0.5 | 2.4 | 2.9 |
| Vir A | 0.5 | 1.8 | 2.5 |

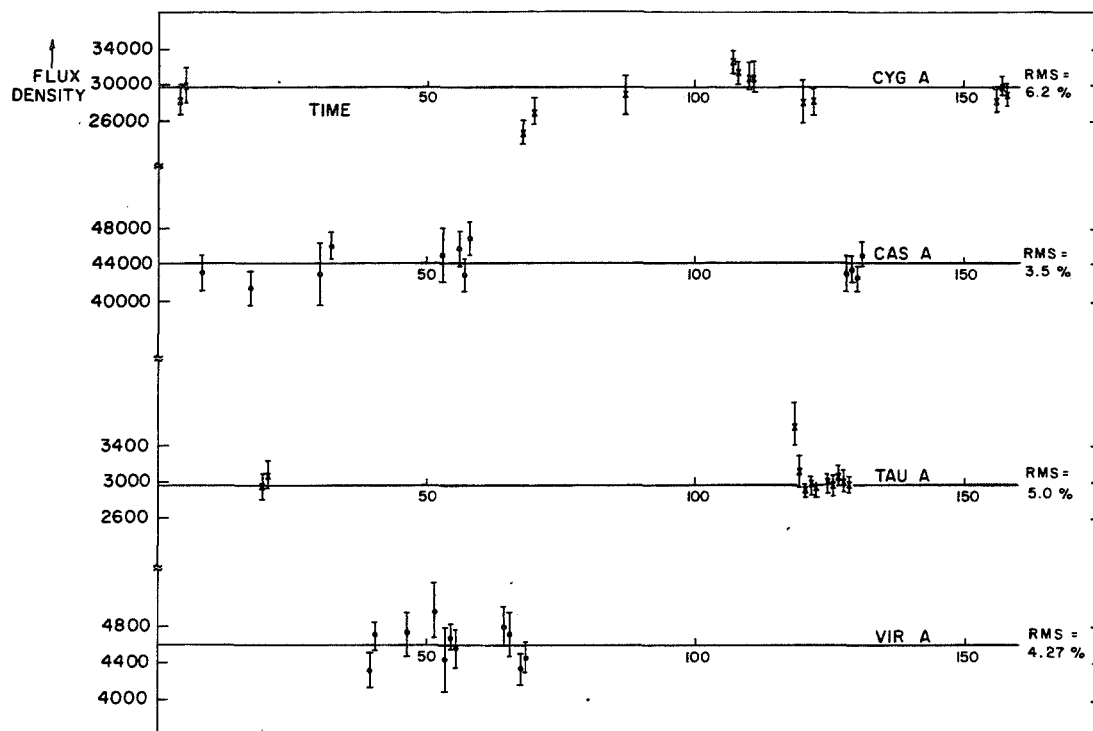


FIG. 6. Absolute flux densities of Cyg A, Tau A, and Vir A plotted as a function of time in days from an arbitrary starting point for each source.

More important is the possibility of a *personal bias* in scaling records in the presence of noise. It is reasonable to assume that any personal bias will be smaller than $\frac{1}{10}$ of the peak-to-peak noise fluctuation level. The corresponding errors in the mean flux density for each source are listed in column 3 of Table VI, based on measured noise levels.

Finally, even in the absence of noise fluctuations, the thickness of the pen trace and the limits of resolution of the eye suggest that chart deflections cannot be measured more accurately than 0.01–0.02 in. The equivalent percent error in the flux density for each source, based on the typical chart deflections obtained in the experiment, is quoted in column 4 of Table VI.

The personal bias and chart resolution errors quoted in Table VI are quadratic sums of the errors for all three chart recorders used for the absolute measurements.

VII. TIME VARIATIONS

Braude *et al.* (1969) report that they have detected intrinsic time variations in the flux densities of Cas A, Tau A, and 3C84 at frequencies below 30 MHz. The 12.6-MHz flux densities of Cas A and 3C84 were found to change by 2.5 dB over a time span of two to three months, while the intensity of Tau A fluctuated by 4 dB within one month. The amplitude of the variations decreased linearly with the observing frequency up to 25 MHz for all three sources.

Such variations would make these sources useless as standards of absolute flux density at low frequencies, and would have important consequences for theoretical models of radio sources. Hence, it is important to verify or refute claims of variability using independent observations.

This has already been done at 10 MHz (Bridle and Caswell 1970) and at 22 MHz (Roger 1970) for 3C84 using data which partially overlapped Braude's observations. No evidence of variability was found at either frequency, and upper limits of 20% and 12%, respectively, were set on the rms of any undetected variability. In addition, Bridle and Caswell offer reasonable explanations for the apparent variability in Braude's measurements in terms of ionospheric phenomena.

Figure 6 shows the 26.3-MHz absolute flux-density measurements for Cyg A, Cas A, Tau A, and Vir A plotted as a function of time in days from an arbitrary starting point for each source. The vertical lines represent the relative standard deviations (σ_{REL}) for each run, while the long horizontal lines show the mean flux density for each source. The rms scatter about the mean is given in percent at the right-hand side of the figure for each source.

No evidence of systematic variations is apparent in the flux densities of Cyg A or Cas A over periods of a few months. Assuming that the observations were not taken at fortuitous times, any undetected variability must be less than 6% rms and 3.5% rms, respectively.

Similarly, Tau A and Vir A appear to have constant flux densities over periods of ten days and one month, respectively, although the distribution of data points on the time basis is too small to refute the possibility of variations on a longer time scale.

It might also be noted that Braude *et al.* consider the source Vir A to have no intrinsic variations. Yet the scatter of data for Vir A at 26.3 MHz is not significantly different from that of the other three sources studied. Therefore, it is tentatively concluded that all four sources have constant flux densities on a time scale of days or months during the period of the present observations.

VIII. CONCLUSIONS

This paper has demonstrated that a grating array used in conjunction with a standard dipole and two receivers can be a powerful tool for measuring absolute flux densities of radio sources at low radio frequencies where ionospheric scintillations are a major problem.

The limiting accuracy of this method at 26.3 MHz should be about 3.3% for the strongest sources. In order to approach this limit, we would require a reduced delay-line attenuation, better knowledge of receiver parameters, and better standards for noise power, attenuation, and resistance.

It is most important that this method be extended to frequencies below 20 MHz, where absolute flux scales are very poorly known and ionospheric effects are a limiting factor for other methods. With small changes in the grating array and delay line, it should be possible to measure the absolute flux densities of up to ten discrete sources with an accuracy of 5%–10% at frequencies as low as 10 MHz.

ACKNOWLEDGMENTS

The author would like to thank Dr. William C. Erickson for suggesting the project and providing helpful advice and encouragement, Mr. John Petrich for his assistance in operating and maintaining the equipment, and the staffs of the National Aeronautics and Space Administration at Goddard, the National Radio Astronomy Observatory at Green Bank, and the General Radio Corporation for the loan of essential equipment. Ionospheric data was provided by World Data Center A in Boulder, Colorado. This work is supported by the National Science Foundation under grant GP-19401 and by the National Aeronautics and Space Administration under grant NGR 21-002-367.

REFERENCES

- Braude, S. Ya., Lebedeva, O. M., Megn, A. V., Ryabov, B. P., and Zhouck, I. N. (1961). *Mon. Not. R. Astron. Soc.* **143**, 289.
- Bridle, A. H. (1967). *Observatory* **87**, 60.
- Bridle, A. H., and Caswell, J. L. (1970). *Nature* **225**, 356.
- Christiansen, W. N., and Högbom, J. A. (1969). *Radiotelescopes* (Cambridge U. P., Cambridge).
- Erickson, W. C. (1965). *IEEE Trans. Antennas Propag.* **AP-13**, 422.
- Hubbard, J. W., and Erickson, W. C. (1967). *IEEE Trans. Antennas Propag.* **AP-15**, 291.
- Kraus, J. D. (1950). *Antennas* (McGraw-Hill, New York).
- Little, A. G. (1958). *Aust. J. Phys.* **11**, 70.
- Parker, E. A. (1968). *Mon. Not. R. Astron. Soc.* **138**, 407.
- Roger, R. S. (1970). *Astrophys. Lett.* **4**, 139.
- Schellkunoff, S. A., and Friis, H. T. (1952). *Antennas, Theory and Practice* (Wiley, New York).
- U. S. Standard Atmosphere Suppl. 1966 (U. S. GPO, Washington, D. C.).
- Viner, M. R. (1973). Ph.D. thesis, University of Maryland.
- Viner, M. R., and Erickson, W. C. (1975). In preparation.
- von Hoerner, S. (1961). *Publ. Natl. Radio Astron. Obs.* **1**, No. 2.
- Whalen, A. D. (1971). *Detection of Signals in Noise* (Academic, New York).
- Wilson, A. C., and Cottony, H. V. (1960). *IRE Trans. Antennas Propag.* **AP-8**, 144.
- Yates, K. W., and Wielebinski, R. (1966). *Aust. J. Phys.* **19**, 389.

VLBI OBSERVATIONS OF THE CRAB NEBULA PULSAR

N. R. VANDENBERG, T. A. CLARK, W. C. ERICKSON, AND G. M. RESCH

Astronomy Program, University of Maryland,
College Park, and Radio Astronomy Branch,
Goddard Space Flight Center

J. J. BRODERICK AND R. R. PAYNE

National Astronomy and Ionosphere Center, Arecibo Observatory

AND

S. H. KNOWLES AND A. B. YOUMANS

Naval Research Laboratory, Washington, D.C.
Received 1972 October 20; revised 1972 December 4

ABSTRACT

Observations of the Crab Nebula pulsar at meter wavelengths using VLBI techniques have been made. At 196.5 MHz we observe no resolution of the pulsar, all the pulse shapes observed with the interferometers are similar to single-dish profiles, and all the power pulsates. At 111.5 MHz besides the pulsing power there is always a steady component, presumably due to multipath propagation effects. The pulsar is slightly resolved at 111.5 MHz with an apparent angular diameter of $0''.07 \pm 0''.01$. We observe 50 percent linear polarization of the time-averaged power at 196.5 MHz; at 111.5 MHz, 20 percent of the total time-averaged power is polarized, 35 percent of the pulsing power is polarized. The steady component is unpolarized. The total flux of the steady plus pulsating component appears to remain constant while the distribution of power between these components varies.

Subject headings: pulsars — Crab Nebula

I. INTRODUCTION

From 1971 November through 1972 March we observed the Crab Nebula pulsar (PSR 0531+21) at monthly intervals using very long baseline interferometry (VLBI) techniques at meter wavelengths. The results presented in this *Letter* are based on the November and December observations. The purpose of the experiment was to monitor the apparent angular size of the pulsar and to compare variations in the pulse shape, as reported by Rankin and Counselman (1973), to changes in angular size. The relation between spatial and temporal broadening can indicate the general location of the scattering screen.

The telescopes used were the 305-m (1000-foot) Arecibo dish, the 92-m (300-foot) NRAO dish, and the 46-m (150-foot) dish at Sugar Grove, West Virginia. Table 1 gives the interferometer parameters. The standard NRAO Mark I recording terminals were used, and the normal Arecibo Crab pulsar timing observations were made simultaneously. The VLBI data were coherently de-dispersed and analyzed into the Fourier components of the pulse shape using the technique described by Erickson *et al.* (1972).

II. RESULTS

a) Positional Agreement of Pulsar and Compact Source

The 111.5-MHz data indicate that the average deviation of the phase of the Fourier components (associated with the pulsar) from the fundamental phase (associated with the compact source) is about $1''.2$. This corresponds to a positional agreement of about

TABLE 1
INTERFEROMETER PARAMETERS

| BASELINE | 111.5 MHz | | | 196.5 MHz | | |
|--|----------------------|----------------------|---------------------------------|----------------------|----------------------|---------------------------------|
| | D (wavelengths) | S_{\min} (f.u.) | Fringe Spacing (arc seconds) | D (wavelengths) | S_{\min} (f.u.) | Fringe Spacing (arc seconds) |
| Arecibo-NRAO (2000 km) | 0.94×10^6 | 0.3 | 0.20 | 1.7×10^6 | 0.3 | 0.12 |
| Arecibo-Sugar Grove (2000 km) | 0.93×10^6 | 0.5 | 0.20 | 1.6×10^6 | 0.5 | 0.12 |
| NRAO-Sugar Grove (50 km) | 1.9×10^4 | 1.5 | 10 | 3.3×10^4 | 0.8 | 6 |

0''01, and supports the previous conclusion that the compact source in the Crab Nebula must be identified with the pulsar.

b) Profiles

At 196.5 MHz, the pulse profiles observed with both low and high resolution are similar to the single-dish Arecibo profiles, and all the power pulsates. We conclude that there is no resolution of the pulsar at 196.5 MHz and place an upper limit on its apparent size of 0''04. Both the high- and low-resolution observations at 111.5 MHz show a broad pulse shape and a steady component, implying that the temporal and angular scattering are not simply related and probably do not occur at the same place along the intervening path.

The average fringe visibility at 111.5 MHz is 0.8 ± 0.1 , corresponding to an apparent angular diameter of $0''07 \pm 0''01$, assuming a Gaussian brightness distribution. The angular size predicted on the basis of interstellar scattering by Harris, Zeissig, and Lovelace (1970) is 0''09 at 111.5 MHz. The average value of the ratio of steady to total flux is 0.45 ± 0.1 for both months' observations, in good agreement with the scattering function proposed by Rankin *et al.* (1970) which predicts 0.5 ± 0.2 .

c) Total flux

The total flux of the small-diameter source was constant throughout the entire observing program. Each epoch yields a time-averaged total flux of 35 ± 5 f.u. at 111.5 MHz and 6 ± 1 f.u. at 196.5 MHz. The variations in pulsar strength observed with a single dish at 111.5 MHz should be attributed not to intrinsic changes in the total flux, but to different distributions of the power between the pulsing and steady components.

d) Polarization

In figure 1 we have superposed the 111.5-MHz pulse profiles from several runs. Observations made with feeds of opposite circular polarization at the ends of the baselines make the interferometer sensitive to *only* linearly polarized radiation of *any* position angle. When crossed circular feeds were used, the steady component of the pulse disappeared on both the high- and low-resolution observations, implying that this is a polarization, not a resolution, effect. The disappearance of the steady component means that it is unpolarized while the pulsing component retains partial linear polarization.

We observe 50 percent linear polarization of the average power at 196.5 MHz. At 111.5 MHz, 20 percent of the total time-averaged power is linearly polarized. Since the interferometer observes all the power from the small-diameter source, some of which is not detected by single-dish observers, this is a true measure of the polarization.

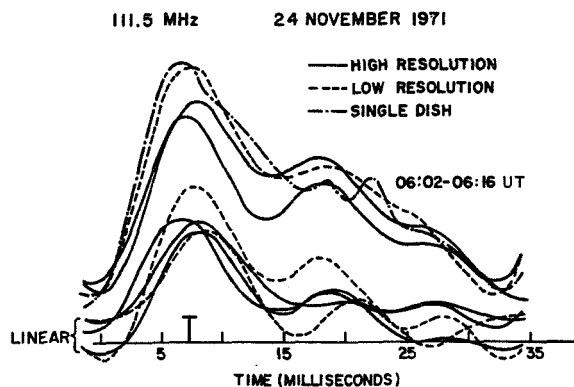


FIG. 1.—Superposition of 111.5-MHz average pulse profiles. The height of the bar under the main pulse represents the amplitude of the instrumental polarization.

If we consider only the pulsating power, we agree with the observations of Manchester, Huguenin, and Taylor (1972).

In order to study the transmission characteristics of the intervening medium, an analysis of the Fourier components of the pulse shapes from all five months' observations is in progress.

We are indebted to L. K. Hutton for painstaking reduction of the total-power data; much of this work is based on these calibrations. We also thank L. K. Hutton, G. E. Marandino, R. B. Miller, and R. A. Perley for assistance with the observations, W. Brundage for technical assistance, and J. M. Rankin for the single-dish timing scheme. This work was supported in part by grants NSF-GP-19401, NASA-NGL-21-002-029, and NASA-NGL-21-002-033. The National Astronomy and Ionosphere Center is operated by Cornell University under contract with the National Science Foundation. The National Radio Astronomy Observatory is operated by Associated Universities, Inc., under contract to the National Science Foundation.

REFERENCES

- Erickson, W. C., Kuiper, T. B. H., Clark, T. A., Knowles, S. H., and Broderick, J. J. 1972, *Ap. J.*, **177**, 101.
 Harris, D. E., Zeissig, G. A., and Lovelace, R. V. 1970, *Astr. and Ap.*, **8**, 98.
 Manchester, R. N., Huguenin, G. R., and Taylor, J. H. 1972, *Ap. J. (Letters)*, **174**, L19.
 Rankin, J. M., Comella, J. M., Craft, H. D., Richards, D. W., Campbell, D. B., and Counselman, C. C. 1970, *Ap. J.*, **162**, 707.
 Rankin, J. M., and Counselman, C. C. 1973, *Ap. J.*, submitted.

26.3-MHz radio source survey. II. Radio source positions and fluxes

M. R. Viner* and W. C. Erickson

Clark Lake Radio Observatory, Astronomy Program, University of Maryland, College Park, Maryland 20742

(Received 22 July 1975; revised 17 September 1975)

The results of the Clark Lake 26.3-MHz Sky Survey are presented. Data concerning the apparent fluxes and positions of 471 radio sources in the declination range $3^{\circ} < \delta < 63^{\circ}$ are given. Almost all of these sources are identified with 3CR or 4C sources, and upper limits are placed on the fluxes of all 3CR sources which could not be found. The flux scale for this survey is based upon the absolute flux determinations of Viner (1975, Paper I of this series). The procedures employed and the errors are discussed in detail. Low-frequency flux scales are discussed and comparisons are made with other workers. The Kellermann, Pauliny-Toth, and Williams (1969) scale should be raised by 11% to agree with the Clark Lake scale. The Penttinen scale (Roger, Bridle, and Costain 1973) and the Clark Lake scale agree very well. The Grakovo scale (Bruk *et al.* 1968; Braude *et al.* 1969a) appears to be highly nonlinear and about 30% above the Clark Lake scale.

INTRODUCTION

THE spectra of many radio sources are poorly known at decametric wavelengths. Data in this wavelength range are difficult to obtain because large apertures are needed to produce the small beamwidths required to reduce confusion to an acceptable level, ionospheric refraction and absorption perturb the measurements, observations are often ruined by terrestrial interference, and the high galactic background emission raises system noise temperatures and lowers system sensitivity. In this work we have alleviated many of these problems. The survey is referred to a well-determined absolute flux scale (Viner 1975). An aperture of $3000 \times 220 \text{ m}^2$ was used, producing a beam area of less than 0.5 deg^2 and correspondingly low-resolution limits. The data were taken at night when ionospheric absorption was low, and all sources were observed many times to average over the effects of refractive scintillations. The collecting area of the system was sufficient to reach its resolution limits and most of the data were taken with a highly linear receiver (Hubbard and Erickson 1967) which is unaffected by diurnal variations in galactic background level. The errors involved in these measurements have been carefully analyzed so that the reader can easily assess the reliability of the data.

The area of sky covered by the survey is $4/10$ of the celestial sphere in the range $3^{\circ} 20' \leq \delta \leq 63^{\circ} 20'$, with a few missing regions due to sidelobes of strong sources and similar problems. In this area we present reliable measurements of 449 isolated sources which were each observed on an average of 14 times, 22 possible blends of two sources, 60 upper limits of the fluxes of 3CR sources, and less reliable measurements of another 119 sources which may be affected by confusion or which were not observed a sufficient number of times to justify inclusion in the main list. For sources in the main list there is an average of 80 beam area/source. This indicates the low-resolution limit which is the principal

advantage gained by the high angular resolution of the instrument. Also, the identification of sources in our list with those observed at higher frequencies is usually unambiguous due to our relatively high angular resolution.

I. EQUIPMENT

A. Receiver

Relative flux densities of radio sources were measured at 26.3 MHz on a semiregular basis at the Clark Lake Radio Observatory from November 1963 to December 1970. Prior to mid-1965, the receiver configuration consisted of two phase-switching receivers which extracted in-phase and quadrature-phase information from the correlated signals of two arrays. A block diagram of the system is shown in Fig. 1. During this period, the i.f.

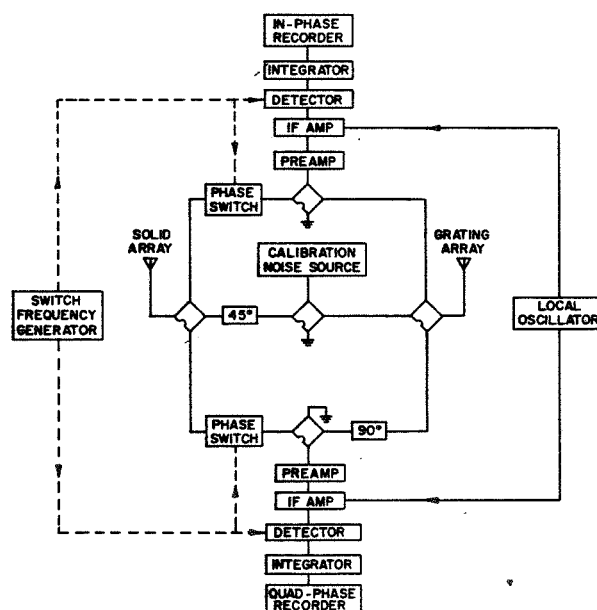


FIG. 1. Block diagram of the receiver configuration used for sky survey observations. After 1965 the system was slightly modified to that described by Hubbard and Erickson (1967).

* Present address: Astronomy Group, Department of Physics, Queen's University, Kingston, Ontario, Canada.

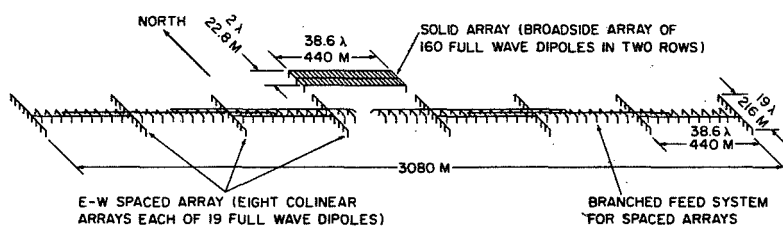


FIG. 2. The antenna system used for the sky survey.

bandpass used was 500 kHz and the postdetection time constant was 10 sec.

After mid-1965, a cross-correlation receiver based on the Ryle-Vonberg principle (Hubbard and Erickson 1967) was installed in order to increase stability with regard to gain and phase changes in the receiver. Intermediate-frequency amplifiers with a bandwidth of 800 kHz were installed. Most of the sky survey data has been obtained using this receiver configuration.

The extraction of in-phase and quadrature-phase information from the correlated signals of the two arrays permits measurement of the declination of a source as well as its flux density in a single observation. The flux density of a source is proportional to the root mean square of the in-phase and quadrature-phase components, while the declination of the source is determined from the ratio of in-phase to quadrature-phase signals.

B. Antenna

The two arrays used to make relative flux-density measurements are a grating array and a solid array (Erickson 1965) as shown in Fig. 2. When the grating array is phase switched with the solid array, the resulting antenna pattern is a fan beam on the local meridian with an EW beamwidth of 14 arcmin and a NS beamwidth of 92 arcmin at the zenith.

The relative flux densities of Tau A, Vir A, Cyg A, and Cas A obtained with this equipment have been

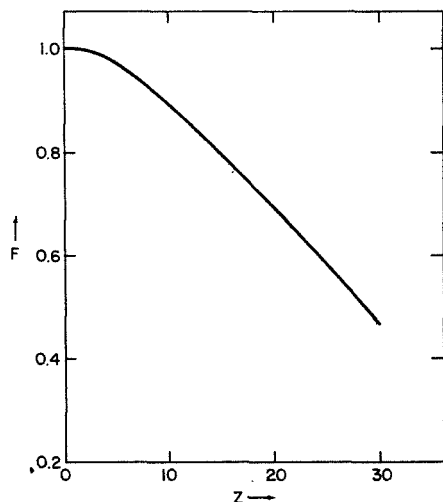


FIG. 3. The gain of the sky survey array as a function of zenith distance Z in degrees.

compared with precise absolute fluxes of the same sources at 26.3 MHz (Viner 1973, 1975) to derive the gain versus zenith distance relation shown in Fig. 3 and to determine the overall flux scale.

It should be stressed that the curve shown in Fig. 3 is based on absolute data, and is independent of the flux scales used by any other observer. The accuracy of the curve is $\pm 10\%$ over the zenith angle range 0° – 30° .

II. OBSERVATIONS

A. Confusion Limits

Following Burns (1972), the rms fluctuation level on a record due to confusing sources weaker than S_L is taken as

$$\sigma_{S_L} = \left[\int_0^{S_L} S^2 N(S) dS \int_{4\pi} G^2(\Omega) d\Omega \right]^{1/2}, \quad (1)$$

where $N(S)$ represents the number of sources per steradian with flux $> S$, $G(\Omega)$ is the normalized antenna gain, and $d\Omega$ is an element of solid angle.

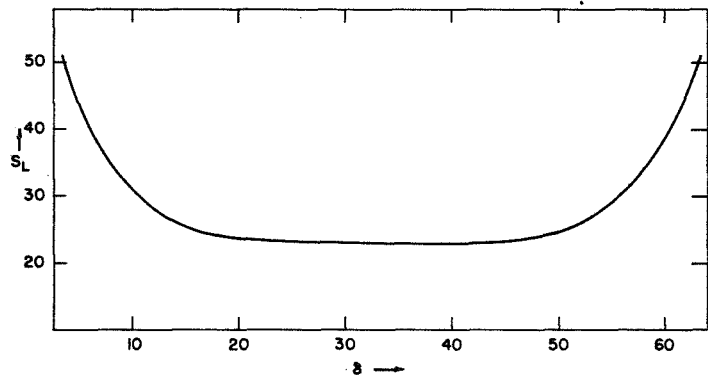
Since the $N(S)$ curve has not been measured at low radio frequencies down to very low flux levels, we have approximated it by assuming that it has the same shape as that measured at 178 MHz (Gower 1966) and at 408 MHz (Pooley and Ryle 1968); and we have also assumed that the flux-density scales according to the mean spectral index $\bar{\alpha}(\nu)$ as determined by Williams and Bridle (1967). In addition, we assume that the slope of the $\log N$, $\log S$ relation falls continuously to zero at very low flux levels.

The antenna pattern $G(\Omega)$ has sidelobe levels which depend on the declination to which the arrays are phased. Hence, the fluctuation level σ_{S_L} will be a function of declination.

Taking the confusion limit to be $S_L = 5 \sigma_{S_L}$, Eq. 1 was evaluated numerically for several declination settings of the array in the range $\delta = 3^\circ$ – 63° . The resulting confusion limit of the sky survey as a function of declination is shown in Fig. 4.

The uncertainty in S_L could be as high as a factor of 1.5 due to errors in the assumptions on $\bar{\alpha}(\nu)$, on the shape of the $N(S)$ curve at very low flux levels, and on whether or not the shape of $N(S)$ is actually the same as that observed at higher frequencies. The shape of the curve may be significantly affected by the class of low-frequency steep-spectrum sources (Williams and

FIG. 4. The confusion limit of the sky survey S_L in janskys as a function of declination in degrees.



Bridle 1967) whose number, flux-density relation is at present unknown.

Thermal noise fluctuations at the receiver output, due to receiver noise and galactic background radiation, are small compared to the fluctuations due to confusion and do not contribute significantly to the flux limit.

Since some 149 connectors must be adjusted in order to change the pointing of the antenna beam, there is some noninfinitesimal probability that at least one connection is not set properly at any given time. In addition, one or more dipoles may have a broken connection due to the flexing of cables and the aging effects of Sun, wind, and sandstorms.

Serious errors involving many wrongly adjusted connections are evident in the response of the array, or the lack of it, to a strong (>100 Jy) source. However, minor errors will more likely be reflected in an increased sidelobe level in some part of the sky. This will cause a slight increase in the confusion noise level due to weak sources, and will produce spurious apparent sources on the records when strong sources pass through the enhanced sidelobes.

B. Procedure

Because of the time and effort required to rephase the arrays, the antenna beam was usually left at a given declination setting for 3–5 days. Hence, each “run” constitutes several scans of a given declination strip taken on consecutive days.

During this period, several calibrations per day equivalent to a source of 180 Jy were applied to the records by means of the calibration noise source and a variable step attenuator. The noise source has previously been described by Viner (1975). The receiver is highly linear for flux densities up to several hundred janskys, but for declination strips containing sources stronger than about 300 Jy, additional calibrations approximately equal to the source strength were added to the records. For sources strong enough to saturate the receiver, attenuation was added between the hybrids (where the calibration signal is added to the antenna signal) and the input to the cross-correlation receiver. This attenuation reduces the signal to the region of receiver line-

arity but does not affect the ratio of source/calibration signals.

The antennas were tested about twice per month using a pulsing technique (Erickson 1965) to check for broken connectors and cables, or for tangled transmission lines. Attenuation of the various transmission lines and ionospheric data were not measured at the time of the observations. The Local Sidereal Time markers on the chart recorders were calibrated once or twice per day by means of WWV radio time signals and LST/Solar Time conversion tables. The time calibration was accurate to 0.1 min.

A total of 288 independent runs were taken intermittently with other research programs between November 1963 and December 1970. The early runs were taken at scattered declinations to look for interesting sources (Erickson and Cronyn 1965) and were interference free for about 20 h/day. Later data were taken more systematically but increased interference due to solar activity and the encroachments of civilization had reduced observation periods to 8–12 h/day, generally at night.

C. Sky Coverage

A given declination strip δ_0 was considered to be completely covered if there were data at all right ascensions from at least two days on each of at least two independent runs taken at dates separated by at least one month. Since adjacent declination strips are separated by $\frac{1}{2}$ of the NS beamwidth, coverage on at least two days in both adjacent declination strips was considered equivalent to two days coverage at δ_0 .

This definition ensures that in the area of sky covered, every source is observable at least four times, with at least two independent intermittent sidelobe patterns (see confusion discussion above). The coverage obtained by the Clark Lake instrument is shown graphically in Fig. 6 as a function of right ascension and declination.

However, this definition of sky coverage is independent of the confusion noise limit in various parts of the sky. The variation of S_L with declination was shown in Fig. 4. In addition, the flux limit increases strongly at

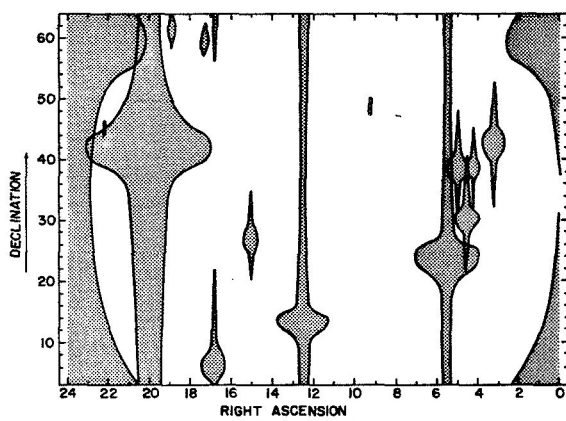


FIG. 5. Regions of enhanced confusion due to sidelobes of sources stronger than 300 Jy at 26.3 MHz.

all declinations near the right ascensions of very strong sources, due to NS sidelobes and to incomplete cancellation of the spaced-array-grating responses by the solid array. An indication of these regions of enhanced confusion caused by sources stronger than 300 Jy is shown in Fig. 5.

III. RESULTS AND ANALYSIS

A. Data Reduction

During the sky survey program preliminary data reduction was performed on each run. Upon completion of the observational program, all of the data were re-analyzed systematically starting with the declination strip at $63^{\circ} 20'$.

First, all in-phase records for a given strip were compared side by side. The positions of all apparent sources stronger than 0.8 times the confusion flux limit S_L were marked. Then the position of all the 3CR catalogue [the revised version of the third Cambridge catalogue of radio sources at 178 MHz (Bennett 1962)] sources in the strip were checked. The in-phase and quadrature-phase deflections were then scaled at each source position and upper limits to the deflections estimated for 3CR sources which were not detected.

For weak sources ($< 2S_L$), neighboring declination strips were rechecked for evidence of the sources on both in-phase and quadrature-phase records. The deflections were scaled and tabulated for antenna settings up to 70 arcmin away from the source positions in declination, and a note was made of the presence or absence of the effects of the source on the quadrature-phase records for a further 40-arcmin displacement in declination. These extra measurements were made to ensure that each source recorded was not due to an intermittent sidelobe in a given run and to improve the statistics when all observations of a given source were later averaged.

The apparent flux density obtained from each observation was corrected for displacement of the source from the center of the NS beam; for time constant effects; for daily and seasonal variations in transmission line attenuation with temperature; and for daily, seasonal, and solar cycle variations in ionospheric absorption (Viner 1973). The observed right ascension (corrected for time constant) and declination for each observation were precessed to 1950.0.

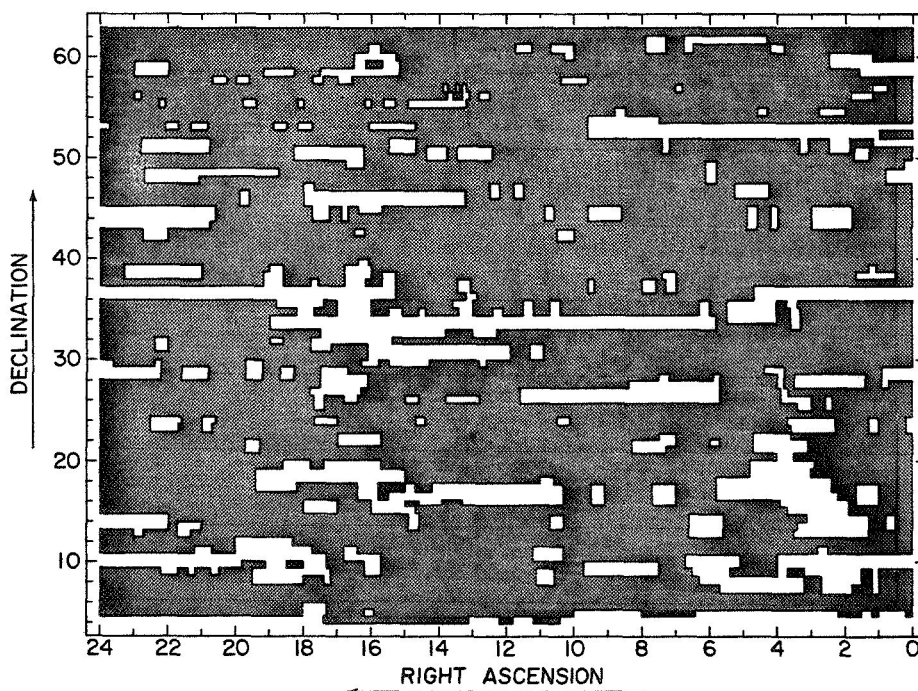


FIG. 6. Area of sky covered by the sky survey program as defined in Sec. II-C.

The width of the source drift curve was also measured for each observation in order to check on possible beam broadening due to extended sources. Primarily because of ionospheric effects, the uncertainty in beam broadening for a given drift curve is quite high; but the average of many such values can give significant results for sources equal to or larger than the beam size. For strong sources, it is possible to detect beam broadening due to angular structure as small as 6 arcmin when many observations are averaged.

Because the correction for ionospheric absorption was quite uncertain, each observation was assigned a weight from 1.0 to 0.3 depending on the size of the absorption correction applied to it. An additional weighting factor of 0.2 was applied to any observation which appeared to be affected by ionospheric scintillations. The derivation of this factor is discussed below.

All the observations of each source were collected together and the weighted mean positions, flux densities, and angular sizes were calculated for each source. Since the major sources of error in the flux densities are expected to be multiplicative, the flux densities were averaged on a logarithmic base.

Table I(a) gives the results for 471 sources in order of increasing right ascension. All sources are stronger than the flux limit derived above.

The first column gives the source designation based on the Parkes numbering system (CSIRO staff 1969). Any further reference to a source will use the letters CL followed by this designation.

In those cases in which a source has been previously catalogued, column 2 gives the most common catalogue name. The names are taken primarily from the 3CR (Bennett 1962), 4C (Pilkington and Scott 1965; Gower *et al.* 1967; Caswell and Crowther 1969), WKB (Williams *et al.* 1966), P (Shimmings and Day 1968), and VRO (MacLeod *et al.* 1965; Dickel *et al.* 1967; Wendker *et al.* 1970; Dickel *et al.* 1971) radio source catalogues.

Identification with a catalogued source is considered uncertain when the observed position differs from the catalogued position by more than twice the standard deviation in right ascension or declination. In these cases, the catalogue name is enclosed in brackets. Sources more than 3σ from any in these catalogues are labeled NPC in column 2.

The observed right ascension and declination (epoch 1950.0) and their standard errors are listed in columns 3 and 4, respectively.

Column 5 gives the mean flux density in janskys, corrected for partial resolution, and its error.

Column 6 gives the total number of observations and column 7 the sum of the weights of those data points. A comparison of the values gives some idea of the quality of the data for each source.

Comments on individual sources are made in column 8. The comment "E" means that the present data or high-frequency measurements show the source to be

extended in right ascension, and a partial resolution correction $\geq 3\%$ was required to obtain the integrated flux density. If the flux-density correction was $>10\%$, the flux is shown in brackets.

For sources stronger than ~ 100 Jy within 2° in right ascension and 90 arcmin in declination of known sidelobes of strong sources, the effects of the sidelobe confusion were taken into account in the quoted position, flux density, and errors, and the comment "C" was added to column 8. When the comment is given in parentheses, such an analysis has not been performed and the source parameters must be treated with caution.

Sources with $0^\circ 5'$ in right ascension and 30 arcmin in declination of known sidelobes were listed in Table I(b) because of the large errors involved.

Additional comments on sources of particular interest are given at the end of Table I. Table I(b) is identical to Table I(a) except that it lists 119 sources for which the observations are less reliable. Table I(c) gives upper limits on the fluxes of the small-diameter 3CR sources which were not detected at 26.3 MHz.

The quoted error bars are all standard deviations. They are calculated as the square root of the sum of the squares of statistical scatter, confusion errors, systematic measuring errors, and the uncertainties in the corrections applied to the right ascension and apparent flux. The quoted errors in flux density do not include the 10% uncertainty in the flux scale derived in the Sec. I-B. All sources thought to be extended at 26.3 MHz are listed in Table II along with the adopted factors used in calculating integrated flux densities. Of the sources observed, 16 showed significant beam broadening, in which $\bar{W} - W_0 > \sigma_W$. The value of σ_W , which is the uncertainty in the mean drift curve width measurement \bar{W} , includes statistical scatter, systematic chart scaling errors, and confusion errors. Two additional sources showed significant beam broadening on total-power records obtained for the absolute flux measurements (Viner 1973). Table II lists these 18 sources along with those sources known to be extended at higher frequencies for which partial resolution by the 14-arcmin EW beam is expected to be $\geq 3\%$. Sources for which there is substantial lack of agreement in high-frequency structure measurements by different authors were not included.

The first two columns of Table II give the source designation and the corresponding catalogue name. Column 3 gives the significance of the observed beam broadening $(\bar{W} - W_0)/\sigma_W$, and column 4 the equivalent Gaussian source size in the EW direction after deconvolution of the observed drift curves.

The next three columns summarize the high-frequency structure measurements, extrapolated to 26.3 MHz where possible. Column 5 states the structure class, whether double (D), core-halo (H), or a complex brightness distribution (C). If column 5 is left blank, the source is assumed to consist of a single component with a Gaussian or disk-shaped brightness distribution.

Column 6 gives the EW extent of each source to the half-brightness points. For double sources with small angular diameter components, the source separation is given, and for double sources with extended components, the mean component size is given, followed by the separation. References to the high-frequency structure measurements are given in column 7.

The adopted correction factors for partial resolution are listed in column 8, along with the error correspond-

ing to the uncertainty in the quoted structure and the possibility of non-Gaussian brightness distributions. These correction factors have been applied to the peak flux densities quoted in Table I but there may be errors inherent in the extrapolation of high-frequency structure data. The true structure of a given source at 26.3 MHz may be considerably different from that quoted at high frequencies if it contains one or more components with very steep spectra which would not be de-

TABLE I(a). Clark Lake 26.3-MHz Sky Survey source list. Values quoted are weighted averages corrected for ionospheric absorption, temperature effects, and time constant, and all errors are one standard deviation. Errors include statistical scatter, confusion, measuring uncertainty, and uncertainties in the various correction factors. Allowance has been made for partial resolution of extended sources.

| Source | Name | R.A. | Err | Dec. | Err | Flux | Err | Nobs | Sumwt | Remark |
|-----------|---------------------|---------|-----|----------|-----|-------|-----|------|-------|--------|
| CL0017+15 | 3C 9 | 00 17.7 | .2 | 15 40 19 | | 99. | 18. | 8 | 2.8 | (C) |
| CL0022+62 | (3C 10) | 00 22.5 | .2 | 62 42 25 | | 345. | 53. | 8 | 8.0 | C, E |
| CL0031+25 | NPC | 00 31.3 | .2 | 25 23 18 | | 32. | 7. | 13 | 9.2 | |
| CL0031+39 | 3C 13 | 00 31.5 | .2 | 39 23 13 | | 46. | 7. | 15 | 8.5 | |
| CL0033+18 | 3C 14 | 00 33.9 | .2 | 18 19 11 | | 69. | 7. | 11 | 7.4 | |
| CL0034+38 | 4C38.03 | 00 34.8 | .3 | 38 02 20 | | 29. | 6. | 14 | 8.6 | |
| CL0035+12 | 3C 16 | 00 35.1 | .2 | 12 57 9 | | 99. | 9. | 6 | 3.0 | (C) |
| CL0038+09 | 3C 18 | 00 38.4 | .2 | 09 30 17 | | 127. | 27. | 11 | 8.4 | C |
| CL0038+32 | 3C 19 | 00 38.5 | .2 | 32 48 14 | | 44. | 6. | 20 | 16.1 | |
| CL0038+25 | 4C25.02 | 00 38.8 | .2 | 25 36 16 | | 39. | 6. | 5 | 3.2 | |
| CL0040+51 | 3C 20 | 00 40.0 | .3 | 51 47 10 | | 152. | 13. | 10 | 9.8 | C |
| CL0048+51 | 3C 22 | 00 48.3 | .2 | 51 09 12 | | 76. | 9. | 12 | 14.2 | C |
| CL0053+26 | 3C 28 | 00 53.3 | .1 | 26 26 9 | | 115. | 9. | 24 | 20.2 | |
| CL0055+26 | 4C26.03 | 00 55.8 | .2 | 26 56 13 | | 44. | 6. | 16 | 12.6 | |
| CL0100+25 | 4C25.03 | 01 00.4 | .2 | 25 46 19 | | 31. | 6. | 12 | 9.6 | |
| CL0104+32 | 3C 31 | 01 04.7 | .2 | 32 21 11 | | 65. | 7. | 23 | 19.5 | |
| CL0105+53 | NPC | 01 05.1 | .3 | 53 51 11 | | 79. | 9. | 10 | 6.4 | |
| CL0106+13 | 3C 33 | 01 06.2 | .1 | 13 19 8 | | 222. | 26. | 12 | 5.6 | |
| CL0107+31 | 3C 34 | 01 07.5 | .1 | 31 48 11 | | (86.) | 13. | 22 | 15.8 | E |
| CL0109+49 | 3C 35 | 01 09.4 | .3 | 49 27 14 | | 47. | 6. | 12 | 7.0 | |
| CL0115+45 | 3C 36 | 01 15.5 | .2 | 45 42 15 | | 41. | 7. | 15 | 15.0 | |
| CL0119+37 | 4C37.04 | 01 19.2 | .4 | 37 51 24 | | 25. | 7. | 9 | 6.8 | |
| CL0122+27 | NPC | 01 22.4 | .3 | 27 56 22 | | 28. | 7. | 7 | 6.0 | |
| CL0124+32 | 3C 41 + 4C32.07 | 01 24.8 | .3 | 32 44 22 | | 28. | 6. | 11 | 9.4 | |
| CL0125+29 | 3C 42 | 01 25.9 | .2 | 29 11 14 | | 41. | 6. | 12 | 8.6 | |
| CL0127+23 | 3C 43 | 01 27.2 | .2 | 23 15 13 | | 46. | 6. | 22 | 16.7 | |
| CL0128+25 | 4C25.07 | 01 28.8 | .2 | 25 15 13 | | 46. | 6. | 22 | 13.5 | |
| CL0129+06 | 3C 44 | 01 29.1 | .2 | 06 26 17 | | 72. | 12. | 11 | 6.7 | (C) |
| CL0132+37 | 3C 46 | 01 32.6 | .2 | 37 43 11 | | 58. | 6. | 17 | 11.6 | |
| CL0133+20 | 3C 47 | 01 33.7 | .1 | 20 47 6 | | 190. | 13. | 24 | 16.8 | |
| CL0134+30 | 4C29.03 | 01 34.0 | .2 | 30 16 13 | | 43. | 8. | 15 | 12.1 | |
| CL0135+32 | 3C 48 | 01 35.0 | .2 | 32 48 16 | | 37. | 6. | 13 | 10.9 | |
| CL0136+39 | 4C39.04 | 01 36.7 | .2 | 39 49 10 | | 64. | 6. | 25 | 19.0 | |
| CL0143+27 | 4C27.05 | 01 43.7 | .3 | 27 59 18 | | 33. | 6. | 10 | 8.7 | |
| CL0145+53 | 3C 52 | 01 45.5 | .4 | 53 23 14 | | 50. | 7. | 8 | 5.0 | |
| CL0150+16 | 4C16.04 | 01 50.4 | .2 | 16 30 18 | | 36. | 8. | 5 | 4.4 | |
| CL0150+40 | 4C40.07 | 01 50.8 | .2 | 40 49 18 | | 33. | 6. | 30 | 23.7 | |
| CL0153+43 | 3C 54 | 01 53.0 | .3 | 43 28 13 | | 51. | 9. | 11 | 5.5 | |
| CL0154+28 | 3C 55 | 01 54.5 | .1 | 28 49 8 | | 88. | 7. | 18 | 13.0 | |
| CL0157+40 | 4C40.08 | 01 57.5 | .2 | 40 41 12 | | 52. | 6. | 36 | 27.2 | E |
| CL0200+20 | 4C19.07 | 02 00 5 | .3 | 20 05 19 | | 34. | 6. | 10 | 8.6 | |
| CL0204+29 | 3C 59 | 02 04.2 | .2 | 29 32 11 | | 52. | 7. | 18 | 12.8 | |
| CL0208+20 | 3C 60 | 02 08.5 | .2 | 20 54 19 | | 31. | 7. | 5 | 4.3 | |
| CL0212+35 | 4C36.03+ 4C34.06 | 02 12.2 | .3 | 35 27 24 | | 25. | 7. | 10 | 10.0 | |
| CL0214+27 | 4C27.07 | 02 14.0 | .4 | 27 56 19 | | 31. | 9. | 5 | 3.3 | |

TABLE I(a) (continued)

| Source | Name | R.A. | Err | Dec. | Err | Flux | Err | Nobs | Sumwt | Remark |
|-----------|-----------|---------|-----|----------|-----|--------|------|------|-------|--------|
| CL0449+52 | 3C130 | 04 49.4 | .2 | 52 09 11 | | 75. | 8. | 10 | 9.0 | |
| CL0450+31 | 3C131 | 04 50.0 | .2 | 31 26 8 | | (119.) | 14. | 15 | 13.4 | E |
| CL0454+22 | 3C132 | 04 54.1 | .2 | 22 37 11 | | 63. | 8. | 23 | 10.9 | (C) |
| CL0500+25 | 3C133 | 05 00.0 | .2 | 25 03 10 | | 97. | 21. | 19 | 15.5 | C |
| CL0501+37 | 3C134 | 05 01.3 | .1 | 37 58 5 | | 469. | 18. | 26 | 22.4 | |
| CL0513+51 | 3C136 | 05 13.0 | .3 | 51 13 19 | | 36. | 7. | 10 | 9.0 | |
| CL0513+24 | 3C136.1 | 05 13.1 | .2 | 24 47 10 | | 105. | 26. | 19 | 15.2 | C, E |
| CL0513+45 | 4C45.08 | 05 13.8 | .3 | 45 31 15 | | 39. | 6. | 9 | 7.0 | |
| CL0515+50 | 3C137 | 05 15.9 | .3 | 50 58 15 | | 45. | 7. | 13 | 11.7 | |
| CL0521+28 | 3C139.2 | 05 21.1 | .2 | 28 23 10 | | 78. | 11. | 15 | 13.2 | (C) |
| CL0522+51 | 4C51.18 | 05 22.4 | .3 | 51 39 19 | | 36. | 7. | 13 | 11.4 | |
| CL0523+32 | 3C141 | 05 23.7 | .2 | 32 44 9 | | 71. | 6. | 16 | 13.8 | (C) |
| CL0529+06 | 3C142.1 | 05 29.1 | .2 | 06 25 15 | | 160. | 38. | 20 | 12.2 | C |
| CL0531+22 | 3C144 | 05 31.6 | .1 | 22 09 6 | | 2829. | 133. | 56 | 37.0 | E |
| CL0538+48 | 3C147 | 05 38.5 | .3 | 48 22 16 | | 39. | 7. | 15 | 12.8 | (C) |
| | 4C47.16 | | | | | | | | | |
| CL0548+28 | 3C149 | 05 48.1 | .2 | 28 53 15 | | 40. | 6. | 17 | 14.2 | |
| CL0548+37 | 4C37.14 | 05 48.5 | .3 | 37 22 17 | | 36. | 6. | 8 | 5.4 | |
| CL0555+15 | 4C15.17 | 05 55.7 | .2 | 15 53 16 | | 49. | 8. | 6 | 4.7 | |
| CL0559+42 | 3C151 | 05 59.8 | .2 | 42 31 17 | | 36. | 6. | 18 | 17.4 | |
| CL0601+24 | 4C24.11 | 06 01.8 | .2 | 24 35 15 | | 40. | 7. | 11 | 9.3 | (C) |
| CL0606+48 | 3C153 | 06 06.1 | .3 | 48 20 15 | | 42. | 8. | 8 | 6.4 | |
| CL0610+26 | 3C154 | 06 10.9 | .2 | 26 17 10 | | 119. | 16. | 12 | 11.2 | C |
| CL0611+42 | 4C42.17 | 06 11.4 | .3 | 42 51 17 | | 34. | 6. | 12 | 9.4 | |
| CL0613+54 | 4C54.09+ | 06 13.8 | .4 | 54 54 23 | | 35. | 8. | 9 | 6.3 | |
| | 4C55.12 | | | | | | | | | |
| CL0614+22 | 3C157 | 06 14.1 | .2 | 22 35 10 | | (600.) | 48. | 55 | 39.1 | E |
| CL0614+37 | 4C37.16 | 06 14.3 | .3 | 37 34 23 | | 26. | 7. | 10 | 7.8 | |
| CL0617+29 | VR0290603 | 06 17.4 | .2 | 29 22 16 | | 37. | 6. | 21 | 19.2 | |
| CL0619+14 | 3C158 | 06 19.3 | .3 | 14 40 12 | | 73. | 7. | 6 | 5.0 | |
| CL0622+40 | 3C159 | 06 22.0 | .2 | 40 15 10 | | 67. | 6. | 32 | 30.0 | |
| CL0628+25 | 3C162 | 06 28.7 | .2 | 25 06 10 | | 72. | 7. | 18 | 13.6 | (C) |
| CL0630+47 | 4C46.12 | 06 30.5 | .3 | 47 33 23 | | 28. | 7. | 16 | 12.9 | |
| CL0631+44 | NPC | 06 31.5 | .3 | 44 32 17 | | 35. | 7. | 4 | 3.7 | |
| CL0636+29 | 4C29.23 | 06 36.7 | .3 | 29 57 19 | | 31. | 6. | 10 | 9.2 | |
| CL0640+23 | 3C165 | 06 40.1 | .2 | 23 22 11 | | 58. | 7. | 19 | 7.4 | |
| CL0642+21 | 3C166 | 06 42.3 | .1 | 21 25 8 | | 108. | 8. | 18 | 11.1 | |
| CL0647+45 | 3C169.1 | 06 47.7 | .3 | 45 14 12 | | 50. | 6. | 15 | 10.7 | |
| CL0647+41 | 4C41.17 | 06 47.8 | .3 | 41 40 17 | | 36. | 6. | 9 | 7.0 | |
| CL0651+54 | 3C171 | 06 51.7 | .3 | 54 20 11 | | 97. | 10. | 11 | 8.8 | |
| CL0656+36 | 4C35.14 | 06 56.2 | .3 | 36 01 15 | | 39. | 6. | 9 | 9.0 | |
| CL0658+23 | 4C23.18 | 06 58.3 | .2 | 23 19 12 | | 50. | 6. | 31 | 17.4 | (C) |
| CL0659+38 | 3C173 | 06 59.1 | .3 | 38 04 18 | | 33. | 6. | 11 | 8.1 | |
| CL0659+25 | 3C172 | 06 59.4 | .2 | 25 21 9 | | 71. | 6. | 16 | 13.2 | |
| CL0703+42 | 4C42.23 | 07 03.3 | .2 | 42 51 16 | | 39. | 7. | 12 | 11.5 | E |
| CL0704+38 | 4C38.20 | 07 04.1 | .2 | 38 26 12 | | 51. | 6. | 13 | 12.7 | |
| CL0710+12 | 3C175 | 07 10.3 | .1 | 12 02 8 | | 132. | 10. | 27 | 19.5 | |
| CL0711+45 | 4C45.13 | 07 11.0 | .3 | 45 44 18 | | 33. | 7. | 13 | 12.4 | |
| CL0713+37 | NPC | 07 13.9 | .2 | 37 15 18 | | 34. | 6. | 8 | 6.7 | |
| CL0718+36 | 4C35.17 | 07 18.3 | .3 | 36 12 18 | | 32. | 7. | 13 | 13.0 | |
| CL0721+19 | 4C19.29 | 07 21.2 | .2 | 19 00 21 | | 42. | 6. | 21 | 18.4 | |
| CL0721+31 | 4C31.27 | 07 21.8 | .3 | 31 36 21 | | 28. | 7. | 11 | 10.0 | |
| CL0722+15 | 3C177 | 07 22.3 | .2 | 15 42 13 | | 56. | 7. | 6 | 5.2 | |
| CL0724+31 | 4C31.28 | 07 24.4 | .2 | 31 22 19 | | 31. | 7. | 5 | 5.0 | |
| CL0725+14 | 3C181 | 07 25.9 | .2 | 14 34 13 | | 57. | 8. | 7 | 6.2 | |
| CL0726+24 | 3C182 | 07 26.4 | .1 | 24 38 8 | | 114. | 8. | 21 | 16.4 | |
| CL0732+43 | 3C183 | 07 32.0 | .2 | 43 59 15 | | 38. | 9. | 3 | 3.0 | |
| CL0732+29 | 4C29.25 | 07 32.9 | .3 | 29 08 27 | | 23. | 7. | 16 | 13.0 | |
| CL0734+36 | 4C36.13 | 07 34.2 | .3 | 36 13 22 | | 27. | 6. | 12 | 11.0 | |
| CL0736+21 | 4C21.23 | 07 36.6 | .2 | 21 06 16 | | 36. | 6. | 10 | 8.5 | |

TABLE I(a) (continued)

| Source | Name | R.A. | Err | Dec. | Err | Flux | Err | Nobs | Sumwt | Remark |
|-----------|-----------|---------|-----|----------|-----|--------|-----|------|-------|--------|
| CL0741+38 | 3C186 | 07 41.0 | .2 | 38 11 11 | | 54. | 7. | 14 | 12.1 | |
| CL0742+31 | 4C31.30 | 07 42.8 | .2 | 31 51 15 | | 38. | 6. | 17 | 16.0 | |
| CL0745+55 | 4C56.16 | 07 45.3 | .3 | 55 52 14 | | (130.) | 25. | 16 | 13.4 | E |
| CL0749+29 | 4C29.26 | 07 49.9 | .3 | 29 50 19 | | 31. | 7. | 15 | 13.2 | |
| CL0752+17 | 4C18.23 | 07 52.8 | .3 | 17 57 25 | | 27. | 7. | 5 | 4.0 | |
| CL0758+50 | WKB | 07 58.2 | .3 | 50 36 19 | | 34. | 7. | 11 | 10.4 | |
| CL0759+14 | 3C190 | 07 59.1 | .2 | 14 32 12 | | 64. | 8. | 11 | 7.3 | |
| CL0800+45 | 4C45.14 | 08 00.5 | .4 | 45 36 21 | | 30. | 7. | 12 | 10.2 | |
| CL0802+10 | 3C191 | 08 02.2 | .2 | 10 37 18 | | 46. | 8. | 27 | 18.7 | |
| CL0802+24 | 3C192 | 08 02.5 | .1 | 24 24 7 | | 136. | 9. | 28 | 17.9 | |
| CL0806+42 | 3C194 | 08 06.8 | .2 | 42 26 16 | | 40. | 8. | 16 | 13.4 | |
| CL0810+36 | 4C37.23+ | 08 10.2 | .3 | 36 18 20 | | 30. | 7. | 11 | 10.0 | |
| | 4C35.19 | | | | | | | | | |
| CL0810+48 | 3C196 | 08 10.2 | .2 | 48 30 7 | | 218. | 14. | 29 | 21.3 | |
| CL0815+52 | 4C52.18 | 08 15.7 | .5 | 52 46 29 | | 27. | 11. | 6 | 4.2 | |
| CL0817+10 | 4C09.28 | 08 17.8 | .2 | 10 04 18 | | 48. | 10. | 4 | 2.3 | |
| CL0818+18 | 4C18.24 | 08 18.1 | .2 | 18 25 19 | | 34. | 7. | 5 | 4.2 | |
| CL0818+47 | 3C197.1 | 08 18.5 | .2 | 47 03 13 | | 49. | 6. | 15 | 14.0 | (C) |
| CL0820+06 | 3C198 | 08 20.0 | .2 | 06 14 16 | | 74. | 11. | 27 | 22.9 | |
| CL0820+42 | 3C199 | 08 20.4 | .3 | 42 46 21 | | 29. | 6. | 12 | 10.4 | |
| CL0822+34 | NPC | 08 22.9 | .2 | 34 38 17 | | 34. | 6. | 12 | 12.0 | |
| CL0824+29 | 3C200 | 08 24.5 | .1 | 29 33 10 | | 68. | 6. | 25 | 21.6 | |
| CL0825+35 | (4C35.20) | 08 25.4 | .3 | 35 32 19 | | 31. | 7. | 5 | 5.0 | |
| CL0825+24 | 4C24.17 | 08 25.9 | .2 | 24 35 11 | | 58. | 6. | 19 | 13.6 | |
| CL0827+45 | 4C45.16 | 08 27.4 | .3 | 45 48 18 | | 36. | 6. | 11 | 7.4 | |
| CL0829+51 | 4C51.25 | 08 29.7 | .3 | 51 25 19 | | 36. | 7. | 14 | 11.5 | |
| CL0830+12 | 4C11.28 | 08 30.9 | .2 | 12 03 16 | | 47. | 8. | 15 | 13.7 | |
| CL0831+55 | 4C55.16 | 08 31.7 | .4 | 55 35 24 | | 35. | 8. | 8 | 7.4 | |
| CL0834+44 | 4C45.17 | 08 34.8 | .2 | 44 59 15 | | 41. | 6. | 17 | 14.0 | |
| CL0834+58 | 3C205 | 08 34.9 | .3 | 58 28 20 | | 60. | 10. | 10 | 7.4 | |
| CL0836+51 | (4C50.27) | 08 36.1 | .4 | 51 34 22 | | 32. | 7. | 13 | 13.0 | |
| CL0838+13 | 3C207 | 08 38.1 | .2 | 13 29 13 | | 61. | 7. | 15 | 12.1 | |
| CL0840+29 | 4C29.31 | 08 40.3 | .2 | 29 51 12 | | 50. | 6. | 18 | 16.2 | |
| CL0843+15 | (4C15.26) | 08 43.9 | .2 | 15 09 18 | | 37. | 7. | 8 | 7.4 | |
| CL0845+32 | 4C31.32 | 08 45.0 | .3 | 32 00 22 | | 27. | 7. | 15 | 15.0 | |
| CL0848+49 | 4C49.18 | 08 48.1 | .4 | 49 19 25 | | 29. | 7. | 7 | 6.0 | |
| CL0850+14 | 3C208 | 08 50.7 | .2 | 14 10 10 | | 83. | 10. | 15 | 11.8 | |
| CL0852+14 | 3C208.1 | 08 52.2 | .2 | 14 34 15 | | 48. | 7. | 10 | 7.9 | |
| CL0853+29 | 4C29.32 | 08 53.1 | .3 | 29 10 23 | | 26. | 7. | 16 | 13.4 | |
| CL0854+10 | 4C09.32 | 08 54.5 | .2 | 10 09 23 | | 40. | 9. | 14 | 10.3 | |
| CL0854+34 | 3C211 | 08 54.5 | .2 | 34 20 15 | | 38. | 6. | 8 | 5.7 | |
| CL0855+28 | 3C210 | 08 55.2 | .2 | 28 15 11 | | 63. | 6. | 20 | 15.8 | |
| CL0856+14 | 3C212 | 08 56.3 | .2 | 14 35 14 | | 51. | 7. | 12 | 9.1 | |
| CL0857+29 | 3C213.1+ | 08 58.0 | .2 | 29 36 16 | | 35. | 6. | 16 | 15.0 | |
| | 4C29.34 | | | | | | | | | |
| CL0858+55 | 4C56.17 | 08 58.2 | .5 | 55 53 26 | | 33. | 9. | 13 | 13.0 | |
| CL0904+17 | 3C215 | 09 04.1 | .2 | 17 02 12 | | 66. | 8. | 8 | 5.3 | |
| CL0904+41 | 4C41.19 | 09 04.6 | .3 | 41 10 23 | | 28. | 6. | 28 | 26.0 | E |
| CL0906+37 | 3C217 | 09 06.0 | .2 | 37 48 14 | | 43. | 6. | 14 | 10.8 | |
| CL0906+43 | 3C216 | 09 06.5 | .2 | 43 03 9 | | 88. | 7. | 16 | 12.8 | |
| CL0907+18 | NPC | 09 07.7 | .2 | 18 33 14 | | 45. | 9. | 12 | 9.3 | |
| CL0909+37 | 4C38.27 | 09 09.0 | .2 | 37 58 8 | | 98. | 7. | 18 | 14.8 | |
| CL0909+17 | 4C16.27 | 09 09.5 | .2 | 17 03 19 | | 33. | 7. | 2 | 2.0 | |
| CL0911+17 | 4C17.48 | 09 11.5 | .2 | 17 31 13 | | 47. | 11. | 6 | 5.2 | |
| CL0918+45 | 3C219 | 09 18.2 | .2 | 45 42 6 | | 212. | 11. | 17 | 14.2 | |
| CL0922+14 | 4C14.31 | 09 22.2 | .3 | 14 44 17 | | (55.) | 11. | 13 | 9.8 | E |
| CL0922+42 | 4C42.29 | 09 22.7 | .3 | 42 27 16 | | 40. | 6. | 12 | 9.6 | |
| CL0924+39 | 4C39.25 | 09 24.2 | .3 | 39 23 18 | | 33. | 6. | 13 | 12.0 | |
| CL0927+06 | 4C06.36 | 09 27.8 | .3 | 06 46 27 | | 43. | 11. | 23 | 20.4 | |
| CL0927+36 | 3C220.2 | 09 27.9 | .2 | 36 08 13 | | 44. | 6. | 13 | 10.4 | |

TABLE I(a) (continued)

| Source | Name | R.A. | Err | Dec. | Err | Flux | Err | Nobs | Sumwt | Remark |
|-----------|------------|---------|-----|----------|-----|------|-----|------|-------|--------|
| CL0932+40 | 3C221 | 09 32.0 | .2 | 40 12 15 | | 41. | 6. | 21 | 19.2 | |
| CL0936+40 | 3C40.23 | 09 36.3 | .2 | 40 36 18 | | 35. | 6. | 19 | 14.2 | |
| CL0937+36 | 3C223 | 09 37.0 | .2 | 36 10 8 | | 82. | 7. | 14 | 11.3 | |
| CL0938+39 | 3C223.1 | 09 38.4 | .2 | 39 50 11 | | 59. | 6. | 30 | 27.5 | |
| CL0939+14 | 3C225 | 09 39.8 | .1 | 14 16 9 | | 94. | 9. | 19 | 16.6 | |
| CL0941+10 | 3C226 | 09 41.8 | .2 | 10 12 10 | | 97. | 9. | 20 | 15.0 | |
| CL0943+54 | 4C54.19.1 | 09 43.6 | .3 | 54 36 19 | | 41. | 8. | 10 | 6.5 | |
| CL0945+07 | 3C227 | 09 45.3 | .1 | 07 47 9 | | 162. | 10. | 17 | 12.0 | |
| CL0945+41 | 4C41.20+ | 09 45.9 | .3 | 41 30 15 | | 42. | 6. | 5 | 4.0 | |
| | 4C40.24 | | | | | | | | | |
| CL0947+14 | 3C228 | 09 47.8 | .2 | 14 53 11 | | 68. | 8. | 15 | 13.2 | |
| CL0949+24 | 3C229 | 09 49.2 | .2 | 24 34 13 | | 46. | 7. | 13 | 9.7 | |
| CL0949+52 | (4C53.20) | 09 49.6 | .4 | 52 35 24 | | 31. | 8. | 8 | 7.1 | |
| CL0951+25 | 4C25.29 | 09 51.2 | .3 | 25 39 22 | | 28. | 7. | 9 | 6.4 | |
| CL0955+32 | 4C32.32+ | 09 55.1 | .3 | 32 09 22 | | 27. | 6. | 15 | 14.6 | |
| | 4C32.33 | | | | | | | | | |
| CL0956+48 | 4C47.31 | 09 56.3 | .4 | 48 02 22 | | 30. | 7. | 17 | 15.0 | |
| CL0959+29 | 3C234 | 09 59.0 | .1 | 29 10 7 | | 177. | 12. | 28 | 21.9 | |
| CL1001+32 | 4C32.34 | 10 01.7 | .2 | 32 08 14 | | 40. | 6. | 18 | 15.6 | |
| CL1002+35 | 3C236 | 10 02.8 | .3 | 35 29 20 | | 29. | 6. | 16 | 11.6 | |
| CL1003+48 | 3C235 | 10 03.8 | .4 | 48 34 24 | | 27. | 9. | 9 | 8.0 | |
| CL1004+44 | 4C44.19 | 10 04.5 | .3 | 44 40 16 | | 38. | 6. | 8 | 6.6 | |
| CL1004+34 | NRA0346 | 10 04.7 | .3 | 34 46 20 | | 29. | 6. | 10 | 5.4 | |
| CL1005+08 | 3C237 | 10 05.9 | .3 | 08 16 24 | | 43. | 10. | 15 | 7.9 | |
| CL1006+41 | 4C41.21 | 10 06.9 | .3 | 41 57 22 | | 27. | 7. | 7 | 7.0 | |
| CL1008+07 | 3C238 | 10 08.7 | .2 | 07 08 18 | | 62. | 10. | 11 | 9.4 | |
| CL1009+46 | 3C239 | 10 09.0 | .2 | 46 35 9 | | 78. | 8. | 16 | 11.6 | |
| CL1012+31 | VRO311001 | 10 12.5 | .3 | 31 35 23 | | 26. | 7. | 11 | 10.0 | |
| CL1013+41 | (4C41.22) | 10 13.7 | .3 | 41 19 17 | | 35. | 6. | 9 | 9.0 | |
| CL1014+27 | 3C240 | 10 14.6 | .3 | 27 40 24 | | 26. | 7. | 11 | 9.4 | |
| CL1014+39 | (4C39.29+) | 10 14.9 | .2 | 39 30 13 | | 45. | 8. | 7 | 7.0 | |
| | (4C39.30) | | | | | | | | | |
| CL1018+31 | 4C31.35 | 10 18.0 | .2 | 21 43 22 | | 28. | 6. | 15 | 3.0 | |
| CL1022+20 | 3C242 | 10 22.6 | .2 | 20 14 14 | | 43. | 9. | 19 | 13.6 | |
| CL1024+07 | 3C243 | 10 24.3 | .2 | 07 01 19 | | 57. | 10. | 13 | 9.4 | |
| CL1024+46 | 4C46.21 | 10 24.3 | .3 | 46 10 18 | | 34. | 6. | 10 | 8.0 | |
| CL1025+48 | (3C244) | 10 25.5 | .4 | 48 25 23 | | 30. | 8. | 7 | 7.0 | |
| CL1029+35 | NPC | 10 29.1 | .2 | 35 19 17 | | 34. | 7. | 7 | 3.9 | |
| CL1030+25 | 4C25.33 | 10 30.3 | .3 | 25 11 19 | | 32. | 7. | 15 | 9.6 | |
| CL1030+58 | 3C244.1 | 10 30.5 | .3 | 58 34 14 | | 99. | 10. | 16 | 13.3 | |
| CL1039+50 | 4C50.31 | 10 39.3 | .3 | 50 45 17 | | 39. | 7. | 13 | 12.0 | |
| CL1040+12 | 3C245 | 10 40.0 | .2 | 12 17 11 | | 73. | 8. | 24 | 19.9 | |
| CL1043+54 | 4C55.21 | 10 43.5 | .3 | 54 59 17 | | 49. | 8. | 12 | 10.4 | |
| CL1043+37 | 4C37.28 | 10 43.8 | .4 | 37 24 24 | | 25. | 7. | 6 | 5.3 | |
| CL1055+20 | 4C20.24 | 10 55.7 | .2 | 20 34 13 | | 47. | 7. | 19 | 14.9 | |
| CL1056+43 | 3C247 | 10 56.0 | .3 | 43 17 21 | | 29. | 7. | 13 | 10.5 | |
| CL1057+09 | 4C09.38 | 10 57.2 | .2 | 09 06 16 | | 57. | 9. | 13 | 11.7 | |
| CL1057+30 | 3C248 | 10 57.2 | .2 | 30 40 12 | | 51. | 6. | 9 | 7.4 | |
| CL1059+56 | 4C56.18 | 10 59.6 | .4 | 56 19 24 | | 37. | 9. | 12 | 10.0 | |
| CL1104+16 | 4C16.30 | 11 04.6 | .3 | 16 34 19 | | 34. | 7. | 5 | 5.0 | |
| CL1104+36 | 4C36.18 | 11 04.8 | .3 | 36 27 22 | | 27. | 7. | 9 | 9.0 | |
| CL1106+25 | 3C250 | 11 06.4 | .2 | 25 24 8 | | 105. | 8. | 22 | 15.9 | |
| CL1107+37 | 4C37.29 | 11 07.2 | .2 | 37 46 12 | | 50. | 6. | 10 | 9.2 | |
| CL1109+41 | 4C41.23 | 11 09.0 | .2 | 41 04 14 | | 45. | 6. | 21 | 18.4 | |
| CL1109+35 | 3C252 | 11 09.1 | .2 | 35 55 8 | | 96. | 8. | 13 | 9.8 | |
| CL1112+41 | 3C254 | 11 12.0 | .2 | 41 01 9 | | 96. | 8. | 26 | 22.5 | |
| CL1113+59 | NPC | 11 13.7 | .6 | 59 49 32 | | 39. | 13. | 8 | 8.0 | |
| CL1114+29 | 4C29.41 | 11 14.0 | .2 | 29 21 17 | | 34. | 7. | 14 | 11.6 | |
| CL1118+23 | 3C256 | 11 18.0 | .2 | 23 41 15 | | 41. | 6. | 27 | 14.9 | |
| CL1121+31 | NPC | 11 21.4 | .3 | 31 33 21 | | 28. | 7. | 7 | 6.0 | |

(C), E

TABLE I(a) (continued)

| Source | Name | R.A. | Err | Dec. | Err | Flux | Err | Nobs | Sumwt | Remark |
|-----------|-----------|---------|-----|----------|-----|--------|------|------|-------|--------|
| CL1121+44 | VRO431102 | 11 21.5 | .2 | 44 06 15 | | 40. | 7. | 12 | 11.0 | |
| CL1123+30 | 4C30.21 | 11 23.6 | .3 | 30 17 20 | | 29. | 7. | 9 | 7.6 | |
| CL1125+26 | 4C25.35 | 11 25.7 | .3 | 26 19 23 | | 26. | 7. | 11 | 9.4 | |
| CL1128+43 | VRO431103 | 11 28.3 | .3 | 43 48 22 | | 28. | 7. | 11 | 9.2 | |
| CL1131+49 | NPC | 11 31.1 | .3 | 49 53 17 | | 39. | 7. | 25 | 23.1 | |
| CL1131+33 | 4C33.28+ | 11 31.2 | .3 | 33 42 20 | | 31. | 6. | 6 | 3.0 | |
| | 4C33.27 | | | | | | | | | |
| CL1132+30 | 3C261 | 11 32.7 | .3 | 30 28 14 | | 43. | 6. | 9 | 6.0 | |
| CL1136+31 | WKB | 11 36.0 | .2 | 31 26 18 | | 33. | 6. | 7 | 4.9 | |
| CL1140+58 | 4C58.22 | 11 40.2 | .5 | 58 28 28 | | 38. | 11. | 8 | 7.3 | |
| CL1140+49 | 4C49.21 | 11 40.4 | .4 | 49 17 26 | | 26. | 7. | 9 | 7.0 | |
| CL1140+21 | 3C263.1+ | 11 40.8 | .2 | 21 51 12 | | 83. | 7. | 33 | 23.6 | |
| | P1140+21 | | | | | | | | | |
| CL1142+20 | 3C264 | 11 42.8 | .2 | 20 02 7 | | 141. | 10. | 29 | 18.7 | |
| CL1143+31 | 3C265 | 11 43.0 | .1 | 31 51 7 | | 129. | 7. | 18 | 14.9 | |
| CL1143+50 | 3C266 | 11 43.4 | .3 | 50 10 20 | | 33. | 8. | 14 | 12.4 | |
| CL1147+12 | 3C267 | 11 47.5 | .2 | 12 56 11 | | 69. | 7. | 9 | 6.9 | (C) |
| CL1151+51 | 4C51.28 | 11 51.4 | .4 | 51 04 26 | | 28. | 7. | 14 | 13.0 | |
| CL1151+38 | 4C38.32 | 11 51.7 | .3 | 38 36 22 | | 28. | 7. | 14 | 12.2 | |
| CL1151+29 | 4C29.44 | 11 51.9 | .2 | 29 37 11 | | 55. | 7. | 21 | 19.2 | |
| CL1153+55 | 4C55.22 | 11 53.0 | .3 | 55 21 14 | | 60. | 8. | 10 | 9.0 | E |
| CL1156+27 | 4C26.35 | 11 56.1 | .2 | 27 01 17 | | 37. | 8. | 7 | 6.4 | |
| CL1158+32 | 3C268.2 | 11 58.6 | .2 | 32 00 19 | | 31. | 7. | 13 | 11.4 | |
| CL1158+25 | 4C25.38 | 11 58.9 | .3 | 25 30 21 | | 29. | 6. | 11 | 8.2 | |
| CL1201+24 | P1201+24 | 12 01.2 | .3 | 24 28 22 | | 28. | 7. | 9 | 8.0 | |
| CL1202+29 | 4C29.46 | 12 02.5 | .2 | 29 42 12 | | 53. | 6. | 19 | 16.2 | |
| CL1202+49 | NPC | 12 02.8 | .4 | 49 21 27 | | 25. | 7. | 10 | 9.0 | |
| CL1205+39 | 4C39.35 | 12 05.5 | .3 | 39 07 20 | | 29. | 6. | 19 | 18.0 | |
| CL1206+43 | 3C268.4 | 12 06.6 | .3 | 43 57 18 | | 34. | 8. | 11 | 10.0 | |
| CL1213+53 | 4C53.24 | 12 13.2 | .3 | 53 56 14 | | 55. | 9. | 7 | 4.3 | |
| CL1216+20 | 4C20.28 | 12 16.6 | .2 | 20 21 12 | | 57. | 7. | 12 | 6.5 | |
| CL1216+06 | 3C270 | 12 16.7 | .1 | 06 25 10 | | (162.) | 21. | 24 | 17.7 | E |
| CL1218+33 | 3C270.1 | 12 18.3 | .2 | 33 40 10 | | 60. | 8. | 7 | 3.0 | |
| CL1219+31 | 4C31.40 | 12 19.4 | .2 | 31 55 15 | | 37. | 6. | 12 | 8.4 | |
| CL1222+42 | 3C272 | 12 22.3 | .2 | 42 52 18 | | 35. | 6. | 16 | 9.3 | |
| CL1228+12 | 3C274 | 12 28.4 | .1 | 12 33 6 | | 4341. | 232. | 28 | 20.3 | E |
| CL1232+21 | 3C274.1 | 12 32.9 | .2 | 21 38 10 | | 113. | 24. | 15 | 11.2 | C |
| CL1244+26 | WKB | 12 44.0 | .2 | 26 19 14 | | 43. | 6. | 14 | 13.2 | |
| CL1244+38 | 4C38.33 | 12 44.6 | .3 | 38 49 20 | | 30. | 8. | 15 | 14.0 | |
| CL1249+50 | 3C277 | 12 49.4 | .3 | 50 48 16 | | 51. | 7. | 11 | 7.0 | |
| CL1250+47 | 3C276 | 12 50.1 | .2 | 47 29 13 | | 49. | 9. | 9 | 6.6 | |
| CL1251+16 | 3C277.2 | 12 51.1 | .2 | 16 00 13 | | 62. | 8. | 10 | 3.4 | |
| CL1251+27 | 3C277.3 | 12 51.8 | .2 | 27 34 15 | | 40. | 6. | 14 | 12.6 | |
| CL1254+37 | 4C37.35 | 12 54.1 | .3 | 37 16 21 | | 29. | 7. | 8 | 7.3 | |
| CL1254+47 | 3C280 | 12 54.9 | .2 | 47 46 10 | | 94. | 10. | 14 | 12.1 | |
| CL1256+44 | 4C44.22 | 12 56.1 | .3 | 44 42 14 | | 43. | 6. | 11 | 9.0 | |
| CL1256+28 | COMA C | 12 56.9 | .2 | 28 03 13 | | (148.) | 27. | 13 | 12.0 | E |
| CL1256+36 | 4C36.22 | 12 56.9 | .4 | 36 48 24 | | 27. | 7. | 9 | 8.3 | |
| CL1258+40 | 3C280.1 | 12 58.4 | .2 | 40 17 15 | | 41. | 6. | 28 | 26.2 | |
| CL1303+09 | 4C09.45 | 13 03.1 | .2 | 09 15 15 | | 61. | 13. | 15 | 11.5 | |
| CL1305+46 | WKB | 13 05.0 | .2 | 46 41 9 | | 74. | 10. | 9 | 7.1 | |
| CL1305+24 | NPC | 13 05.2 | .2 | 24 52 18 | | 32. | 7. | 12 | 9.5 | |
| CL1308+27 | 3C284 | 13 08.6 | .1 | 27 41 9 | | 81. | 6. | 16 | 13.8 | |
| CL1316+30 | 4C29.47 | 13 16.7 | .2 | 30 02 16 | | 37. | 6. | 12 | 10.4 | |
| CL1319+42 | 3C285+ | 13 19.3 | .2 | 42 58 12 | | 55. | 6. | 14 | 11.5 | |
| | 4C43.27 | | | | | | | | | |
| CL1321+31 | VRO311301 | 13 21.3 | .3 | 31 24 24 | | 25. | 7. | 4 | 2.3 | |
| CL1321+41 | 4C41.25 | 13 21.3 | .4 | 41 55 24 | | 26. | 7. | 8 | 7.0 | |
| CL1325+22 | (4C22.38) | 13 25.0 | .2 | 22 43 18 | | 34. | 6. | 14 | 13.9 | |
| CL1327+47 | 4C47.36.1 | 13 27.8 | .4 | 47 42 23 | | 31. | 8. | 11 | 11.0 | E |

TABLE I(a) (continued)

| Source | Name | R.A. | Err | Dec. | Err | Flux | Err | Nobs | Sumwt | Remark |
|-----------|-----------|---------|-----|----------|-----|------|-----|------|-------|--------|
| CL1329+30 | 3C286 | 13 29.0 | .3 | 30 45 17 | | 34. | 8. | 6 | 3.7 | |
| CL1329+25 | 3C287+ | 13 29.1 | .2 | 25 06 10 | | 71. | 7. | 18 | 12.2 | |
| | 4C25.44 | | | | | | | | | |
| CL1329+50 | 4C50.36 | 13 29.3 | .5 | 50 31 23 | | 30. | 8. | 5 | 5.0 | |
| CL1333+41 | 4C41.26 | 13 33.5 | .2 | 41 21 12 | | 49. | 6. | 28 | 26.0 | |
| CL1336+39 | 3C288 | 13 36.8 | .2 | 39 07 8 | | 97. | 6. | 18 | 16.0 | |
| CL1339+26 | 4C26.41 | 13 39.7 | .2 | 26 39 11 | | 57. | 6. | 9 | 7.7 | |
| CL1343+50 | 3C289 | 13 43.7 | .4 | 50 03 21 | | 33. | 8. | 10 | 7.0 | |
| CL1343+37 | 4C37.39 | 13 43.9 | .3 | 37 01 21 | | 28. | 6. | 13 | 11.3 | |
| CL1346+28 | 4C28.34 | 13 46.3 | .2 | 28 43 17 | | 35. | 6. | 19 | 15.2 | |
| CL1346+26 | 4C26.42 | 13 46.9 | .3 | 26 47 20 | | 34. | 8. | 3 | 3.0 | |
| CL1347+21 | 3C291 | 13 47.3 | .2 | 21 28 11 | | 62. | 8. | 12 | 7.6 | |
| CL1350+31 | 3C293 | 13 50.2 | .2 | 31 36 13 | | 44. | 6. | 9 | 7.7 | |
| CL1351+32 | NPC | 13 51.9 | .4 | 32 08 27 | | 23. | 7. | 8 | 6.9 | |
| CL1352+16 | 3C293.1 | 13 52.5 | .2 | 16 38 14 | | 50. | 7. | 10 | 8.6 | |
| CL1354+39 | 4C39.41 | 13 54.2 | .3 | 39 44 19 | | 31. | 6. | 22 | 19.0 | |
| CL1354+32 | 4C32.46 | 13 54.6 | .3 | 32 29 21 | | 29. | 7. | 10 | 9.4 | |
| CL1354+19 | 4C19.44 | 13 54.8 | .2 | 19 53 16 | | 37. | 7. | 23 | 18.1 | |
| CL1404+34 | 3C294 | 14 04.8 | .2 | 34 22 10 | | 69. | 7. | 12 | 6.5 | |
| CL1405+23 | 4C23.36+ | 14 05.9 | .2 | 23 43 15 | | 39. | 6. | 28 | 14.9 | |
| | 4C24.30 | | | | | | | | | |
| CL1408+17 | 4C17.57 | 14 08.0 | .2 | 17 50 15 | | 43. | 10. | 8 | 7.7 | |
| CL1408+31 | 4C31.44 | 14 08.0 | .3 | 31 49 23 | | 26. | 7. | 11 | 8.4 | |
| CL1409+52 | 3C295 | 14 09.6 | .3 | 52 31 14 | | 72. | 10. | 9 | 7.2 | |
| CL1412+08 | 4C08.41 | 14 12.2 | .3 | 08 19 29 | | 36. | 10. | 8 | 5.4 | |
| CL1415+35 | 4C36.25 | 14 15.0 | .3 | 35 53 25 | | 25. | 7. | 10 | 7.7 | |
| CL1415+48 | 4C48.38 | 14 15.0 | .3 | 48 26 17 | | 37. | 7. | 15 | 15.0 | |
| CL1416+06 | 3C298 | 14 16.7 | .2 | 06 55 21 | | 53. | 11. | 14 | 11.6 | |
| CL1417+27 | 4C27.28 | 14 17.8 | .3 | 27 04 22 | | 28. | 7. | 14 | 11.3 | |
| CL1420+20 | 3C300 | 14 20.7 | .1 | 20 03 8 | | 96. | 8. | 23 | 15.7 | |
| CL1422+26 | 4C27.29+ | 14 22.0 | .2 | 26 53 18 | | 33. | 7. | 8 | 6.2 | |
| | VR0261401 | | | | | | | | | |
| CL1422+20 | 4C20.33 | 14 22.6 | .2 | 20 34 14 | | 46. | 6. | 15 | 11.0 | |
| CL1423+24 | 4C24.31 | 14 23.6 | .2 | 24 20 12 | | 54. | 7. | 16 | 11.7 | |
| CL1424+37 | 4C38.39 | 14 24.2 | .2 | 37 59 8 | | 88. | 9. | 9 | 7.0 | |
| CL1424+27 | 4C27.30 | 14 24.6 | .3 | 27 10 17 | | 36. | 6. | 20 | 16.1 | |
| CL1433+31 | 3C301 | 14 33.2 | .2 | 31 52 19 | | 30. | 6. | 9 | 8.0 | |
| CL1437+43 | 4C42.39 | 14 37.7 | .3 | 43 00 19 | | 32. | 6. | 10 | 9.4 | |
| CL1441+52 | 3C303 | 14 41.3 | .3 | 52 20 15 | | 50. | 10. | 13 | 12.2 | |
| CL1443+44 | 4C44.23 | 14 43.0 | .4 | 44 12 22 | | 27. | 7. | 3 | 3.0 | |
| CL1443+23 | 4C23.39 | 14 43.4 | .2 | 23 50 17 | | 34. | 6. | 17 | 11.9 | |
| CL1443+56 | 4C56.22 | 14 43.4 | .5 | 56 24 20 | | 45. | 11. | 4 | 4.0 | |
| CL1446+44 | 4C44.24 | 14 46.4 | .3 | 44 15 24 | | 26. | 7. | 11 | 11.0 | |
| CL1446+21 | 4C20.34+ | 14 46.8 | .2 | 21 08 17 | | 37. | 7. | 17 | 12.5 | |
| | 4C21.43 | | | | | | | | | |
| CL1447+40 | 4C40.33 | 14 47.5 | .4 | 40 02 25 | | 25. | 7. | 16 | 15.0 | |
| CL1450+39 | 4C39.42 | 14 50.5 | .3 | 39 33 24 | | 26. | 7. | 10 | 10.0 | |
| CL1454+27 | NPC | 14 54.8 | .3 | 27 32 19 | | 33. | 7. | 8 | 7.2 | (C) |
| CL1455+28 | 4C28.38 | 14 55.9 | .2 | 28 52 18 | | 33. | 7. | 6 | 6.0 | |
| CL1458+21 | 4C21.44 | 14 58.1 | .2 | 21 37 13 | | 54. | 9. | 8 | 7.2 | |
| CL1502+26 | 3C310 | 15 02.9 | .1 | 26 15 6 | | 382. | 31. | 18 | 8.7 | |
| CL1508+07 | 3C313 | 15 08.8 | .2 | 07 50 12 | | 91. | 11. | 19 | 14.6 | |
| CL1510+45 | 4C44.25+ | 15 10.2 | .3 | 45 13 17 | | 36. | 6. | 12 | 9.7 | |
| | 4C45.29 | | | | | | | | | |
| CL1511+26 | 3C315 | 15 11.7 | .2 | 26 16 8 | | 133. | 9. | 17 | 8.1 | |
| CL1513+36 | 4C37.43 | 15 13.4 | .2 | 36 59 15 | | 38. | 6. | 9 | 9.0 | |
| CL1514+07 | 3C317 | 15 14.4 | .1 | 07 20 8 | | 232. | 15. | 24 | 16.2 | |
| CL1517+20 | 3C318 | 15 17.6 | .2 | 20 34 21 | | 31. | 7. | 12 | 7.1 | |
| CL1519+07 | 3C318.1 | 15 19.6 | .1 | 07 58 8 | | 218. | 17. | 17 | 11.2 | |
| CL1519+51 | 4C51.31.2 | 15 19.7 | .2 | 51 10 14 | | 52. | 7. | 11 | 10.0 | E |

TABLE I(a) (continued)

| Source | Name | R.A. | Err | Dec. | Err | Flux | Err | Nobs | Sumwt | Remark |
|-----------|-------------|---------|-----|----------|-----|-------|-----|------|-------|--------|
| CL1522+54 | 3C319 | 15 22.5 | .3 | 54 22 11 | | 91. | 9. | 6 | 5.0 | |
| CL1529+24 | 3C321 | 15 29.6 | .1 | 24 23 8 | | 107. | 8. | 30 | 18.7 | |
| CL1529+35 | 3C320 | 15 29.7 | .3 | 35 41 13 | | 45. | 8. | 5 | 4.3 | |
| CL1530+41 | NPC | 15 30.2 | .3 | 41 05 20 | | 30. | 7. | 15 | 10.2 | |
| CL1545+21 | 3C323.1 | 15 45.6 | .2 | 21 03 13 | | 49. | 7. | 15 | 12.3 | |
| CL1546+48 | 4C48.39 | 15 46.6 | .4 | 48 51 20 | | 33. | 7. | 10 | 10.0 | |
| CL1547+30 | 4C30.29 | 15 47.4 | .2 | 30 46 11 | | 56. | 7. | 6 | 3.0 | |
| CL1547+21 | 3C324 | 15 47.7 | .2 | 21 32 11 | | 63. | 7. | 14 | 12.0 | |
| CL1549+33 | 4C33.36+ | 15 49.3 | .3 | 33 51 17 | | 34. | 7. | 9 | 7.7 | |
| | 4C33.37 | | | | | | | | | |
| CL1549+20 | 3C326 | 15 49.8 | .2 | 20 16 10 | | 67. | 7. | 17 | 11.4 | |
| CL1553+20 | 3C326.1 | 15 53.9 | .2 | 20 28 19 | | 32. | 7. | 13 | 8.9 | |
| CL1555+43 | 4C43.35 | 15 55.2 | .2 | 43 07 14 | | 46. | 7. | 15 | 14.4 | |
| CL1556+27 | NPC | 15 56.4 | .3 | 27 18 20 | | 29. | 8. | 6 | 6.0 | |
| CL1557+11 | 4C12.56+ | 15 57.0 | .2 | 11 54 19 | | 42. | 8. | 22 | 21.0 | |
| | 4C11.51 | | | | | | | | | |
| CL1559+34 | 4C34.43 | 15 59.9 | .3 | 34 30 21 | | 28. | 7. | 5 | 4.4 | |
| CL1603+24 | 4C24.36 | 16 03.0 | .3 | 24 43 23 | | 26. | 7. | 2 | 1.4 | |
| CL1603+44 | 4C44.27 | 16 03.0 | .3 | 44 35 19 | | 32. | 7. | 9 | 9.0 | |
| CL1606+28 | 4C28.40 | 16 06.6 | .3 | 28 57 19 | | 31. | 8. | 8 | 8.0 | |
| CL1608+32 | 3C329 | 16 08.5 | .2 | 32 53 12 | | 57. | 7. | 5 | 3.7 | |
| CL1609+22 | 3C331 | 16 09.9 | .2 | 22 31 11 | | 57. | 7. | 8 | 6.4 | |
| CL1613+13 | 4C13.57 | 16 13.9 | .2 | 13 04 17 | | 43. | 7. | 26 | 24.2 | |
| CL1614+21 | 3C333 | 16 14.7 | .2 | 21 14 14 | | 43. | 7. | 6 | 5.3 | |
| CL1615+32 | 3C332 | 16 15.8 | .2 | 32 23 14 | | 42. | 6. | 6 | 5.1 | |
| CL1615+35 | 4C35.40 | 16 15.8 | .2 | 35 30 13 | | 51. | 7. | 8 | 5.4 | (C), E |
| CL1618+17 | 3C334 | 16 18.4 | .2 | 17 47 9 | | 82. | 6. | 7 | 5.2 | |
| CL1620+24 | 4C24.37 | 16 20.0 | .3 | 24 38 18 | | 37. | 7. | 8 | 4.9 | |
| CL1622+23 | 3C336 | 16 22.5 | .2 | 23 59 10 | | 64. | 7. | 31 | 14.5 | |
| CL1623+26 | 4C26.48 | 16 23.2 | .4 | 26 23 17 | | 39. | 6. | 5 | 5.0 | |
| CL1626+28 | 3C341 | 16 26.0 | .2 | 28 03 13 | | 65. | 6. | 9 | 6.6 | |
| CL1627+39 | 3C338 | 16 27.2 | .2 | 39 36 6 | | 314. | 14. | 20 | 14.7 | |
| CL1627+23 | 3C340 | 16 27.6 | .2 | 23 21 14 | | 41. | 6. | 27 | 14.6 | (C) |
| CL1627+44 | 3C337 | 16 27.7 | .2 | 44 22 14 | | 62. | 12. | 12 | 9.6 | C |
| CL1634+26 | 3C342 | 16 34.3 | .4 | 26 41 17 | | 34. | 6. | 5 | 5.0 | |
| CL1635+16 | 4C15.56 | 16 35.7 | .3 | 16 09 16 | | 45. | 8. | 6 | 4.8 | |
| CL1641+37 | 3C344 | 16 41.5 | .3 | 37 20 17 | | 36. | 10. | 5 | 4.7 | |
| CL1641+39 | 3C345 | 16 41.6 | .3 | 39 55 17 | | 34. | 6. | 18 | 11.5 | |
| CL1648+05 | 3C348 | 16 48.8 | .1 | 05 03 6 | | 1797. | 97. | 35 | 22.3 | |
| CL1703+38 | 3C350 | 17 03.5 | .2 | 38 40 12 | | 56. | 7. | 14 | 9.5 | |
| CL1709+46 | 3C352 | 17 09.3 | .3 | 46 14 13 | | 70. | 25. | 5 | 5.0 | C |
| CL1710+39 | (4C39.49.1) | 17 10.0 | .2 | 39 48 13 | | 49. | 8. | 17 | 11.1 | E |
| CL1711+19 | 4C19.57 | 17 11.5 | .3 | 19 49 20 | | 33. | 8. | 6 | 3.2 | |
| CL1718+26 | NPC | 17 18.4 | .2 | 26 34 14 | | 44. | 6. | 9 | 6.7 | |
| CL1721+34 | 4C34.47 | 17 21.8 | .3 | 34 19 22 | | 28. | 7. | 8 | 3.6 | |
| CL1722+51 | 3C356 | 17 22.8 | .3 | 51 05 12 | | 69. | 10. | 12 | 8.1 | |
| CL1727+32 | 3C357 | 17 27.1 | .4 | 32 19 22 | | 39. | 6. | 6 | 2.6 | |
| CL1729+49 | 4C49.29+ | 17 29.9 | .4 | 49 42 15 | | 47. | 7. | 5 | 5.0 | |
| | 4C50.43 | | | | | | | | | |
| CL1732+16 | 4C16.49 | 17 32.1 | .3 | 16 29 25 | | 42. | 9. | 4 | 4.0 | |
| CL1738+28 | 4C27.37 | 17 38.6 | .3 | 28 21 17 | | 37. | 7. | 8 | 7.0 | |
| CL1743+26 | 4C26.53 | 17 43.3 | .3 | 26 14 19 | | 32. | 7. | 7 | 5.7 | |
| CL1749+29 | 4C29.53 | 17 49.9 | .3 | 29 55 19 | | 35. | 7. | 6 | 2.6 | |
| CL1752+58 | 4C58.34 | 17 52.1 | .4 | 58 50 17 | | 68. | 17. | 4 | 2.7 | |
| CL1802+11 | 3C368 | 18 02.5 | .2 | 11 04 11 | | 96. | 10. | 13 | 7.4 | |
| CL1806+48 | 4C48.45 | 18 06.6 | .2 | 48 33 9 | | 94. | 7. | 17 | 11.8 | |
| CL1806+33 | 3C370 | 18 06.7 | .3 | 33 00 18 | | 39. | 6. | 7 | 3.1 | |
| CL1810+26 | 4C26.55 | 18 10.3 | .2 | 26 24 9 | | 74. | 7. | 14 | 8.9 | |
| CL1828+48 | 3C380 | 18 28.3 | .3 | 48 44 7 | | 271. | 23. | 18 | 12.5 | |
| CL1832+47 | 3C381 | 18 32.1 | .3 | 47 29 13 | | 80. | 13. | 6 | 6.0 | (C) |

TABLE I(a) (continued)

| Source | Name | R.A. | Err | Dec. | Err | Flux | Err | Nobs | Sumwt | Remark |
|-----------|-----------|---------|-----|----------|-----|---------|-------|------|-------|--------|
| CL1833+32 | 3C382 | 18 33.3 | .2 | 32 56 12 | | 108. | 11. | 13 | 7.7 | E |
| CL1836+17 | 3C386 | 18 36.3 | .2 | 17 21 12 | | 91. | 13. | 7 | 7.0 | |
| CL1843+45 | 3C388 | 18 43.0 | .2 | 45 28 12 | | 111. | 19. | 11 | 8.4 | C |
| CL1843+10 | 3C390 | 18 43.1 | .2 | 10 02 11 | | 123. | 19. | 10 | 5.8 | |
| CL1857+13 | 3C394 | 18 57.3 | .2 | 13 11 10 | | 87. | 9. | 16 | 11.8 | |
| CL1937+21 | 4C21.53 | 19 37.9 | .2 | 21 29 10 | | 157. | 34. | 18 | 12.8 | C |
| CL1957+40 | 3C405 | 19 57.7 | .2 | 40 30 05 | | 31184. | 1445. | 46 | 33.3 | E |
| CL2012+23 | 3C409 | 20 12.2 | .3 | 23 25 15 | | 381. | 98. | 18 | 9.7 | C |
| CL2017+29 | 3C410 | 20 17.7 | .2 | 29 41 12 | | 170. | 38. | 6 | 1.3 | C |
| CL2048+29 | CYG LOOP | 20 47.4 | .3 | 30 07 15 | | (1029.) | 276. | 12 | 6.0 | C, E |
| CL2054+31 | CYG LOOP | 20 54.7 | .2 | 31 05 12 | | (144.) | 31. | 9 | 6.5 | C, E |
| CL2106+49 | 3C428 | 21 06.9 | .3 | 49 24 10 | | 91. | 12. | 18 | 11.8 | C |
| CL2109+32 | 4C32.62 | 21 09.6 | .2 | 32 57 16 | | (58.) | 13. | 7 | 3.6 | E |
| CL2117+49 | 3C431 | 21 17.2 | .2 | 49 27 8 | | 129. | 9. | 19 | 12.7 | |
| CL2120+16 | 3C432 | 21 20.1 | .2 | 16 55 15 | | 42. | 7. | 5 | 4.0 | |
| CL2121+24 | 3C433 | 21 21.4 | .2 | 24 54 6 | | 267. | 16. | 21 | 11.8 | |
| CL2123+51 | (3C434.1) | 21 23.9 | .3 | 51 17 10 | | 78. | 7. | 19 | 14.3 | |
| CL2142+28 | 3C436 | 21 42.3 | .2 | 28 00 8 | | 113. | 10. | 23 | 17.3 | |
| CL2145+15 | 3C437 | 21 45.2 | .3 | 15 20 15 | | 46. | 8. | 9 | 2.8 | |
| CL2153+37 | 3C438 | 21 53.7 | .2 | 37 49 6 | | 228. | 12. | 13 | 8.0 | |
| CL2203+29 | 3C441 | 22 03.8 | .2 | 29 28 11 | | 56. | 7. | 15 | 7.8 | |
| CL2243+27 | 4C27.48 | 22 43.1 | .2 | 27 33 14 | | 41. | 8. | 9 | 8.4 | |
| CL2243+39 | 3C452 | 22 43.4 | .2 | 39 25 6 | | 288. | 18. | 19 | 9.3 | |
| CL2321+58 | 3C461 | 23 21.2 | .3 | 58 26 6 | | 46330. | 2073. | 28 | 23.9 | E |
| CL2336+26 | 3C465 | 23 36.0 | .2 | 26 54 10 | | 194. | 23. | 17 | 13.0 | C, E |
| CL2356+27 | 4C27.54 | 23 56.0 | .2 | 27 29 19 | | 31. | 6. | 9 | 7.9 | (C) |

tectable at the higher frequency. One such example may be CL 0450+31 (3C131), which appears to be much larger in angular diameter at 26.3 MHz than at 178 MHz (Bennett 1962) or at 1425 MHz (Fomalont 1967). The structure of CL 0450+31 is expected to be in the core-halo class at 26.3 MHz because the measured source position agrees very well with the high-frequency position while the spectrum curves upward sharply at very low frequencies (Roger, Bridle, and Costain 1973).

The true correction factors for partial resolution cannot be fully determined until high-resolution measurements of the brightness distributions of the sources are made at frequencies well below 100 MHz. Once the low-frequency angular structures are known, the corrections for partial resolution can be calculated by convolution of the beam pattern with the source structure.

A check on the limiting accuracy of the sky survey measurements can be obtained by studying the 45 best observed sources. Histograms of the differences $\Delta R.A. \cos \delta$ and $\Delta \delta \cos Z$ between the observed positions and the 4C catalogue positions are plotted in Fig. 7. On the average, the observed sources have right ascensions 0^m1 too high and declinations 4 arcmin too high.

The systematic error in right ascension is probably due to a small chart reading error. The output charts ran at 12 in./h so a 0^m1 error corresponds to only 0.02 in. on this record and is easily accounted for by some small systematic error between the time marks

and the data recording. The systematic error in declination is certainly due to a very small phase error between the solid and the grating arrays. The rms deviations in right ascension and declination are $\pm 0^m2$ and ± 6 arcmin, respectively, in good agreement with the values expected for confusion and systematic errors.

In Fig. 8, two flux-density scatter histograms are plotted for the 45 sources, one histogram for all the data known to be affected by ionospheric scintillations, and histogram for the rest of the data. The histograms are plotted in terms of $\log_{10}(S/\bar{S})$ in order to combine the data from all 45 sources.

Both histograms in Fig. 8 appear to be symmetrical about 0.0, implying that the major errors affecting the observations are in fact multiplicative as expected. It should also be noted that the rms deviation of the scintillated data from the mean is 45%, while the deviation of the rest of the data is 18%. This provides the justification for weighting the scintillated data by a factor of 0.2 when averaging it with the rest of the data. The wings seen in the histogram for ordinary data are probably caused by undetected scintillation activity.

For weak sources, the effects of ionospheric scintillations may not be obvious from the drift curves, and we should expect the data to have an rms scatter of about 22%. In that case, a minimum of five observations will be necessary to define the mean flux density of a weak source with a precision of $\pm 10\%$.

B. Error Analysis

The various sources of error are discussed roughly in order of increasing importance as follows:

(1) The temperature correction could well be in error by 2.5% for a given observation. However, the net error in the mean flux for several observations is expected to be $\lesssim 1\%$.

(2) The maximum correction applied to a given observation due to the fact that the source is not centered in the NS beam is 1.19, with an error of $\pm 1.8\%$ corresponding to the uncertainty of ± 0.15 in the NS beam-width of the spaced array (Viner 1973). The mean error for several observations at different antenna settings is expected to be about 1%.

(3) The maximum correction applied for time-con-

TABLE I(b). Clark Lake 26.3-MHz Sky Survey supplementary list of sources below the confusion limit, sources which may be antenna sidelobes of strong sources, and sources for which too little data has been obtained to justify inclusion in the main list.

| Source | Name | R.A. | Err | Dec. | Err | Flux | Err | Nobs | Sumw |
|-----------|------------|---------|-----|----------|-----|------|-----|------|------|
| CL0008+32 | NRAO 8 | 00 08.5 | .3 | 32 06 22 | | 30. | 6. | 8 | 4.0 |
| CL0015+29 | NPC | 00 15.7 | .3 | 29 34 26 | | 24. | 7. | 6 | 5.0 |
| CL0051+31 | 4C30.02 | 00 51.4 | .3 | 31 40 26 | | 25. | 8. | 15 | 10.8 |
| CL0113+25 | NPC | 01 13.1 | .4 | 25 16 30 | | 22. | 8. | 12 | 9.4 |
| CL0140+31 | NPC | 01 40.2 | .4 | 31 39 29 | | 22. | 7. | 7 | 5.0 |
| CL0157+24 | NPC | 01 57.6 | .3 | 24 57 27 | | 23. | 7. | 2 | 2.0 |
| CL0202+26 | 4C26.07 | 02 02.9 | .5 | 26 40 22 | | 32. | 6. | 2 | A.5 |
| CL0208+21 | 4C21.09 | 02 08.6 | .5 | 21 09 15 | | 41. | 6. | 2 | 2.0 |
| CL0216+25 | NPC | 02 16.8 | .3 | 25 09 21 | | 28. | 6. | 7 | 6.0 |
| CL0221+27 | 3C 67 | 02 21.2 | .5 | 27 59 32 | | 21. | 8. | 4 | 4.0 |
| CL0230+23 | NPC | 02 30.5 | .2 | 23 29 16 | | 38. | 6. | 17 | 15.9 |
| CL0302+20 | NPC | 03 02.0 | .4 | 20 19 34 | | 22. | 7. | 4 | 3.0 |
| CL0308+39 | 4C39.11 | 03 08.9 | .2 | 39 13 12 | | 50. | 7. | 12 | 8.2 |
| CL0311+20 | NPC | 03 11.1 | .2 | 20 49 18 | | 35. | 7. | 9 | 6.2 |
| CL0318+50 | 4C51.07 | 03 18.5 | .3 | 50 52 16 | | 42. | 10. | 5 | 5.0 |
| CL0326+57 | 4C57.07+ | 03 26.5 | .4 | 57 09 20 | | 45. | 10. | 6 | 6.0 |
| | 4C56.07 | | | | | | | | |
| CL0328+24 | 4C24.08 | 03 28.1 | .3 | 24 59 28 | | 30. | 9. | 2 | 2.0 |
| CL0348+17 | 4C17.19 | 03 48.4 | .5 | 17 23 18 | | 40. | 20. | 2 | 2.0 |
| CL0348+57 | 4C57.08 | 03 48.7 | .6 | 57 44 20 | | 51. | 13. | 4 | 4.0 |
| CL0350+22 | (4C22.06+) | 03 50.3 | .2 | 22 19 16 | | 41. | 6. | 7 | 5.4 |
| | (4C23.07) | | | | | | | | |
| CL0408+16 | 4C17.23 | 04 08.9 | .2 | 16 35 16 | | 40. | 14. | 2 | 2.0 |
| CL0418+25 | 4C25.14 | 04 18.1 | .2 | 25 18 17 | | 48. | 7. | 6 | 4.8 |
| CL0428+44 | 4C44.11 | 04 28.3 | .2 | 44 44 14 | | 46. | 6. | 12 | 7.8 |
| CL0433+39 | 4C38.14 | 04 33.7 | .3 | 39 05 13 | | 47. | 7. | 11 | 11.0 |
| CL0438+25 | 4C25.15 | 04 38.4 | .3 | 25 31 18 | | 34. | 7. | 8 | 8.0 |
| CL0506+25 | NPC | 05 06.9 | .2 | 25 14 12 | | 51. | 6. | 4 | 4.0 |
| CL0507+29 | 4C29.17 | 05 07.1 | .2 | 29 18 14 | | 48. | 6. | 19 | 15.4 |
| CL0512+37 | 4C37.13 | 05 12.9 | .3 | 37 53 17 | | 36. | 6. | 5 | 5.0 |
| CL0545+32 | 4C32.19 | 05 45.2 | .6 | 32 38 36 | | 19. | 7. | 5 | 4.0 |
| CL0550+31 | 4C31.21 | 05 50.4 | .3 | 31 34 21 | | 28. | 7. | 5 | 5.0 |
| CL0553+29 | (4C30.09) | 05 53.7 | .2 | 29 53 20 | | 32. | 7. | 3 | 3.0 |
| CL0554+35 | 4C35.11 | 05 54.5 | .3 | 35 43 25 | | 27. | 8. | 4 | 4.0 |
| CL0556+25 | NPC | 05 56.8 | .2 | 25 02 19 | | 31. | 6. | 3 | 3.0 |
| CL0602+48 | 4C47.19 | 06 02.9 | .6 | 48 15 36 | | 20. | 8. | 9 | 6.4 |
| CL0607+30 | 4C29.21 | 06 07.4 | .3 | 30 02 28 | | 22. | 7. | 8 | 6.0 |
| CL0613+32 | 4C32.20 | 06 13.8 | .4 | 32 13 28 | | 23. | 7. | 8 | 7.0 |
| CL0615+33 | (4C34.24) | 06 15.6 | .3 | 33 14 23 | | 26. | 10. | 2 | 1.0 |
| CL0632+19 | 4C19.22 | 06 32.4 | .2 | 19 32 19 | | 32. | 7. | 11 | 10.4 |
| CL0638+38 | NPC | 06 38.0 | .4 | 38 35 29 | | 22. | 7. | 6 | 5.0 |
| CL0658+35 | 4C35.15 | 06 58.2 | .4 | 35 38 24 | | 26. | 7. | 5 | 5.0 |
| CL0722+12 | NPC | 07 22.4 | .2 | 12 10 18 | | 42. | 8. | 2 | .8 |
| CL0742+57 | 4C57.14 | 07 42.6 | .3 | 57 10 16 | | 63. | 10. | 2 | 2.0 |
| CL0820+36 | NPC | 08 20.9 | .4 | 36 13 29 | | 21. | 7. | 8 | 8.0 |
| CL0822+45 | 4C44.17 | 08 22.2 | .3 | 45 02 16 | | 40. | 7. | 6 | 6.0 |
| CL0828+37 | 4C37.24 | 08 28.5 | .4 | 37 46 21 | | 28. | 7. | 4 | 2.3 |
| CL0832+14 | 4C14.27 | 08 32.4 | .3 | 14 28 21 | | 33. | 8. | 6 | 4.4 |
| CL0836+25 | 4C25.22 | 08 36.2 | .2 | 25 37 19 | | 31. | 6. | 5 | 5.0 |

TABLE I(b) (continued)

| Source | Name | R.A. | Err | Dec. | Err | Flux | Err | Nobs | Sumw |
|-----------|-----------|---------|-----|----------|-----|------|-----|------|------|
| CL0852+31 | NPC | 08 52.3 | .3 | 31 23 25 | | 25. | 7. | 6 | 6.0 |
| CL0856+17 | 4C17.46 | 08 56.0 | .2 | 17 31 17 | | 39. | 7. | 2 | 2.0 |
| CL0913+59 | 4C58.18 | 09 13.4 | .6 | 59 20 25 | | 44. | 11. | 4 | 4.0 |
| CL0915+22 | 4C22.23 | 09 15.5 | .2 | 22 51 14 | | 44. | 7. | 19 | 8.4 |
| CL0917+30 | NPC | 09 17.5 | .3 | 30 52 22 | | 28. | 7. | 8 | 8.0 |
| CL0923+51 | 4C52.21 | 09 23.4 | .4 | 51 53 23 | | 30. | 7. | 4 | 4.0 |
| CL0926+59 | 4C59.10 | 09 26.9 | .4 | 59 10 21 | | 50. | 13. | 4 | 4.0 |
| CL0940+28 | 4C28.23 | 09 40.6 | .3 | 28 56 28 | | 23. | 7. | 19 | 17.0 |
| CL0941+51 | NPC | 09 41.4 | .5 | 51 09 33 | | 23. | 8. | 9 | 8.0 |
| CL0944+62 | 4C62.13.2 | 09 44.8 | .5 | 62 14 24 | | 61. | 14. | 5 | 3.8 |
| CL0951+21 | 4C21.26 | 09 51.3 | .2 | 21 38 17 | | 43. | 6. | 10 | 6.2 |
| CL0952+35 | 4C35.21 | 09 52.9 | .5 | 35 24 35 | | 19. | 7. | 6 | 3.6 |
| CL1004+13 | (4C13.41) | 10 04.2 | .2 | 13 05 20 | | 37. | 8. | 3 | 3.0 |
| CL1008+21 | 4C21.27 | 10 08.5 | .2 | 21 28 15 | | 40. | 9. | 7 | 3.6 |
| CL1008+32 | NPC | 10 08.8 | .4 | 32 22 28 | | 22. | 7. | 11 | 10.0 |
| CL1011+53 | 4C54.20 | 10 11.6 | .4 | 53 50 23 | | 34. | 8. | 4 | 1.4 |
| CL1017+48 | 4C48.29 | 10 17.8 | .3 | 48 44 17 | | 37. | 7. | 13 | 12.3 |
| CL1018+36 | 4C37.27 | 10 18.6 | .5 | 36 59 31 | | 20. | 8. | 3 | 3.0 |
| CL1036+36 | 4C36.17 | 10 36.5 | .5 | 36 12 36 | | 19. | 7. | 8 | 7.0 |
| CL1037+46 | (4C47.32) | 10 37.1 | .3 | 46 49 21 | | 31. | 7. | 5 | 5.0 |
| CL1049+50 | NPC | 10 49.0 | .5 | 50 56 27 | | 25. | 7. | 9 | 8.0 |
| CL1049+34 | 4C34.33 | 10 49.3 | .4 | 34 08 29 | | 21. | 7. | 5 | 1.9 |
| CL1054+49 | NPC | 10 54.3 | .6 | 49 06 38 | | 19. | 8. | 12 | 10.3 |
| CL1055+31 | NPC | 10 55.0 | .5 | 31 37 40 | | 17. | 8. | 9 | 7.4 |
| CL1059+35 | 4C35.24 | 10 59.7 | .4 | 35 13 29 | | 22. | 7. | 4 | 3.0 |
| CL1110+43 | 4C43.21 | 11 10.2 | .2 | 43 51 15 | | 41. | 6. | 10 | 8.2 |
| CL1112+54 | 4C54.23 | 11 12.1 | .3 | 54 56 19 | | 40. | 8. | 3 | 2.0 |
| CL1113+52 | NPC | 11 13.7 | .2 | 52 52 16 | | 51. | 11. | 5 | 4.0 |
| CL1114+27 | (4C26.31) | 11 14.0 | .3 | 27 02 25 | | 25. | 7. | 4 | 4.0 |
| CL1118+19 | 4C19.37 | 11 18.5 | .3 | 19 39 22 | | 28. | 7. | 7 | 5.4 |
| CL1133+25 | 4C26.32+ | 11 33.5 | .3 | 25 43 23 | | 27. | 7. | 8 | 6.6 |
| | 4C24.24 | | | | | | | | |
| CL1139+27 | NPC | 11 39.2 | .4 | 27 27 27 | | 23. | 7. | 3 | 3.0 |
| CL1139+23 | 4C23.28 | 11 39.4 | .2 | 23 16 13 | | 48. | 6. | 21 | 9.3 |
| CL1141+47 | NPC | 11 41.5 | .3 | 47 36 20 | | 35. | 6. | 10 | 9.0 |
| CL1142+37 | 4C37.32 | 11 42.2 | .3 | 37 20 22 | | 28. | 7. | 7 | 6.0 |
| CL1149+38 | 4C38.31 | 11 49.3 | .4 | 38 41 29 | | 22. | 7. | 12 | 10.2 |
| CL1153+40 | NPC | 11 53.6 | .4 | 40 39 26 | | 24. | 7. | 14 | 14.0 |
| CL1154+31 | 4C31.38 | 11 54.0 | .3 | 31 49 24 | | 25. | 7. | 7 | 5.4 |
| CL1158+34 | 4C34.36 | 11 58.4 | .5 | 34 49 35 | | 19. | 7. | 6 | 4.7 |
| CL1201+31 | 4C30.24 | 12 01.0 | .3 | 31 18 21 | | 28. | 7. | 9 | 7.4 |
| CL1205+35 | 4C35.27 | 12 05.6 | .7 | 35 17 44 | | 16. | 8. | 5 | 3.4 |
| CL1245+32 | 4C32.41 | 12 45.0 | .3 | 32 20 26 | | 25. | 7. | 6 | 5.0 |
| CL1313+39 | NPC | 13 13.1 | .4 | 39 08 32 | | 20. | 7. | 12 | 11.0 |
| CL1332+32 | NPC | 13 32.5 | .5 | 32 03 39 | | 17. | 8. | 4 | 4.0 |
| CL1338+29 | 4C28.33 | 13 38.5 | .3 | 29 10 21 | | 28. | 7. | 9 | 8.7 |
| CL1340+35 | 4C35.30 | 13 40.3 | .5 | 35 21 31 | | 20. | 7. | 6 | 4.7 |
| CL1357+27 | 4C26.43+ | 13 57.4 | .3 | 27 10 22 | | 27. | 7. | 7 | 6.0 |
| | 4C27.27 | | | | | | | | |
| CL1359+41 | NPC | 13 59.7 | .4 | 41 52 26 | | 24. | 7. | 6 | 6.0 |
| CL1403+20 | 4C20.32 | 14 03.2 | .3 | 20 53 17 | | 35. | 6. | 2 | 2.0 |
| CL1439+35 | 4C35.33 | 14 39.3 | .3 | 35 45 23 | | 27. | 7. | 4 | 2.3 |
| CL1456+25 | (4C25.47) | 14 56.2 | .2 | 25 25 19 | | 32. | 8. | 6 | 2.3 |
| CL1521+28 | 4C27.31+ | 15 21.3 | .2 | 28 02 21 | | 31. | 7. | 9 | 9.0 |
| | 4C28.39 | | | | | | | | |
| CL1540+34 | 4C34.42 | 15 40.1 | .5 | 34 14 29 | | 22. | 7. | 6 | 5.0 |
| CL1553+24 | 4C24.35 | 15 53.1 | .5 | 24 25 15 | | 42. | 6. | 9 | 6.1 |
| CL1556+35 | 4C35.39 | 15 56.0 | .4 | 35 54 28 | | 23. | 7. | 6 | 4.7 |
| CL1654+25 | 4C25.49 | 16 54.3 | .3 | 25 10 20 | | 30. | 6. | 2 | .9 |
| CL1720+07 | 4C07.45 | 17 20.5 | .4 | 07 21 22 | | 51. | 11. | 7 | 5.1 |

TABLE I(b) (continued)

| Source | Name | R.A. | Err | Dec. | Err | Flux | Err | Nobs | Sumw |
|-----------|-----------|---------|-----|----------|-----|------|-----|------|------|
| CL1721+31 | NPC | 17 21.1 | .4 | 31 41 19 | | 31. | 9. | 5 | 3.2 |
| CL1729+26 | 4C26.52 | 17 29.4 | .3 | 26 19 18 | | 34. | 6. | 7 | 6.0 |
| CL1734+40 | NPC | 17 34.9 | .3 | 40 40 20 | | 30. | 6. | 12 | 7.2 |
| CL1741+49 | 4C48.42 | 17 41.1 | .4 | 49 21 18 | | 39. | 8. | 5 | 5.0 |
| CL1745+18 | NPC | 17 45.9 | .2 | 18 35 19 | | 38. | 7. | 4 | 4.0 |
| CL1749+25 | 4C25.52 | 17 49.6 | .3 | 25 48 17 | | 37. | 6. | 5 | 4.4 |
| CL1753+57 | NPC | 17 53.2 | .4 | 57 24 21 | | 45. | 10. | 4 | 4.0 |
| CL1809+40 | 4C40.36 | 18 09.6 | .2 | 40 47 17 | | 56. | 10. | 2 | 1.4 |
| CL1817+50 | 4C50.44 | 18 17.6 | .4 | 50 32 13 | | 54. | 9. | 8 | 7.0 |
| CL1819+24 | 4C24.45 | 18 19.8 | .3 | 24 57 16 | | 43. | 6. | 5 | 3.0 |
| CL1855+35 | NPC | 18 55.6 | .3 | 35 29 12 | | 48. | 7. | 4 | 4.0 |
| CL1855+52 | 4C52.44 | 18 55.6 | .5 | 52 42 16 | | 47. | 7. | 3 | 1.0 |
| CL2051+26 | 4C26.58 | 20 51.5 | .3 | 26 01 13 | | 45. | 7. | 7 | 5.4 |
| CL2106+21 | (4C21.58) | 21 06.0 | .1 | 21 33 12 | | 51. | 7. | 5 | 5.0 |
| CL2115+18 | 4C18.62 | 21 15.9 | .3 | 18 00 18 | | 43. | 10. | 3 | 3.0 |

stant smoothing of source deflections was 1.079 ± 0.025 for a point source at a declination of 3° . For extended sources and sources at higher declinations, the correction and its uncertainty decrease inversely as the square of the drift curve width. The uncertainties in the corrections for transit time and source width were generally less than the systematic measuring errors in those parameters.

(4) Since accurate measurements of the angular size of radio sources have not been performed at low radio frequencies, the suggested corrections for partial resolution could be seriously in error. That error will generally be in the sense that the adopted correction was too small.

(5) The ionospheric absorption correction could be in error by as much as 10% for a given daytime observation. Although the data taken during the daytime was given low weight, systematic errors could arise if many of the data points for a given source were obtained during the day.

(6) The statistical scatter among the observations of a given source will include the random parts of the errors discussed above, as well as the effects of slow ionospheric scintillations and any intrinsic variability that may exist in the source. As derived above, the error in the mean flux density of a given source due to random scatter is expected to be about $22/\sqrt{N}\%$ for a series of N observations.

(7) Confusion errors are a function of source intensity and dominate the sources of error for weak radio sources, while systematic measuring errors are generally significant only for the strongest radio sources and for measurements of right ascension. Both effects are combined in Fig. 9, in which, following the analysis of von Hoerner (1961), the errors in flux density and position are plotted as a function of source strength relative to the confusion limit S_L .

Sources confused with sidelobes or with nearby sources of comparable strength will have larger errors

than those indicated by Fig. 9 and must be considered on an individual basis.

(8) The uncertainty in the calibration of the gain-versus-zenith-distance dependence of the arrays can yield errors of $\pm 10\%$.

IV. LOW-FREQUENCY FLUX SCALES

A. The Absolute Calibration of this Survey

Paper I (Viner 1975) discussed the absolute calibration of the fluxes of 3C144, 274, 405, and 461. The flux scale of this survey was adjusted to agree, on the aver-

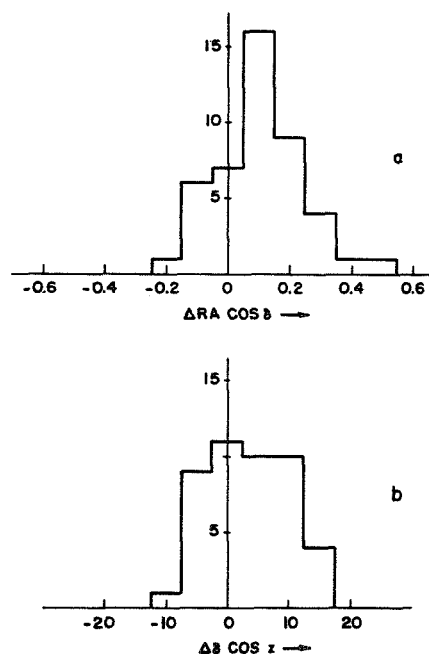


FIG. 7. Histograms of differences between the sky survey positions of sources and those given by the 4C catalogue: (a) differences in right ascension in minutes of time, normalized to the equator ($\delta=0$), and (b) differences in declination in minutes of arc, normalized to the zenith ($Z=0$).

age, with these absolute measurements. The average ratio of the fluxes of the four sources given in Paper I to those given in Table I(a) is $1.00 \pm 3\%$.

B. General Considerations

Radio source flux scales have been quite uncertain at low frequencies. The CKL (Conway, Kellermann, and

Long 1963) scale, based upon Cambridge 178- and 38-MHz data, is widely believed to be too low by 10%-40%. Various data are inconsistent and some flux scales are apparently nonlinear with source intensity (Scott and Shakeshaft 1971). In their comprehensive study Kellermann, Pauliny-Toth, and Williams (1969) (hereafter referred to as KPW) acknowledged these problems but felt that the situation was too uncertain to justify

TABLE I(c). Upper limits to the flux densities of 3CR sources that were not detected in the survey.

| Source name | R.A. | Dec. | Flux limit | Nobs | Sumwt |
|-------------|---------|-------|------------|------|-------|
| 3C 11.1 | 00 26.9 | 63 44 | 187. | 3 | 3.0 |
| 3C 14.1 | 00 33.3 | 58 39 | 316. | 8 | 8.0 |
| 3C 49 | 01 38.5 | 13 39 | 50. | 3 | 1.4 |
| 3C 65 | 02 20.6 | 39 48 | 68. | 23 | 18.7 |
| 3C105 | 04 04.8 | 03 33 | 77. | 4 | 3.4 |
| 3C119 | 04 29.1 | 41 32 | 38. | 21 | 20.7 |
| 3C138 | 05 18.3 | 16 36 | 55. | 7 | 6.3 |
| 3C139.1 | 05 19.4 | 34 00 | 31. | 8 | 6.8 |
| 3C152 | 06 01.5 | 20 22 | 47. | 12 | 9.5 |
| 3C153.1 | 06 06.7 | 21 12 | 68. | 14 | 9.8 |
| 3C175.1 | 07 11.2 | 14 40 | 43. | 8 | 7.2 |
| 3C222 | 09 33.9 | 4 36 | 73. | 6 | 4.1 |
| 3C241 | 10 19.1 | 22 14 | 24. | 18 | 17.1 |
| 3C257 | 11 20.6 | 05 45 | 51. | 12 | 10.5 |
| 3C258 | 11 22.2 | 19 32 | 32. | 14 | 10.4 |
| 3C272.1 | 12 22.5 | 13 02 | 361. | 13 | 14.0 |
| 3C275.1 | 12 41.5 | 16 39 | 98. | 6 | 5.2 |
| 3C277.1 | 12 50.3 | 56 48 | 47. | 8 | 8.0 |
| 3C288.1 | 13 40.5 | 60 37 | 62. | 14 | 9.1 |
| 3C296 | 14 14.4 | 08 31 | 61. | 8 | 6.6 |
| 3C299 | 14 19.1 | 42 00 | 37. | 8 | 8.0 |
| 3C322 | 15 33.8 | 55 46 | 92. | 3 | 3.0 |
| 3C323 | 15 40.8 | 60 25 | 102. | 6 | 5.0 |
| 3C325 | 15 49.2 | 62 50 | 128. | 5 | 4.2 |
| 3C343 | 16 34.0 | 62 53 | 70. | 6 | 2.5 |
| 3C343.1 | 16 37.9 | 62 41 | 81. | 6 | 2.5 |
| 3C346 | 16 41.6 | 17 20 | 44. | 4 | 3.2 |
| 3C349 | 16 58.1 | 47 07 | 85. | 10 | 10.0 |
| 3C351 | 17 04.1 | 60 48 | 79. | 10 | 7.2 |
| 3C396 | 19 01.6 | 05 21 | 131. | 12 | 12.0 |
| 3C397 | 19 05.1 | 07 04 | 105. | 12 | 11.2 |
| 3C398 | 19 08.7 | 09 00 | 109. | 11 | 11.0 |
| 3C399.1 | 19 14.0 | 30 13 | 91. | 9 | 3.1 |
| 3C399.2 | 19 15.7 | 10 36 | 120. | 4 | 4.0 |
| 3C400.1 | 19 22.7 | 35 17 | 125. | 10 | 7.0 |
| 3C400.2 | 19 36.5 | 17 24 | 88. | 3 | 1.3 |
| 3C401 | 19 39.6 | 60 34 | 256. | 13 | 13.0 |
| 3C402 | 19 40.4 | 50 29 | 230. | 12 | 12.0 |
| 3C410.1 | 20 19.6 | 40 06 | 577. | 11 | 5.3 |
| 3C411 | 20 19.7 | 09 53 | 143. | 6 | 6.0 |
| 3C415.1 | 20 31.1 | 43 18 | 256. | 10 | 4.0 |
| 3C415.2 | 20 31.4 | 53 32 | 153. | 15 | 14.2 |
| 3C416.1 | 20 33.4 | 46 52 | 106. | 8 | 7.4 |
| 3C416.2 | 20 34.0 | 41 33 | 343. | 7 | 2.6 |
| 3C418 | 20 37.1 | 51 08 | 121. | 9 | 8.2 |
| 3C419.1 | 20 39.1 | 42 06 | 188. | 6 | 2.3 |
| 3C424 | 20 45.7 | 06 50 | 108. | 13 | 9.5 |
| 3C430 | 21 17.0 | 60 35 | 254. | 9 | 9.0 |
| 3C434 | 21 20.9 | 15 35 | 46. | 6 | 4.8 |
| 3C435 | 21 26.6 | 07 20 | 85. | 10 | 7.9 |

TABLE I(c) (continued)

| Source name | R.A. | Dec. | Flux limit | Nobs | Sumwt |
|-------------|---------|-------|------------|------|-------|
| 3C437.1 | 21 48.5 | 13 47 | 67. | 6 | 4.7 |
| 3C442 | 22 12.9 | 13 35 | 123. | 7 | 4.7 |
| 3C449 | 22 29.1 | 39 03 | 100. | 6 | 4.0 |
| 3C454 | 22 49.1 | 18 32 | 98. | 5 | 4.2 |
| 3C454.3 | 22 51.5 | 15 54 | 252. | 9 | 6.6 |
| 3C455 | 22 52.6 | 12 54 | 113. | 4 | 3.0 |
| 3C456 | 23 09.9 | 09 03 | 362. | 10 | 8.2 |
| 3C458 | 23 10.3 | 05 00 | 517. | 11 | 9.8 |
| 3C460 | 23 19.0 | 23 32 | 425. | 13 | 11.2 |
| 3C470 | 23 56.0 | 43 47 | 163. | 6 | 2.1 |

Notes to Table I

CL0134+32 [3C48]: Flux density appears low by comparison with Williams *et al.* (1966) at 38 MHz and Roger *et al.* (1969) at 22 MHz. The explanation may lie in different degrees of confusion produced in the three dissimilar beam shapes.

CL0220+42 [3C66]: Component No. 3 in Macdonald *et al.* (1966) has not been detected at 26.3 MHz despite a rather steep high-frequency spectrum. The possibility of a turnover in the spectrum of this component is supported by the small (<10 arcsec) angular size measured by Macdonald *et al.*

CL0314+41 [3C83.1B]: Well resolved from 3C84. On the basis of the measured position, the source seen here is component B of Ryle and Windram (1968); a double source with an elongated halo of about 3-arcmin extent EW. Neither component A nor IC310 were seen at 26.3 MHz to a limit of about 70 Jy. The spectrum of 3C83.1B becomes steeper at low frequencies, indicating that the halo probably has a steep spectrum and dominates at low frequencies.

CL0316+41 [3C84]: Low-frequency spectrum is dominated by a 6-arcmin halo (Ryle and Windram 1968) with spectral index $\alpha=1.4$. The $30' \times 10'$ extended halo discussed by Ryle and Windram was not detected, to a flux limit of 150 Jy (integrated).

CL0324+55 [3C86]: Individual components not resolved.

CL0346+43 [4C34.15]: WKB (Williams *et al.* 1966) flux is quoted as sum of 4C33.08 and 4C34.15. Source 4C33.08 is not detected at 26.3 MHz with greater EW resolution.

CL0425+54 [4C54.06]: WKB flux is sum of 4C54.06 and 4C55.08. Source 4C55.08 is not detected at 26.3 MHz.

CL0445+44 [3C129/129.1]: Individual components not resolved (see Table II).

CL0450+31 [3C131]: Spectrum becomes steeper below 40 MHz. Previously undetected 11-arcmin halo is reported in this paper (see Table II).

CL0531+22 [3C144]: Tau A. Spectrum becomes steeper below 50 MHz.

CL0538+48 [3C147/4C47.16]: Sources are resolved by WKB. Confusion by Tau A sidelobes prevents resolution of sources at 26.3 MHz.

CL0614+22 [3C157]: IC443. Extended source with stronger emission on high right ascension (eastern) side as seen at high frequencies (see Table II).

CL0840+29 [4C29.31]: Spectrum turns up steeply below 50 MHz with spectral index $\alpha \approx 1.8$.

CL0854+09 [4C09.32]: Spectrum may become steeper below 40 MHz.

CL0922+14 [4C14.31]: Previously undetected 14-arcmin halo is reported in this paper (see Table II). Source may be associated with Abell 795 cluster of galaxies.

CL0938+39 [3C223.1]: Our flux is very high compared with WKB flux and KPW spectrum. 86-MHz flux (Artyukh *et al.* 1969) is also far above KPW spectrum.

CL1216+06 [3C270]: Source size at 26.3 MHz is significantly larger than at 960 or 1400 MHz, indicating possible halo structure (see Table II).

CL1256+28 [Coma C]: Extended source with two major components at 26.3 MHz (see Table II).

CL1409+52 [3C295]: Spectrum turns over at ~ 60 MHz. Braude *et al.* (1969a) report an extended (1°) halo with steep spectrum below 25 MHz, possibly confirmed by Roger *et al.* (1973) at 22 MHz. Flux density of halo at 26.3 MHz must be <100 Jy.

CL1416+06 [3C298]: Spectrum turns over at ~ 60 MHz. Braude *et al.* (1969a) report an extended (1°) halo with steep spectrum below 25 MHz, confirmed by Roger *et al.* (1969). Halo not seen at 26.3 MHz, to flux limit of 150 Jy (integrated).

CL1519+07 [3C318.1]: A steep-spectrum source, with spectral index $\alpha \approx 1.5$ and increasing with frequency. From sky survey data, EW source size is <5 arcmin.

CL1648+05 [3C348]: Her A. Our flux appears to be anomalously low by 25% when compared with all other observers. We can find no simple explanation for this fact.

CL1957+40 [3C405]: Cyg A. Spectrum turns over at about 23 MHz.

CL2047+30 and CL2054+31 [Cyg Loop]: Extended source confused by sidelobes of Cyg A. Western component is very broad and double peaked. Eastern component is more compact and is not linked to western component by an emission bridge. General appearance agrees with high-frequency data (see Table II).

CL2321+58 [3C461]: Cas A, epoch 1967.8. Spectrum turns over at about 20 MHz.

CL2336+26 [3C465]: Component No. 6 in Macdonald *et al.* (1966) has probably not been detected at 26.3 MHz despite a steep high-frequency spectral index ($\alpha \approx 1.5$ from 408 to 1407 MHz).

revision of the CKL scale in the 38–750-MHz range. There have now been several major surveys at frequencies below 30 MHz, and the situation is somewhat clarified.

In the comparison of flux scales presented below, it is important to specify carefully the criteria used in selecting the sources used as calibrators. Unfortunately, the errors involved in the measurement of any one source are too large to permit the use of only a few sources for intercomparison. If only a few of the strongest sources were used this would minimize statistical errors but

most of the strongest sources have curved spectra and have such large angular sizes that they are partly resolved by some of the instruments. Flux-scale non-linearity in some of the surveys would also seriously confuse the situation. It has been suggested by many authors that Cas A should be used as a primary standard but it is one of the worst possible choices at decimeter wavelengths. It suffers from all of the problems mentioned above and, in addition, there is evidence that it may be randomly variable at low frequencies (Braude *et al.* 1969b; Erickson and Perley 1975).

TABLE II. Extended sources listed in the sky survey.

| Source | Identification | $\bar{W}-W_0$ σ_W | Measured size | Struc- ture class ^a | EW extent | Ref. ^b | Adopted correction factor |
|---------|----------------------|-----------------------------|----------------------|--------------------------------------|--------------|-------------------|---------------------------------|
| 0022+62 | 3C10 | 1.6 | 7'5±3' | D | 7'0±0'5 | 1,2 | 1.06 ±0.03 |
| 0107+31 | 3C34 | | | | 0'5 | 3 | 1.13 ±0.13 |
| 0157+40 | 4C40.08 | | | | 4'2 | 11 | 1.03 ±0.02 |
| 0255+06 | 3C75 | 1.2 | 9' ±6' | D | 1'0, 3'0 | 1,2,6 | 1.09 ±0.08 |
| 0314+41 | 3C83.1B | | | | 3' ±1' | 1,4 | 1.03 ±0.02 |
| 0316+41 | 3C84 | 2.0 | 7' ±2' | H | 6' ±1' | 1,4 | 1.10 ±0.05 |
| 0403+30 | 4C30.06 ^c | 1.6 | 10' ±3' | | | | 1.00 ±0.05 |
| 0415+37 | 3C111 | 1.4 | 5' ±3' | D | 3'0 | 1,5,6 | 1.02 ±0.01 |
| 0445+44 | 3C129/129.1 | 5 | 19' ±1'5 | C | 22' | 1,3 | 2.0 ±0.3 |
| 0450+31 | 3C131 | 2.5 | 11' ±2' | | <0'25 | 1,2 | 1.25 ±0.10 |
| 0513+24 | 3C136.1 | | | | 4'2 | 10 | 1.04 ±0.02 |
| 0531+22 | 3C144 | | <3'7 ^d | H | 3'5 | ... ^d | 1.02 ±0.01 |
| 0614+22 | 3C157 | 20. | 25' ±1' | C | 27' | 7,8,9 | 2.30 ±0.15 |
| 0703+42 | 4C42.23 | | | C | 4'2 | 10 | 1.03 ±0.02 |
| 0745+55 | 4C56.16 | 3.8 | 17' ±2' | D | 7', 17' | 10 | 2.2 ±0.3 |
| 0904+41 | 4C41.19 | | | | 4'7 | 10 | 1.04 ±0.02 |
| 0922+14 | 4C14.31 | 2.4 | 14' ±3' | | 2' | 11 | 1.35 ±0.15 |
| 1107+37 | 4C37.29 | | | C | 5'2 | 10 | 1.05 ±0.03 |
| 1153+55 | 4C55.22 | | | C | 3'8 | 10,11 | 1.03 ±0.02 |
| 1216+06 | 3C270 | 2.9 | 10' ±1'5 | D | 2'5, 5' | 1,6 | 1.2 ±0.1 |
| 1228+12 | 3C274 | 1.5 | 6' ±2' | H | 6.5 ±0'5 | ... ^d | 1.078±0.024 |
| | | 3.5 ^d | 5'9±0'9 ^d | | | | |
| 1256+28 | Coma C | 6.5 | 28' ±3' | C | 32' | 12 | 2.8 ±0.4 |
| 1327+47 | 4C46.36.1 | | | | 6'5 | 11 | 1.09 ±0.05 |
| 1519+51 | 4C51.31.2 | | | | 4'3 | 11 | 1.03 ±0.02 |
| 1615+35 | 4C35.40 | | | C | 5'7 | 10 | 1.06 ±0.03 |
| 1710+39 | (4C39.49.1) | | | | 5'8 | 11 | 1.07 ±0.04 |
| 1833+32 | 3C382 | 1.3 | 7'5±2'5 | D | 1'0, 1'5 | 1,3 | 1.07 ±0.06 |
| 1957+40 | 3C405 | 1.7 ^d | 3'2±1'2 ^d | D | 2'05 | ... ^d | 1.02 ±0.01 |
| 2048+29 | Cygnus Loop | 10 | 48' ±4' | C | 80' | 13,14 | 8.5 ±2. |
| 2054+31 | | 1.7 | 12' ±3' | C | 17' | 13,14 | 1.5 ±0.2 |
| 2109+32 | 4C32.62 | 2 | 16' ±3' | | | | 1.60 ±0.25 |
| 2321+58 | 3C461 | 1.8 ^d | 4'0±1'8 ^d | | 4'1 | ... ^d | 1.045±0.030 |
| 2336+26 | 3C465 | | | D | 7' | 1,3 | 1.05 ±0.03 |

^a D: Double source.

H: Core-halo source.

C: Complex brightness distribution.

^b 1. Fomalont 1967.

2. Bennett 1962.

3. MacDonald *et al.* 1968.

4. Ryle and Windram 1968.

5. Mackay 1969.

6. Moffet and Maltby 1962.

7. Hogg 1964.

8. Colla *et al.* 1971.

9. Kundu and Velusamy 1969.

10. Bridle *et al.* 1972.^c Confused by 4C29.11.^d From absolute measurements (Viner 1973; 1975).

11. Caswell and Crowther 1969.

12. Willson 1970.

13. Kundu and Velusamy 1967.

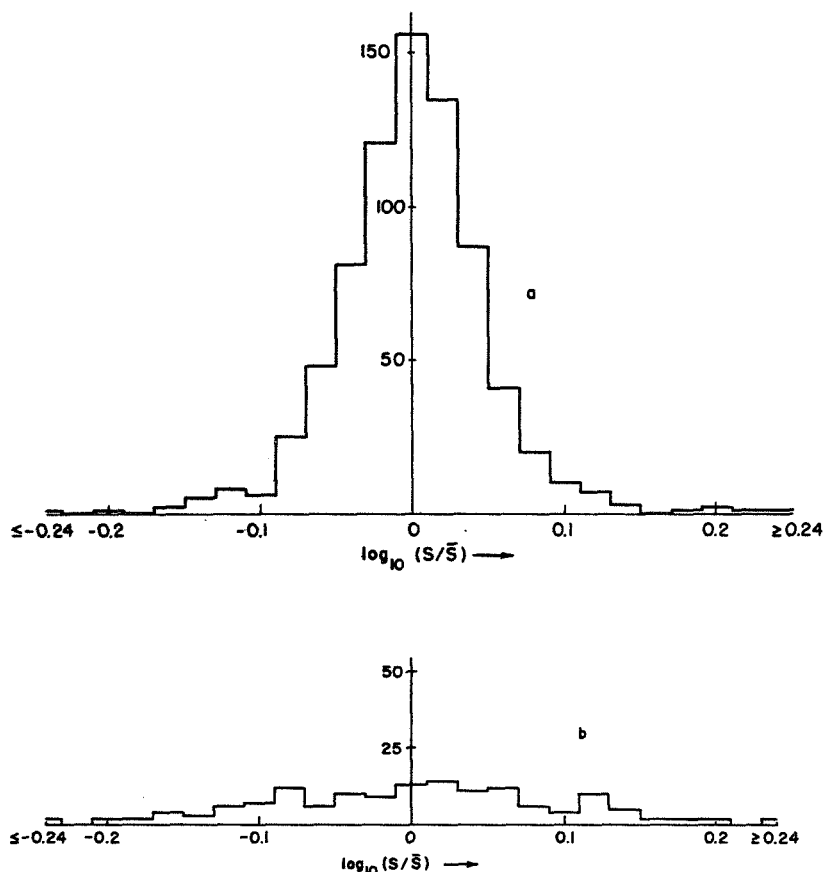
14. Kundu 1969.

It is no surprise to find that the factors that we determine for intercalibrating the various flux scales are sensitive to the criteria used in selecting the standard sources, so in every case we have used as large a number of sources as possible considering spectral curvature, partial resolution, and confusion. This means that we cannot use a single list of calibration sources for intercomparison of all surveys for when we combine these criteria with the sky coverage, the flux ranges, and the sidelobe confusion of the different instruments, we are left with too few sources for reliable intercomparison. Therefore, we have used similar criteria for selecting the sources to be used in comparing our flux scale with each of the others but then have used all sources common to the two surveys which satisfy these criteria.

C. Comparison with KPW Scale

It is of interest to compare the absolute flux measurements in Paper I of the four strongest sources (3C144, 3C274, 3C405, 3C461) with the fluxes obtained by extrapolating the 38-MHz data to 26.3 MHz according to the KPW spectral indices. Better estimates of the low-frequency spectral indices, such as those given by Roger, Bridle, and Costain (1973), do not appreciably alter the result. For these sources we find a correction factor of only 1.02 ± 0.04 is needed to adjust KPW fluxes to our scale. Therefore, the scales agree as best they can be determined for these strong sources ($S_{CL} > 2000$ Jy at 26.3 MHz). However, for the reasons given in the preceding section calibration with these strong sources should not be considered very reliable.

FIG. 8. Histograms of the scatter of each observation about the mean flux density of the source \bar{S} for 45 sources: (a) data not obviously affected by ionospheric scintillations, and (b) data seen to be affected by ionospheric scintillations.



KPW provides a list of suggested calibration sources. This is not an optimum selection of sources for us because Roger, Bridle, and Costain (1973) find that the spectra of many of them curve at decametric wavelengths and several require significant resolution corrections. However, calibration based upon the KPW calibrators found in Table I yields a correction factor of

$$\left(\frac{S_{CL}}{S_{KPW}}\right) = 1.15 \pm 0.10, \quad 14 \text{ sources.}$$

A more reliable intercomparison can be obtained by predicting the 26.3-MHz fluxes of a much larger sample of KPW sources and comparing them with the determinations presented here. Fifty sources, common to the two lists, were selected under the following criteria:

- (1) KPW find a straight (S) spectrum.
- (2) The Clark Lake flux given in Table I must be greater than 50 Jy. (This is true for most KPW sources and the inclusion of the dozen weaker sources does not modify the results.)
- (3) There is no evidence of confusion or partial resolution.

These criteria eliminate the four strongest sources and

we find a correction factor of

$$\left(\frac{S_{CL}}{S_{KPW}}\right) = 1.11 \pm 0.03, \quad 2000 > S_{CL} > 50 \text{ Jy,}$$

51 sources.

The linearity of the flux scales can be assessed by dividing the sources into two groups, those for which $S_{CL} > 100$ Jy and those for which $S_{CL} < 100$ Jy. These groups yield identical results:

$$\left(\frac{S_{CL}}{S_{KPW}}\right) = 1.11 \pm 0.04, \quad 2000 > S_{CL} > 100 \text{ Jy,}$$

15 sources,

and

$$\left(\frac{S_{CL}}{S_{KPW}}\right) = 1.11 \pm 0.05, \quad 100 > S_{CL} > 50 \text{ Jy,}$$

36 sources.

These factors differ only slightly from the one found above in the $S_{CL} > 2000$ -Jy range, so we do not find as large a nonlinearity in the KPW scale as that found at 81.5 MHz by Scott and Shakeshaft (1971).

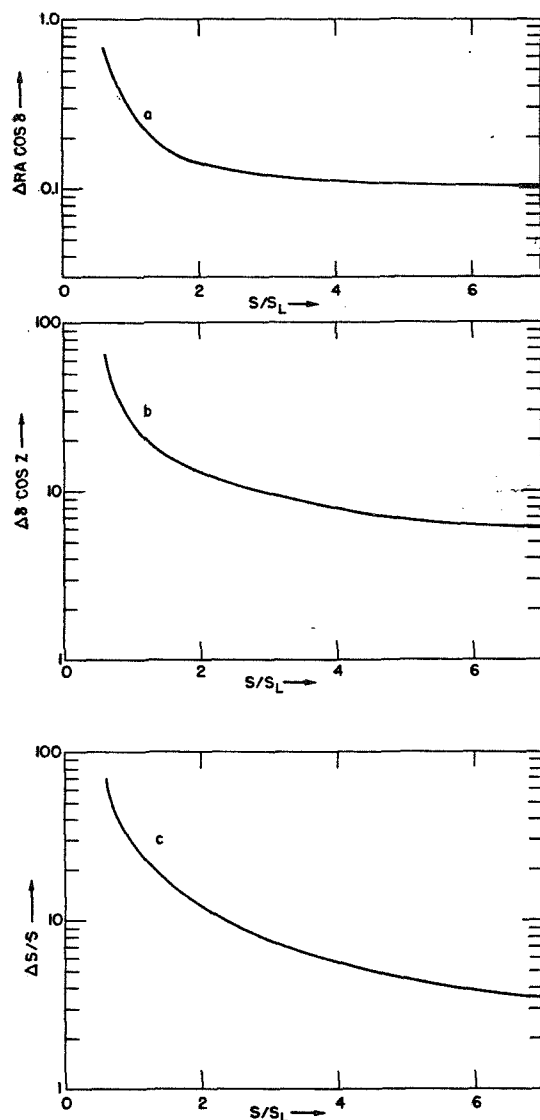


FIG. 9. Sky survey position and flux-density errors due to confusion and systematic measuring errors, as a function of the ratio of source flux density S to confusion limit S_L : (a) error in right ascension in minutes of time, normalized to the celestial equator, (b) error in declination in minutes of arc, normalized to the zenith, and (c) percent error in measured flux density.

As a final check on the validity of these results, we have made a similar calculation with the additional source selection criterion that Roger, Bridle, and Costain (1973) must find an S-type spectrum and we have used their determinations of spectral index. For the 22 sources satisfying this criterion, we find $(\overline{S_{CL}}/S_{KPW}) = 1.07 \pm 0.06$. This ratio does not significantly differ from those given above.

In summary, it appears that the KPW scale should be raised by 11% at 26.3 MHz to agree with our Clark Lake flux scale and that the KPW scale is linear to about 10% at decametric wavelengths.

D. Comparison with the Penticton Flux Scale

The Penticton arrays have been used to produce two radio source catalogues, one at 10.03 MHz (Bridle and Purton 1968) and one at 22.25 MHz (Roger, Costain, and Lacey 1969; hereafter referred to as RCL). These data have been interpreted by Roger, Bridle, and Costain (1973, hereafter referred to as RBC), who derive low-frequency radio spectra for 226 sources and also provide new or revised data on a number of sources. RBC suggest ten well-measured calibration sources, but after elimination of those that are outside our declination range or which we partly resolve, too few sources remain for accurate flux-scale comparison. Therefore, we base a comparison on all those sources common to the two catalogues and have used RBC spectral indices to convert the 22.25-MHz data to 26.3 MHz. These frequencies are close enough that it is unnecessary to require that the comparison sources have straight spectra. However, a separate comparison was made imposing this additional restriction and the results were essentially unaltered. We eliminate all sources that are resolved or confused in either catalogue and correct the RCL fluxes by the factor of 1.15 suggested by RBC. The following correction factors are found:

$$\left(\frac{\overline{S_{CL}}}{S_P}\right) = 1.00 \pm 0.06, \quad S_{CL} > 2000 \text{ Jy}, \quad 4 \text{ sources},$$

$$\left(\frac{\overline{S_{CL}}}{S_P}\right) = 1.04 \pm 0.04, \quad 2000 > S_{CL} > 100 \text{ Jy}, \quad 34 \text{ sources},$$

$$\left(\frac{\overline{S_{CL}}}{S_P}\right) = 1.07 \pm 0.04, \quad 100 > S_{CL} > 50 \text{ Jy}, \quad 23 \text{ sources}.$$

Thus, the Clark Lake and Penticton flux scales agree well for $S_{CL} > 50$ Jy but we did find that significant nonlinearity appears below this flux level where the average flux ratio appears to drop by 20%. This flux level is near the resolution limit of the Penticton instrument. Near the flux limit of almost any survey there is a well-known tendency to catalogue those sources which are overestimated and to discriminate against those that are underestimated. Since Clark Lake instrument has considerably higher angular resolution, our survey may be expected to go somewhat deeper before this effect occurs. The agreement is excellent and the overall correction factor turns out to be

$$\left(\frac{\overline{S_{CL}}}{S_P}\right) = 1.05 \pm 0.02, \quad S_{CL} > 50 \text{ Jy}, \quad 62 \text{ sources}.$$

In many cases RCL indicate the presence of confusing sources. None of the sources for which there was a confusing source present were used in the calculation of the factor given above. A similar calculation for these

sources above yields a factor of 0.91 ± 0.06 (39 sources). Therefore, the presence of a confusing source does appear to cause an overestimation of the flux in the Penticton survey. If both sets of sources were used, the correction factor would be precisely unity. This illustrates the degree of sensitivity of this procedure to comparison source selection.

E. Comparison with the Grakovo Flux Scale

Two catalogues of source fluxes have been produced with the UTR-1 telescope at Grakovo (Braude *et al.* 1969a, 1970a). We extrapolate the Grakovo 25-MHz fluxes to 26.3 MHz for comparison with our data. These frequencies are so close that the spectral index of each source is unimportant but those given in the Grakovo catalogues were used. A strong nonlinearity is found, so the average ratio between Clark Lake and Grakovo fluxes is given for several flux ranges:

$$\left(\frac{S_{CL}}{S_G}\right) = 0.88 \pm 0.05, \quad S_{CL} > 2000 \text{ Jy}, \quad 4 \text{ sources},$$

$$\left(\frac{S_{CL}}{S_G}\right) = 0.94 \pm 0.07, \quad 2000 > S_{CL} > 200 \text{ Jy}, \quad 10 \text{ sources},$$

$$\left(\frac{S_{CL}}{S_G}\right) = 0.76 \pm 0.06, \quad 200 > S_{CL} > 100 \text{ Jy}, \quad 14 \text{ sources},$$

$$\left(\frac{S_{CL}}{S_G}\right) = 0.67 \pm 0.05, \quad 100 > S_{CL} > 50 \text{ Jy}, \quad 26 \text{ sources}.$$

Our present flux scale is quite linear with respect to the KPW scale, the Penticton scale, and our old scale (Erickson and Cronyn 1965). Therefore, these data suggest strongly that the Grakovo scale is nonlinear. A similar conclusion was reached by RBC. The Grakovo data have been extensively interpreted (Braude *et al.* 1969b, 1970a, 1970b) and used to recalibrate other flux scales. The conclusions reached in these papers should be carefully reexamined from the standpoint of this apparent nonlinearity.

V. CONCLUSIONS

The Clark Lake radio source survey reported in this paper has been carefully calibrated and should define low-frequency flux scales quite reliably. We now have two decametric surveys, the Penticton and Clark Lake surveys, which agree with each other very well. Also, both of these surveys are in reasonable agreement with the Williams, Kenderdine, and Baldwin (1966) survey at 38 MHz. We suggest that the 38-MHz fluxes should be raised by 11% while the Penticton group (Roger, Bridle, and Costain 1973) suggest an 18% correction factor. The difference between these correction factors

is apparently due to different selections of intercomparison sources and the possible inclusion of some comparison sources that are confused by the Penticton instrument. In any event, if the 38-MHz fluxes were raised uniformly by about 15%, all three surveys would be in excellent agreement.

ACKNOWLEDGMENTS

We wish to acknowledge the dedicated work of the staff of the Clark Lake Radio Observatory in obtaining these observations. This work was supported by the National Science Foundation under Grant GP-19401 and by the National Aeronautics and Space Administration under Grant NGR 21-002-367. The computational work was supported in full by the Computer Science Center of the University of Maryland.

REFERENCES

- Artyukh, V. S., Vitkevich, V. V., Valsov, V. I., Kafarov, G. A., and Matveenko, L. I. (1966). *Sov. Astron.* **10**, 9.
 Bennett, A. S. (1962). *Mem. R. Astron. Soc.* **68**, 163.
 Braude, S. Ya., Lebedeva, D. M., Megn, A. W., Ryabov, B. P., and Zhouch, I. N. (1969a). *Mon. Not. R. Astron. Soc.* **143**, 289.
 Braude, S. Ya., Lebedeva, D. M., Megn, A. W., Ryabov, B. P., and Zhouch, I. N. (1969b). *Mon. Not. R. Astron. Soc.* **143**, 301.
 Braude, S. Ya., Lebedeva, D. M., Megn, A. W., Ryabov, B. P., and Zhouch, I. N. (1970a). *Astrophys. Lett.* **5**, 129.
 Braude, S. Ya., Lebedeva, D. M., Megn, A. W., Ryabov, B. P., and Zhouch, I. N. (1970b). *Astrophys. Space Sci.* **8**, 275.
 Bridle, A. H., and Purton, C. R. (1968). *Astron. J.* **73**, 717.
 Bridle, A. H., Davis, M. M., Fomalont, E. B., and Lequeux, J. (1972). *Astron. J.* **77**, 405.
 Bruk, Yu. M., Goncharov, N. Yu., Zhuk, I. N., Inyutin, G. A., Men, A. V., Sodin, L. G., and Sharykin, N. K. (1968). *Radio Phys. Quant. Mech.* **11**, 14.
 Burns, W. R. (1972). *Astron. Astrophys.* **19**, 41.
 Caswell, J. L., and Crowther, J. H. (1969). *Mon. Not. R. Astron. Soc.* **145**, 181.
 Colla, G., Fanti, C., Fanti, R., Ficarra, A., Formigini, L., Gandolfi, E., Lari, C., Marano, B., Padrielli, L., Salter, C. J., Setti, G., and Tomasi, P. (1971). *Astron. J.* **76**, 953.
 Conway, R. G., Kellermann, K. I., and Long, R. J. (1963). *Mon. Not. R. Astron. Soc.* **125**, 261.
 CSIRO staff (1969). *Aust. J. Phys. Astrophys. Suppl.* No. 7.
 Dickel, J. R., Webber, J. C., Yang, K. S., and staff (1971). *Astron. J.* **76**, 294.
 Erickson, W. C. (1965). *IEEE Trans. Ant. Propag.* **AP-13**, 422.
 Erickson, W. C., and Cronyn, W. M. (1965). *Astrophys. J.* **142**, 1156.
 Erickson, W. C., and Perley, R. A. (1975). *Astrophys. J. Lett.* **200**, L83.
 Fomalont, E. B. (1967). *Astrophys. J. Suppl.* **15**, 203.
 Gower, J. F. R. (1966). *Mon. Not. R. Astron. Soc.* **133**, 151.
 Gower, J. F. R., Scott, P. F., and Wills, D. (1967). *Mem. R. Astron. Soc.* **71**, 49.
 Hogg, D. E. (1964). *Astrophys. J.* **140**, 992.
 Hubbard, J. W., and Erickson, W. C. (1967). *IEEE Trans. Ant. Propag.* **AP-15**, 291.
 Kellermann, K. I., Pauliny-Toth, I. I. K., and Williams, P. J. S. (1969). *Astrophys. J.* **157**, 1.
 Kundu, M. R. (1969). *Astrophys. J.* **158**, L103.
 Kundu, M. R., and Velusamy, T. (1967). *Ann. Astrophys.* **30**, 723.
 Kundu, M. R., and Velusamy, T. (1969). *Astrophys. J.* **155**, 807.
 MacDonald, G. H., Neville, A. C., and Ryle, M. (1966). *Nature* **211**, 1241.
 MacDonald, G. H., Kenderdine, S., and Neville, A. C. (1968). *Mon. Not. R. Astron. Soc.* **138**, 259.
 Mackay, C. D. (1969). *Mon. Not. R. Astron. Soc.* **145**, 31.

- MacLeod, J. M., Swenson, S. W., Yang, K. S., and Dickel, J. R. (1965). *Astron. J.* **70**, 756.
- Moffet, A. T., and Maltby, P. (1962). *Astrophys. J. Suppl.* **7**, 141.
- Pilkington, J. D. H., and Scott, J. F. (1965). *Mem. R. Astron. Soc.* **69**, 183.
- Pooley, G. G., and Ryle, M. (1968). *Mon. Not. R. Astron. Soc.* **139**, 515.
- Roger, R. S., Costain, C. H., and Lacey, J. D. (1969). *Astron. J.* **74**, 366.
- Roger, R. S., Bridle, A. H., and Costain, C. H. (1973). *Astron. J.* **78**, 1030.
- Ryle, M., and Windram, M. D. (1968). *Mon. Not. R. Astron. Soc.* **138**, 1.
- Scott, P. F., and Shakeshaft, J. R. (1971). *Mon. Not. R. Astron. Soc.* **154**, 19P.
- Shimmins, A. J., and Day, G. A. (1968). *Aust. J. Phys.* **21**, 377.
- Viner, M. R. (1973). Ph.D. thesis.
- Viner, M. R. (1975). *Astron. J.* **80**, 83.
- von Hoerner, S. (1961). *Publ. Natl. Radio Astron. Obs.* **1**, No. 2.
- Wendker, H. J., Dickel, J. R., Yang, K. S., and staff (1970). *Astron. J.* **75**, 148.
- Williams, P. J. S., and Bridle, A. H. (1967). *Observatory* **87**, 280.
- Williams, P. J. S., Kenderdine, S., and Baldwin, J. E. (1966). *Mem. R. Astron. Soc.* **70**, 53.
- Willson, M. A. G. (1970). *Mon. Not. R. Astron. Soc.* **151**, 1.

AN ANOMALY IN THE FLUX OF CASSIOPEIA A AT 38 MHz

W. C. ERICKSON AND R. A. PERLEY

Clark Lake Radio Observatory, Astronomy Program, University of Maryland

Received 1975 February 3; revised 1975 June 5

ABSTRACT

The secular decrease in the flux of the supernova remnant Cassiopeia A has been measured at many radio frequencies. We present new observations that indicate that this flux decrease has halted at 38 MHz, and that the flux is increasing at this frequency. This may indicate that a new era of activity has begun in this object.

Subject headings: radio sources, variable — supernova remnants

I. INTRODUCTION

It is important to know the spectrum and secular variation of Cassiopeia A because this source is used as a flux density calibrator throughout the radio spectrum. Shklovsky's (1960) original model predicts a constant secular decrease in flux at all frequencies. Dent, Aller, and Olsen (1974) have suggested that the spectrum of Cas A is flattening with time, and that the rate of secular decrease varies from 1.29 ± 0.08 percent per annum at 81.5 MHz to 0.70 ± 0.07 percent per annum at 8.0 GHz. In this letter we present evidence for an *increase* in flux of Cas A at 38 MHz. This would be difficult to explain under any current model.

While completing the construction of the Clark Lake Telescope (Erickson and Fisher 1974), we have been measuring the relative fluxes of a number of sources at many frequencies throughout the 20–120 MHz operating range of the instrument. This has been done as a systems test and to set flux-calibration standards for later use.

The initial measurements, made with the E-W arm of the array, revealed a flux ratio of Cas A to Cyg A of about 1.60 (epoch 1974.8) at 38 MHz. This is above the older value, 1.42 ± 0.04 (epoch 1966.9) derived from Parker's (1968) measurements at the same frequency. If we apply a 1.29 percent per annum secular decrease (Scott, Shakeshaft, and Smith 1969) to Parker's ratio, the flux ratio should now be 1.28 (epoch 1974.8), so our value seemed 25 percent too high.

Parker's careful measurements have been widely accepted and used as the basis for meter-wavelength flux scales, so we rechecked our data using a number of different antenna and receiver configurations.

II. THE MEASUREMENTS

The array consists of fixed, vertical, log-spiral elements which receive left-circular polarized radiation. It is electronically steerable, and most of the observations were made by alternately tracking each source for several hours. The response is modulated by the primary pattern of the fixed elements, which is approximately independent of azimuth, and the responses due to the two sources were compared at equal zenith distances.

If the full E-W arm of 480 elements is employed, the response due to Cas A and Cyg A is tremendous; it is necessary to attenuate the antenna outputs by about 20 db and to add random noise to these attenuated signals in order to keep the receivers within their linear ranges. Various subarrays were formed to lower the output levels and to degrade the angular resolution ($8'$ at 38 MHz) so as to avoid large corrections for partial resolution. Some observations were also taken without tracking; grating arrays were formed with spaced elements, and the two sources were observed in total power as they drifted through the resulting multilobed grating pattern. All of these observations, taken between 1974.2 and 1974.8, yielded flux ratios in the range of 1.6 ± 0.1 . However, we feared that some undetected azimuthal dependence of the primary gain pattern might be influencing our results; and we awaited confirmation of the data taken with the E-W arm by data taken with the perpendicularly oriented N-S arm.

The N-S arm of the instrument was completed in mid-1974, and the most definitive data were taken in 1974 October. E-W and N-S interferometers were formed from individual banks of 15 elements, each separated by 150 wavelengths. Each bank of elements continuously tracked the source under observation, and sine and cosine components of the interference pattern were simultaneously recorded. Each channel was linearly integrated, digitized, and recorded on magnetic tape once a second. By digitally squaring and summing these sine and cosine components, a measurement of source amplitude was obtained for each second of observation. Noise calibration signals were introduced for two seconds each minute. Slow variations in receiver gain were monitored; no nonlinearity was detected. For each source, the data were averaged over 1° intervals in zenith distance. Such data are shown in Figure 1.

Data taken on different days are practically indistinguishable, but flux comparisons were always made in data taken only a few hours apart. The shapes of the Cas A and Cyg A curves are also indistinguishable. No significant differences have ever been found between data taken at negative or positive hour angles. However, the N-S and E-W

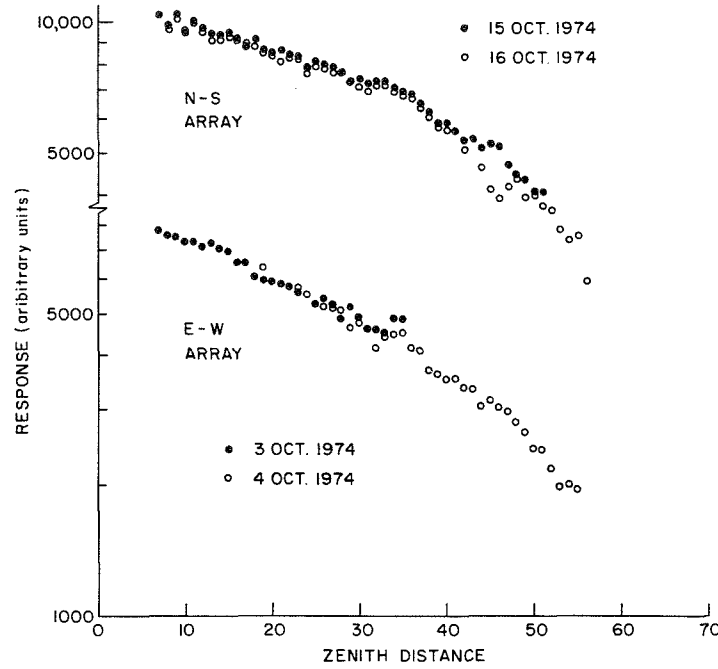


FIG. 1.—Sample data concerning the gain-zenith distance dependence of the system obtained from tracking Cyg A with E-W and N-S interferometer combinations. Center frequency is 38.0 MHz with a 50 kHz bandwidth. In each case, only the data obtained before transit are plotted because ionospheric scintillations occurred after transit.

curves have slightly different shapes. Presumably this is due to a small azimuthal asymmetry in the gain pattern of the array, which in turn is probably due to mutual interaction or partial shadowing effects between elements. The tracks of the two sources with respect to the axis of each array are shown in Figure 2. Assuming that E-W and N-S patterns are identical, the best way to eliminate the influence of the azimuthal asymmetry is to consider the responses at the points where the source tracks cross, labeled points 1 and 2 in Figure 2. These points are both at a zenith distance of 30° . If the responses of the two arrays to the two sources are given by

$$\begin{aligned} R_{N-S,1}(\text{Cas A}) &= K_{N-S} G_1 S_{\text{Cas A}} \\ R_{E-W,1}(\text{Cyg A}) &= K_{E-W} G_1 S_{\text{Cyg A}} \\ R_{N-S,2}(\text{Cyg A}) &= K_{N-S} G_2 S_{\text{Cyg A}} \\ R_{E-W,2}(\text{Cas A}) &= K_{E-W} G_2 S_{\text{Cas A}} \end{aligned} \quad (1)$$

where $G_{1,2}$ are the antenna gain factors at points 1 and 2, $K_{N-S, E-W}$ are combined preamplifier gain and transmission-line attenuation factors, and $S_{\text{Cas A}}, S_{\text{Cyg A}}$ are the source fluxes. All gain factors cancel from the combination

$$\begin{aligned} \frac{S_{\text{Cas A}}}{S_{\text{Cyg A}}} &= \left[\left(\frac{R_{N-S,1}}{K_{N-S} G_1} \right) \left(\frac{R_{E-W,2}}{K_{E-W} G_2} \right) / \left(\frac{R_{E-W,1}}{K_{E-W} G_1} \right) \left(\frac{R_{N-S,2}}{K_{N-S} G_2} \right) \right]^{1/2} \\ &= \left(\frac{R_{N-S,1} R_{E-W,2}}{R_{E-W,1} R_{N-S,2}} \right)^{1/2}. \end{aligned} \quad (2)$$

Combining all data taken within 2° of points 1 and 2 on 1974 October 2, 3, 15, and 16, we obtain

$$\frac{S_{\text{Cas A}}}{S_{\text{Cyg A}}} = 1.60 \pm 0.07 \quad (\text{epoch 1974.8}). \quad (3)$$

A correction for partial resolution was applied to the responses given in equations (1). It was calculated by convolving the appropriate interference pattern with the Cas A and Cyg A brightness distributions given by Ryle, Elsmore, and Neville (1965). This resolution correction was ~ 6 percent.

The error quoted above is not a standard deviation but rather a confidence level derived from estimates of the

various systematic errors that might affect the determination. The standard deviation of the set of observations obtained on a single day is often less than 1 percent under quiet ionospheric conditions. From day to day, data are often reproducible to this level. On the other hand, when the ionosphere is disturbed, 10 to 20 percent deviations are not uncommon. In addition, systematic errors in the determination of the antenna response patterns, thermal variations, and receiver calibration can all affect the results by 1 percent or more. Evaluation of these effects leads to the ~ 4 percent confidence level which we quote.

The relative antenna gains are given by

$$\frac{G_2}{G_1} = \left(\frac{R_{E-W,2} R_{N-S,2}}{R_{N-S,1} R_{E-W,1}} \right)^{1/2} = 1.12 \pm 0.05. \quad (4)$$

The consistency of these results can be checked by consideration of Cyg A drift curves such as those shown in Figure 1. These drift curves can be normalized at point 3 in Figure 2 where they cross at a zenith distance of 11° , then the relative antenna gains at points 1 and 2 (zenith distance 30°) can be read off directly. This method yields

$$\frac{G_2}{G_1} = 1.14 \pm 0.02.$$

The agreement between the two methods of determining G_1/G_2 lends strong support to the value of $S_{\text{Cas A}}/S_{\text{Cyg A}}$ given in eq. (3).

A preliminary study of the frequency dependence of $S_{\text{Cas A}}/S_{\text{Cyg A}}$ was carried out. The data in Table 1 were obtained with various array and receiver configurations.

Drift scans of the sources were also taken with the NRAO 94-m dish when it was instrumented at four metric wavelengths. These yielded the flux ratios given in Table 2.

III. INTERPRETATION OF THE MEASUREMENTS

Extrapolation of the flux-density decrease determined by Scott, Shakeshaft, and Smith (1969) at 81.5 MHz to 1974.0 yields a value of $S_{\text{Cas A}}/S_{\text{Cyg A}} = 1.175$. Similar extrapolations of Parker's (1968) data at 152 MHz and Adgie and Smith's (1956) data at 210 MHz yield ratios of 1.10 and 1.25, respectively. Therefore, we see by comparison of these extrapolations with Tables 1 and 2 that all data except those at 38 MHz are consistent with a constant secular decrease in Cas A. If our data and Parker's data are accepted at face value, they imply a secular *increase* in Cas A

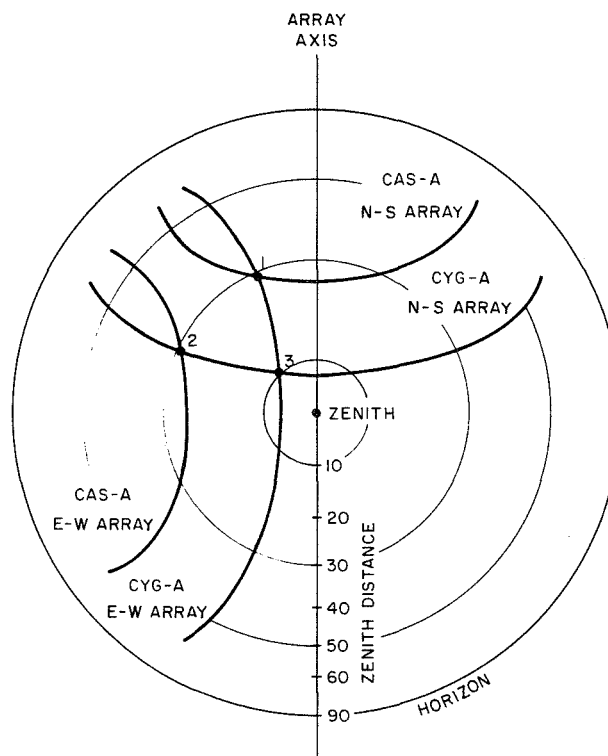


FIG. 2.—The tracks of Cas A and Cyg A with respect to the N-S and E-W arrays

TABLE 1
FREQUENCY DEPENDENCE OF CASSIOPEIA A
AND CYGNUS A

| Frequency (MHz) | $S_{\text{Cas A}}/S_{\text{Cyg A}}$ | Epoch |
|-----------------|-------------------------------------|----------------|
| 26.3..... | 1.4 ± 0.2 | 1974.2 |
| 38.0..... | 1.60 ± 0.07 | 1974.8 |
| 80.0..... | 1.15 ± 0.10 | 1974.0, 1974.2 |
| 121.5..... | 1.15 ± 0.10 | 1974.0 |

TABLE 2
FLUX RATIOS OF CASSIOPEIA A
AND CYGNUS A

| Frequency (MHz) | $S_{\text{Cas A}}/S_{\text{Cyg A}}$ | Epoch |
|-----------------|-------------------------------------|--------|
| 114..... | 1.18 ± 0.10 | 1974.0 |
| 144..... | 1.16 ± 0.07 | 1974.0 |
| 184..... | 1.18 ± 0.06 | 1974.0 |
| 236..... | 1.15 ± 0.06 | 1974.0 |

of 1.5 ± 0.6 percent per annum at 38.0 MHz between 1966.9 and 1974.8, while a combination of Adgie and Smith's (1956) data with Parker's data suggests an earlier secular decrease at this frequency. Based upon various unpublished measurements between 12 and 38 MHz taken from 1955 to 1966, Braude *et al.* (1969) have suggested that the flux of Cas A may be varying randomly by about ± 15 percent at 38 MHz, with no obvious secular decrease. Our measurements tend to confirm this suggestion. All of the data are shown in Figure 3. It is difficult to determine how to weight the data quoted by Braude *et al.* (1969) because no estimation of errors was given. Our data are consistent with Viner's (1975) absolute flux measurements at 26.3 MHz, but the time span of these measurements is too short to confirm a decrease or increase in flux.

How can these data be explained? (1) Perhaps Parker's 38 MHz data are seriously in error. This seems unlikely, and his data agree with those of Adgie and Smith at 38 MHz, as well as with many other determinations at neighboring frequencies. Even if we discard the older 38 MHz data, our flux ratio of 1.60 implies a Cas A flux of 40,800 Jy and a spectral index between 38 and 80 MHz of -0.9 to -1.0 . Thus the spectrum would now steepen sharply below 80 MHz while retaining an index of -0.77 above 80 MHz. (2) Our data were taken in left-circular polarization. If either of the sources were strongly polarized, the anomaly might be explained. However, no polarization in either of these sources has even been found at meter wavelengths. (3) Cyg A has decreased in flux. The compact components of Cyg A produce less than 1 percent of its flux at meter wavelengths (Erickson *et al.* 1972; Slee and Wraith 1967). It is implausible that the large components could vary. (4) Ionospheric absorption might influence the data, but this is unlikely because the estimated total absorption was always less than 1 percent during the measurements, and the relative absorption should be negligible. Refractive scintillations are certainly observed, but they will not change the average observed flux. (5) The most likely explanation is that the supernova remnant Cas A has entered a new era of activity. The new emission would have to be generated by a new compact component (Hutton *et al.* 1974), since no such component was found by Slee and Wraith (1967). If due to synchrotron radiation, the data are consistent with the production of an essentially monoenergetic flux of electrons with critical frequencies near 38 MHz. It seems likely that this might be associated with optical variations (Van den Bergh and Dodd 1970) or with the compact components mapped at centimeter wavelengths (Rosenberg 1970 *a, b*).

Our results need confirmation with other instruments. We are now repeating them at many frequencies between 22 and 80 MHz. Preliminary analysis of data taken in 1975 January show good agreement with the data presented here.

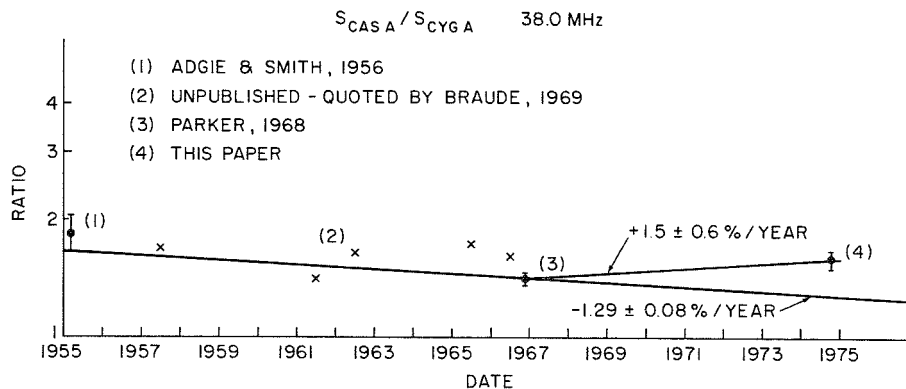


FIG. 3.—A compilation of 38.0 MHz determinations of the flux ratio, $S_{\text{Cas A}}/S_{\text{Cyg A}}$, at various epochs compared with the 81.5 MHz of secular decrease.

We wish to acknowledge the dedicated work of the staff of the Clark Lake Radio Observatory. We also wish to thank Dr. J. R. Fisher, who was a coinvestigator with one of us (W. C. E.) in the NRAO observations. The Clark Lake Radio Observatory is supported by the National Science Foundation under grant GP-19401, and by the National Aeronautics and Space Administration under grant NCL 21-002-367. The computational work was supported in full by the Computer Science Center of the University of Maryland.

REFERENCES

- Adgie, R., and Smith, F. G. 1956, *Observatory*, **76**, 181.
Braude, S. Ya., Lebedeva, O. M., Megn, A. V., Ryabov, R. B., and Zhouck, I. N. 1969, *M.N.R.A.S.*, **143**, 301.
Dent, W. A., Aller, H. D., and Olsen, E. T. 1974, *A.p. J. (Letters)*, **188**, L11.
Erickson, W. C., and Fisher, J. R. 1974, *Radio Science*, **9**, 387.
Erickson, W. C., Kuiper, T. B. H., Clark, T. A., Knowles, S. H., and Broderick, J. J. 1972, *A.p. J.*, **177**, 101.
Hutton, L. K., Clark, T. A., Erickson, W. C., Resch, G. M., Vandenberg, N. R., Knowles, S. H., and Youmans, A. B. 1974, *A.J.*, **79**, 1248.
Parker, E. A. 1968, *M.N.R.A.S.*, **138**, 407.
Rosenberg, I. 1970a, *M.N.R.A.S.*, **147**, 215.
———. 1970b, *ibid.*, **151**, 109.
Ryle, M., Elsmore, B., and Neville, Ann C. 1965, *Nature*, **205**, 1259.
Scott, P. F., Shakeshaft, J. R., and Smith, M. A. 1969, *Nature*, **223**, 1139.
Shklovsky, I. S. 1960, *Astr. Zh.*, **37**, 256.
Slee, D. B. and Wraith, P. K. 1967, *Nature*, **214**, 971.
Van den Bergh, S., and Dodd, W. W. 1970, *A.p. J.*, **162**, 485.
Viner, M. R., 1975, *A.J.*, **80**, 83.

W. C. ERICKSON and R. A. PERLEY: Astronomy Program, University of Maryland, College Park, MD 20742

METER-WAVELENGTH VLBI. III. PULSARS

N. R. VANDENBERG, T. A. CLARK, W. C. ERICKSON, AND G. M. RESCH

University of Maryland, College Park; and Goddard Space Flight Center

AND

J. J. BRODERICK

Virginia Polytechnic Institute and State University

Received 1975 October 23

ABSTRACT

The results and analysis of observations of pulsars, especially the Crab Nebula pulsar, taken during a series of meter-wavelength very long baseline interferometry (VLBI) experiments are discussed. Based on a crude 144 MHz visibility curve which is consistent with a Gaussian brightness distribution, the measured visibilities at 196, 111, and 74 MHz were interpreted to yield apparent angular diameters (at half-power) of $0''.03 \pm 0''.01$, $0''.07 \pm 0''.01$, and $0''.18 \pm 0''.01$, respectively. These sizes scale approximately as wavelength-squared, and the 74 MHz size agrees with recent observations using interplanetary scintillation techniques.

The VLBI-measured total flux densities lie on the extrapolation from higher frequencies of the pulsing flux densities. Variations in the total flux density up to 25 percent were observed. A lack of fine structure other than the pulsar in the nebula is indicated by our simple visibility curves. The pulse shapes observed with the interferometer are similar to single-dish measurements at 196 MHz but reveal a steady, nonpulsing component at 111 MHz. The ratio of pulsing to total power was approximately equal to one-half but varied with time. No pulsing power was detected at 74 MHz. It was found that four strong, low-dispersion pulsars were only slightly resolved.

Subject headings: pulsars — radio sources: general

I. INTRODUCTION

This is the third paper reporting on a series of meter-wavelength very long baseline interferometry (VLBI) experiments. Paper I presented the analysis of observations made on the supernova remnant Cassiopeia A (Hutton *et al.* 1974). Paper II (Clark *et al.* 1975) gave a detailed description of the experimental methods, calibration procedures, and consistency checks; a list of the flux densities observed for the extragalactic sources was presented. The present paper (Paper III) discusses the results and analysis of our observations of pulsars, concentrating on the Crab Nebula pulsar. Subsequent papers will consider various models and interpretations of the results.

Briefly, the experiments began in late 1971 and spanned $1\frac{1}{2}$ years. There were five two- or three-day observing sessions monthly from 1971 November through 1972 March, and week-long sessions in 1972 December and 1973 February. The telescopes used were Arecibo (305 m), NRAO (92 m), and Sugar Grove (46 m); they form two long baselines (2550 km) and one short baseline (50 km). The observing frequencies were 196 and 111 MHz for the five 1971-1972 experiments and 111 and 74 MHz for the two 1971-1972 experiments. (See Table I and Fig. 1 of Paper II.)

The Crab Nebula pulsar was the primary source in all of the experiments. The other pulsars included four strong, low-dispersion pulsars (PSRs 0834+06, 0950+08, 1133+16, and 1919+21) and four weak, high-dispersion pulsars (PSRs 1858+03, 1933+17, 1946+

35, and 2003+31). The Crab Nebula pulsar will be discussed in § II of this paper, and the other pulsars in § III.

II. CRAB NEBULA PULSAR

a) Definitions

The signal from a pulsar can be represented as either a time-varying periodic pulse train or a time-averaged continuous source level. The time-varying or "pulsing" flux density is associated with the object called the pulsar, while the constant time-averaged "total" flux density is associated with the so-called "compact source" in the Crab Nebula. The various components of the intensity are illustrated in Figure 1. The total flux density, I_T , is obtained by normal processing of the data as for a continuum source. The time-averaged pulsing flux density, I_p , and the pulse profile are obtained by detecting each Fourier component of the pulse shape and then adding these in a complex Fourier sum. The algebraic difference between the total flux density and the time average of the pulsing flux density is the continuous or "steady" flux density, I_s . Each of these quantities was determined for observations on both the long and short baselines. We assumed that the source is unresolved on the short baseline, and we observed that it is partially resolved on the long baselines. Therefore, the fringe visibility is defined as the ratio of the flux density observed with the long baseline to that with the short baseline: $\gamma = I_{TR}/I_T$ where we

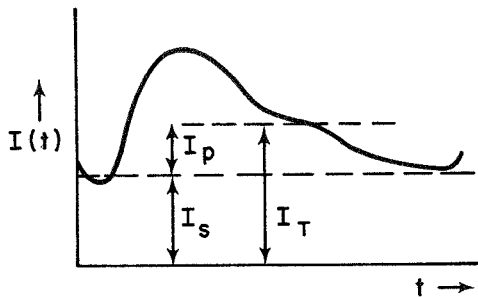


FIG. 1.—Components of the total intensity of a pulsar

denote the partially resolved quantities by a subscript *R*. More details on the processing procedures can be found in the thesis by Vandenberg (1974) and the paper by Erickson *et al.* (1972).

b) Total Flux Density Observations

i) Data

The average flux densities observed during each experiment are plotted in Figure 2; Table 1 lists the

overall average flux densities and the fringe visibility at each frequency. The flux densities in the table are weighted averages, and the associated error represents the rms deviation of the mean flux density. Figures 3 and 4 are plots of the individual-run flux densities (3-minute averages) for 111 and 74 MHz in 1973 February. These plots comprise our “visibility curves” for the compact source in the Crab Nebula. The values for the fringe visibility shown in Figure 3 are surprisingly constant in spite of the large and rapid variations in total flux density. Figure 2 shows this phenomenon on a yearly time scale. Some of the variation in flux density from month to month could be due to unknown systematic errors although the discussion of Paper II shows that their magnitude should be less than 10 percent. The total flux density varied by up to 10 percent at 111 MHz between our observing sessions in winter 1971–1972 and winter 1972–1973, although the fringe visibility remained about the same. The variation in total flux density is therefore probably intrinsic to the source. Changes in the pulsing flux density of up to a factor of 3 in a few weeks’ time are common at 430 MHz (Rankin *et al.* 1974) where all of the flux density is pulsing, while at lower frequencies the

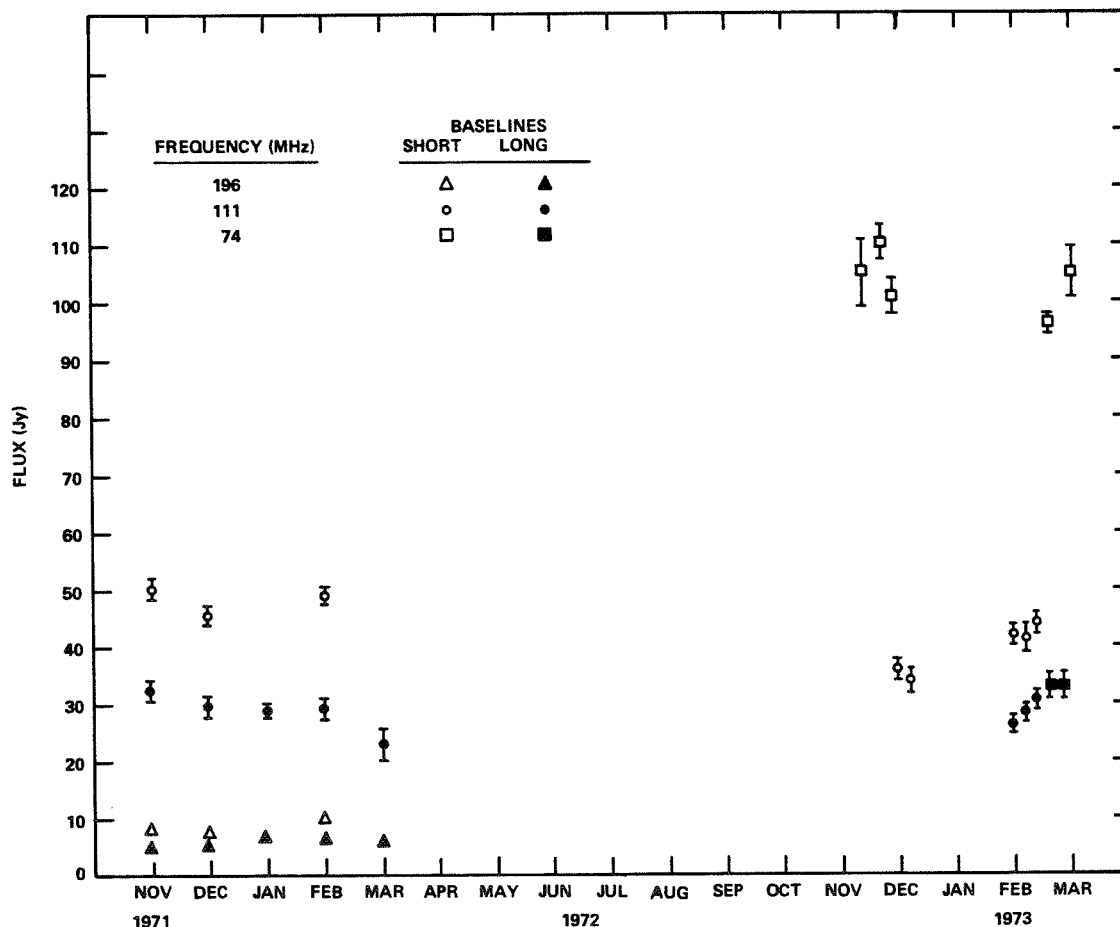


FIG. 2.—Total average flux density of the Crab Nebula pulsar. The error bars are the standard deviation of the data points. The errors at 196 MHz are the same size as the points.

TABLE 1
TOTAL AVERAGE FLUX DENSITIES OF THE CRAB NEBULA PULSAR
(1971 November–1973 February)

| Frequency (MHz) | I_T (Jy) | Number of Runs | I_{TR} (Jy) | Number of Runs | γ |
|-----------------|----------------|----------------|----------------|----------------|-----------------|
| 196.5..... | 8.3 ± 0.4 | 12 | 6.2 ± 0.2 | 47 | 0.74 ± 0.06 |
| 111.5..... | 40.5 ± 0.6 | 66 | 31.2 ± 1.2 | 111 | 0.72 ± 0.03 |
| 74.0..... | 105 ± 2.1 | 41 | 33.5 ± 1.7 | 29 | 0.32 ± 0.02 |

changes in pulsing flux density, though still apparent, are not so drastic.

The data represented in Table 1 and Figures 2, 3, and 4 provide only a small range of points on the visibility curve because the sparse hour-angle coverage allowed little foreshortening of the long baselines. Interpretation of the measured fringe visibility for any of the data can therefore be done only by assuming a source brightness distribution. In a 1971 March 144 MHz VLBI experiment between Sugar Grove, Vermilion River, and Owens Valley Observatories, the Crab Nebula was observed at many different hour angles so that each baseline was foreshortened and a crude visibility curve is available. The data points are

plotted in Figure 5. The fringe visibility scale was set by normalizing each observed correlation coefficient to the correlation observed on the shortest baseline.

If the apparent angular size of the Crab Nebula pulsar is due to interstellar scattering, then we expect the size of the scattering disk to depend on the observing frequency to some power. For certain types of irregularity spectra, we also expect the apparent source to have a Gaussian brightness distribution at all frequencies. Our 144 MHz data points are consistent with many brightness distributions, and several visibility curves are superposed on the data of Figure 5 to illustrate this. From our data alone, we can claim consistency with a Gaussian brightness distribution.

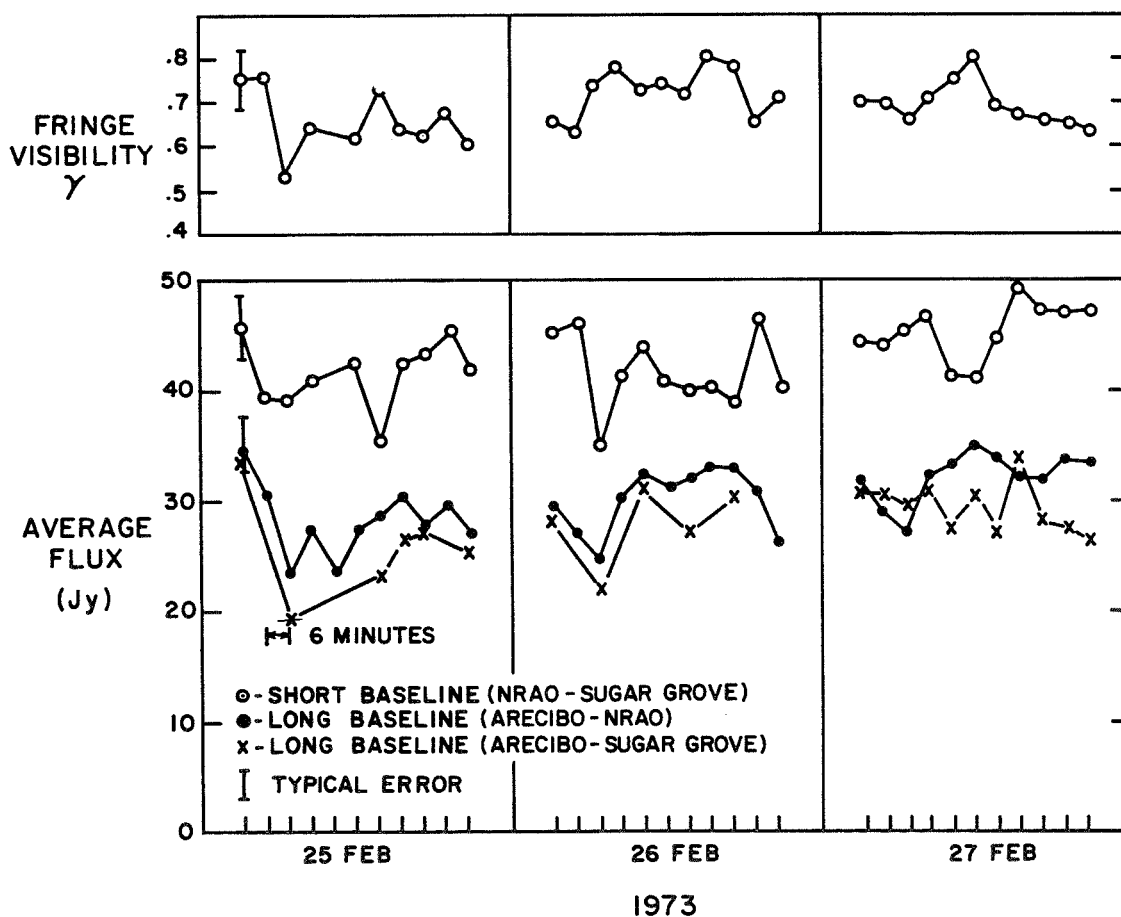


FIG. 3.—Total average flux density of the Crab Nebula pulsar at 111 MHz, observed on 3 days in 1973 February. Each point is a 3-minute average.

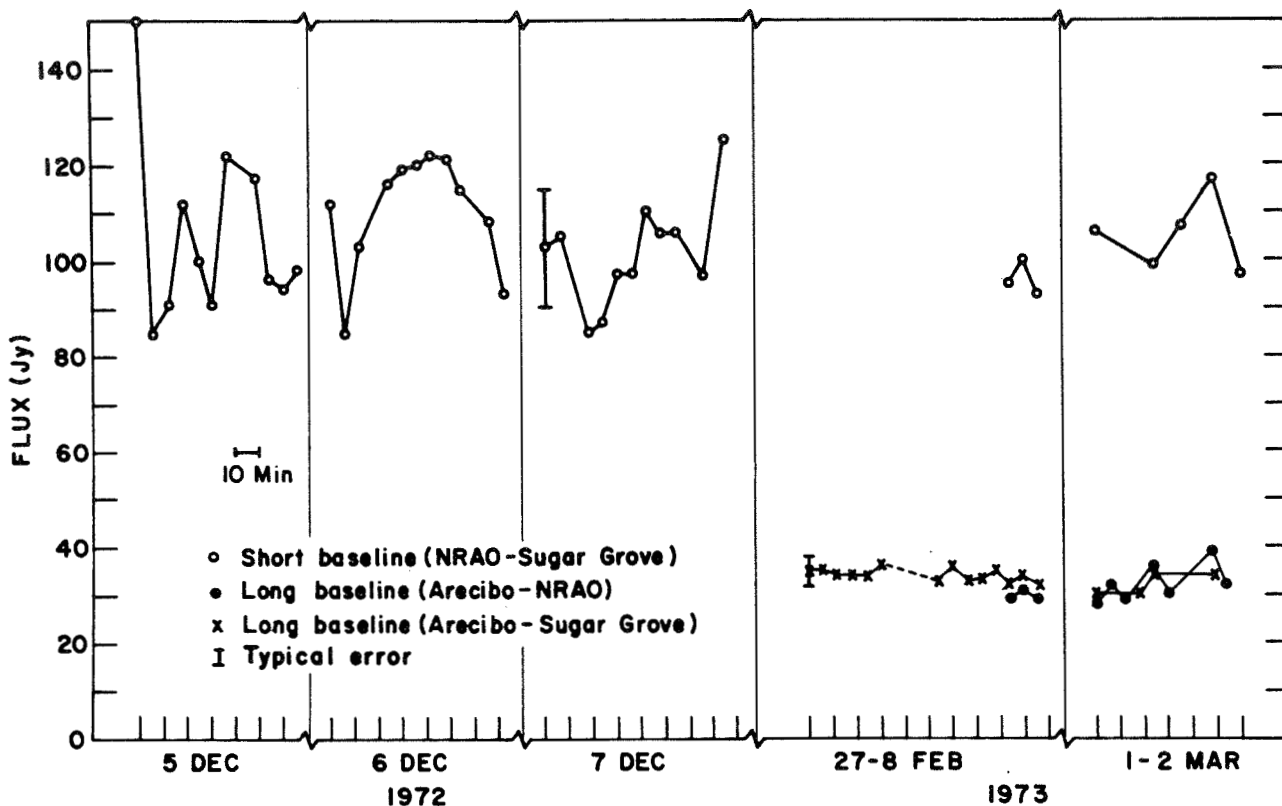


FIG. 4.—Total average flux density of the Crab Nebula pulsar at 74 MHz, observed on several days in 1972 December and 1973 February. Each point is a 3-minute average.

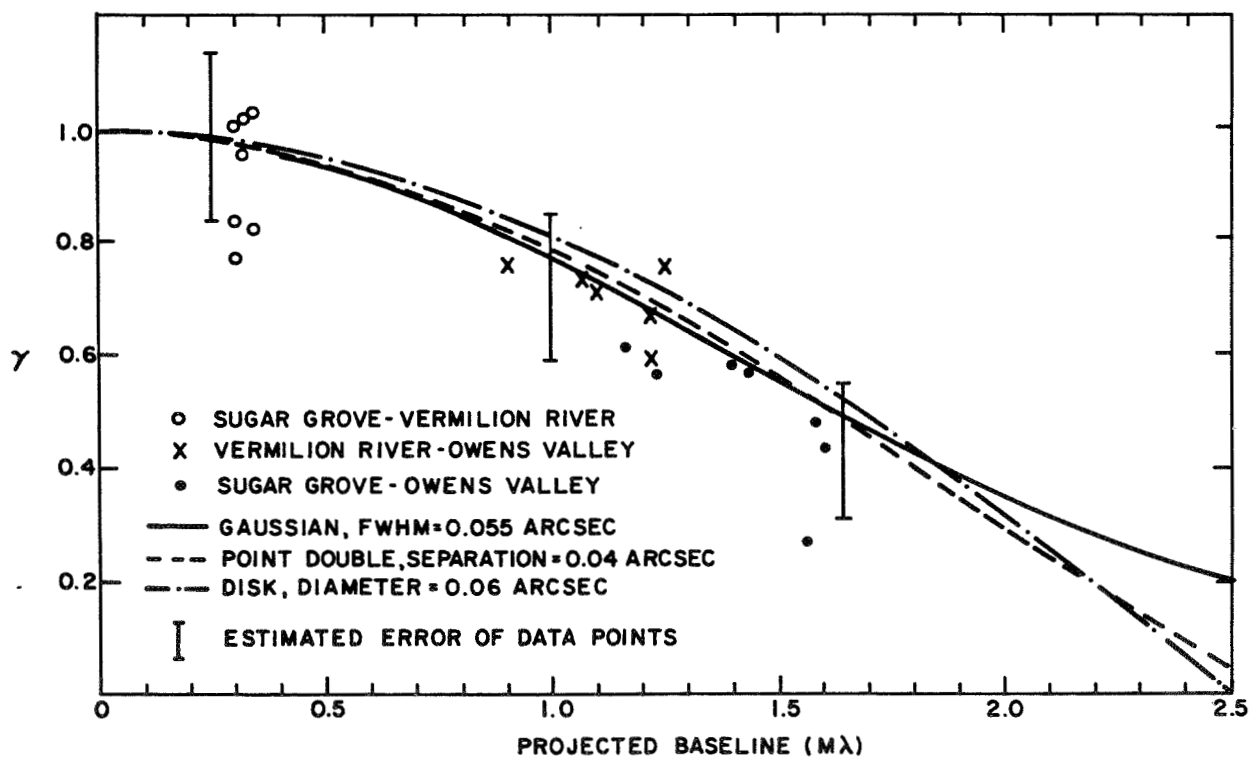


FIG. 5.—Fringe visibilities of the Crab Nebula pulsar observed in 1971 March at 144 MHz. Model visibility curves for three brightness distributions are shown.

TABLE 2
APPARENT ANGULAR DIAMETERS OF THE CRAB NEBULA PULSAR

| Frequency (MHz) | Baseline (km) | Baseline ($10^6\lambda$) | γ | θ_s (arcsec) |
|-----------------|---------------|----------------------------|-----------------|---------------------|
| 196.5..... | 2550 | 1.7 | 0.74 ± 0.06 | 0.03 ± 0.01 |
| 144.3..... | 2700 | 1.3 | 0.65 ± 0.15 | 0.05 ± 0.03 |
| 111.5..... | 2550 | 0.94 | 0.72 ± 0.03 | 0.07 ± 0.01 |
| 74.0..... | 2550 | 0.63 | 0.32 ± 0.02 | 0.18 ± 0.01 |

In addition, recent observations of strong scintillations of the compact source in the Crab Nebula by Armstrong *et al.* (1973) revealed a brightness distribution which fits a Gaussian shape down to the noise level. Therefore, based on the 144 MHz visibility curve and these interplanetary scintillation (IPS) observations, fringe visibilities observed in the later experiments were interpreted by assuming a Gaussian source distribution. Table 2 lists the values of the full width at half-maximum, here called θ_s , of the apparent angular sizes derived under this assumption.

A weighted least-squares fit to a power-law wavelength dependence was made for the four values of θ_s in Table 2. An exponent of 2.0 ± 0.4 was obtained, which is consistent with the wavelength-squared dependence found in many scattering theories. The wavelength dependence of interstellar scattering is discussed in more detail by Mutel *et al.* (1974). They have also collected many measurements of the apparent angular size of the compact source in the Crab Nebula, and a fit to all of the data yields a power law of exponent 2.05 ± 0.25 .

ii) Spectrum

The flux densities measured at our three frequencies (Table 1) give a spectral index of -2.9 ± 0.4 , which is the same value and error quoted by Rankin *et al.* (1970) from observations of the pulsar between 430 and 196 MHz. Our total flux density measurement at 196 MHz agrees with the Arecibo flux density measurement at that frequency, and our measured total flux densities at the lower frequencies therefore lie on the extrapolation of the spectrum of the pulsing flux density. Figure 6 shows the spectrum of the compact source, including pulsar, IPS, and VLBI measurements.

The usefulness of a spectral index for this source can be questioned, however, because of the variability observed in both the pulsing and the total flux density. Simultaneous measurements at several frequencies have shown there is no correlation between variations in the pulsing power at 430 and 111 MHz on time scales of minutes or less (Rankin *et al.* 1974), which means that even the shape of the spectrum is variable.

The behavior of the pulsing flux density contrasts with our observations of the total flux density. We observed up to 25 percent variations in the total flux density at 111 MHz, and no significant variations ($<15\%$) at 74 MHz. This behavior also differs from that of other pulsars which seem to be highly variable at meter wavelengths (Huguenin, Taylor, and Helfand 1973).

iii) Small Structure in the Nebula

Several lines of evidence suggest that there could be small-scale emission structure (other than the pulsar) in the Crab Nebula at low frequencies. The observations of Matveenko (1968) indicate there are two compact sources in the nebula. It is also possible that the wealth of detail present in the filaments, wisps, and continuum emission at optical wavelengths might continue to low frequencies. High-resolution maps at centimeter wavelengths (Wilson 1972) reveal "ridges" which are coincident with the filaments and have spectral indices approximately equal to that of the continuum radiation. This information hints that these structures might also be detectable at meter wavelengths.

Although our coverage of the (u, v) -plane is meager, we can draw some conclusions about small-scale emission structure in the nebula. A lack of fine structure is indicated by our flat visibility curves at 111 and 74 MHz (Figs. 3 and 4): the fringe visibility as a function of hour angle at 111 MHz does not vary except for noise fluctuations. Also, there is no systematic trend in the time-delay and fringe-rate residuals which might indicate the presence of other sources. At 74 MHz the data spans $2\frac{1}{2}$ hours, and again no changes in fringe visibility or residual parameters are evident.

If there were fine structure besides the pulsar in the nebula at our frequencies, that is, if there were many small sources, the visibility curve should show large fluctuations with small changes in hour angle. Except for a fortuitous arrangement of sources we conclude that there is no structure in the nebula on an angular scale of the order of the fringe spacing ($0''.3$ at 74 MHz) or smaller. Similarly the smoothness of the short-baseline interferometer visibility curves also indicates a lack of structure with angular sizes smaller than $15''$. More extended observations at these frequencies should be made in order to consider this problem in more detail.

Another argument which supports the absence of structure in the nebula is based on our observations (presented in the next section) that all of the power at 196 MHz is contained in the pulsing component, and that at 111 MHz the phase of the pulsar's radiation agrees with that of the compact source. This is evidence that the pulsar is truly the only small object in the nebula, because if we were observing the coherent sum of radiation from the pulsar plus fine structure or other compact objects, then part of the total power would not be pulsing at 196 MHz, and the continuous radiation would have a different phase from that of the

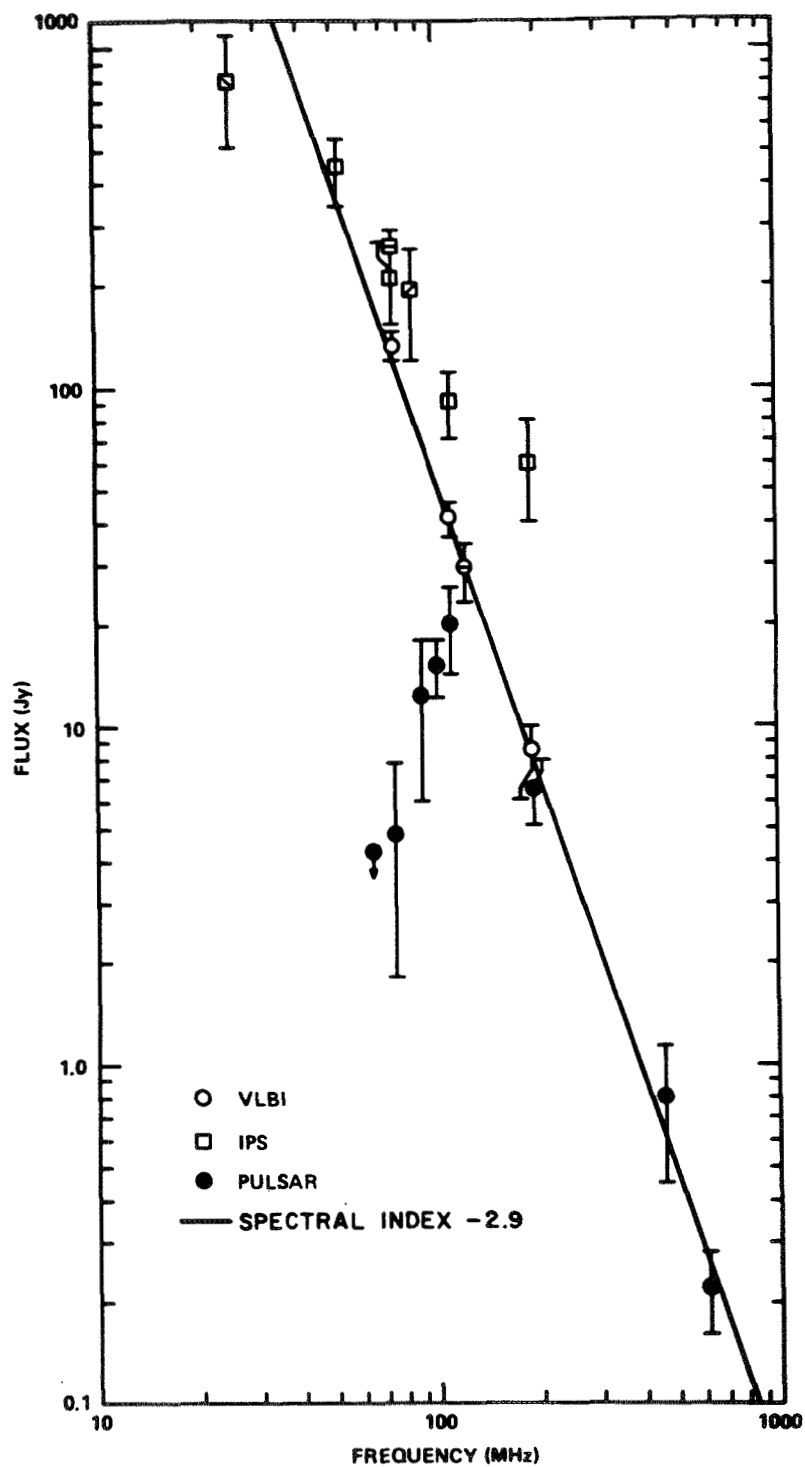


FIG. 6.—Spectrum of Crab Nebula compact source and pulsar. References for the spectral points are: \square , Cronyn 1970; \square , Harris 1973; \square , Readhead and Hewish 1974; \square , Armstrong *et al.* 1973; \ominus , Erickson *et al.* 1972; \circ , this paper; \bullet , Rankin *et al.* 1970.

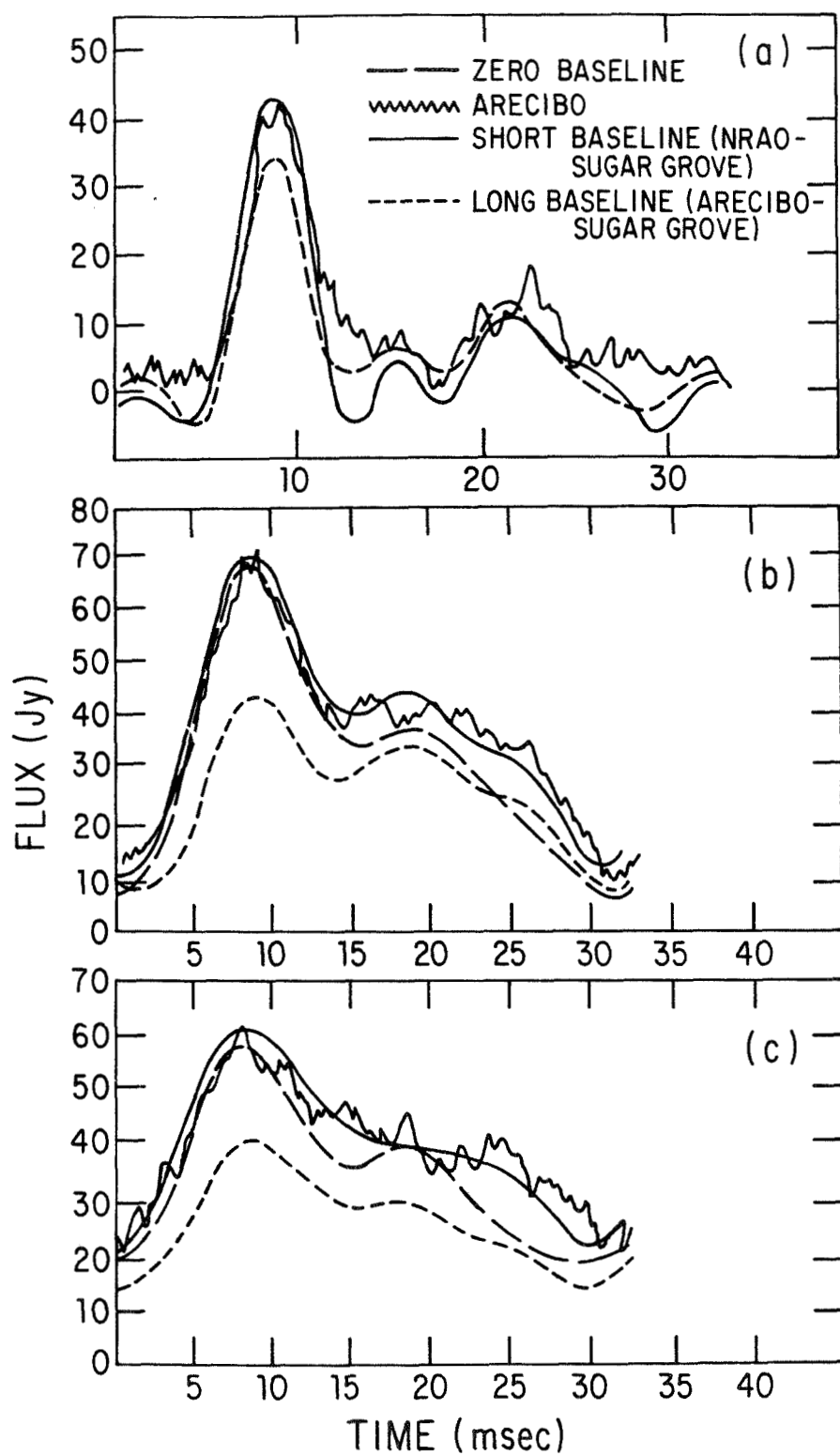


FIG. 7.—Typical pulse profiles: (a) 196 MHz; (b) 111 MHz, 1971 November; (c) 111 MHz, 1973 February

pulsar. This is not the case, and we conclude there are no compact objects or structure in the nebula (other than the pulsar) stronger than ~ 10 percent of the pulsar's total flux density.

iv) Comparison with IPS Measurements

IPS observations of the compact source in the Crab Nebula at 74 MHz have been reported by Armstrong *et al.* (1973). They derive an angular diameter of $0''.18 \pm 0''.01$ at $1/e$ which corresponds to a half-power diameter of $0''.15$ and is consistent with our observations. The amount of scintillating flux density which they quote is a factor of 2 higher than the total flux density observed with VLBI techniques, although their value for the flux density agrees with other IPS observations of the compact source by Harris (1973) and Readhead and Hewish (1974) (refer to Fig. 6).

In a more recent paper, Coles, Rickett, and Rumsey (1974) used a new theoretical treatment of their IPS data which removes the disagreement with our results on the flux density of the Crab Nebula compact source. The 74 MHz VLBI and IPS observations are thus in agreement on the apparent diameter and total flux density for this source. However, the application of this same analysis to other sources produces discrepancies which did not exist before between the VLBI and IPS flux densities of many extragalactic sources. This problem will be discussed in more detail in another paper (cf. Resch *et al.* 1975).

c) Pulsing Flux Density and Correlated Profiles

i) 196 MHz

We usually detected five Fourier components of the pulse shape at 196 MHz in one 3-minute average (one run). The fringe amplitudes and phases for each run were added in a Fourier sum, interpolated, and the resulting smooth profile was plotted. Figure 7a shows typical pulses from the short and long baseline and Arecibo. Both of the interferometer profiles and the Arecibo profile are similar, and the amount of angular resolution is small. All of the power is pulsing ($I_T = I_P$), and the baseline level set by the interferometer is the same as that of the single-telescope observation. Thus the interferometer shows no essential differences with respect to the single-telescope profiles.

ii) 111 MHz

At 111 MHz three Fourier components were usually detectable in one run, although the actual number varied from one to four with changes in the pulse shape and level of pulsing power. At this frequency, the pulsing and steady components contribute about equally to the total flux density from the compact source ($I_P \approx I_S \approx I_T/2$). Thus the ratio I_P/I_T is approximately equal to one-half although it was found to vary with time. The pulse shapes are broader than the 196 MHz pulse shapes, and they also have an offset baseline bias and continuous nonpulsing power. Pulses from a typical run in 1971 November are shown in Figure 7b. The comparison Arecibo pulse has been raised above the baseline to coincide with the short-baseline interferometer pulse. The value of I_S is taken as the minimum of the pulse profile, and I_P is calculated as $I_P = I_T - I_S$. For the 1971–1972 observing sessions, the average value of I_P/I_T was 0.6 for both long- and short-baseline profiles. For the 1972–1973 experiments, most of the data revealed only two Fourier components, and $I_P/I_T \approx 0.4$ for all the profiles. The typical pulse shape shown in Figure 7c is clearly broader than that in Figure 7b, and the offset baseline bias is larger.

The total amount of pulsing power was determined by a variety of methods: with the short-baseline cross-correlation interferometer, by autocorrelating the Arecibo tape to form a zero-baseline interferometer, and from the single-telescope observations made at Arecibo. All three methods give approximately the same value of I_P , and the Mark I autocorrelation data agree well with the Arecibo flux densities which were observed simultaneously with the VLBI experiment.

According to simple one- and two-screen interstellar scattering models, a larger temporal delay is associated with a large angular size, and therefore we should observe a systematic increase of apparent source size with phase across the pulse profile. Equivalently, we should observe a narrower pulse if we partially resolve the apparent scattering disk with an interferometer, and the higher Fourier components should have a higher fringe visibility. However, the observations indicate that the fringe visibility shows no systematic trend toward unity for higher values of n . Also, the values for I_P/I_T calculated for the long and short baselines are equal to within the rather large error limits.

A quantitative test for the variation of fringe visibility

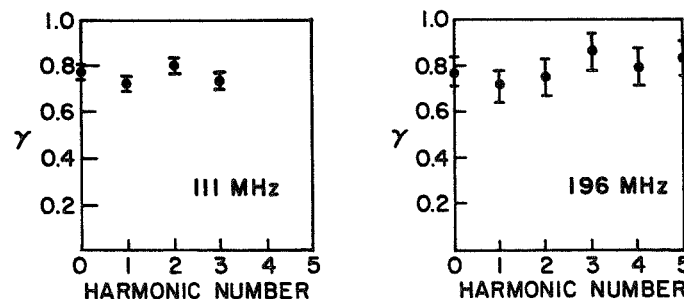


FIG. 8.—Fringe visibility versus harmonic number for (a) 111 MHz and (b) 196 MHz

with Fourier component number was made by computing the mean values for the flux density of each Fourier component using all the available data. Then the fringe visibility was calculated for each component at both 111 and 196 MHz, and the results are plotted in Figure 8. The error bars represent the standard deviation of γ as calculated from the standard deviations of the mean flux densities. The figures show that each component has approximately the same visibility as the $n = 0$ component, and within the errors there is no trend toward unity. This shows that the pulse is *not* narrower when the source is partially resolved on the long baselines.

All of the phenomena mentioned in this section are of course interrelated, and they all give useful ways of indicating the lack of evidence for a source which expands with pulse phase. This result is important for interpretations of the scattering phenomena because it implies that the temporal and angular broadening of the radiation do not occur at the same location along the line of sight. In the most likely configuration, the temporal broadening occurs in the nebula, while the angular broadening occurs all along the path to the observer. This interpretation will be discussed further in Paper IV (Vandenberg 1976).

Erickson *et al.* (1972) compared the fringe phase of the compact source with that of the pulsing source and concluded that the two sources are coincident. The present observations have much higher resolution, and many more runs are available. From 98 long-baseline observations, the average phase difference between the compact source and pulsar is 1.4 ± 3.6 corresponding to 0.8 ± 2.0 milli-arcsec or a linear separation of 0.4 ± 1 AU at an assumed distance of 2 kpc for the Crab Nebula.

iii) 74 MHz

At 74 MHz we never detected any Fourier components with the long- or short-baseline interferometers, although the single-telescope (zero-spacing) waveforms observed at Arecibo can usually be analyzed into at least one Fourier component. This discrepancy is not readily understandable. Our short-baseline sensitivity is nearly the same as that of Arecibo, but no Fourier components were detected on a few test runs. This lack of detection is not due to the flux density being below the detection limit, since on these same runs the Arecibo system recorded 15 to 25 Jy of

pulsing flux density (Rankin *et al.* 1974). With the long baselines, the interferometer partially resolved the total flux density. If the amplitudes of the Fourier components are reduced by this factor also, this puts even the $n = 1$ component well below the detection limit on the long baselines.

One possible reason for our lack of detection of pulses on the short baseline involves curvature of the pulses across our relatively wide passband. Our data processing requires that we approximate the dispersion of the pulses by a straight line. The time difference between the pulse time-of-arrival at the top and bottom of the passband was calculated using both the straight-line approximation and the true dispersion relation. At 74 MHz the difference between these times is about 3 ms, corresponding to about $\frac{1}{2}$ radian of phase difference. This results in a total signal degradation of about a factor 0.7, which is not enough to account for our lack of detection.

III. PULSARS

a) Strong Pulsars

Four strong, low-dispersion pulsars were observed during each session. Table 3 lists the average flux densities, fringe visibilities and apparent angular sizes at 111 MHz for all available runs. The total flux density is S_P (observed with the short baselines), and the partially resolved flux density is S_{PR} (observed with the long baselines). The angular sizes were obtained by assuming Gaussian brightness distributions as for the Crab Nebula pulsar. All of the pulsars have fringe visibilities on the order of, but definitely less than, unity, and therefore appear to be slightly resolved. The apparent angular sizes in Table 3 are consistent with values calculated from the theoretical predictions of Harris, Zeissig, and Lovelace (1970).

The large error bars on the fringe visibilities are due to difficulties in processing the pulsar VLBI data and in normalizing the fringe amplitudes. Since the scattering angle should be a stable quantity, the apparent variations in θ_s most likely stem from these difficulties also.

It was found that the fringe visibilities of individual strong pulses were the same as the visibility of the average flux densities. Figure 9 is a plot of the pulse-to-pulse amplitude and phase for an observation of PSR 0834+06 in 1973 February. The data were

TABLE 3
PULSAR OBSERVATIONS AT 111 MHz

| Pulsar | Date | Number of Runs | S_P (Jy) | S_{PR} (Jy) | γ | θ_s (arcsec) |
|--------------|------------------|----------------|----------------|----------------|-----------------|---------------------|
| 0834+06..... | 1971 November 24 | 3 | 7.4 ± 0.9 | 3.6 ± 1.3 | 0.49 ± 0.19 | 0.10 ± 0.05 |
| | 1973 February 24 | 6 | 36.4 ± 2.7 | 38.3 ± 2.6 | 1.05 ± 0.10 | < 0.04 |
| | 1973 February 25 | 4 | 39.0 ± 1.8 | 30.5 ± 2.1 | 0.78 ± 0.06 | 0.06 ± 0.02 |
| 0950+08..... | 1973 February 24 | 5 | 13.1 ± 2.3 | 10.5 ± 2.3 | 0.80 ± 0.06 | 0.05 ± 0.03 |
| 1133+16..... | 1973 February 24 | 2 | 15.6 | 14.7 ± 1.1 | 0.78 ± 0.17 | 0.06 ± 0.04 |
| 1919+21..... | 1971 December 19 | 3 | 37.7 ± 4.1 | 33.6 ± 6.6 | 0.89 ± 0.11 | < 0.04 |
| | 1973 February 25 | 3 | 31.2 ± 5.1 | 23.3 ± 6.0 | 0.75 ± 0.13 | 0.06 ± 0.03 |

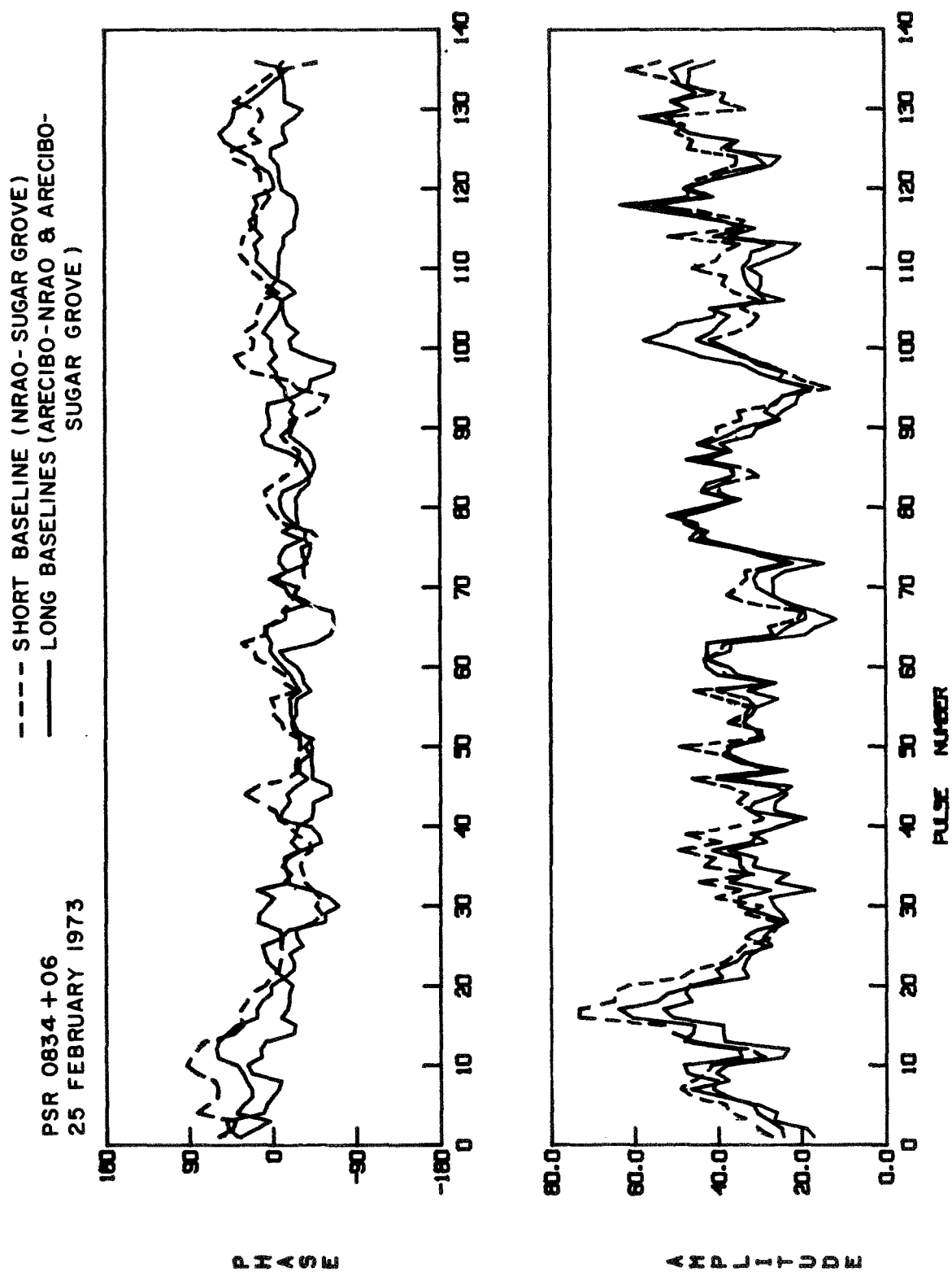


FIG. 9.—Pulse-to-pulse amplitude and phase at 111 MHz for PSR 0834 + 06 in 1973 February. The data were smoothed with a five-pulse running average. The total length of the pulse series is 3 minutes.

smoothed with a five-pulse running average. The time variations in flux density are similar on all baselines, indicating that the fringe visibility remains approximately constant on a short time scale. On time scales of several minutes (run-to-run) the flux density may vary considerably but the fringe visibility remains approximately constant. This behavior was also exhibited by the Crab Nebula pulsar (see Fig. 2).

The observed fluctuations in intensity occurred over time scales from single pulses to over one year and are probably intrinsic to the sources. Huguenin, Taylor, and Helfand (1973) note that changes of up to a factor of 10 occur on characteristic time scales which are different for each pulsar. As shown by the values in Table 3, over several months we observed large changes in flux density, but from day-to-day within an observing session the average flux density stayed approximately the same.

The possibility of apparent position variations due to interstellar scattering is discussed by Lovelace (1970). Depending on the physical parameters of the irregularities, phase excursions of at least several turns over time intervals of up to several years are predicted. Our observations of pulsars, however, show no position variations which cannot be attributed to the ionosphere. To properly investigate source motion, differential techniques should be used in which one measures the phase difference between the pulsar and another source also in the telescope beam which is not susceptible to apparent motion.

b) Weak Pulsars

Several weak, high-dispersion pulsars were also observed during the last two experiments: PSRs 1858+03, 1933+17, 1946+35, and 2003+31. These pulsars were treated as continuum sources, since they have little pulsing power at low frequencies. No correlated flux density was detected for any of these pulsars on either the long or short baselines. Without better knowledge of the spectra we cannot interpret the lack of detection on the long baselines quantitatively. The apparent angular sizes of these pulsars are probably partially unresolved, but actual total flux density measurements rather than limits are needed to calculate even a limit on the fringe visibility.

IV. SUMMARY

This paper presented apparent angular size measurements for five pulsars with the body of data heavily weighted toward the Crab Nebula pulsar. A visibility function for the Crab Nebula pulsar which is consistent

with a Gaussian brightness distribution was measured in an early 144 MHz experiment. Assuming a Gaussian distribution at all frequencies, we have also made estimates of apparent angular sizes at 196, 111, and 74 MHz. These sizes scale approximately as wavelength-squared in accordance with interstellar scattering theories.

We have also measured the flux density of the compact source in the Crab Nebula at 196, 111, and 74 MHz, and find that the measurements lie on the extrapolation from high frequencies of the pulsing flux density. Using differential fringe phase measurements we have tightened the limit on the coincidence of the pulsar and compact source to a separation of 0.2 AU at the distance of the nebula.

Reconstruction of the pulse profiles revealed shapes similar to single-dish measurements at 196 and 111 MHz. Additionally, a steady, nonpulsing component appears at the low frequency, and its strength was found to be time-variable. No pulsing power was detected at 74 MHz. The visibility of the pulsing flux density was found to be independent of pulse phase, implying that the regions in which temporal and angular scattering occur are well separated.

Pulsars other than the Crab Nebula pulsar were found to be only slightly resolved, and the fringe visibilities of individual strong pulses are the same as the visibility of the average flux densities.

Further high-resolution low-frequency observations of pulsars should be made in order to confirm and extend the results presented in this paper. More complete coverage of the (u, v) -plane at low frequencies would provide a good test of our inferences concerning the lack of fine structure in the Crab Nebula, and also of our assumption that the brightness distribution of the scattering disk is Gaussian.

We would like to thank Dr. G. W. Swenson for providing observing time and support at the University of Illinois Vermilion River Observatory, Dr. G. Stanley for observing time at Owens Valley Radio Observatory, and the Naval Research Laboratory for observing time at the Sugar Grove Observatory. The National Radio Astronomy Observatory is operated by Associated Universities, Inc., under contract with the National Science Foundation. The National Astronomy and Ionosphere Center is operated by Cornell University under contract with the National Science Foundation. Part of this work was done with support from NASA grants NGL-21-002-29 and NGL-21-002-33, and NSF grant G-19401.

REFERENCES

- Armstrong, J. W., Coles, W. A., Kaufman, J. J., and Rickett, B. J. 1973, *Ap. J. (Letters)*, 186, L141.
 Clark, T. A., Erickson, W. C., Hutton, L. K., Resch, G. M., Vandenberg, N. R., Broderick, J. J., Knowles, S. H., and Youmans, A. B. 1975, *A.J.*, 80, 923 (Paper II).
 Coles, W. A., Rickett, B. J., and Rumsey, V. H. 1974, *Solar Wind III* (Los Angeles: Inst. of Geophys. and Planetary Phys., UCLA), p. 351.
 Cronyn, W. M. 1970, Ph.D. thesis, University of Maryland.
 Erickson, W. C., Kuiper, T. B. H., Clark, T. A., Knowles, S. H., and Broderick, J. J. 1972, *Ap. J.*, 177, 101.
 Harris, D. E. 1973, *A.J.*, 78, 231.
 Harris, D. E., Zeissig, G. A., and Lovelace, R. V. E. 1970, *Astr. and Ap.*, 8, 98.
 Huguenin, G. R., Taylor, J. H., and Helfand, D. J. 1973, *Ap. J. (Letters)*, 181, L139.

- Hutton, L. K., Clark, T. A., Erickson, W. C., Resch, G. M., Vandenberg, N. R., Knowles, S. H., and Youmans, A. B. 1974, *A.J.*, **79**, 1248 (Paper I).
- Lovelace, R. V. E. 1970, Ph.D. thesis, Cornell University.
- Matveenko, L. I. 1968, *Soviet Astr.—AJ*, **12**, 552.
- Mutel, R. L., Broderick, J. J., Carr, T. D., Lynch, M., Desch, J., Warnock, W. W., and Klemperer, W. K. 1974, *Ap. J.*, **193**, 279.
- Rankin, J. M., Comella, J. M., Craft, H. D., Richards, D. W., Campbell, D. B., and Counselman, C. C. 1970, *Ap. J.*, **162**, 707.
- Rankin, J. M., Payne, R. R., and Campbell, D. B. 1974, *Ap. J. (Letters)*, **193**, L71.
- Readhead, A. C. S., and Hewish, A. 1974, *Mem. R.A.S.*, **78**, 1.
- Resch, G. M., Vandenberg, N. R., Erickson, W. C., and Clark, T. A. 1975, *Bull. AAS*, **7**, 437.
- Vandenberg, N. R. 1974, Ph.D. thesis, University of Maryland.
- . 1976, *Ap. J.*, in press (Paper IV).
- Wilson, A. S. 1972, *M.N.R.A.S.*, **157**, 229.

J. J. BRODERICK: Physics Department, Virginia Polytechnic Institute and State University, Blacksburg, VA 24061

T. A. CLARK: Radio Astronomy Branch, Goddard Space Flight Center, Greenbelt, MD 20771

W. C. ERICKSON: Astronomy Program, University of Maryland, College Park, MD 20742

G. M. RESCH: Jet Propulsion Laboratory, 4800 Oak Grove Drive, Pasadena, CA 91103

N. R. VANDENBERG: NRAO, Edgemont Road, Charlottesville, VA 22901

The log-periodic array at the Clark Lake Radio Observatory

W. C. Erickson and T. B. H. Kuiper

Clark Lake Radio Observatory, Astronomy Program, University of Maryland,
College Park, Maryland 20742

(Received April 18, 1973; revised July 20, 1973.)

A log-periodic array, three km in length, is operating at Clark Lake Radio Observatory. It makes one-dimensional sweeps of the solar brightness distribution in the frequency range 20 to 65 MHz once per sec. The phasing of the array and the receiving system are described, as well as how the dynamic spectra are analyzed for the positions of solar radio sources. Simultaneous measurements at many frequencies enable the observer to remove the effects of ionospheric refraction and to obtain fundamental positions to an accuracy of about one arc min at decametric wavelengths. Fundamental positions are given for Cassiopeia A.

INTRODUCTION

In order to obtain decametric wavelength observations, a swept frequency array [Sheridan, 1963; Begovich, 1966] has been designed, constructed, and is now in operation at the Clark Lake Radio Observatory near Borrego Springs, California. In all phases, this is a cooperative program between the Laboratory for Extraterrestrial Physics at NASA Goddard Space Flight Center and the Astronomy Program at the University of Maryland. The array was designed to be a useful solar instrument in its own right, and also to provide decametric observations of the positions of solar emission regions to complement hectometric observations made from satellites.

The observing frequency of the array is swept from 20 to 60 MHz once per sec. This causes the array's response pattern to be swept many times across the sun to determine one-dimensional brightness distributions and positions of solar emission regions. The time evolution of solar bursts may thus be studied in both angular and frequency coordinates. Data concerning the brightness distributions and positions of solar emission regions are being obtained each day between 16 and 24 hr UT. The data are being analyzed both at the University of Maryland and at Goddard Space Flight Center [Kundu *et al.*, 1970; Kuiper and Pasachoff, 1973]. At the former the analysis emphasizes the study of the radio sun at decametric wavelengths and at the latter the analysis

emphasizes the complementary aspects of decametric and hectometric emission.

THE ANTENNAS

The antennas are equatorially-mounted log-periodic elements identical to those built at Stanford University by Howard [1965] (Figure 1). The primary beamwidth of each element is 60° in both the *E* and *H* planes, and each element gives a gain of 9 db with respect to an isotropic radiator. Each element is fed at its apex and presents a 450-ohm balanced impedance with a VSWR of less than 2 to 1 over the frequency range from 20 to 65 MHz. A wide-band balun is placed at the apex to match this impedance to a 50-ohm coaxial cable and a pair of General Electric IN916 diodes are soldered across the balanced antenna terminals to protect the system from excessive signal levels.

The equatorial mounts have polar axes which can be driven electrically in increments of 4° under control from the observatory. Because of the large amount of maintenance required for the tracking system, it is not normally used with the wide beamwidth of the elements. This does not seriously detract from the normal operation. For special observations, however, tracking is accomplished by stepping in rapid succession. Declination adjustment is accomplished manually.

THE ARRAY

Sixteen antennas are spaced at equal intervals of 220 m on an east-west baseline (Figures 2, 3). Con-

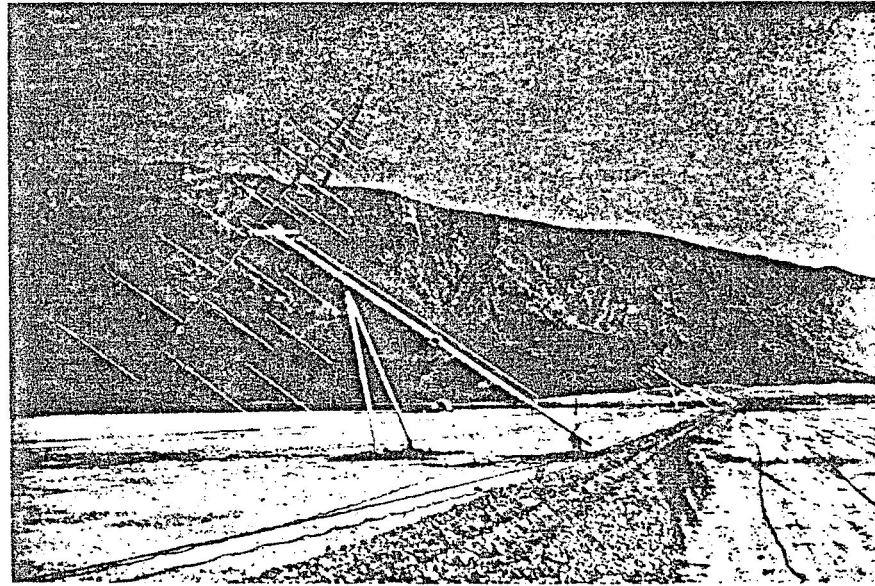


Fig. 1. A log-periodic element of the array.

sequently the voltage pattern is given by the Fraunhofer diffraction pattern of a 16-slit grating [Kraus, 1966],

$$E(\psi) = \frac{\sin(n\psi/2)}{n \sin(\psi/2)} \quad (1)$$

$$\psi = (2\pi l/\lambda) \sin \theta + \delta$$

where

- $n = 16$,
- l = average antenna separation, $220.000 \pm .003$ m,
- θ = complement of the angle between the interferometer axis and the radius vector in the direction of radiation (the "interferometer angle"),

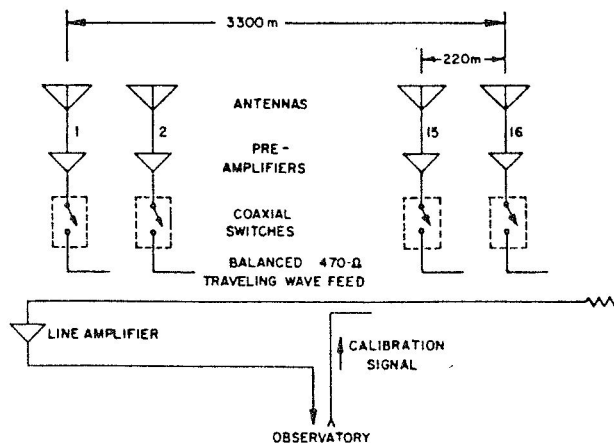


Fig. 2. Schematic of the log-periodic array and its feed system.

$\lambda = c/f$, f = frequency at which the antenna is being operated,

δ = progressive phase difference between antennas.

The pattern has nulls when the numerator of equation 1 is zero, that is, when $16\psi = 2\pi k$, except when k is a multiple of sixteen. In that case, the denominator is also zero, and $E(\psi)$ achieves a maximum value of unity.

In a conventional grating array the observing fre-

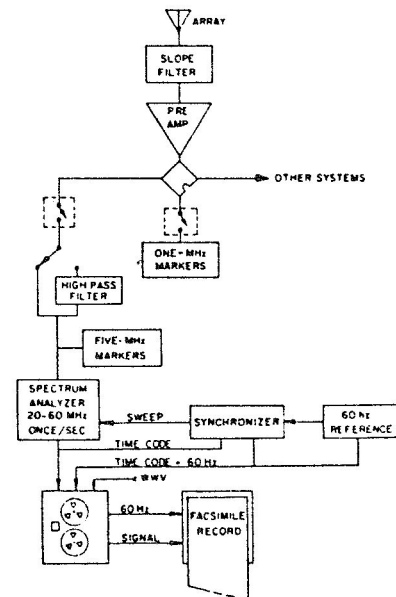


Fig. 3. Schematic of the electronics.

quency, f , is fixed. Equation 1 then gives the voltage pattern as a function of the angular coordinate, θ . If we decrease the observing frequency (increase the wavelength), the diffraction pattern will broaden; the fringes will move away from the white-light fringe and become correspondingly fatter. Thus, by smoothly altering the observing frequency, we can sweep a fringe (or several adjacent fringes) across a source which we want to observe.

There is another way to look at the operation of this array. Equation 1 achieves a maximum whenever

$$(l/\lambda) \sin \theta + (\delta/2\pi) = k \quad k = \text{integer} \quad (2)$$

In conventional arrays, λ is kept fixed. The earth's rotation moves the antenna pattern across the celestial sphere and the telescope shows a maximum response whenever the interferometer angle of the source, θ , is such that equation 2 is satisfied. This scanning process is far too slow for the highly transient solar events, so for rapid scanning we alter λ . By noting the wavelengths at which the response of the array is maximized, we can deduce the position, θ , of the source.

From (2) it is easily shown that the beamspacing and beamwidth are given by

$$\Delta\theta = \lambda/l \cos \theta \quad (3)$$

and

$$\delta\theta = \lambda/16l \cos \theta \quad (4)$$

respectively. Near transit, $\theta \simeq 0^\circ$, so that at 20 MHz $\Delta\theta \simeq 4^\circ$ and $\delta\theta \simeq 15$ arc min; at 60 MHz, $\Delta\theta \simeq 1.3^\circ$ and $\delta\theta \simeq 5$ arc min. The spacing of the fringes is such that the position of a solar radio burst can be unambiguously identified.

ARRAY FEED SYSTEM

The array is fed from the western end of an east-west, open-wire, traveling-wave transmission line 3.3 km in length (Figure 2). The line is built of two strands of 1/4-in. diameter copperweld wire at 6-in. spacing, giving a characteristic impedance of 470 ohm. These wires are placed under approximately 1,000 lb tension and are fixed mechanically to the earth at each end, thus minimizing the thermal variation of the length of the line since variations in temperature cause only a change in tension, not physical length. They are supported by 1/4-in. phenolic hangers at random intervals of about 35 m. After preamplification, the signals are lightly coupled

to this transmission line by means of directional couplers [Oliver, 1954]. The attachment points for the couplers were determined through SWR measurements with the east end of the feed line short-circuited. Two measurements, made independently several months apart, agreed within 6 cm at each coupling point. The velocity factor of the line is 0.99932 ± 0.00003 with respect to free space. The spacing of the coupling points, l_{line} , was found to be 0.9999415 ± 0.000003 of the antenna separation, l . Consequently the increment of phase introduced between antennas by the transmission line is

$$\delta = 2\pi l_{line}/\lambda_{line} \quad \begin{aligned} l_{line} &= (0.9999415 \pm 0.000003)l \\ \lambda_{line} &= (0.99932 \pm 0.00003)\lambda \end{aligned}$$

and thus equation 2 takes the form

$$\sin \theta + (1.00062 \pm 0.00003) = k\lambda/l \quad k = \text{integer} \quad (5)$$

The effect of the velocity factor of the transmission line is to shift the antenna pattern eastward by $(2.14' \pm 0.1') \cos \theta$ with respect to the pattern expected for a velocity factor of unity and a coupler spacing of exactly 220 m.

In order to find the frequency difference between fringes centered on the same angle, θ , we differentiate (5) and find that for $\Delta k = 1$

$$\Delta f = c/l(\sin \theta + 1.00062) \quad (6)$$

The ratio $c/l = 1.362695$.

One property of the transmission line which is not understood is that the attenuation of the line is proportional to frequency, rather than $f^{1/2}$, in spite of the fact that dielectric losses are negligible [King *et al.*, 1965]. The degree of coupling at each antenna was adjusted so that each antenna delivers approximately equal power at the line amplifier (Figure 2) in spite of the attenuation on the line. This cannot be achieved exactly for all frequencies so the coupling was designed to achieve uniform illumination at 35 MHz. The illumination deviates from uniform by less than 25% at 20 or 60 MHz.

A serious problem in decametric observations at our site are very strong shortwave broadcast signals in the 19, 25, and 31 m bands. Intermodulation of these signals in the preamplifiers must be avoided. Accordingly, the preamplifiers were chosen for their high linearity, and they incorporate filters to attenuate signals outside the frequency range of 20 to 60 MHz. They have a measured noise temperature of 950 K. After preamplification, coupling losses, and line losses, each antenna delivers 450 to 500 K of

noise power at the west end of the transmission line. Thus, a total noise power at 7000 to 8000 K from all sixteen antennas is delivered to the amplifier at the end of the line. This amplifier also has a noise temperature of 950 K and thus contributes 13 to 14% to the total noise. The gain in this amplifier exceeds subsequent losses in the transmission to the observatory by 8 to 13 db, depending on the frequency. The signal level at this point is so high that no further degradation of the noise figure occurs.

We should note that any deviation from uniform aperture illumination does not affect the pointing of the antenna, but only the resolution and side-lobe level. If the phases have been accurately adjusted, then the aperture illumination of the array is purely real, except for the linear phase gradient which affects only the pointing of the beam. The voltage pattern, the Fourier transform of the aperture illumination, is therefore Hermitian and the power pattern is consequently symmetrical [Bracewell, 1965]. Any variation in the illumination, which might be caused by gain variations in the preamplifiers or changes in the coupling coefficients, will affect the beam in a symmetrical way and have no serious influence on determinations of source positions.

ELECTRONICS SYSTEM

Figure 3 is a schematic diagram of the receiving system. The galactic background temperature varies approximately as $f^{-2.5}$ across our operating band. In addition, transmission line attenuation increases with frequency. These effects result in a decrease of nearly 20 db in output noise level from 20 to 60 MHz. This is undesirable because it greatly reduces the dynamic range of solar signals which can be accommodated by the detectors and recording apparatus. Therefore, a slope filter is introduced which attenuates the low frequency portion of the band and results in an approximately uniform noise level. It also weakens the strong signals below 20 MHz which tend to cause intermodulation. The slope filter overcompensates slightly for the fact that the collecting area of the constant gain log-periodic elements varies as f^2 . Thus a source of constant flux will result in an output deflection which is slightly larger at 60 MHz than at 20 MHz.

One-MHz frequency calibration markers are injected into the system for a brief period every six min. The antenna is disconnected during the retrace of the sweep receiver in order to separate the sweeps clearly. This facilitates digital processing of the data.

In addition to the part of the system shown, a variety of other systems is available. For a two-year period ending September 1971, four additional spectrum analyzers swept each 10-MHz segment of the 20 to 60 MHz range four times per sec. These analyzers are now devoted to new arrays.

Signal path lengths through various elements of the array differ by as much as 6600 m and these differences depend upon the position of the source. The coherence bandwidth of the array is therefore narrow and dependent upon source position. In order to insure coherence at all positions, a receiver bandwidth of 10 kHz is employed. This does result in somewhat less than optimum sensitivity, but the narrow bandwidth has the advantage of discriminating against terrestrial interference. The effective integration time can be computed from the frequency sweep rate.

For the purpose of determining the total solar flux without the angular resolution of the array, one additional receiver records the signal received by a single element.

RECORDING AND DISPLAY OF SIGNAL

The output from the receiver is amplified, and the baseline adjusted as required. The signal is then recorded on an FM analog tape recorder which has a bandwidth of approximately 1-1/2 kHz at 1-7/8 in. sec⁻¹ recording speed. The Fourier transform of such a frequency response is a function in the time domain having a width of approximately 0.4 msec. Since the receiver is sweeping at a rate of about 50 MHz sec⁻¹, this corresponds to an RF bandwidth of 20 kHz. Only late in the afternoon when the coherence bandwidth is very narrow in frequency will there be a broadening of the fringes due to the bandwidth limitation of the tape recorder.

One channel of the tape records a 60-Hz reference signal from the observatory's frequency standard. It also contains timing information. This channel is used to synchronize a facsimile recorder (see Figure 3).

The facsimile recorder is a fathometer recorder adapted to this purpose because of its high resolution and wide dynamic range. The recording paper is 19 in. wide and the effective resolution is ≤ 0.001 in. Its dynamic range is about 12 db. The dynamic range of the receivers and the tape recorder is about 30 db. This dynamic range can only be utilized by digital processing of the tape-recorded data or by redisplaying the data on the facsimile recorder at

different levels. Figure 4 shows a solar radio event seen on the facsimile records. The pen of the recorder is drawn across the paper at the rate of once per sweep. The pen is driven by the recorded 60-Hz reference signal and synchronized to time marks on the data channel (see Figure 3). The signal modulates the intensity of the pen trace so that the intensity as a function of frequency is displayed by each trace. The paper moves continuously so that the time evolution of the spectrum is recorded.

CALIBRATION

Proper calibration of the array would require that coherent signals of known strength be injected at each of the elements. This would require an independent feed system. Instead, great care was taken to insure the gain and phase stability of the feed system and the electronics from the line amplifier onward are calibrated daily. An underground coaxial cable from the observatory couples signals to the center of the transmission line (Figure 2). Noise calibration signals are inserted on the transmission line at the beginning of each observing day, resulting in a series of gray shades on the facsimile record. These can be compared to the density of the fringes to provide a flux calibration to within 3 db for bursts on the linear portion of the facsimile record's density scale.

In order to establish the flux scale, the calibration noise source was compared to Cassiopeia A at three discrete frequencies using fixed frequency receivers. The fringes and calibrations were recorded on a chart recorder and compared. It was found that the calibration noise source provided a signal equivalent to about $3 \pm 1 \times 10^{-20} \text{ Wbm}^{-2} \text{ Hz}^{-1}$. The flux densities of Cassiopeia A were taken from a spectrum compiled by Parker [1968] and corrected for secular variation. By calibrating the calibration noise source in terms of antenna temperature, the collecting area is found. The collecting area as a function of frequency is given in Table 1. Pattern measurements of a single log-periodic element yielded an estimated collecting area of about one square wavelength.

It appears that the array performs as expected at the higher frequencies where the sixteen elements give a combined collecting area of about sixteen square wavelengths, but that the collecting area falls below the predicted area at lower frequencies. As the wavelength increases, the radiating region moves down the log-periodic antenna structure. The decrease in collecting area at longer wavelengths may

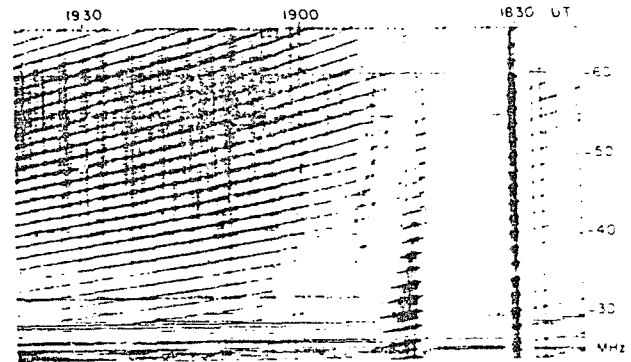


Fig. 4. A typical facsimile record.

be caused by a partially reflected wave from the ends of the antenna booms, or by radiation from the booms themselves.

DATA REDUCTION

In Figure 4 we show a record of solar activity in which the spectrum is modulated by a periodic pattern $E^2(\psi)$ of the grating array (see equation 1). Thus by measuring f at the maxima of the pattern, the position of the source, θ , can be known. Any uncertainty in the fringe order can usually be resolved. It is our concern, at this point, to see how f and t may be accurately determined.

Actual measurement of the facsimile record is done on an x, y coordinate digital converter. This has a table top surface on which a pointer can move along two orthogonal axes, x and y . The facsimile record is aligned as accurately as possible on this surface. The axis parallel to the flow of time is the x axis and the axis parallel to the frequency scale the y axis. We are concerned, then, with converting the coordinate (x, y) to the coordinate (t, f) . If t is linear with x and f is linear with y , the calibration is easy and the conversion trivial.

It has been our experience that t is a very linear function of x . We find that we are generally able to calibrate the time scale on our charts to one sec (or 0.007 in.). There is a variety of effects which complicates the calibration of the frequency scale. The

TABLE 1. The collecting area as a function of frequency.

| Frequency (MHz) | Collecting area (m ²) | (λ ²) |
|--------------------|--------------------------------------|-------------------|
| 31 | 890 ± 80 | 9.5 ± 0.9 |
| 38 | 880 ± 440 | 14 ± 7 |
| 48 | 610 ± 110 | 15.5 ± 3 |

receiver is tuned over the frequency range, 20 to 60 MHz, in response to a sawtooth sweep voltage (see Figure 3). Although this sweep is highly linear, our criteria are extremely severe and the response of the receiver to the sweep voltage is not perfectly linear. Another effect which is important is phase jitter in the synchronization between the pen drive and the reference signal, which causes tiny displacements of the frequency scale. We must be able to establish the frequency of a fringe to about 15 kHz, which amounts to an accuracy of 0.005 in.

To the first order, the frequency of a point on the facsimile record is given by $f = a_1 + a_2 y$. The center frequency to which the receiver is tuned affects a_1 . The sweep range of the receiver affects both a_1 and a_2 . Drifts in the local oscillators, lateral motion of the paper during recording, and changes in the sawtooth voltage will result in changes in a_1 and a_2 . Consequently, in calibrating the frequency scale of the facsimile records, allowance must be made for variations of a_1 and a_2 with time.

The frequency versus voltage response of the sweep circuit of the receiver is slightly nonlinear, so that

$$f = a_1 + a_2 y + \text{voltage-dependent correction term}$$

Since the frequency of the receiver has a one-to-one correspondence with the voltage applied to the sweep circuit, the correction term can also be expressed as a function of frequency. We have found that the calibration function can best be written as

$$f = a_1 + a_2 y + a_3 \cos [(f - a_4)/a_5] + a_6 \cos [(f - a_7)/a_8] + a_9 \cos [(f - a_{10})/a_{11}] \quad (7)$$

The coefficients a_3 to a_{11} are characteristic of the receiver and thus do not vary during the day. Since the correction terms are small, we can approximate the calibration function by

$$f \simeq a_1 + a_2 y + a_3 \cos [(a_1 + a_2 y - a_4)/a_5] + a_6 \cos [(a_1 + a_2 y - a_7)/a_8] + a_9 \cos [(a_1 + a_2 y - a_{10})/a_{11}] \quad (8)$$

The coefficients a_3 to a_{11} are determined once for the day under reduction. Coefficients a_1 and a_2 are determined periodically and interpolated as required.

Having established the frequency of a series of fringes at some instant of time we can deduce the position angle θ . The antenna pattern (see equation 6) has many lobes and so the position, θ , of radiation

observed at some frequency, f , will always be ambiguous in the order of the lobe, n . There are, however, two possibilities for removing this ambiguity.

Since we are concerned mostly with radiation from sources whose position is known with sufficient accuracy (i.e., in the immediate vicinity of the sun), we can use this information to find the fringe order, k . We compute, for a measurement of frequency f ,

$$k^* = (\sin \theta + 1.00062)/1.362695 \quad (9)$$

where k^* is, in general, nonintegral. The fringe order is almost always the integer nearest to the value k^* . This is the approach we normally use. It is not possible to confuse radiation from the sun (or the source being observed) with radiation from a source elsewhere in the sky. Radiation associated with a given source will always have approximately the same value of θ , regardless of frequency. The fringe spacing in frequency (equation 6) can therefore be used to evaluate θ approximately as a check that the radiation is coming from the solar vicinity.

If we wish to localize the position of unknown radiation, we can use equation 6 to find the approximate value of θ . We would then use the procedure outlined in the above paragraph to find the fringe orders.

We compute $\theta - \theta_s$ in solar radii for each fringe, θ_s being the position of the center of the sun,

$$\sin \theta_s = \cos \delta_s \sin H A_s$$

The position angle of the fringes with respect to celestial north is also noted,

$$\cos (90^\circ - \phi_s) = \tan \theta_s \tan \delta_s$$

In order to improve the accuracy of position measurements, we generally measure three points on each fringe: the high frequency edge, the center, and the low frequency edge. The edges are defined as the points where the intensity gradient is steepest, and for fringes which are not so intense as to saturate the record, they might be expected to correspond to the half-power points. All three measured points are converted to positions (in solar radii) and plotted (see Figure 5). The center measurement is plotted as a one-digit number representing the nearest sec in time. The upper and lower edges are plotted as the symbol Δ . The position of the source is then taken to be the mean of these three positions. Analysis of all the fringes at one time thus results in measurements of position as a function of frequency.

It should be noted that this method of finding the

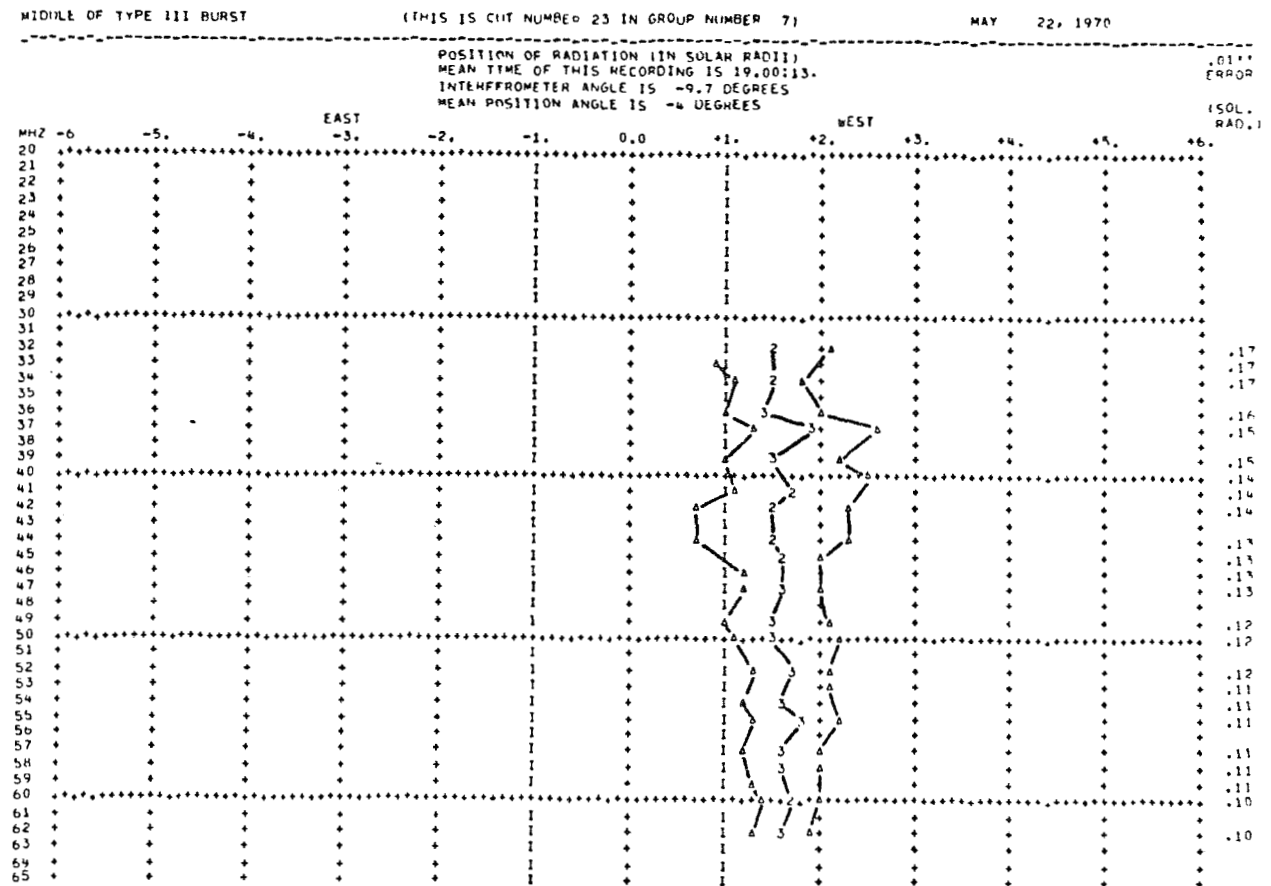


Fig. 5. Position of a type III burst as a function of frequency. Triangles give the positions corresponding to the high and low frequency edges of the fringes. The numbers give the positions corresponding to the peaks or centers of the fringes, the number representing the time to the nearest sec. On the right-hand side of the plot is given the uncertainty in position (in solar radii) if the measurement error on the xy coordinate converter is .01 in.

position of a source generally assumes that both the antenna beam and the source are symmetrical. Consider a fringe which is saturated on the record. (Because of the limited dynamic range of the facsimile record, this is often the case.) The sides of the fringes are taken to be those frequencies at which the density of the record appears to fall off most sharply. These frequencies will not represent, then, the half-power points but some lower, often significantly lower, power level. The person scanning the fringe will take the peak to be some frequency which is an average of the two side frequencies. When these frequencies are converted to positions and averaged together to yield the position of the fringe, we end up with a position which is defined by some power level near the base of the fringe. If the source or the beam is significantly asymmetrical the

position defined by the peak-power or half-power points may be quite different.

RESULTS

A full-scale analysis of solar type III and IV events is under way, the results of which will be reported in later papers [e.g., *Kuiper*, 1973].

As a check on both the array and the data reduction program, observations were made of Cassiopeia A for about two hours around transit on November 10 and 11, 1970, and on March 16, 1972. The position lines of the source were measured at 45 MHz relative to an assumed right ascension of 23h 21m 10s and declination of $+58^{\circ}32'30''$ (epoch 1950.0). Because of the rotation of the earth, the position angle of the antenna fringes projected on the source varied from about -20° to $+30^{\circ}$. The

best intersection of the position lines was found to be

November 10 and 11, 1970:

$$23^{\text{h}} 20^{\text{m}} 58.7^{\text{s}} \pm 1.9^{\text{s}} \quad +58^{\circ}37.0' \pm 0.8'$$

March 16, 1972:

$$23^{\text{h}} 20^{\text{m}} 41.4^{\text{s}} \pm 1.9^{\text{s}} \quad +58^{\circ}24.3' \pm 0.8'$$

The effect of stellar aberration has been taken into account, but no correction for ionospheric refraction was made. Refractive effects cause most of the discrepancy between these positions.

The position of Cassiopeia A was measured simultaneously at frequencies from 25 to 50 MHz. Assuming that the centroid of the source's intensity distribution at these frequencies is the same, we can correct for ionospheric refraction by fitting each set of measurements at a given time to the function

$$\rho = A + Bf^{-2}$$

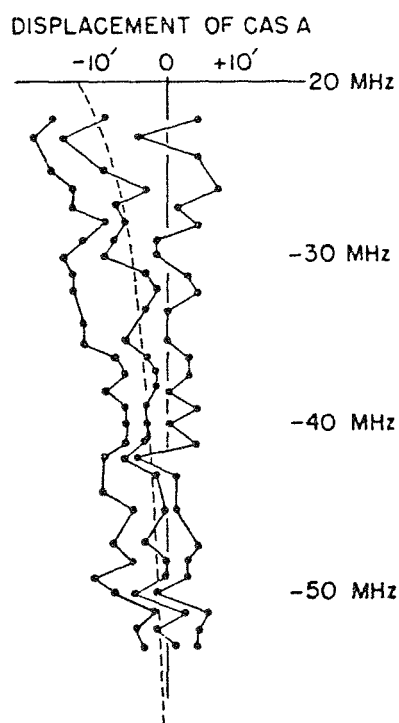


Fig. 6. Observed position as a function of frequency of Cassiopeia A. Measurements of the high frequency edge, middle, and low frequency edge (dots) are connected respectively with solid lines. The dashed line represents the function $\rho = (1.0' \pm 0.9') + (5.83' \pm 1.2') \times 10^3 \times f^{-2}$ where frequency is given in MHz. The refraction is thus determined to be $6.5'$ at 30 MHz.

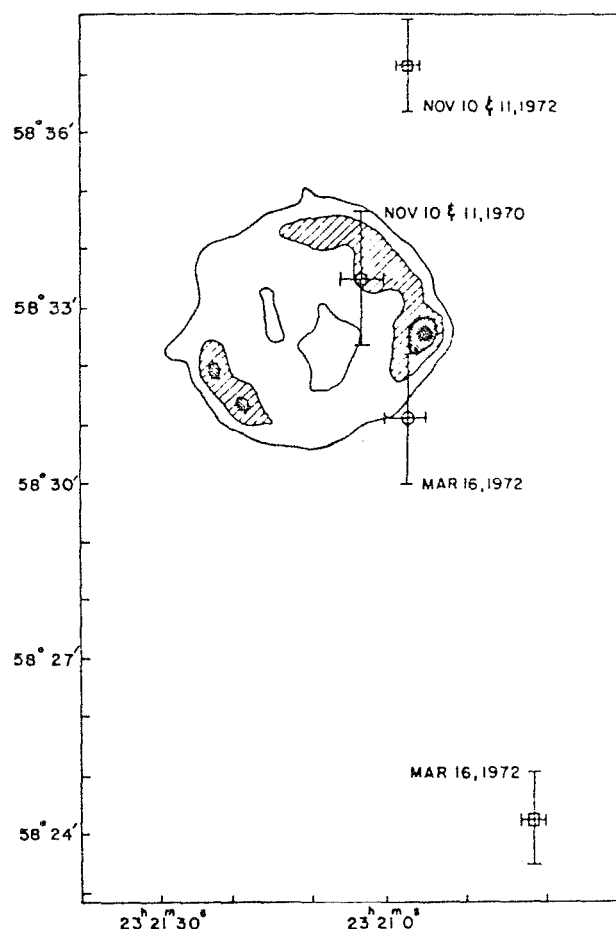


Fig. 7. The positions of Cassiopeia A at decametric wavelengths, uncorrected for refraction (\square), and corrected for refraction (\circ), superimposed on a 1.4 GHz contour map based on the results of Ryle *et al.* [1965]. The contour interval is 15,000 K. Unless all parts of Cassiopeia A have identical spectra, the centroids of the brightness distributions need not necessarily coincide at centimeter and decameter wavelengths.

where A represents the position of the centroid in the absence of ionospheric refraction (Figure 6). We found that the uncertainty in determining A for any given set of measurements was comparable to the scatter in position at 45 MHz. Consequently, for the measurements at any given time, the position represented by the parameter A is not any more reliable than the measured position at 45 MHz. However, when we solve for the best intersection of all the position lines which have been corrected for refraction, we find that the data are much more consistent:

November 10 and 11, 1972:

$$23^{\text{h}} 21^{\text{m}} 3.7^{\text{s}} \pm 2.5^{\text{s}} \quad +58^{\circ}33.5' \pm 1.1'$$

March 16, 1972:

23h 20m 57.5s \pm 2.5s +58°31.1' \pm 1.1'

These positions, as well as the positions obtained when the effect of refraction is neglected, are plotted in Figure 7 on a contour map of Cassiopeia A based on the Cambridge observations at 1.4 GHz [Ryle *et al.*, 1965]. These results demonstrate the potential of simultaneous multifrequency observations to obtain accurate fundamental positions at decametric wavelengths. Our two position measurements agree to 0.8 arc min in right ascension, the direction in which the array has high angular resolution. Better agreement could not be expected because 0.8 arc min is approximately one-tenth of a beamwidth.

CONCLUSION

We have described an instrument which has been on solar patrol since March 1969. Dynamic spectra are recorded daily from 1600 to 2400 UT. From the fringe pattern on the dynamic spectra one can obtain the position of radio sources as a function of frequency in the range 20 to 65 MHz. The pointing of the array is known to an accuracy of 0.1 arc min. Positions can usually be measured to an accuracy of about 1 arc min.

It has been suggested that ionospheric refraction can be measured by simultaneous observations at two or more frequencies [Lawrence *et al.*, 1964], but that refractive effects might not behave in the expected way below 50 MHz. We have made observations of Cassiopeia A in the range 25 to 55 MHz and find that the inverse square dependence on frequency is followed in this frequency range. We have used this dependence to correct the observations and have found that we are able to determine the position of Cassiopeia A to within 1.0 arc min in right ascension. More sensitive arrays, such as the one now being built at Clark Lake, will be able to use this principle to obtain accurate fundamental positions of radio sources in the decametric wavelength range.

Acknowledgments. We wish to acknowledge the work of J. Fainberg and J. Hubbard who played major roles in the design and construction of this instrument. R. Stone has enthusiastically supported the work at Goddard Space

Flight Center. Most of the daily operation is conducted by P. Dooley. We are especially grateful to T. Gergely for many helpful discussions and constant feedback on the behavior and misbehavior of the data reduction programs, and to N. Roth, who cheerfully repeated again and again the measurements of the Cas A calibration data, as the reduction procedure was being developed. Clark Lake Radio Observatory is supported by the National Science Foundation under grant NSF GP 19411, and the National Aeronautics and Space Administration under grant NGR 21-002-367.

REFERENCES

- Begovich, N. A. (1966), Frequency scanning, in *Microwave Scanning Antennas*, vol. 3, edited by R. C. Hansen, pp. 35-215, Academic, New York.
- Bracewell, R. (1965), *The Fourier Transform and its Applications*, p. 15, McGraw-Hill, New York.
- Howard, H. T. (1965), An antenna array for radar astronomy studies in the 20 to 55 Mc range, *IEEE Trans. Antennas Propagat.*, AP-13, 365.
- King, R. W. P., H. R. Mimno, and A. H. Wing (1965), *Transmission Lines, Antennas, and Wave Guides*, p. 14, Dover, New York.
- Kraus, J. D. (1966), *Radio Astronomy*, pp. 162-165, McGraw-Hill, New York.
- Kuiper, T. B. H. (1973), On the density of the corona in regions of type III activity, in *High Energy Phenomena on the Sun*, Symposium Proceedings, edited by R. Ramaty and R. G. Stone, *NASA X-693-73-193*, pp. 540-551, Washington, D. C.
- Kuiper, T. B. H., and J. Pasachoff (1973), Detailed correlation of type III radio bursts with $H\alpha$ activity, 1, Active region of 22 May 1970, *Solar Phys.*, 28, 187-196.
- Kundu, M. R., W. C. Erickson, P. D. Jackson, and J. Fainberg (1970), Positions and motions of solar bursts at decameter wavelengths, *Solar Phys.*, 14, 394-403.
- Lawrence, R. S., C. G. Little, and H. J. A. Chivers (1964), A survey of ionospheric effects upon earth-space radio propagation, *Proc. IEEE*, 52, 4-27.
- Oliver, B. M. (1954), Directional electromagnetic couples, *Proc. IRE*, 42, 1686-1692.
- Parker, E. A. (1968), Precise measurements of the flux densities of the radio sources Cas A and Cyg A at metre wavelengths, *Mon. Notic. Roy. Astron. Soc.*, 138, 407-422.
- Ryle, M., B. Elsmore, and A. C. Neville (1965), High-resolution observations of the radio sources in Cygnus and Cassiopeia, *Nature*, 205, 1259-1262.
- Sheridan, K. V. (1963), Techniques for the investigation of solar radio bursts at metre wavelengths, *Proc. IRE Aust.*, 24, 174.

Reprinted from PROCEEDINGS OF THE IEEE
VOL. 61, NO. 9, SEPTEMBER, 1973
pp. 1276-1277

COPYRIGHT © 1973—THE INSTITUTE OF ELECTRICAL AND ELECTRONICS ENGINEERS, INC.
PRINTED IN THE U.S.A.

The Clark Lake Array

WILLIAM C. ERICKSON

Abstract—A powerful new instrument for meter and dekameter wavelength radio astronomy is described. It will soon be available for both solar and sidereal studies.

A FULLY STEERABLE array of 720 conical log spiral antennas is near completion at the University of Maryland's Clark Lake Radio Observatory in southern California. It is capable of operation at any frequency between 15 and 130 MHz with an instantaneous bandwidth of 3 MHz. The array is a pencil-beam instrument with a beamwidth proportional to the wavelength; it varies from 3' to 27' across the frequency range. Both the beam position and operating frequency will be computer controlled on a time scale of much less than 1 ms. The array will be used for solar studies and discrete radio source studies. For the radioheliograph application, 49 simultaneous beams will be formed.

The array is described in more detail elsewhere [1], [2]. The antennas are arranged in a T with an east-west arm of 480 elements, 3000 m in length, and a north-south arm of 240 elements, 1800 m in length. The elements are fixed in a vertical direction with a primary frequency-independent beamwidth of 100°. This limits the sky coverage of the instrument to

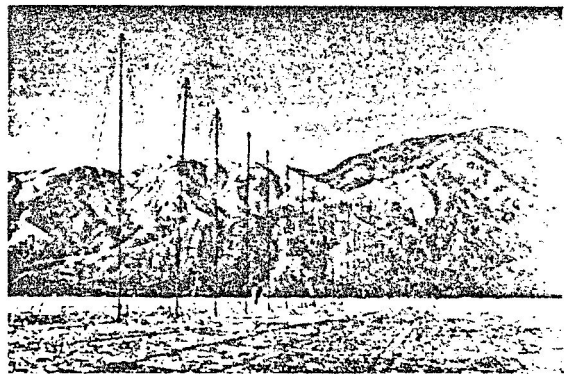


Fig. 1. This is a photograph of the east-west arm of the instrument. It consists of 480 log spiral elements.

zenith distances of approximately 50°. Each element is a teepee-shaped structure of 8 wires and is 7.8 m tall. (For this reason the array has been called the TPT.) Fig. 1 is a photo of the east-west arm of the instrument. This arm is now complete and in operation.

Beam positioning is accomplished entirely by adjustment of the relative phases between the elements. No physical motion is involved. The primary phasing scheme employs electrical rotation of the left circularly polarized elements. Since a properly designed log spiral antenna maintains circular polarization well off axis, this scheme can be used at zenith distances of 50° or greater. The excitation of each multifilar spiral antenna is rotated by means of a diode switch installed

Manuscript received February 2, 1973. This work was supported by the National Science Foundation under Grant GP 19401 and by the National Aeronautics and Space Administration under Grant NGR 21-002-367.

The author is with the Astronomy Program at the University of Maryland, College Park, Md. 20742.

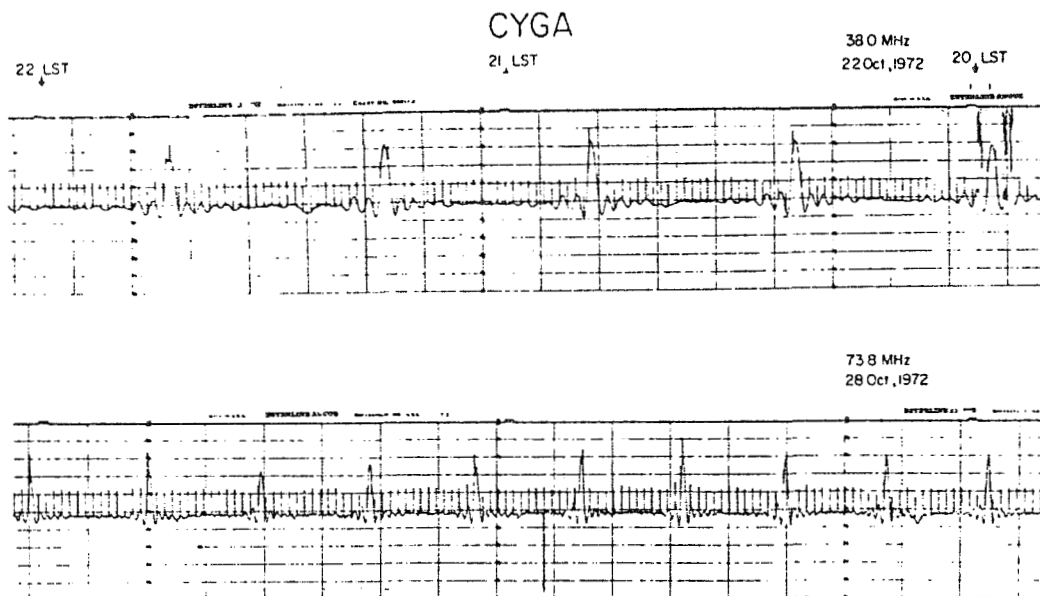


Fig. 2. Drift scans of Cyg A at two frequencies. To make these recordings, a 32-element grating array consisting of each fifteenth element was used. This grating array was correlated with an element at the center of the array to form a $\sin 32x/32 \sin x$ pattern for testing purposes. The spikes which occur on the record each minute are noise calibrations.

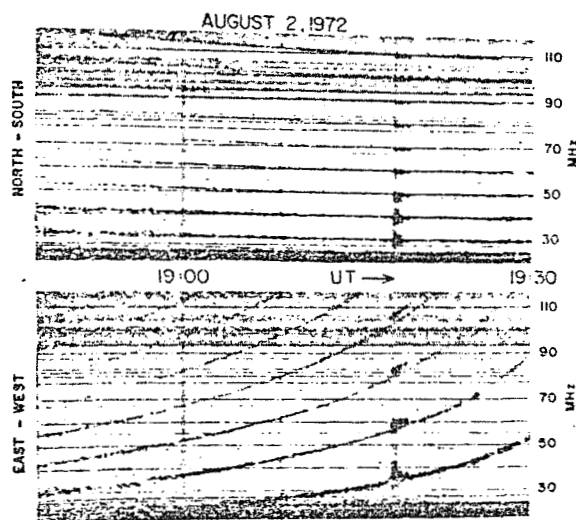


Fig. 3. Radio spectrograms of solar continuum obtained shortly before the great flares of August 1972. These recordings were taken with swept frequency receivers attached to the output of north-south and east-west grating arrays consisting of each fifteenth element. The receivers sweep the 20-120-MHz spectrum twice per second; as they sweep, lobes of the grating array's response cross the sun. Determination of time and frequency gives the position of the source. The rather steady sloping bands of continuum originate $9'$ east and $3'$ south of the sun's center. The Type III bursts at 1918-1920 UT are $10'$ west and $20'$ south of the sun's center. A second continuum region develops in the 80-120-MHz range between 1918 and 1927 UT. Interference below 30 MHz and FM transmissions in the 88-108-MHz band are plainly visible.

at its apex. The arms of the T are operated in banks which consist of 15 elements each. Each bank of elements is phased identically by means of 60 control wires which run down the length of the arms. The signal from each bank of elements is preamplified and brought back to the observatory on a sepa-

rate coaxial feed line. At the observatory the signals from the banks are delayed and combined to form the pencil beams.

Fig. 2 illustrates some sample drift scans obtained with the east-west arm of the instrument. Since the east-west arm can track a source across the sky, it is being used in a supersynthesis mode to synthesize a pencil-beam response on high declination sources. Fig. 3 illustrates sample fan beam scans of the sun obtained with completed portions of the east-west and north-south arrays.

When completed, the instrument will be used during the day as a multifrequency radioheliograph and at night for radio source studies. "Pictures" of the sun will be obtained at several discrete frequencies every second. Swept frequency fan beam records in the east-west and north-south directions will be simultaneously obtained at intermediate frequencies. These will allow interpolation between the frequencies at which solar "pictures" are obtained.

The sensitivity limit and the resolution limit of the instrument are approximately equal at about 1 flux unit at all frequencies [2]. The instrument can be employed for radio source survey work, detailed studies of radio source spectra, and various other spectral studies. It can also be applied to pulsars, planets, or other dynamic sources. Because of its rapid beam positioning it can be used in a time-share mode between various observers or between calibrators and unknown sources on a 1-s time scale. Obviously, the data-acquisition capability of the instrument far exceeds the analysis capability of our small group. We will invite guest investigators to make use of the instrument.

REFERENCES

- [1] W. C. Erickson and J. R. Fisher, "A new wideband, fully steerable, dekametric array at Clark Lake," submitted to *Radio Sci.*, 1973.
- [2] J. R. Fisher, "Design tests of the fully steerable, wideband, dekametric array at Clark Lake," Ph.D. dissertation, Univ. of Maryland, College Park, Md., 1972.

A new wideband, fully steerable, decametric array at Clark Lake

William C. Erickson and J. Richard Fisher¹

*Astronomy Program,
University of Maryland, College Park, Maryland 20742*

(Received August 20, 1973.)

A new, fully steerable, decametric array for radio astronomy is under construction at the Clark Lake Radio Observatory near Borrego Springs, California. This array will be a "T" of 720 conical spiral antennas (teepee-shaped antennas, hence the array is called the TPT), 3.0 by 1.8 km capable of operating between 15 and 125 MHz. Both its operating frequency and beam position will be adjustable in less than one msec, and the TPT will provide a 49-element picture around the central beam position for extended-source observations.

Considerable experience has been gained in the operation of completed portions of the array, and successful operation of the final array is assured. This paper describes the results of the tests which have been conducted with the conical spirals and outlines the planned electronics.

INTRODUCTION

Most of the radio astronomical observations below 100 MHz have been the result of considerable effort on the part of a relatively small number of astronomers and engineers. The size of the instruments required has precluded the construction of more than a few in the world, and, until three or four years ago, technology had not allowed the design of a large decametric array which would operate over more than a limited frequency range and be steerable in two coordinates with reasonable speed. Consequently, this part of the radio spectrum has attracted very few astronomers even though much information about the physics of celestial objects may be found from the study of radiation at these wavelengths.

Recent advances have been made in the technology of decade bandwidth antennas [Runsey, 1966], and reliable, wideband, solid state devices have reached a price where it is practical to use hundreds or thousands of units in a large system. Around these developments, a design for a fully steerable decametric array has evolved. It is operable anywhere between 15 and 125 MHz with

nearly instantaneous frequency and beam positioning capability.

The instrument has been designed with both solar and sidereal programs in mind. The spacing of the phase centers of the banks of elements has been arranged to provide a "field of view" clear of grating responses several solar diameters across. One of the first uses of the instrument will be as a multi-frequency radioheliograph, similar to the Culgoora instrument. The system has most of the flexibility of a huge paraboloidal antenna, and has a number of advantages and disadvantages. First of all, its resolving power is approximately that of a 3-km paraboloid. The ability to slew rapidly and to change frequency rapidly permits many modes of operation that are impossible with paraboloids. On the other hand, the collecting area of the unfilled aperture is less than 1% of that of a 3 km paraboloid, so the system is most useful for programs where high angular resolution and only modest sensitivity are required.

The system is adaptable to the study of dynamic sources such as the sun, Jupiter, or pulsars, for it can be used in an adaptive sense with priority given to dynamic sources whenever they are active. The beam can be stepped around the sky to monitor the sun, flare stars, planets, or ionospheric scintillations. Spectral observations can be made on many thousands of sidereal radio sources. Sources can be fol-

¹ Present address: National Radio Astronomy Observatory, Green Bank, West Virginia 24944.

lowed across the sky and observed successively at different frequencies for spectral measurements. Observations of calibration sources can be interspersed with observations of unknown sources on a second-to-second basis. At our sensitivity level, lunar occultations of radio sources will occur every few hours.

The instrument, called the TPT because of its geometry and antenna design, is a "T" of 720 conical spiral antennas under construction at the University of Maryland's Clark Lake Radio Observatory near Borrego Springs, California. Elements of the array have been in operation for about 3 years for test purposes and for some limited observations. Experience gained with portions of the array assures the success of the design and allows some definitive statements to be made about the properties of the individual elements and the overall phasing scheme. It is the purpose of this paper to describe the system, to outline the measured parameters of the conical spirals, and to compare the calculated and observed array patterns with particular emphasis on an incremental phasing scheme not normally employed in radio astronomical instruments. The sidelobe structure of the system is complex and affects the confusion limit of the system as estimated by Fisher [1972]. A brief description of the proposed electronics is included to give a coherent picture of the final instrument.

OUTLINE OF ARRAY AND ELECTRONICS

The new array is a 3.0×1.8 km T with the direction of its legs being approximately east, west, and south. The array is laid out in the plane of the

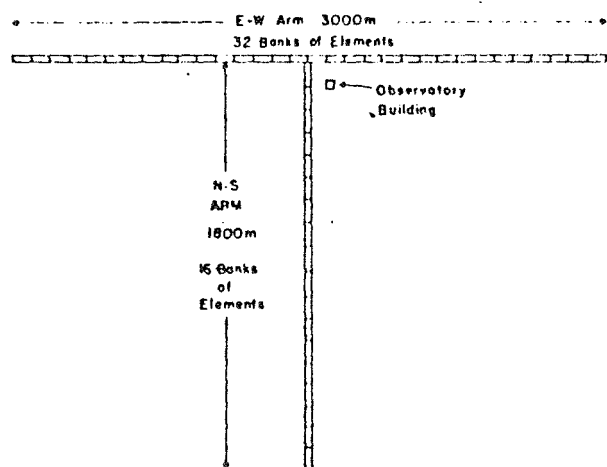


Fig. 1. Array layout.

Clark's dry lake which is not exactly tangential to the geoid. The south arm, which is perpendicular to the E-W arms, has been laid out 18 arc sec from the plane containing the earth's axis and the center of the array. The array's effective coordinates become lat. $33^{\circ}20'29''$, long. $116^{\circ}17'25''$. The signals from each arm are combined to form 7 fan beams and the E-W fan beam signals are multiplied by the N-S fan beam signals to produce pencil beams. The beam shape is equivalent to that obtained with a full cross but the collecting area of the fourth arm is lost with the T. Phase tolerances between the orthogonal arms are more critical in the T array than in a full cross [Christiansen and Höghom, 1969].

Each log spiral element has a collecting area of about $\lambda^2/3$, and is designed to operate between 20 and 125 MHz. The low frequency limit has been extended to 15 MHz at reduced efficiency by terminating the base of the spiral with resistors. The teepees are at 6.25-m intervals in the E-W arms and 7.5-m intervals in the south arm. This spacing gives rise to grating responses above 50 MHz which will be discussed in a later section. Since the elements are all fixed in the vertical direction, beam positioning is accomplished purely through adjustment of the phase gradient across each arm. The gain of the system is modulated by the response pattern of the individual elements. For good zenith distance coverage, the response pattern must be wide, and the gain of each element is correspondingly low.

As shown in Figures 1 and 2, phasing of the array is accomplished in two stages. The elements are divided into 48 banks of 15, and the signals from the 15 antennas in each bank are combined, then pre-amplified and sent to the central building on separate coaxial feed lines. Phasing within a bank is accomplished by electronically "rotating" each conical spiral antenna with a diode switch controlled from the central building.

The signals from the 48 banks are processed separately, in carefully matched amplifiers and digital networks. Figures 3 and 4 are block diagrams of the proposed electronics. The slope filter ahead of the postamplifier is a high pass filter with a cutoff of 100 MHz and is designed to compensate approximately for increase of sky noise and decrease of cable attenuation with decreasing frequency. It also reduces the dynamic range requirements on the following electronics, particularly with respect to the strong man-made interference below 30 MHz. The remaining RF and IF components are relatively straightforward.

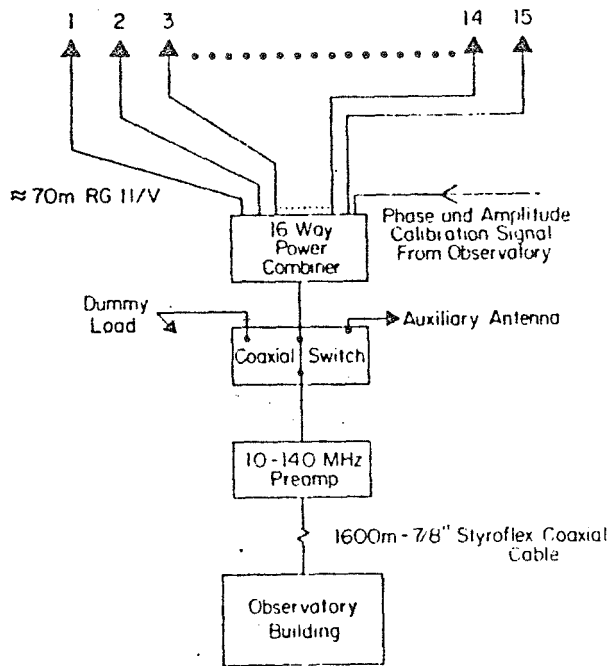


Fig. 2. One bank of 15 conical spiral elements.

ward. Each RF signal goes through two frequency conversions. It is first converted up to an intermediate frequency (IF) of 170 MHz to provide good image rejection. Then the signal is converted to 10 MHz, where bandwidths between 0.1 and 3 MHz can be selected. The first local oscillator (LO) is variable from 185 to 295 MHz to select the appropriate operating frequency. The second LO is fixed in frequency at 160 MHz.

The high level outputs of the 10 MHz IF ampli-

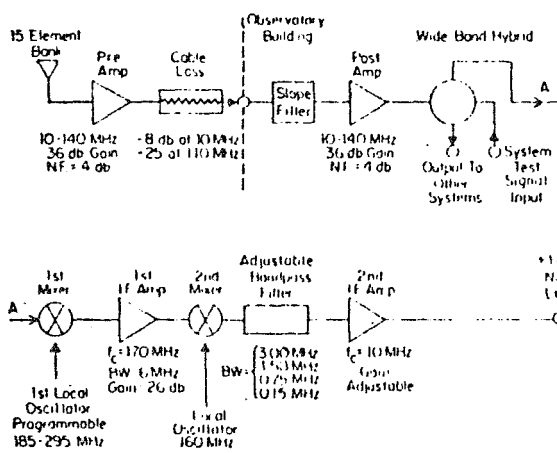


Fig. 3. Block diagram of one of 48 channels in which signals from the 15-element banks are processed.

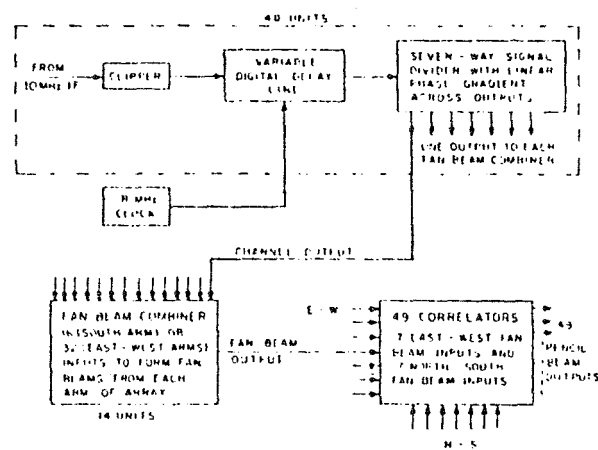


Fig. 4. Block diagram of digital delay and correlation system.

fiers are digitized in 2-bit levels and delayed in random access memories. All of the real-time delays are controlled by the memory combinations. Phase adjustment between the channels is accomplished by appropriate bit permutations. Finally, the digital signals are converted to analog levels and combined in resistor networks to form 7 E-W and 7 N-S fan beams. All fan beams are cross-correlated to form 49 picture elements around the primary direction for which the array is phased. The instrument's specifications and capabilities are listed in Table 1.

For comparison, the total collecting area of the elements in this array is equivalent to the geometrical area of a 50-cm (165-ft) dish at 100 MHz and a 250-m (800-ft) dish at 20 MHz. The conical spiral has a constant gain with respect to an isotropic radiator, and its collecting area varies as the wavelength squared. At 80 MHz the total collecting area is half that of the Culgoora array. The resolution values given in Table 1 are approximate and depend on

TABLE 1. TPT specifications.

| | |
|---|--|
| Frequency range | 15 to 125 MHz |
| Instantaneous bandwidth | 0.10 to 3 MHz |
| Total collecting area | $250 \lambda^2$ |
| Resolution | 20 MHz 100 MHz |
| | 20 arc min 4 arc min |
| Steering and frequency changing time | $\ll 1$ msec |
| Sky coverage | $< 45^\circ$ zenith distance |
| Sensitivity ($\tau = 10^\circ$; BW = 2 MHz) | $\sim 1 \text{ Jy}^1$ at all frequencies |
| Confusion limit | $\sim 1 \text{ Jy}^1$ at all frequencies |
| Polarization | Left circular |

¹ 1 Jy (Jansky, flux unit) = $10^{-26} \text{ W m}^{-2} \text{ Hz}^{-1}$.

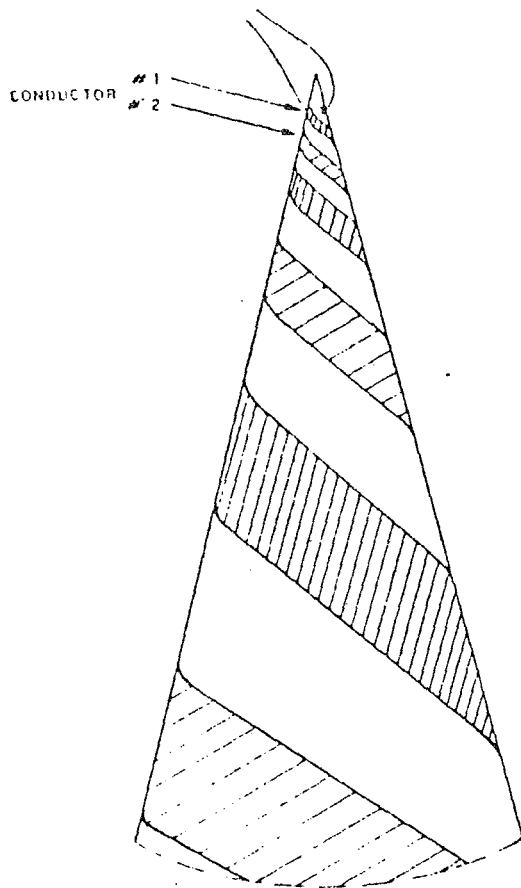


Fig. 5. Basic form of conical log spiral antenna.

taper and digital processing of the correlated output and on the zenith distance of the observed sources.

SINGLE ELEMENT CONSTRUCTION AND OPERATION

The basic building block of the array is the conical log spiral antenna. Ideally this antenna would consist of two conducting sheets wound on the surface of a cone as shown in Figure 5. It is a self-conjugate antenna with a characteristic impedance of $189\ \Omega$ and is fed by a balanced transmission line at its apex.

The electrical and radiative properties of this antenna are as follows. First, the low-frequency limit of the antenna is determined by the size of the base of the spiral (circumference $\sim \lambda_{\min}$) and the high frequency limit is set by the point at which the top of the spiral is truncated and the accuracy with which it is wound. The low frequency limit of the antenna is extended by terminating the base of the spiral with a resistive load. Power that would ordinarily be reflected from the base of the antenna is dissipated in

the load, and the same impedance at the antenna terminals is then maintained to very low frequencies. At frequencies where $\lambda > \lambda_{\min}$ some of the power on the antenna is lost in the resistive loads before it can be launched into space. Therefore the limit on the operating frequency is set by the loss of efficiency one can tolerate. In principle, at least, the radiation pattern and the circularity of the polarization should not change at lower frequencies.

Second, the antenna is unidirectional toward the apex and the polarization is in the opposite sense from the opening direction of the spiral, i.e., a right-hand (clockwise opening) spiral as viewed from the top radiates predominately a left circular wave. The far field radiation pattern is determined by the apex angle of the cone and the pitch angle of the conductors. Considerably more detail may be obtained from other sources [Rumsey, 1966; Dyson, 1965; Yeh and Mei, 1967, 1968].

In actual practice the use of conducting sheets is very difficult because of cost and wind resistance for large antennas. A good approximation to a conducting sheet can be made by using three wires, one at the location of each edge of the conductor and one in the center. Thus the elements in this array use six coaxially wound spiral wires, three connected to each side of the transmission line.

Each element in the array is phased by electrically rotating it in 45° increments. Antenna rotation is a practical phasing scheme in this array only if the polarization remains very nearly circular in all directions observed. The conical spiral antennas meet this requirement quite well between half-power points of their radiation pattern. Antenna rotation is accomplished by winding the spirals with eight instead of six wires and a diode switch has been devised to select six of the wires at any given time. With the simplicity of this phasing scheme comes the disadvantage of not having continuous rotation. The phase error of any element can be as much as 22.5° due to incremental phasing.

Figure 6 shows the appearance of the antennas after the supports and switch circuitry are added. The diode switch is inside the top of the central pipe; the signal passes through a balanced-to-unbalanced transformer and is brought down the center of the pipe with $75\ \Omega$ coaxial cable.

ELEMENT GROUPING AND PHASING SCHEME

The phasing within each bank is accomplished by rotating each element, so there is no real time delay

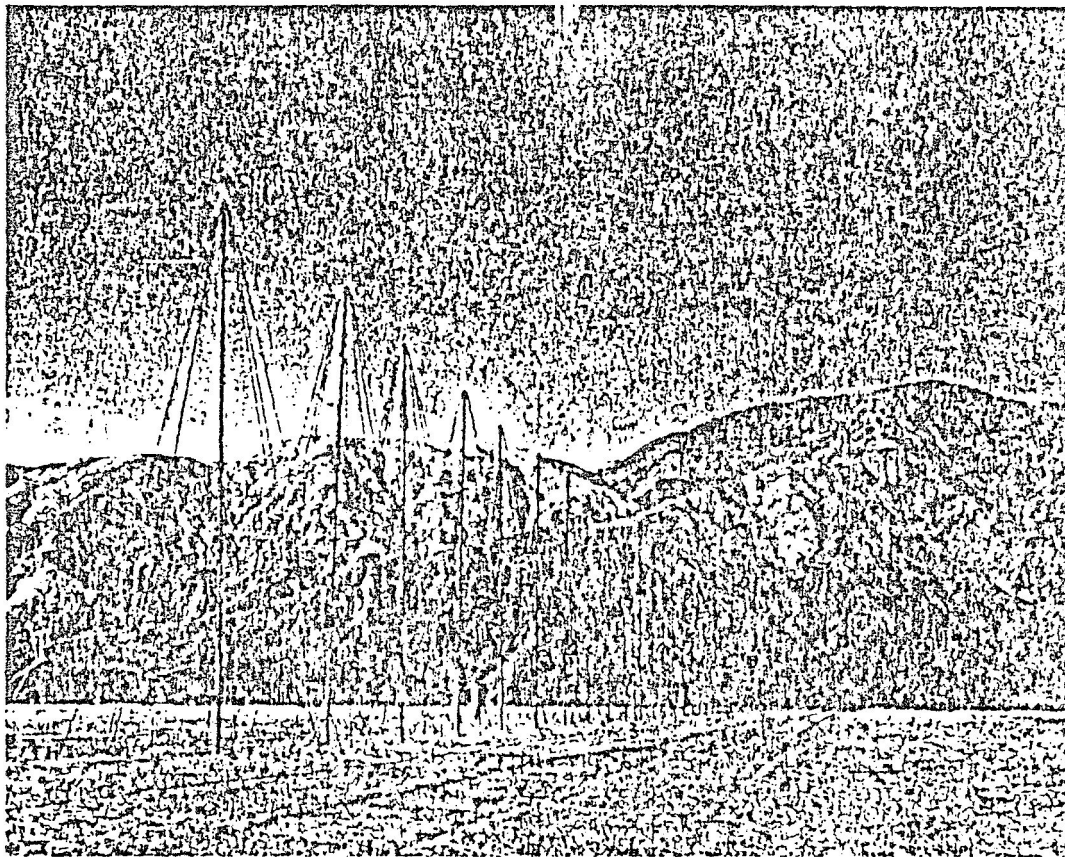


Fig. 6. The working version of the TP antenna in the array.

added to the signals from individual elements. All time delays are added to the 48 signal paths in the central building.

The use of simple phasing as opposed to delays in the 15-element banks limits the size of banks due to coherence loss with wide receiver bandwidths. One bank is approximately 100 m in length. This results in a coherence loss of 9% with a bandwidth of 3 MHz at a zenith distance of 45° . It is normally much less with smaller bandwidths and zenith distances.

In actual operation a computer-controlled set of power transistors supplies the phasing signals. Every bank in each arm is identically phased, and elements with the same position in each bank have their control wires connected in parallel. Also, the east and west arms are normally phased alike, so only 120 independent control wires are needed for the full array (4 wires per element times 15 elements per bank times 2 independent arms).

Normally, equal lengths of transmission line would be run to the 15 elements in each bank, but in this

array the line lengths have been cut pseudo-randomly to reduce the array's response to unwanted right-circularly polarized radiation [Svenson and Lo, 1961]. The basic idea is the following. Each element has a small response to right circular polarization (cross polarization). When an element is rotated, the phase of the right-hand polarized signal is changed in the opposite direction from that of the left-circularly polarized signal, i.e., when the left-polarized phase is advanced the right-polarized phase is retarded. The result for an array with equal feeder lengths is that a "ghost beam" is formed with cross-polarized radiation on the opposite side of the zenith from the main beam. This ghost beam can be substantially reduced by staggering the lengths of the cables feeding the elements in a bank of 15. Thus, if a feeder cable is shorter than normal, the antenna is rotated counterclockwise to retard the left-polarized wave to bring it back into phase. In the process the cross-polarized wave gets advanced by the shorter cable and again by rotation and, in general, is out of phase with respect to similarly polarized waves from

other elements. Also, after the signals from the 48 banks are delayed and combined, the chance of having a pencil beam fall in one of the cross-polarized ghost beams is quite small.

As shown in Figure 2, the signals from the 15 elements in each bank are combined, and the resulting signal is amplified approximately 36 db in a wide-band amplifier. This preamplifier has a noise figure less than 4 db (400 K) and a bandpass extending from 10 to 140 MHz. It is particularly designed to handle large interfering signals without producing spurious intermodulation products.

After amplification the combined signal enters an air-filled coaxial cable of 1600 m length for transmission to the central building. The loss in this cable is proportional to the square root of the frequency and is about 25 db at 110 MHz. Even at the highest frequency the preamplifier has adequate gain so that noise produced by succeeding components has little effect on the system noise figure. After accounting for the loss in all the cable and transformers ahead of the preamplifier, the system noise temperature is 1800 K at 110 MHz. At this frequency the sky noise is about 1000 K so $T_{\text{sys}} + T_{\text{sky}} \approx 2800$ K. The galactic background radiation (T_{sky}) is approximately proportional to λ^2 , and the losses ahead of the preamplifier decrease in proportion to the square root of the frequency, so below about 70 MHz the system noise is insignificant compared to sky noise.

ARRAY PATTERN CALCULATIONS

To the authors' knowledge, the use of incremental phasing in linear arrays for radio astronomy has not

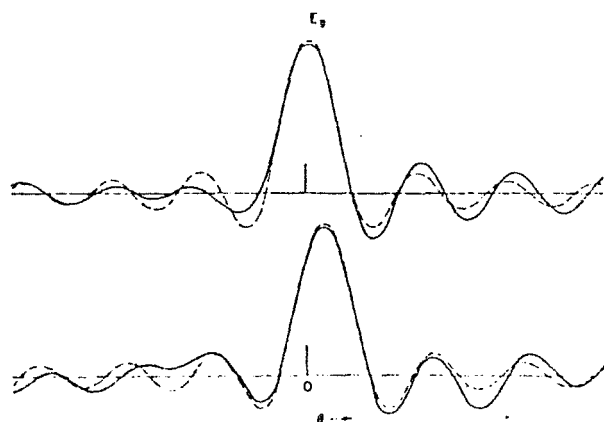


Fig. 7. 15-element array patterns with incremental phasing (solid lines) compared to perfectly phased array pattern (dashed lines).

been treated in detail. A considerable number of fundamental pattern calculations had to be performed to assure the feasibility of the scheme. We had to determine the magnitude of the sidelobes generated by phase errors up to 22.5° and calculate the confusion limits due to these sidelobes. The confusion calculation was carried out by Fisher [1972].

For pattern calculations the array is most conveniently divided into two levels. First, the electric field pattern of a bank of 15 elements is calculated using incremental element phases. Then the pattern of one bank is multiplied by the array factor generated by isotropic radiators at the phase center of each bank to obtain the total response pattern.

To illustrate incremental phasing effects, assume that the elements are fed with equal lengths of transmission line. Figure 7 shows two examples of calculated patterns resulting from incremental phasing (solid lines). Superimposed on each is a plot of pattern with perfect phasing (dashed lines). The most important difference between perfect and incremental phasing in Figure 7 is that the zero crossings are not identical. Therefore, when the 32-element grating response is multiplied by the 15-element pattern, the grating lobes which ordinarily would fall on zeroes of the 15-element pattern will no longer be completely cancelled. Another way of looking at this is that there will be a periodic phase error distribution in the array which repeats every 15 elements. This will create small grating responses with angular spacings of $(\lambda/15d)$ radians, where d is the distance between individual elements.

The slight degradation of the main beam is a quasi-random function of direction so there will be about a 3% peak-to-peak modulation of the response as the array tracks a source. This is also a result of the imperfect phasing.

The randomized feed cable lengths mentioned above do not introduce larger phase errors, but they do change the pattern obtained with a 15-element bank. Some of the patterns calculated using the feeder system actually incorporated in the array are shown in Figures 8 and 9. Equal and unequal feeder systems give the same average sidelobe level, so the sidelobe and confusion calculations given by Fisher [1972] are valid for the actual system although they were made for equal feeder lengths. Incremental phasing is not the only source of phase errors, but it is by far the most important.

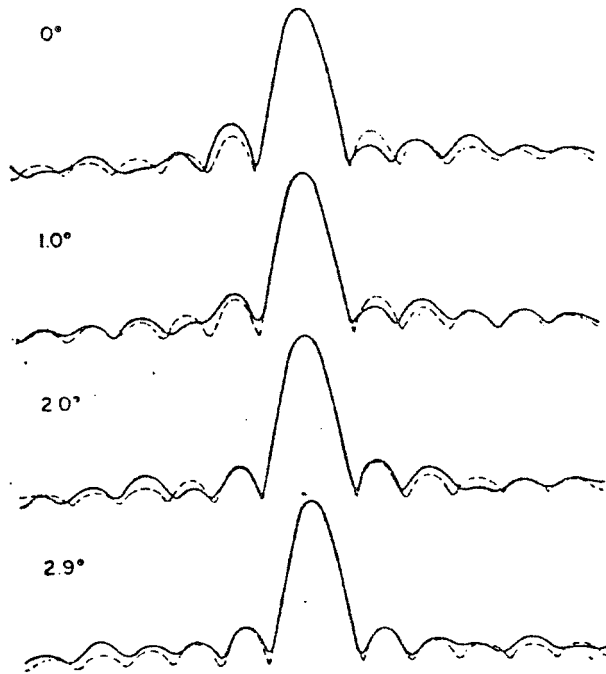


Fig. 8. Representative voltage pattern of incrementally phased 15-element banks at 28 MHz using staggered feeder cable lengths (solid lines) compared to perfect phasing patterns ($\sin x$, dashed lines). Only the amplitude of the resultant voltage vector is plotted (see text).

TOTAL ARRAY PATTERN

With unequal feeder lengths in the 15-element banks the element phases are not antisymmetric around the center element, #8; e.g., the incremental phasing error of element #7 is not necessarily equal in amplitude and opposite in sign to the phase error of element #9. As a result, the phase center of the 15-element banks can be displaced by as much as 0.02 wavelength (7°) from the center element. Because all of the banks within an arm are identically phased, the phase center displacement produces no additional phase error between the banks in one arm. The south arm is phased differently from the E-W arms, so there will be a variation in relative phase of the combined signal from the south arm with respect to the combined signal from the E-W arms. This phase error can be calculated in the controlling computer's phasing program and compensated by adding a small phase shift in the signal paths from the south arm.

Another consequence of the asymmetric phasing in the 15-element banks is that the amplitude of the voltage vector which is the resultant of the addition of the 15 signals does not go through zero between

sidelobe maxima (see Figures 8 and 9). This, and the phase center motion, are results of the incomplete cancellation of the imaginary part of the vector sum. In other words, the phase of the resultant vector varies continuously from 0° to 180° but, after the signals from the E-W and south arms are multiplied, the combined pattern in the cosine receiver output will have zero amplitude when the E-W and south arm signals are in phase-quadrature.

Note that the 15-element patterns are voltage patterns and that the pattern resulting from the correlation of the E-W and south arm signals is a product of two voltages. At a given direction in the sky the array response is a vector product of the voltage response of the E-W arm, the voltage response of the south arm, and the individual element power response in that direction.

After compensating for phase center motion the relative phases of the signals from the 48 banks will be within a few degrees of the perfect phasing case so the 32-element grating response is a $\sin x = (\sin \pi x)/(\pi x)$ pattern.

SIDELOBES

In principle, to get a complete picture of the side-lobes, the array pattern should be evaluated for all directions in the sky for all beam positions at many wavelengths. This is a formidable task even for a

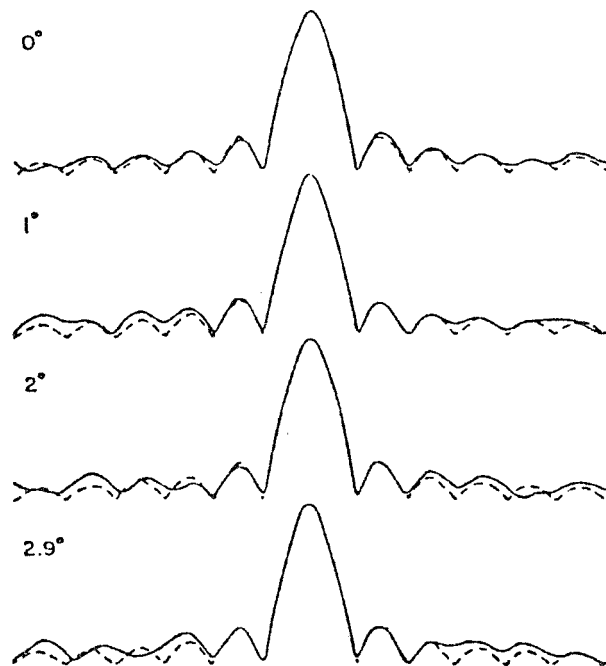


Fig. 9. Same as Figure 8 but at a frequency of 110 MHz.

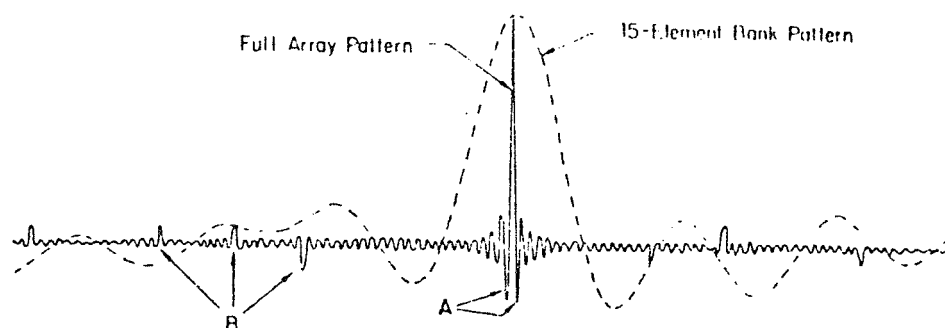


Fig. 10. Total one-dimensional array voltage pattern (solid line). The dashed envelope is the 15-element pattern.

high speed computer, so some simplifications are made.

Figure 10 is a representative plot of a portion of the pattern of the full array (solid line). The dashed line is a plot of the 15-element bank pattern. This figure illustrates two of the three basic types of sidelobes characteristic of this array. First, very close to the main beam are the sidelobes typical of any uniform linear array. The first negative sidelobe (A) is 21% of the main beam, and the close-in sidelobes fall off to less than a few percent about 8 beamwidths away. This type of sidelobe can be reduced either by tapering the illumination of the array or by adding a portion of the responses of 2 adjacent beams at the zero crossings of the central pattern so as to cancel the $\text{sinc } x$ sidelobes [Perini, 1964]. Both methods broaden the main beam slightly.

The second type of sidelobe (B) is due to the imperfect phasing of the array. The zeroes of the 15-element pattern do not fall on the maxima of the 32-element grating response, resulting in sidelobes averaging about 5% of the main beam which occur every 32 beamwidths on either side of the main beam. Below 50 MHz these are the most important sidelobes as far as confusion is concerned.

Above 50 MHz the spacing of the individual elements is greater than one wavelength, giving rise to primary grating responses equal in amplitude to the main beam. These will be treated as a third type of sidelobe (C). The only method for reducing types B and C is through the use of a receiver bandwidth large enough to reduce the coherence of the radiation at the position of these sidelobes. Bandwidths of a few percent are needed to lower these sidelobes to manageable levels for weak source observations.

It must be remembered that the above discussion is only for the one-dimensional case. When the E-W

and south arms are combined, sidelobe responses occur wherever a main beam in one direction crosses a significant response from the orthogonal arm. Figure 11 is a projection of the celestial sphere onto the plane of the horizon and shows the positions of the various types of sidelobes at 70 MHz. Figure 12 is an expansion of the area around the main beam.

TP IMPEDANCE CHARACTERISTICS

Because the conical spiral elements in this array incorporate several features which have not been tried with these antennas before, it was imperative that impedance and radiation characteristics be investigated before building 720 units. For practical reasons the antenna impedance could not be measured directly. There was a length of cable, a transformer, and the phase switch between the impedance bridge and the antenna terminals. Since we are interested in the operation of the total system, the standing wave ratio (VSWR) and impedance measured through these components are perfectly valid provided the power loss in the individual components is not more than 20% or so.

Significant stray reactances in the feed system arise due to the physical layout of the diode switch inside the central support pipe. These reactances were measured and compensated with small inductors incorporated in the switch. The combination of stray and lumped reactances forms a nearly symmetrical low pass filter with a cutoff frequency of about 250 MHz in series with each antenna wire.

Figure 13 is a Smith chart plot of the antenna impedance as a function of frequency. The measurement was made at the base of the TP and corrected for delay in the 20-ft feeder cable. The maximum VSWR encountered is 1.4:1, which corresponds to a reflected power loss of 4%. Ohmic losses in the

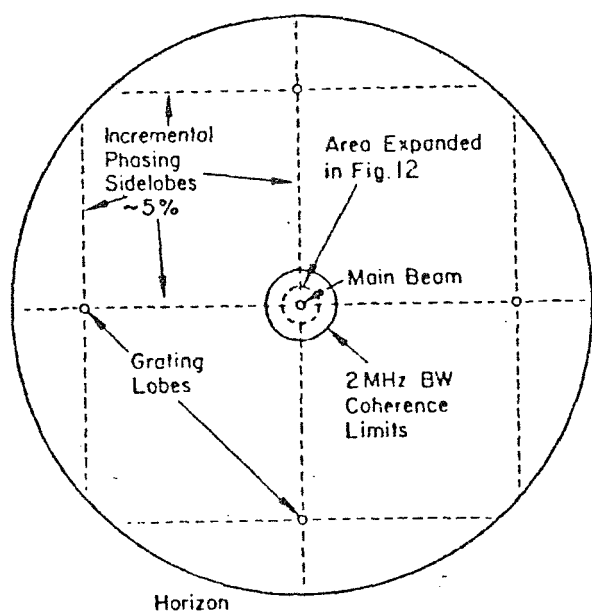


Fig. 11. Projection of the 70 MHz TPT array pattern onto the plane of the horizon. Beam sizes are not to scale.

transformer and switch are less than 1 db (20%) and the loss in the 20-ft coaxial cable is 0.4 db (8%) at 110 MHz. When one takes the 75:200 impedance transformer into account it is evident that the characteristic impedance of the antenna is close to 189 Ω , which is the theoretical value for a self-conjugate antenna.

ANTENNA EFFICIENCY

Determination of the efficiency of a single element is very difficult because it requires an absolute measurement. There are no isolated radio sources with accurately known intensities which are strong enough to be measured with a single antenna. The next best alternative is to compare the noise output of the TP due to the galactic background with that of dipoles at two frequencies. This type of measurement does not give the gain of the antenna in any particular direction, but it should account for ohmic losses in the antenna and absorption of radiation by the ground. Since the galactic background is concentrated in the galactic plane, this measurement has to assume that the radiation patterns of the TP and dipole are approximately the same and that the measurements are taken at the same sidereal time. A half-wave dipole, one quarter wavelength above a conducting plane, produces a power pattern not too different from that of the conical spiral antenna with which it is compared. Because the galactic background is

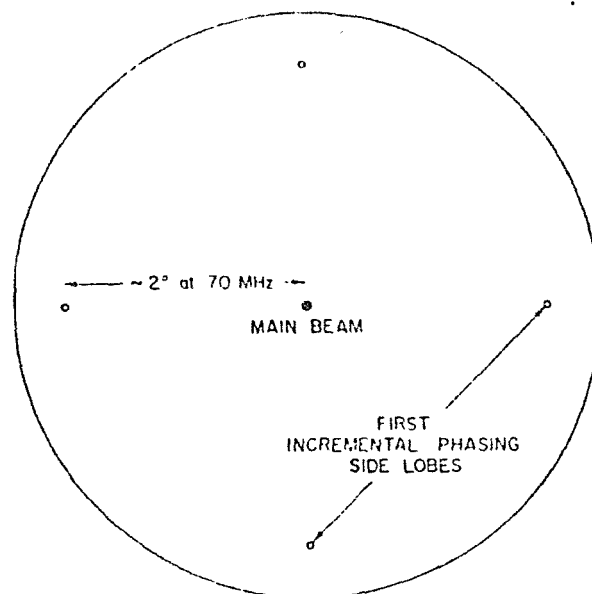


Fig. 12. Expansion of Figure 11 around the main beam. Beam sizes are approximately to scale.

randomly polarized, the difference in polarization of the two antennas should be of little consequence.

Half-wave folded dipoles were constructed for 110 and 33 MHz. The test procedure at 110 MHz was to record the total power from the TP for 24 hr and then to repeat the observation using the dipole.

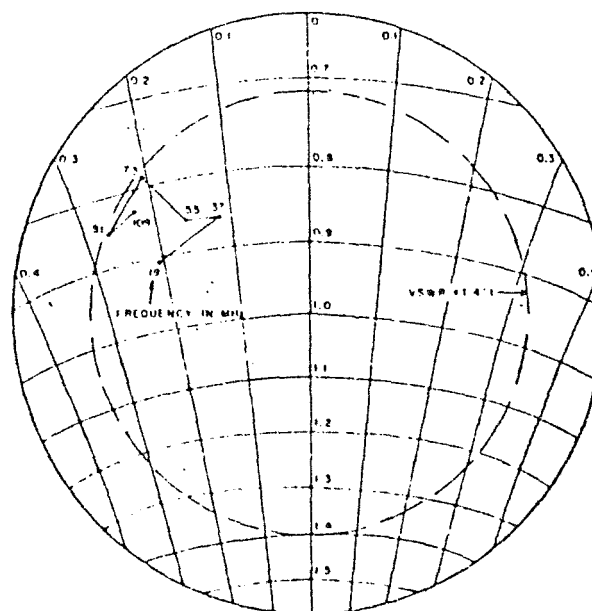


Fig. 13. Impedance characteristics of the production version of the TP antenna corrected for delay in the feeder cable.

The antenna temperature was calibrated by substituting a noise source for the antenna at the preamplifier input and recording a series of noise levels. The noise output from both antennas peaked at the same sidereal time and the ratio of their outputs was approximately the same throughout the sidereal day. This confirms the assumption that the two antennas have nearly the same radiation patterns.

The dipole antenna temperatures at similar sidereal times, corrected for cable losses, are plotted on Figure 14 as x's. The error bars represent outside limits on the uncertainty in reflection losses and calibration errors. Other points on the graph have approximately the same error estimate. The dipole measurements fit the expected background spectrum as shown by the straight line. The solid circles are the TP measurements which were directly compared with the dipole values. The 110 MHz TP antenna temperature is $20\% \pm 20\%$ below the dipole value and the 33 MHz TP antenna temperature was $50\% \pm 20\%$ below the dipole standard.

To get an estimate of the efficiency of the TP at other frequencies, its noise output was measured at discrete frequencies down to 14 MHz. After correction for losses between the antenna and the preamplifier, the antenna temperatures are plotted as open circles on Figure 14. These values were normalized to agree with the TP/dipole ratios. Below 30 MHz the sky noise increases less rapidly with decreasing frequency, but the exact value of the integrated sky temperature in the antenna beam is not known because it is very difficult to take the effects of the

ionosphere and ground reflections into account. The construction of a lower-frequency dipole at Clark Lake was impractical.

It can be seen from Figure 14 that the antenna begins to lose efficiency rapidly below 25 MHz, where a considerable fraction of the power is absorbed by the terminations. As a result the conical spiral efficiency below 25 MHz is not well known. The system temperature is still dominated by sky noise down to at least 12 MHz as is easily shown by replacing the antenna with a 300 K termination and noting the output noise level variation.

ELEMENT POWER PATTERNS

Many components of the elements were too small to be scaled down in size by any significant factor, so all pattern measurements were made on full size antenna elements. The most convenient far-field sources for the measurements were natural ones and they were used for all of the pattern measurements.

In order to discriminate against galactic background emission and to allow the observation of discrete radio sources, an interferometer was constructed of two elements. The response of the antenna elements as a function of direction was determined in two stages. First, the azimuthal dependence of the power pattern was determined at several frequencies by observing a radio source at a given elevation on a series of nights with one element fixed and the other one rotated to a different position each night with the phase switch. The zenith angle dependence was studied by comparing the apparent strength of two known radio sources at different elevations on the same interferometer fringe.

The two radio sources used in nearly all of the antenna tests were Cassiopeia A [$\alpha = 23^h 22^m$, $\delta = 58^\circ 41'$ (1970)] and Cygnus A [$\alpha = 19^h 58^m$, $\delta = 40^\circ 36'$ (1970)]. Where the flux ratio of the two sources was needed, the spectra compiled by Viner [1973] were used. Cas A is about 20 to 50% stronger than Cyg A depending on frequency.

The azimuthal pattern was measured at four frequencies and three zenith distances, and the results are shown in Table 2. With four independent samples at a given frequency and zenith distance, the azimuthal voltage pattern can be approximated by an ellipse. Table 2 gives the axial ratio of each ellipse (minor/major). The horizontal extent of the radiating region of this antenna is about λ/π , so it should not produce structure in the azimuthal pattern with a scale size of less than a radian. Thus the 45° sampling

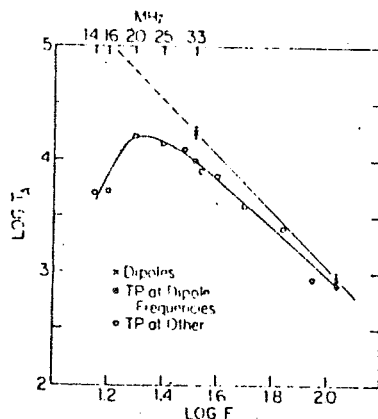


Fig. 14. Spectrum of noise output from a single TP (circles and curved line). The crosses are dipole measurements, and the straight line represents a background spectrum of $T \propto f^{-2}$.

interval should be adequate. Since the values in Table 2 refer to the voltage pattern (not power), they are a direct indication of how the illumination of one element will vary as it is rotated.

One drawback to this method for measuring the electric field pattern of the TP's is that the unwanted right-hand polarization response contributes to the fringe amplitude. This will cause very little error if the right-hand interferometer response remains constant in amplitude and phase as the antennas are rotated. The electric field pattern in the right-hand polarization probably does vary in amplitude in different azimuthal directions, however. This may cause an error in addition to those quoted in Table 2 of as much as ± 0.07 at 110 MHz and ± 0.04 at other frequencies.

Unless otherwise stated, the errors quoted for the measurements are outer limits on the possible range of each value. These limits, which take the signal-to-noise ratio (snr) into account, are mainly derived from the estimated reading error on the strip charts used to record the measurements and from experience with the calibration accuracies and reproducibility of the measurements.

As one might expect, the azimuthal pattern is more nearly circular at small zenith distances. Also, the pattern has a larger variation at 110 MHz, where the antenna is operating near its design limit, than it does at lower frequencies. Naturally, we would like to sample the pattern below 25 MHz, where the antenna operates below its natural frequency limit, but man-made interference prohibits the use of bandwidths necessary to get a sufficient snr using only two antennas.

Measurement of the zenith-distance dependence of the electric field pattern was less straightforward. A method had to be devised to separate the observed intensity variation due to the antenna pattern from that due to coherence loss when using a wide bandwidth and antenna separation.

For this measurement, the two central E-W banks of elements were used as the two components of a phase-switched interferometer. This configuration produced several N-S fan beams which could be judiciously placed so that only one of the two test sources was in a beam at one time. The coherence loss factor was eliminated by comparing the response to Cas A and Cyg A in the same fan beam. Phasing combinations were chosen so that the eight phase positions were fairly evenly represented and the azimuthal antenna pattern tended to average out.

TABLE 2. Axial ratios of azimuthal voltage patterns.

| Frequency | Zenith distances | | | Estimated errors |
|-----------|------------------|------|------|------------------|
| | 20° | 32° | 42° | |
| 28 MHz | 0.86 | 0.95 | 0.87 | ± 0.07 |
| 45 MHz | 0.97 | 0.93 | 0.86 | ± 0.05 |
| 70 MHz | 0.94 | 0.95 | 0.77 | ± 0.04 |
| 110 MHz | 0.91 | 0.83 | 0.79 | ± 0.07 |

The azimuthal dependence should contribute an error of only about $\pm 5\%$ to an individual ratio in the worst case. Also, care was taken to be sure that a cross-polarization (right-hand) fan beam did not fall on one of the sources when a left-hand polarized fan beam measurement was taking place. Thus, the cross-polarized response caused no significant error in this part of the antenna pattern study.

Adopting the flux ratios of Cas A and Cyg A given by Viner [1973] at the several observed frequencies, the procedure was to use a bootstrap technique to construct the zenith distance dependence of the antenna pattern. Ratios of response to Cyg A and Cas A on the same fan beam were measured for five to seven fan beams at each of four different frequencies. The response to Cyg A nearest the zenith was assumed to be unity and the relative value for Cas A, corrected for its higher flux, was plotted at its larger zenith distance as in Figure 15. By interpolating between the first two points, the next largest zenith-distance value for Cyg A could be normalized and the power pattern extended to larger Z with the corresponding Cas A value, and so forth.

As a point of interest, the above method for measuring antenna patterns will work for any linear array of elements which have a pattern that is a surface of rotation whose axis is perpendicular to the array axis e.g., an E-W array of N-S dipoles.

Figure 15 shows the zenith distance dependence of the TP power pattern at four frequencies. In each graph similar symbols refer to measurements of Cas A and Cyg A on the same fan beam. Cyg A is always at the lesser zenith distance. The assumed flux ratio α_0 of Cas A to Cyg A is given on each graph.

The errors in the curves measured in Figure 15 are rather complicated in that they tend to accumulate at higher zenith distances. The initial response ratio has an estimated error limit of $\pm 5\%$ and the point at largest zenith distance may be in error by $\pm 10\%$. The small scatter at large zenith distance indicates fairly small error.

In interpreting the graphs in Figure 15, it should

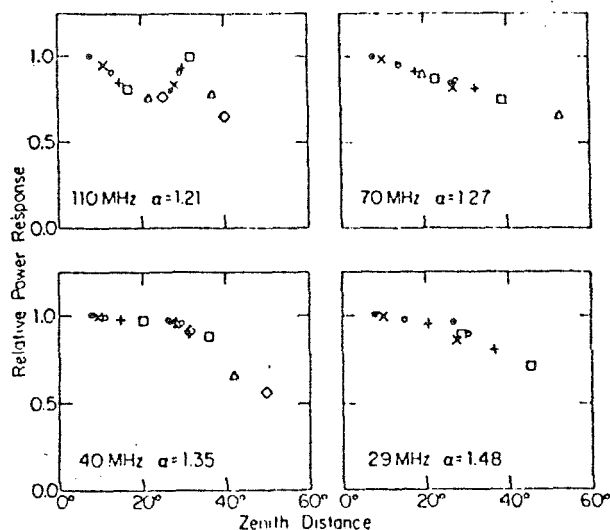


Fig. 15. Zenith distance dependence of the TP power pattern at four frequencies measured with the central banks of elements. α is the ratio of the flux of Cas A to Cyg A at the given frequency.

be remembered that they show an average zenith distance dependence, and a plot of the power pattern at a fixed azimuth will differ slightly from the average curve. The most important result of these curves is that they give the zenith distance to which the array is useful. It appears that the half-power point falls at about $Z = 50^\circ$. At all but 110 MHz the zenith distance dependence is fairly smooth. At 110 MHz there is a roughly sinusoidal component with a 25% peak-to-peak amplitude superimposed on a smooth curve with a half-power width of about 55° . This

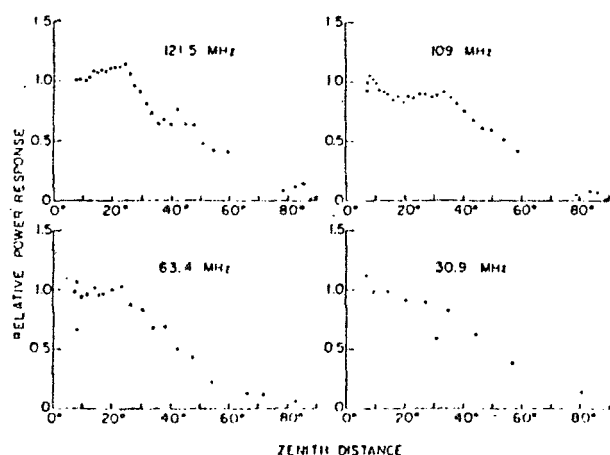


Fig. 16. Zenith distance dependence of the TP power pattern at various frequencies measured using the full E-W arm.

sinusoid could be explained by a ground reflection 20 db below the direct wave (10% in electric field) from a ground plane 7 m below the phase center of the antenna. This would mean the effective ground is about 1 m below the surface of the dry lake. There may be a weak ground-reflected wave at the other frequencies, but it is not possible to distinguish its effect from the direct-wave power pattern features.

In summary, the half-power beamwidth of the conical spiral antenna used in the TPT is about 100° except near 110 MHz where the pattern is apparently distorted by a ground-reflected wave. This ground reflection causes a secondary peak in the zenith distance dependence of the power pattern at $Z \approx 30^\circ$. The variation of the antenna pattern in the azimuthal direction at a constant zenith distance ranges from ± 1 db at 110 MHz and $Z = 45^\circ$ to practically no variation at 45 MHz and $Z = 20^\circ$. In no case is the modulation of the pattern in azimuth large enough to cause unacceptable irregularities in the array illumination.

CROSS-POLARIZATION RESPONSE

The cross-polarization response (response of the antennas to right-hand circular polarization) was measured with the same observations which were used to determine the zenith-distance dependence of the antenna power pattern. As was explained in an earlier section, the cross-polarized wave forms a ghost beam on the opposite side of the zenith from the properly polarized beam.

The amplitude of the right-hand polarized fan beam was measured for at least four different positions in the sky for each frequency. Its amplitude, relative to the left-hand polarized beam, was somewhat dependent on the beam position. All of the measurements were within 25° of the meridian, so coherence and antenna pattern effects were unimportant. Table 3 gives the range or upper limit on the relative amplitudes of the cross-polarized responses with respect to the left-hand polarized fan beam. The detection limit of about 5% was set by confusion with the minor sidelobes of the properly polarized response.

As would be expected, the cross-polarization response is highest at 110 MHz where the antenna is

TABLE 3. Right-hand polarized response relative to the left-hand polarized response.

| Frequency | 110 MHz | 70 MHz | 40 MHz | 20 MHz |
|-----------|-----------|-----------|----------|--------|
| Response | 10 to 20% | <5 to 10% | <5 to 8% | <6% |

working near its design limit. The wires from the phasing switch to the spiral are no doubt radiating a significant amount of power which is linearly polarized. Possibly, at the other design limit below 20 MHz the cross-polarization response will also be fairly high, but it could not be measured because of strong broadcast interference.

In a previous section the method for reducing the cross-polarization response of a bank of elements using staggered lengths of feed cables was outlined. With unequal feeder lengths in both banks, all of the cross-polarized fan beams were below a 4% detection limit at all four frequencies. On the average, the staggering of phases in the right-hand waves should reduce the unwanted fan beams by a factor of $(15)^{1/2}$ provided the phase difference between the shortest and longest cables is more than 2 radians. This appears to be confirmed by the measurements.

The difference in electrical length between the shortest and longest cables is about 11.5 m, so there is not quite enough phase scrambling below 20 MHz to realize the full potential of the cross-polarization reduction. If the difference were made larger, the loss differential in the cables at 110 MHz would cause excessive illumination irregularities across the banks of elements, creating sidelobes more difficult to eliminate than the cross-polarization responses. It should also be noted that a further reduction in the unwanted polarization is realized in the phasing of the full array because the chance of having the overall phasing correct for both the main beam direction and the cross-polarized beam direction is very small. The right-hand polarized wave should cause very few confusion problems.

PHASE MEASUREMENTS

To confirm that the 45° phase-stepping system on the conical spiral antennas does indeed provide the proper phase increments, a pair of TP's were connected in a phase-switched interferometer as in the azimuthal pattern measurements. The fringe phase of this interferometer was measured on successive nights with one of the antennas rotated in steps of 45°.

This technique was not completely definitive, however. There was no practical way to eliminate the response of the antenna to right-hand polarized radiation. The cross-polarized interferometer pattern will cause an apparent phase shift in the fringes measured with the above technique when the oppositely polarized patterns are near phase-quadrature.

TABLE 4. TP phase error upper limits.

| Frequency | 110 MHz | 70 MHz | 40 MHz | 20 MHz |
|-----------|---------|--------|--------|--------|
| Error | <20° | <10° | <5° | <7° |

ture. A 20% cross-polarized response will produce an apparent phase error of up to 20°. The values given in Table 3, then, set upper limits on the accuracy of the phase measurements.

Table 4 lists the limits on the phase errors in the conical spiral antennas as derived from these measurements. The snr and ionospheric seeing set a detection limit of about 5° on the phase errors, and the higher upper limits were due to the cross-polarization response. It can be stated that no phase errors were measured which would not be consistent with the errors expected from the cross-polarization response given in Table 3.

Thus far, all of the discussion of phase errors has been concerned with those produced by the individual elements. There are further phase errors introduced by the transmission lines and amplifiers which are summarized in Table 5. Because the signals are combined in two stages, the phase errors are divided into two groups: those associated with the 15-element banks and those occurring in the 48 signal paths from the 48 banks.

Two values are given in Table 5, the larger of which is the outside limit on the phase deviation due to each component. In practice the phase deviations are considerably smaller than the specification limits, as is indicated by the rms values. Also, the phase errors on items 2 through 6 are given for an operating frequency of 110 MHz with these errors decreasing with decreasing frequency. It can be seen that the largest phase error is due to incremental phasing, as was assumed in the sidelobe calculations.

TABLE 5. Phase error budget. Items 2 through 6 assume a frequency of 110 MHz.

| 15-element bank | | limit | rms |
|-----------------------------------|-----------|--------|--------|
| 1. Incremental phasing | | ±22.5° | ±13.9° |
| 2. Cable, switch, and transformer | | ±5° | ±2° |
| 3. Power combiner | | ±5° | ±2° |
| | rms total | | ±14.1° |
| 48 signal paths | | | |
| 4. Preamps | | ±5° | ±2° |
| 5. High pass filters | | ±5° | ±2° |
| 6. Cables | | ±2° | ±1° |
| 7. RF and IF electronics | | ±5° | ±2° |
| 8. Digital delays | | ±5° | ±2° |
| | rms total | | ±5.8° |

PROTOTYPE T OPERATION

As an initial check on the performance of the full T, the central three banks of elements were combined as a prototype T. This formed a small telescope of about 200 m effective aperture which includes the central region where the arms may interact. Most of the difficulties in the operation of a T usually occur in this central region. A few beam positions were tried at each of the four test frequencies, and the results were as predicted. The pointing accuracy was within limits set by the incremental phasing and the sidelobe level was no higher than expected.

A more detailed analysis was done at 70 MHz, where the best snr was obtained with moderate to low ionospheric scintillation levels. Figure 17 shows 7 drift scans of Cyg A at different beam positions. No attempt was made to maintain receiver gain calibrations over the 7 nights, so the intensities should not be compared directly. The expected beam positions as indicated by the tick marks in Figure 17 coincided with the measured values within the timing accuracy that could be obtained. Some examples of ionospheric intensity scintillations are seen in the drift scans. Observations 4 and 5 are virtually un-

affected by the ionosphere while peak-to-peak scintillations of up to 20% are seen on other nights. The agreement between calculated and observed patterns is excellent.

OPERATIONAL TESTS OF THE FULL APERTURE

The 48 coaxial feed lines, preamplifiers, slope filters, and postamplifiers were next installed. The cables were buried at a depth of about 1 m, but were brought above ground at every splice. All cables are pressurized with dry air. The relative attenuations and electrical lengths of each of the 1600 m cables were found to remain identical at all frequencies and outdoor temperatures within the accuracy of our measurements, about ± 0.2 db and ± 0.3 cm, respectively. The absolute attenuation of the cables varies with underground temperature, as expected, and in the calibration of observed intensities it will be necessary to correct for this effect. The cables and other components appear to operate within the error budget given in Table 5, so we should expect the full aperture to operate in accordance with theory.

The center element of each bank was constructed and each was connected to a preamplifier and feed line. E-W and N-S grating arrays were thus formed. They yield the full angular resolution of the final system, but have large grating responses and only 1/15 of the final array's collecting area. As accurately as we can measure, these arrays produce the expected response of a uniformly illuminated aperture. Below 50 MHz, these response pattern measurements are accurate to a few percent; above 50 MHz, all of the stronger radio sources are partly resolved by the arrays and the interpretation of the observed profiles is complicated. In fact, the arrays are being used for some measurements of the angular structure of strong sources.

The E-W grating array has also been correlated with the completed central, E-W banks of elements. This process eliminates all grating responses except the one that falls within the pattern of the banks of elements. The element banks are pointed under computer control and their response pattern can be placed on any of the grating lobes to form single N-S fan beams. By taking successive drift scans across a given source at many zenith distances, the data shown in Figure 15 have been checked. These newer pattern measurements are shown in Figure 16. In all cases, these patterns represent reasonable interpolations between those shown in Figure 15.

The E-W arm of the instrument is now complete

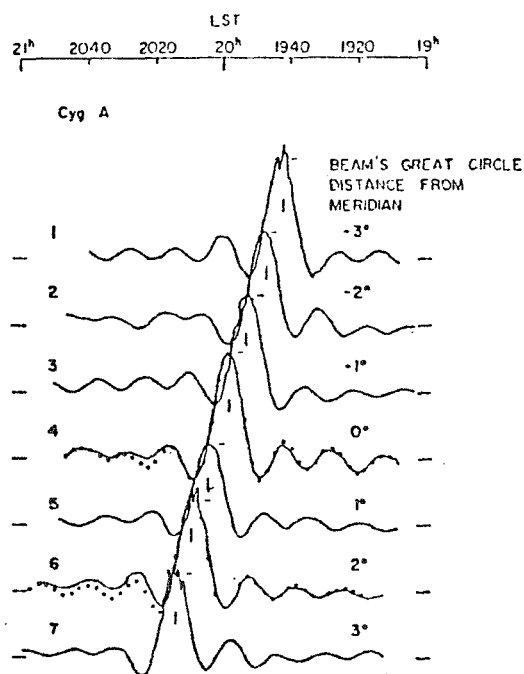


Fig. 17. Drift scans of Cygnus A through the prototype T beam at several beam positions. Points on 4 and 6 are calculated values.

and in full operation. The N-S arm is nearly finished and the electronics system will next be completed. The grating arrays mentioned above are being used for studies of solar bursts, while the E-W arm is being employed in multifrequency observations of the quiet sun, X-ray sources, supernova remnants, and other objects. An example of solar burst data, and the output spectrum of the system, is shown in Figure 18.

All data indicate that the completed system will operate as planned, so its construction is proceeding as rapidly as funds will permit. During the next few months, as the system comes into operation, a powerful new instrument will be available to the

astronomical community. We will welcome visitor usage of the system.

Acknowledgments. The authors wish to acknowledge the work of John Hubbard, Stig Johansson, and Kenneth Barbier. They have all devoted a significant fraction of their professional careers to the design and construction of this instrument. Many other temporary staff and students have devoted themselves tirelessly to this effort. The work is supported by the National Science Foundation under grant GP-19401 and by the National Aeronautics and Space Administration under grant NGR 21-002-367.

REFERENCES

- Christiansen, W. N., and J. A. Högbom, (1969), *Radio-telescopes*, pp. 155-156, Cambridge University Press, London.
- Dyson, J. D. (1965), The characteristics and design of the conical log-spiral antenna, *IEEE Trans. Antennas Propagat.*, AP-13(4), 488-499.
- Fisher, J. R. (1972), Design tests of the fully steerable, wideband, decametric array at the Clark Lake Radio Observatory, Ph.D. thesis, pp. 31-42, University of Maryland, College Park, Maryland.
- Perini, J. (1964), Sidelobe reduction by beam shifting, *IEEE Trans. Antennas Propagat.*, AP-12(6), 791-792.
- Rumsey, V. H. (1966), *Frequency Independent Antennas*, pp. 39-54, Academic, New York.
- Swenson, G. W., Jr., and Y. T. Lo, (1961), The University of Illinois radio telescope, *IRE Trans. Antennas Propagat.*, AP-9(1), 9-16.
- Viner, M. R. (1973), A discrete source survey at 26.3 MHz with an absolute flux basis, Ph.D. thesis, pp. 50-86, University of Maryland, College Park, Maryland.
- Yeh, Y. S., and K. K. Mei, (1967), Theory of conical equiangular-spiral antennas, 1. Numerical technique, *IEEE Trans. Antennas Propagat.*, AP-15(5), 634-639.
- Yeh, Y. S., and K. K. Mei (1968), Theory of conical equiangular-spiral antennas, 2. Current distributions and input impedances, *IEEE Trans. Antennas Propagat.*, AP-16(1), 14-21.

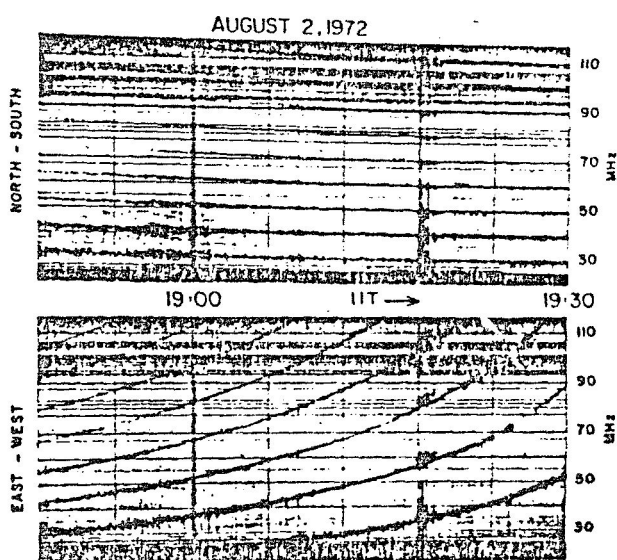


Fig. 18. Swept frequency records of solar radio emission using 32 elements spanning the full E-W aperture.